National Aeronautics and
Space Administration

CYGNSS Handbook

Cyclone Global Navigation Satellite System

Deriving Surface Wind Speeds
in Tropical Cyclones

April 2016

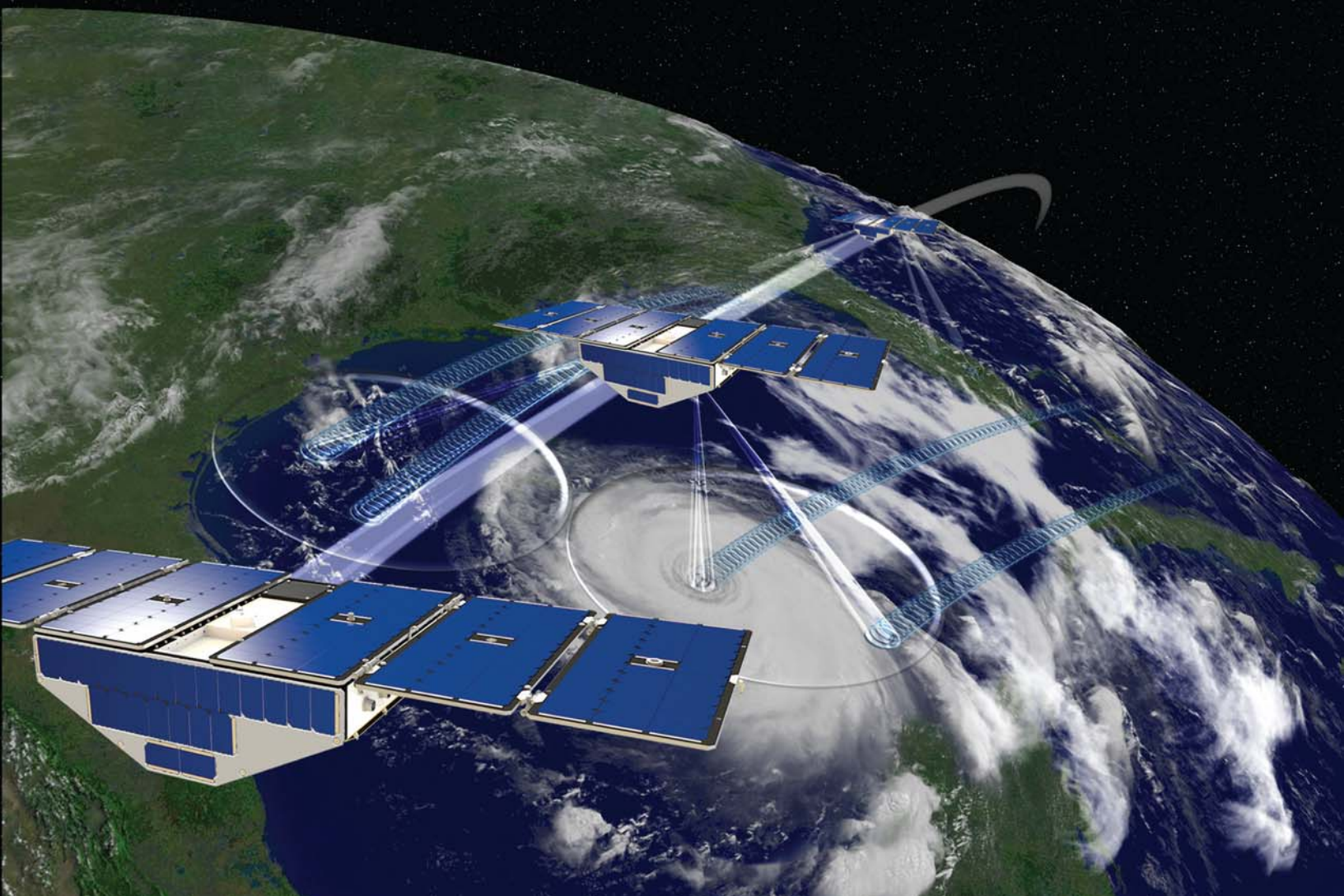

CYGNSS Handbook

Cyclone Global Navigation Satellite System

Deriving Surface Wind Speeds in Tropical Cyclones

CYGNSS Handbook

The research described in this publication was carried out by the University of Michigan under a contract with the National Aeronautics and Space Administration.

Published in the United States of America by Michigan Publishing

Manufactured in the United States of America

Original copy published on 1 April 2016

ISBN 978-1-60785-380-0 (paper)

http://www.publishing.umich.edu/services/

Contents

Revision History

Date	Version
1 April, 2016	First Edition

Key Authors

Chris Ruf (Principal Investigator)
Department of Climate and Space Sciences and Engineering
University of Michigan
Ann Arbor, MI 48109
E-mail: cruf@umich.edu

Paul S. Chang (Coinvestigator)
National Oceanic and Atmospheric Administration
NESDIS/Center for Satellite Applications and Research
College Park, MD 20748
E-mail: paul.s.chang@noaa.gov

Maria-Paola Clarizia (Research Fellow)
Department of Climate and Space Sciences and Engineering
University of Michigan
Ann Arbor, MI 48109
E-mail: clarizia@umich.edu

Scott Gleason (Instrument Scientist)
Southwest Research Institute (SwRI)
Boulder, CO 80302
E-mail: scott.gleason@swri.org

Zorana Jelenak (Coinvestigator)
National Oceanic and Atmospheric Administration
NESDIS/Center for Satellite Applications and Research
College Park, MD 20740
E-mail: zorana.jelenak@noaa.gov

Sharan Majumdar (Coinvestigator)
Department of Atmospheric Sciences
Rosenstiel School of Marine and Atmospheric Science (RSMAS)
Miami, FL 33149
E-mail: smajumdar@rsmas.miami.edu

Mary Morris (Doctoral Candidate)
Department of Climate and Space Sciences and Engineering
University of Michigan
Ann Arbor, MI 48109
E-mail: marygm@umich.com

John Murray (CYGNSS Deputy for Program Applications)
National Aeronautics and Space Administration (NASA) Applied Sciences Program
NASA Langley Research Center
Hampton, VA 23681
E-mail: john.j.murray@nasa.gov

Stephen Musko (Science Operations Center Engineering Lead)
Space Physics Research Laboratory
University of Michigan
Ann Arbor, MI 48109
E-mail: musko@umich.edu

Derek Posselt (Deputy Principal Investigator)
Department of Climate and Space Sciences and Engineering
University of Michigan
Ann Arbor, MI 48109
E-mail: dposselt@umich.edu

Damen Provost (University of Michigan Project Manager)
Space Physics Research Laboratory
University of Michigan
Ann Arbor, MI 48109
E-mail: provostd@umich.edu

Derek Starkenburg (Research Fellow)
Department of Climate and Space Sciences and Engineering
University of Michigan
Ann Arbor, MI 48109
E-mail: dstarken@umich.edu

Valery Zavorotny (Coinvestigator)
National Oceanic and Atmospheric Administration
Earth System Research Laboratory, Physical Sciences Division
Boulder, CO 80305
E-mail: valery.zavorotny@noaa.gov

Preface

The Cyclone Global Navigation Satellite System (CYGNSS) handbook was compiled in 2015 to serve as a source of information about the mission and its data products for potential data users. The collaborative effort of many individuals has enabled its production. The organization of the handbook is as follows:

Section 1 describes the motivation for the project and includes a discussion about tropical cyclones and current technologies for observing and forecasting them, as well as the unique impact that the CYGNSS mission will have on the advancement of our scientific understanding in this field.

Section 2 outlines the science objectives as well as the baseline mission requirements. Additionally, a mission synopsis explains the different phases of the mission and provides an overview of the flow of information, ground data processing, and flight segment hardware required to support the mission.

Section 3 explains the mission design in detail, including the orbital elements, observatory, and science payload.

Section 4 gives the reader an overview of the data products at each level of processing, including descriptions of their temporal and spatial resolution.

Sections 5 through 10 provide relevant excerpts from the project's algorithm theoretical basis documents (ATBDs). The ATBDs give the reader a more comprehensive explanation of each level of data products, including the physical and mathematical descriptions of the algorithms used in the generation of the science data products; an explanation of uncertainty estimates; and considerations of calibration, validation, exception control, and diagnostics.

Section 11 outlines plans for postlaunch calibration and validation, and Section 12 provides a summary of the NASA CYGNSS Applications Workshop held in Silver Springs, Maryland, in May 2015. The handbook concludes with a list of project publications in Section 13 and a list of acronyms in Section 14. The document concludes with an appendix describing the ocean surface bistatic scattering forward model. The forward model relates the state of the ocean to the measurements made by CYGNSS and is a fundamental mathematical framework for the science behind the CYGNSS data products.

The unique role of CYGNSS in our understanding of tropical cyclones derives from its ability to use the reflected signal from the global positioning system (GPS) constellation in order to determine sea surface wind speed with unprecedented spatial and temporal coverage. CYGNSS is a constellation of eight low-Earth-orbiting microsatellites, each capable of measuring four simultaneous reflections for a total of 32 spatially separated wind measurements every second. Its use of L-band GPS signals allows CYGNSS to make measurements within the eyewall of hurricanes with no significant degradation in performance arising from the intense precipitation (a significant concern with higher frequency scatterometers). As such, the CYGNSS mission will enable a more comprehensive understanding of air-sea exchange processes and thus an enhanced capability to forecast tropical storm formation and intensification.

Note: The information in this handbook was prepared during the prelaunch period and is subject to changes and corrections as the mission moves forward.

Acknowledgments

Some of the information in this handbook has been drawn from previously published material or material that was in press or under review at the time this handbook was being compiled. To provide proper recognition conveniently in one location for the reader, the sections of this handbook that come from other material, and their appropriate citations, will be listed below. Each section that contains reused material is listed individually.

Section 1

In Section 1, one figure was taken from the following article, which was under review at the time this handbook was compiled:

Clarizia, M. P., & Ruf, C. (2016). Wind speed retrieval algorithm for the Cyclone Global Navigation Satellite System (CYGNSS) mission. *Geoscience and Remote Sensing, IEEE Transactions On*. Manuscript in review. *© 2016 IEEE*

- Figure 1.1 (top) appears as Figure 1a in Clarizia & Ruf (2016).

Section 4

The text in the first paragraph of Section 4, Part I A, as well as the text in Section 4, Part I B, "Level 2 Wind Speed," are taken from the following article, which was under review during the time this handbook was compiled:

Clarizia, M. P., & Ruf, C. (2016). Wind speed retrieval algorithm for the Cyclone Global Navigation Satellite System (CYGNSS) mission. *Geoscience and Remote Sensing, IEEE Transactions On*. Manuscript in review. *© 2016 IEEE*

In addition, the error quantification described in the last paragraph of Section 4, Part I A, is taken from the text and from Tables II and V of the following article, which was in press at the time this handbook was compiled:

Gleason, S., Ruf, C., Clarizia, M. P., & O'Brien, A. (2016). Calibration and unwrapping of the normalized scattering cross section for the Cyclone Global Navigation Satellite System (CYGNSS). *Geoscience and Remote Sensing, IEEE Transactions On*. doi: 10.1109/TGRS.2015.2502245 *© 2016 IEEE*

Section 5

Much of the material in Section 5 is taken from the following document, which was in press at the time this handbook was compiled:

Gleason, S., Ruf, C., Clarizia, M. P., & O'Brien, A. (2016). Calibration and unwrapping of the normalized scattering cross section for the Cyclone Global Navigation Satellite System (CYGNSS). *Geoscience and Remote Sensing, IEEE Transactions On*. doi: 10.1109/TGRS.2015.2502245 *© 2016 IEEE*

Specifically, much of the text and many equations in Section 5 are taken verbatim from the above article. In addition, the following figures and tables are taken from the above article:

- Figure 5.1 appears as Figure 2 in Gleason et al. (2016).
- Figure 5.2 appears as Figure 3 in Gleason et al. (2016).
- Table 5.3 appears as Table II in Gleason et al. (2016).

Section 6

The text and equations in Section 6, Part I A, are a summary of the material from Section III in the following document, which was in press at the time this handbook was compiled:

Gleason, S., Ruf, C., Clarizia, M. P., & O'Brien, A. (2016). Calibration and unwrapping of the normalized scattering cross section for the Cyclone Global Navigation Satellite System (CYGNSS). *Geoscience and Remote Sensing, IEEE Transactions On*. doi: 10.1109/TGRS.2015.2502245 *© 2016 IEEE*

Section 7

Much of the material in Section 7 is taken from the following document, which was in press at the time this handbook was compiled:

Gleason, S., Ruf, C., Clarizia, M. P., & O'Brien, A. (2016). Calibration and unwrapping of the normalized scattering cross section for the Cyclone Global Navigation Satellite System (CYGNSS). *Geoscience and Remote Sensing, IEEE Transactions On*. doi: 10.1109/TGRS.2015.2502245 *© 2016 IEEE*

Specifically, much of the text and many equations in Section 7 are taken verbatim from the above article. In addition, the following figures and tables are taken from the above article:

- Figure 7.1 appears as Figure 7 in Gleason et al. (2016).
- Figure 7.2 appears as Figure 9 in Gleason et al. (2016).
- Figure 7.3 appears as Figure 10 in Gleason et al. (2016).
- Table 7.2 appears as Table III in Gleason et al. (2016).
- Table 7.3 appears as Table IV in Gleason et al. (2016).
- Table 7.4 appears as Table V in Gleason et al. (2016).

Section 9

Some of the material in Section 9 is taken from the following document, which was under review during the time this handbook was compiled:

Clarizia, M. P., & Ruf, C. (2016). Wind speed retrieval algorithm for the Cyclone Global Navigation Satellite System (CYGNSS) mission. *Geoscience and Remote Sensing, IEEE Transactions On*. Manuscript in review. *© 2016 IEEE*

Specifically, certain portions of the text and some equations in Section 9 are taken verbatim from the above article. In addition, the following figures and tables are taken from or adapted from the above article:

- Figure 9.6 appears as Figure 5a in Clarizia & Ruf (2016).
- Figure 9.8 appears as Figure 6 in Clarizia & Ruf (2016).
- Figure 9.9 appears as Figure 7 in Clarizia & Ruf (2016).
- Figure 9.10 appears as Figure 8 in Clarizia & Ruf (2016).
- Figure 9.15 appears as Figure 10 in Clarizia & Ruf (2016).
- Figure 9.16 appears as Figure 11 in Clarizia & Ruf (2016).
- Figure 9.17 appears as Figure 12 in Clarizia & Ruf (2016).
- Figure 9.18 appears as Figure 13 in Clarizia & Ruf (2016).
- Figure 9.19 appears as Figure 14 in Clarizia & Ruf (2016).
- Figures 9.20 and 9.24 adapted from Figures 16 and 17 in Clarizia & Ruf (2016).
- Figure 9.21 adapted from Figure 15 in Clarizia & Ruf (2016).
- Figure 9.22 appears as Figure 9a in Clarizia & Ruf (2016).
- Figure 9.23 appears as Figure 9b in Clarizia & Ruf (2016).
- Figures 9.26, 9.27, 9.28, and 9.29 adapted from Figure 18 in Clarizia & Ruf (2016).
- Figure 9.31 adapted from Figure 19 in Clarizia & Ruf (2016).
- Table 9.2 adapted from Table 4 in Clarizia & Ruf (2016).
- Tables 9.7 and 9.8 adapted from Table 2 in Clarizia & Ruf (2016).
- Tables 9.9 and 9.10 adapted from Table 3 in Clarizia & Ruf (2016).

In addition, one figure is reused from the following publication:

Nolan, D. S., Atlas, R., Bhatia, K. T., & Bucci, L. R. (2013). Development and validation of a hurricane nature run using the joint OSSE nature run and the WRF model. *Journal of Advances in Modeling Earth Systems*, *5*(2), 382–405. doi: 10.1002/jame.20031, *© 2013 American Geophysical Union (John Wiley and Sons, Inc.)*

- Figure 9.5 appears as Figure 4 in Nolan et al. (2013)

Section 11

In Section 11, certain figures are taken from the following article, which was under review at the time this handbook was compiled:

Said, F., Soisuvarn, S., Jelenak, Z., & Chang, P. (2016). Performance assessment of simulated CYGNSS winds in the tropical cyclone environment. *IEEE Journal of Selected Topics in Applied Earth Observations and Remote Sensing*. Manuscript in review. *© 2016 IEEE*

Specifically, the following figures have been reused from the above article:

- Figure 11.1 (top left panel) appears as Figure 12a in Said et al. (2016).
- Figure 11.2 (top two panels) appears as Figure 3 in Said et al. (2016).

Appendix: Ocean Surface Bistatic Scattering Forward Model

In the Appendix to the CYGNSS Handbook, some of the figures have been taken, with the author's permission, from the following book:

Gleason, S., & Gebre-Egziabher, D. (2009). *GNSS applications and methods*. Norwood, MA: Artech House. *© 2009 Scott Gleason and Demoz Gebre-Egziabher*

- Figure A.2 appears as Figure 16.4 in Gleason & Gebre-Egziabher (2009).
- Figure A.6 appears as Figure 16.8 in Gleason & Gebre-Egziabher (2009).

Also, one figure has been reused from

Voronovich, A. G., & Zavorotny, V. U. (2014). Full-polarization modeling of monostatic and bistatic radar scattering from a rough sea surface. *Antennas and Propagation, IEEE Transactions On*, *62*(3), 1362–1371. doi: 10.1109/TAP.2013.2295235

- Figure A.10 appears as Figure 1 in Voronovich & Zavorotny (2014).

Also, three figures have been reused from

Zavorotny, V. U., & Voronovich, A. G. (2014, July). Recent progress on forward scattering modeling for GNSS reflectometry. In *Geoscience and Remote Sensing Symposium (IGARSS), 2014 IEEE International* (pp. 3814–3817). Quebec, Canada. doi: 10.1109/IGARSS.2014.6947315

- Figure A.11a appears as Figure 1 in Zavorotny & Voronovich (2014).
- Figure A.11b appears as Figure 2 in Zavorotny & Voronovich, (2014).
- Figure A.12 appears as Figure 3 in Zavorotny & Voronovich (2014).

Also, one figure has been reused from

Clarizia, M. P., & Ruf, C. (2016). Wind speed retrieval algorithm for the Cyclone Global Navigation Satellite System (CYGNSS) mission. *Geoscience and Remote Sensing, IEEE Transactions On*. Manuscript in review. *© 2016 IEEE*

- Figure A.3 appears as Figure 1a in Clarizia & Ruf (2016).

1. Introduction and Background

I. Motivation for CYGNSS

A. Tropical Cyclones

Tropical cyclones (TCs) pose a threat to life and property in coastal locations around the globe and to vessels and structures (e.g., wind farms, oil drilling platforms) on the ocean. Impacts include damaging winds, storm surges, and heavy rains. A TC is defined by the National Oceanic and Atmospheric Administration (NOAA) National Hurricane Center (NHC) as "a warm-core, nonfrontal synoptic-scale cyclone, originating over tropical or subtropical waters, with organized deep convection and a closed surface wind circulation about a well-defined center" (http://www.nhc.noaa.gov/aboutgloss.shtml). The vast majority of TCs form and reach their maximum intensity between 35°S and 35°N latitude, and those that make landfall commonly do so within this latitude band (with a few notable exceptions; e.g., Hurricane Sandy in 2012).

TCs form over the ocean through the organization of convective thunderstorms, and air-sea exchange processes are critical to their formation and intensification. Accurate measurements of ocean surface winds, together with temperature and moisture fluxes, are crucial to the understanding and prediction of TCs. In contrast to midlatitude cyclones, TCs possess a warm core due to latent heat released by condensation, and mature TCs tend to have a more axisymmetric structure. TCs play an important role in the global atmospheric energy budget via their transport of heat and moisture from the tropics to higher latitudes.

B. Predicting TC Track and Intensity

Numerical weather prediction (NWP) models are the primary tools used to predict the track (position and movement) and intensity of TCs. These models have traditionally been global in extent and comprise solutions of the atmospheric momentum, mass, and energy and water vapor conservation equations. They are commonly run on horizontal grids with scales of 10–20 km: sufficient to simulate large scale and mesoscale circulations but too coarse to resolve the convective systems that are crucial for TC formation and evolution. As a result, convection, cloud microphysical processes, and turbulence must be approximated (or "parameterized"). In order to more accurately predict the evolution of TCs, NWP centers use data assimilation to combine short-term predictions with a large volume of satellite and in situ data to form initial conditions for NWP models. The main purpose of data assimilation is to provide an improved estimate of atmospheric conditions over what is provided by observations or a previous forecast alone. Improved initial conditions lead to more accurate forecasts of TC track, intensity, and structure. Over the past 20 years, ensembles of global model forecasts have increasingly been used to estimate the range of possible TC forecasts due to uncertainties in both physical parameterization schemes and model initial conditions. More recently, ensembles have been used as part of the data assimilation system as well.

The leading global models used to provide guidance to United States weather prediction are as follows:

- NOAA Global Forecast System (GFS)
- European Centre for Medium-Range Weather Forecasts (ECMWF)
- UK Meteorological Office (UKMET)
- Navy Global Environmental Model (NAVGEM)

In addition to global models, limited-area regional models are used to predict TC structure, track, and intensity. Regional model simulations encompass a smaller geographic area and therefore can be run with higher horizontal resolution than global models. In most TC-specific limited-area simulations, the innermost nested domains with the highest resolution are centered on the TC. As of 2015, the three United States operational regional models currently used for TC prediction, along with their finest horizontal grid spacings, are

- NOAA Hurricane Weather Research and Forecasting (HWRF)—2 km
- Coupled Ocean Atmosphere Mesoscale Prediction System (COAMPS-TC)—5 km
- NOAA Geophysical Fluid Dynamics Laboratory (GFDL)—9 km

In addition to the above listed dynamical models, statistical models such as the Statistical Hurricane Intensity Prediction Scheme (SHIPS) and the Logistic Growth Equation Model (LGEM) are used to predict intensity. Several regions around the world use their own global and regional models to predict TC track and intensity.

After decades of focused research into TC dynamics and evolution, operational centers are now able to predict TC track out to a lead time of five days with a high degree of accuracy. But during this time, forecast skill for TC intensity has not kept the same pace. There are likely many reasons for this slowing improvement in TC intensity forecasts, but the one that is cited often in the community is a *lack of frequent and accurate observations of winds in the inner core of TCs*. Specifically, current satellite observing systems are unable to penetrate through heavy rainfall, and in situ measurements by aircraft and dropsondes are limited in space and time. Paucity of observations of surface wind speeds in the most dynamically active portion of a TC leads to (1) inaccuracies in the initial conditions used in subsequent model forecasts and (2) insufficient information for evaluating parameterizations of convection and surface fluxes. The CYGNSS mission is designed to address these shortcomings by providing more accurate and timely observations of surface winds in all precipitation conditions.

C. Existing Observing Capabilities

Over 90% of the observational data that are routinely assimilated into global forecast models come from geostationary satellites (e.g., the Geostationary Operational Environmental Satellites [GOES]), and polar-orbiting satellites (e.g., the Polar-Orbiting Environmental Satellites [POES]). The data include radiances, atmospheric motion vectors, infrared and microwave soundings, and GPS radio occultations. Another satellite of particular relevance to TCs is the Global Precipitation Measurement (GPM) platform, which is the follow-up to the successful 1997–2014 Tropical Rainfall Measuring Mission (TRMM). GPM provides a three-dimensional view of TC structure using spaceborne scanning radar at two different wavelengths. In addition, there are scatterometers that measure wind speed and direction at the ocean surface. However, these scatterometers are unable to provide accurate measurements in regions of heavy precipitation (e.g., convective regions), and therefore sea surface wind data in the inner core of TCs are lacking. Even those satellites that can penetrate heavy rain and view the inner core of hurricanes have revisit times that are too infrequent to capture the fast evolving processes that lead to rapid TC development.

If a TC poses a potential threat to the United States, NOAA and the United States Air Force deploy the "Hurricane Hunter" aircraft inside and around the TC to better measure its central pressure, as well as thermodynamic and dynamic characteristics of the TC and its immediate environment. Ocean surface wind speeds are measured via a Stepped Frequency Microwave Radiometer (SFMR). However, the quantity, sampling duration, and range of aircraft missions are limited, and therefore only a small fraction of the total TC activity in the Atlantic Basin is sampled by aircraft. No other nations measure ocean surface winds from aircrafts.

D. Unique Role of CYGNSS

The goal of the CYGNSS mission is to understand the coupling between ocean surface properties, moist atmospheric thermodynamics, radiation, and convective dynamics in the inner core of TCs. Near-surface winds are major contributors to, and indicators of, momentum and energy fluxes at the air-sea interface. An understanding of the coupling between the surface winds and the moist atmosphere within the TC inner core is required to properly model and forecast its genesis and intensification. The CYGNSS team hypothesizes that the limited degree of improvement in intensity forecasting in recent decades is largely due to a lack of observations and proper modeling of the TC inner core. The inadequacy in observations results from two causes:

1. Much of the TC inner core ocean surface is obscured from conventional remote sensing instruments by intense precipitation in the eyewall and inner rain bands.
2. Conventional polar-orbiting, wide-swath imagers provide poor temporal sampling of the rapidly evolving processes associated with TC genesis and intensification.

CYGNSS addresses these two limitations by combining the all-weather performance of GPS bistatic radar with the spatial and temporal sampling properties of

a constellation of eight low-Earth orbit observatories at an inclination of 35°.

Each observatory contains a delay Doppler mapping instrument (DDMI), which receives direct signals from GPS satellites as well as signals reflected off the ocean surface. The direct signals pinpoint the location of the observatory, while the reflected signals respond to ocean surface roughness, from which wind speed is derived. Signals are measured at 1 Hz, and each of the 8 observatories is capable of measuring 4 simultaneous reflections, resulting in 32 wind measurements per second around the globe. This provides the ability to measure ocean surface winds with unprecedented temporal resolution and spatial coverage under all precipitating conditions, up to and including those experienced in the hurricane eyewall.

Figure 1.1 (top) illustrates the propagation and scattering geometries associated with the GPS bistatic radar approach to ocean surface scatterometry. The direct GPS signal provides a coherent reference for the coded GPS transmitted signal. It is received by a right-hand circularly polarized (RHCP) receive antenna on the zenith side of the spacecraft. The quasi-specular, forward-scattered signal from the ocean surface is received by a downward-looking left-hand circularly polarized (LHCP) antenna on the nadir side of the spacecraft. The properties of the scattered signal are sensitive to the sea surface roughness, from which local wind speed can be derived (Zavorotny & Voronovich, 2000). The scattering cross-section image produced by the UK-DMC-1 demonstration spaceborne mission is shown in Figure 1.1 (bottom). Variable lag correlation and Doppler shift, the two coordinates of the image, enable the spatial distribution of the scattering cross section to be resolved (Gleason et al., 2005). This type of scattering image is referred to as a delay Doppler map (DDM). Estimation of the ocean surface roughness and wind speed is possible from two properties of the DDM. The maximum scattering cross section (the dark red region in Figure 1.1, bottom) is related to roughness and therefore wind speed. This requires power calibration of the DDM. Wind speed can also be estimated from the shape of the scattering cross section pattern in the DDM (the red and yellow regions in Figure 1.1, bottom). The pattern is produced by scattering from an area surrounding the nominal specular point (SP) on the surface. For a smooth, mirrorlike surface, the pattern would be defined by the GPS bistatic radar ambiguity function. But as the surface becomes rougher, the GPS signal is scattered by a larger area of the surface and into many directions. This causes a reduction in the maximum cross section near the SP and the "spreading" of power into wider delay/Doppler bins. The shape of the DDM pattern also contains information about the sea surface winds. In particular, the shape of its dependence on delay is sensitive to the significant wave height of the sea surface, which is correlated with wind speed.

CYGNSS measures the power in the GPS signal scattered by the ocean surface after the signal is selectively filtered by time delay and Doppler shift to create a DDM. The time delay is the difference in time of arrival between the direct signal (propagating directly from the GPS satellite to the CYGNSS satellite) and the signal scattered by the ocean surface. The Doppler shift is the difference in frequency between the received direct signal and the received ocean-scattered signal. Both delay and Doppler are varied in the DDM across a range that includes the nominal SP on the surface. Shorter delays correspond to locations above the surface, from which there is no significant scattered signal. Longer delays can be mapped to iso-delay contours on the surface surrounding the SP. Varying Doppler of the scattered signals can also be mapped to iso-Doppler contours on the surface that intersect the delay contours to create the DDM. The DDM is thus a map of the diffuse surface scattering in the vicinity of the nominal SP. The transformation between spatial location on the sea surface and location in the DDM is one to one at the DDM specular location but can have ambiguities outside the specular region (i.e., multiple spatial locations mapped to the same DDM location).

CYGNSS spatial sampling produces Level 2 wind speed data products, which consist of 32 simultaneous single pixel "swaths" that are 25 km wide and typically hundreds of kilometers long, as the SPs move across the surface due to orbital motion by CYGNSS and the GPS satellites. Examples of the spatial coverage obtained after 90 minutes (one orbit) and 24 hours are shown in Figure 1.2a–b. Temporal and spatial sampling occurs randomly due to the asynchronous nature of the CYGNSS and GPS satellite orbits. As a result, the CYGNSS revisit time is best described by its probability distribution. The distribution, shown in Figure 1.2c, is derived empirically

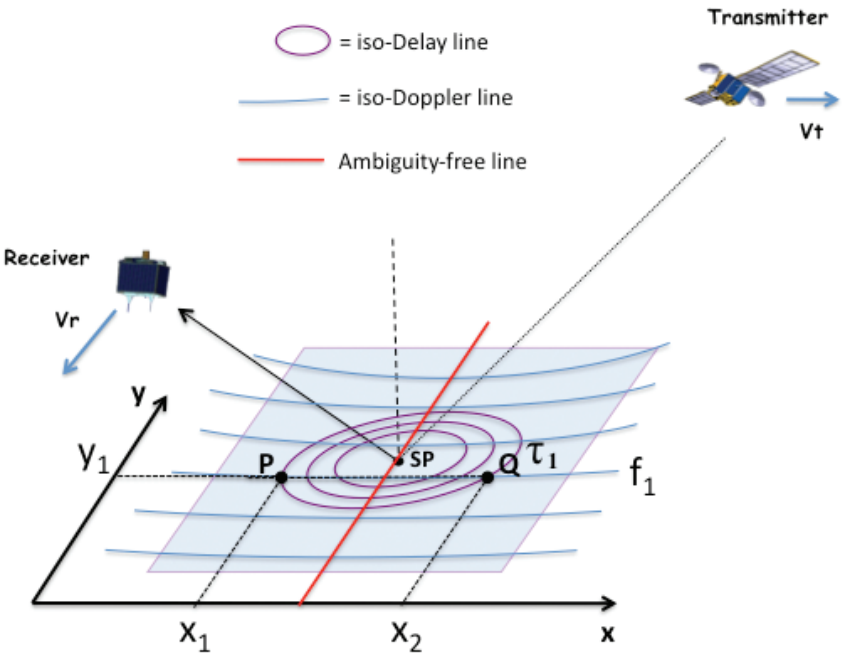

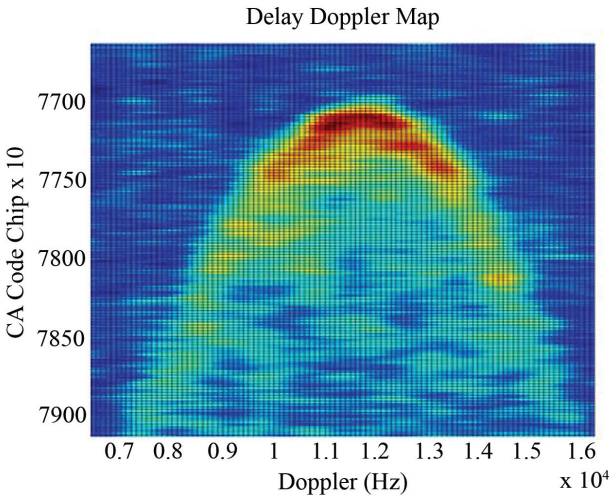

Figure 1.1. Top: GPS signal propagation and scattering geometries for ocean surface bistatic quasi-specular scatterometry. *Reused from Clarizia & Ruf (2016), © 2016 IEEE.* Bottom: Spatial distribution (in delay and Doppler coordinates) of the ocean surface scattering measured by the UK-DMC-1 demonstration spaceborne mission, referred to as the delay Doppler map, or DDM (Gleason, 2005).

using a mission simulator to determine the time and location of each sample within the ±38° latitude coverage zone and then examining the time difference between samples at the same location. The empirical distribution features a high probability of very short revisit times (resulting from sequential samples by trailing satellites spaced dozens of minutes apart) and a long, tapering "tail" at higher revisit times. Its median value is 2.8 hours, and the mean revisit time is 7.2 hours.

E. Description of Previous Airborne and Spaceborne Missions

The first global navigation satellite system reflectometry (GNSS-R) sensor was field tested in 1997 over the Chesapeake Bay, collecting GPS signals scattered from the water surface (Garrison et al., 1998). The first reported wind speed retrieval using GPS ocean-reflected signals occurred in 1999 (Lin et al., 1999) with data taken in 1998. Additional data

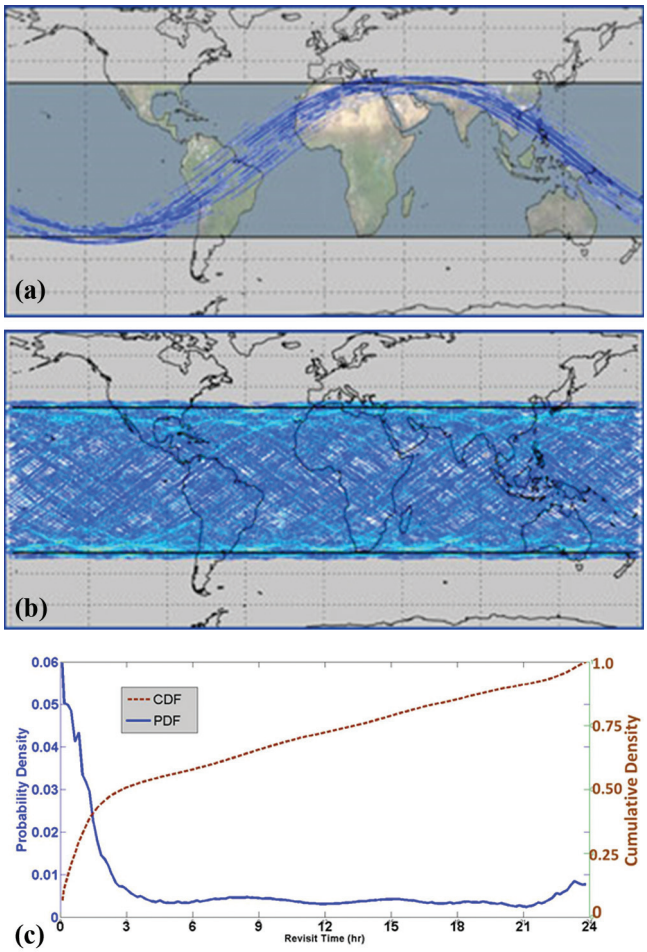

Figure 1.2. Each low-Earth orbiting CYGNSS observatory will orbit at an inclination of 35° and is capable of measuring four simultaneous reflections, resulting in 32 wind measurements per second across the Earth. The configuration is optimized for high temporal resolution wind field imagery of TC genesis, intensification, and decay. Shown here are the CYGNSS spatial coverage tracks after (a) 90 minutes and (b) 24 hours. Temporal sampling is characterized by the probability and cumulative density functions of revisit time, shown in (c). Sampling occurs randomly due to the asynchronous nature of the CYGNSS and GPS satellite orbits, and revisit time is best characterized via statistics of these distributions. The median and mean revisit times are, respectively, 2.8 and 7.2 hours.

were acquired in under-flights of TOPEX/Poseidon in 1998 and during the US Navy EOPACE experiment off the Outer Banks of North Carolina (Garrison et al., 2002). A theoretical framework was then developed that describes the received global navigation satellite system (GNSS) signal as a function of the sea state, the measurement geometry, and the signal processing performed by the receiver (Zavorotny & Voronovich, 2000).

The first effort to study the high wind regimes found in TCs occurred in 1998 via flights into the outer bands of Hurricane Bonnie as it made landfall near Topsail Beach, North Carolina. With the cooperation of NOAA, a GPS delay mapping receiver was installed on one of the Hurricane Hunters in 2000 and acquired the first GPS-reflected data from inside a TC (Katzberg et al., 2001). Since that time, penetration data from TCs has been acquired nearly annually, with only one missing year. Wind speed retrievals have been compared with a large set of dropsonde data and show the GPS method capable of responding well to TC-level wind speeds (Katzberg & Dunion, 2009).

The first successful detection of a GPS surface-reflected signal in space was reported by Lowe et al. (2002). Subsequently, data from the GPS experiment

on the UK-DMC satellite demonstrated that signal retrievals of sufficient signal-to-noise ratio (SNR) could be used to perform successful ocean wave and wind estimation (Gleason et al., 2005; Clarizia et al., 2009, 2014). These results show that it is possible to detect reflected GPS signals from space across a range of surface wind and wave conditions using a relatively modest instrument configuration. Notably, the UK-DMC sensor had a lower receiver antenna gain (11.8 dBi) and is in a higher orbit (686 km) than the CYGNSS design (14 dBi and 510 km, respectively). Therefore, CYGNSS measurements are expected to have better sensitivity to surface roughness.

Results from the UK-DMC experiment demonstrate a connection between the near-surface wind speed and the measured DDMs. The UK-DMC measurements were made when the SP passed within 50 km of an active National Data Buoy Center (NDBC) ocean buoy, which provides near surface wind information (at 10 m height referenced; Gleason, 2013). One example of wind retrieval performance using UK-DMC data is described by Clarizia et al. (2014), in which a minimum variance (MV) wind speed estimator was developed and tested. The estimator is a composite of winds retrieved using five different observables that are derived from the DDMs. Regression-based wind retrievals are developed for each individual observable using empirical geophysical model functions (GMFs) that are derived from NDBC buoy winds. The RMS error in the MV estimator for wind speeds over the range of 2 to 12 m s^{-1} is 1.65 m s^{-1}.

A second GPS bistatic radar satellite experiment, flown on TDS-1, was launched in July 2014 and orbits at an altitude of 635 km with an inclination of 98° and a 9:00 p.m. local time of ascending node (Jales and Unwin, 2015). The spaceborne payload consists of a zenith-pointing antenna, for direct GPS signal acquisition and the determination of SP locations on the ground; a nadir-pointing antenna with a peak gain of 13.3 dBi, for capturing the GPS reflection; and a remote sensing receiver, called the SGR-ReSI. The SGR-ReSI operates for two days out of an eight-day cycle, generating DDMs. Early analysis of TDS-1 measurements of ocean surface wind speed indicate a root mean square (RMS) error of 2.2 m s^{-1} over a dynamic range of 3 to 18 m s^{-1} (Foti et al., 2015).

II. Project Status Overview

CYGNSS was selected by the National Aeronautics and Space Administration (NASA) as its first Earth Venture mission under NASA's Earth System Science Pathfinder (ESSP) program. CYGNSS is classified as Category 3 Class D per NASA Procedural Requirements (NPR) 8704.5. Phase A efforts on the CYGNSS mission began in December 2012. CYGNSS is scheduled to launch in October 2016 and has a two-year design lifetime. Principal Investigator (PI) Dr. Chris Ruf of the University of Michigan (UM), Climate and Space Sciences and Engineering Department, leads the team of institutions. UM is responsible for the science team, communications and public engagement, science operations and data analysis, payload stimulator, and overall successful execution of the mission and implementation of the proposed science investigations. The Southwest Research Institute (SwRI) is a subcontractor to UM and serves as the "implementing organization." SwRI is responsible for overall mission project management, systems engineering, safety and mission assurance, procurement and management of the payload, spacecraft development, oversight of the deployment module (DM), integration and test, launch vehicle interfaces, and commissioning and mission operations. Surrey Satellite Technologies is providing the DDMI, and Sierra Nevada Corp. (SNC) is responsible for delivery of the DM. The eight observatories will be affixed to the DM and then attached to the Orbital ATK Pegasus launch vehicle. An overview of the mission's motivation, goals, objectives, requirements, and design is given in Ruf et al. (2016).

Major project milestones to date include the system requirements review / mission design review (June 2013), preliminary design review (January 2014), critical design review (January 2015), and system integration review (July 2015). Additional major milestones scheduled to occur prior to launch are the reenvironmental review (January 2016), operations readiness review (July 2016), and flight and launch readiness reviews (October 2016). CYGNSS is scheduled to be launched from Cape Canaveral in October 2016.

References

Clarizia, M. P., Gommenginger, C. P., Gleason, S. T., Srokosz, M. A., Galdi, C., & Di Bisceglie, M. (2009). Analysis of GNSS-R delay-Doppler maps from the UK-DMC satellite over the ocean. *Geophysical Research Letters*, *36*(2). doi: 10.1029/2008GL036292

Clarizia, M. P., & Ruf, C. (2016). Wind speed retrieval algorithm for the Cyclone Global Navigation Satellite System (CYGNSS) mission. *Geoscience and Remote Sensing, IEEE Transactions On*. Manuscript in review.

Clarizia, M. P., Ruf, C. S., Jales, P., & Gommenginger, C. (2014). Spaceborne GNSS-R minimum variance wind speed estimator. *Geoscience and Remote Sensing, IEEE Transactions On*, *52*(11), 6829–6843. doi: 10.1109/TGRS.2014.2303831

Foti, G., Gommenginger, C., Jales, P., Unwin, M., Shaw, A., Robertson, C., & Roselló, J. (2015). Spaceborne GNSS reflectometry for ocean winds: First results from the UK TechDemoSat-1 mission. *Geophysical Research Letters*, *42*(13), 5435–5441. doi: 10.1002/2015GL064204

Garrison, J. L., Katzberg, S. J., & Hill, M. I. (1998). Effect of sea roughness on bistatically scattered range coded signals from the global positioning system. *Geophysical Research Letters*, *25*(13), 2257–2260. doi: 10.1029/98GL51615

Garrison, J. L., Komjathy, A., Zavorotny, V. U., & Katzberg, S. J. (2002). Wind speed measurement using forward scattered GPS signals. *Geoscience and Remote Sensing, IEEE Transactions On*, *40*(1), 50–65. doi: 10.1109/36.981349

Gleason, S. (2013). Space-based GNSS scatterometry: Ocean wind sensing using an empirically calibrated model. *Geoscience and Remote Sensing, IEEE Transactions On*, *51*(9), 4853–4863. doi: 10.1109/TGRS.2012.2230401

Gleason, S., Hodgart, S., Sun, Y., Gommenginger, C., Mackin, S., Adjrad, M., & Unwin, M. (2005). Detection and processing of bistatically reflected GPS signals from low earth orbit for the purpose of ocean remote sensing. *Geoscience and Remote Sensing, IEEE Transactions On*, *43*(6), 1229–1241. doi: 10.1109/TGRS.2005.845643

Jales, P., & Unwin, M. (2015). *Mission description-GNSS reflectometry on TDS-1 with the SGR-ReSI* (No. 0248367, Tech. Rep. SSTL. Revision 001). Surrey Satellite Technology Ltd. Retrieved from http://www.merrbys.co.uk

Katzberg, S. J., & Dunion, J. (2009). Comparison of reflected GPS wind speed retrievals with dropsondes in tropical cyclones. *Geophysical Research Letters*, *36*(17). doi: 10.1029/2009GL039512

Katzberg, S. J., Walker, R. A., Roles, J. H., Lynch, T., & Black, P. G. (2001). First GPS signals reflected from the interior of a tropical storm: Preliminary results from Hurricane Michael. *Geophysical Research Letters*, *28*(10), 1981–1984. doi: 10.1029/2000GL012823

Lin, B., Katzberg, S. J., Garrison, J. L., & Wielicki, B. A. (1999). Relationship between GPS signals reflected from sea surfaces and surface winds: Modeling results and comparisons with aircraft measurements. *Journal of Geophysical Research: Oceans (1978–2012)*, *104*(C9), 20713–20727. doi: 10.1029/1999JC900176

Lowe, S. T., Zuffada, C., Chao, Y., Kroger, P., Young, L. E., & LaBrecque, J. L. (2002). 5-cm-Precision aircraft ocean altimetry using GPS reflections. *Geophysical Research Letters*, *29*(10), 13-1–13-4. doi: 10.1029/2002GL014759

Ruf, C. S., Atlas, R., Chang, P. S., Clarizia, M. P., Garrison, J. L., Gleason, S., … & Zavorotny, V. U. (2016). New ocean winds satellite mission to probe hurricanes and tropical convection. *Bulletin of the American Meteorological Society*. doi: 10.1175/BAMS-D-14-00218.1

Zavorotny, V. U., & Voronovich, A. G. (2000). Scattering of GPS signals from the ocean with wind remote sensing application. *Geoscience and Remote Sensing, IEEE Transactions On*, *38*(2), 951–964. doi: 10.1109/36.841977

2. Mission Overview

I. Science Objectives

A. Baseline Science Objectives

The CYGNSS science goals are enabled by meeting the following mission objectives:

- Measure ocean surface wind speed in most naturally occurring precipitating conditions, including those experienced in the TC eyewall.
- Measure ocean surface wind speed in the TC inner core with sufficient frequency to resolve genesis and rapid intensification.

B. CYGNSS Application Areas

A variety of applications for CYGNSS exist outside the required baseline science objectives. These include but are not necessarily limited to soil moisture, hydrology, coastal flooding, ocean wave modeling, and numerical weather prediction.

The CYGNSS mission, which will obtain denser surface wind field observations to improve TC intensity forecasts, is also expected to provide new insights on air-sea interactions related to tropical convection, measurements of soil moisture and surface water extent, as well as observations of ocean surface dynamics in insufficiently sampled regions from the 38°N to 38°S latitude.

In the areas of modeling, forecasting, and tropical convection applications, forecast model representation of the Madden-Julian Oscillation (MJO) could be improved. The ability to provide fast-repeat wind sampling unbiased by the presence of precipitation could enable improved observations of convectively induced phenomena such as westerly wind bursts and gust fronts. The CYGNSS fast-repeat wind sampling, especially in precipitating regions, will complement existing polar satellite ocean surface winds and should improve the prediction of atmospheric phenomena with connections to the tropics, such as monsoons, atmospheric rivers, and the extratropical transitions of TCs.

For monitoring of TCs, CYGNSS surface wind data could be used to assess the intensity and intensity change rate, which is critical for coastal preparations to protect life and property in landfalling storms. In the areas of coastal, terrestrial, and hydrological applications, soil moisture and wetlands extent mapping with CYGNSS is possible. These two applications are the most mature and aligned with the existing capabilities of the L-band sensor and mission design. The fast-repeat sampling characteristics of CYGNSS measurements of soil moisture would add value to existing sensors and possibly allow studies of subdiurnal soil moisture, crop evolution, and flood forecasting.

In the areas of physical oceanography and surface wave applications, more accurate estimation of surface fluxes along with improved surface wind analysis products generated using CYGNSS observations will be highly valuable for evaluating and improving the performance of ocean and wave models within coupled systems. Another application is the use of Level 3 CYGNSS products in conjunction with other atmosphere-ocean observations to study climate modes such as the MJO and El Niño Southern Oscillation (ENSO) cycles that have signatures over the tropics and subtropics.

II. Baseline Science Mission Requirements

The CYGNSS baseline science requirements, defined to meet the mission objectives, are listed as follows:

1. Provide estimates of ocean surface wind speed over a dynamic range of 3 to 70 m s^{-1} as determined by a spatially averaged wind field with a resolution of 5 × 5 km.
2. Provide estimates of ocean surface wind speed during precipitation rates up through 100 mm hr^{-1} as determined by a spatially averaged rain field with a resolution of 5 × 5 km.
3. Retrieve ocean surface wind speeds with a retrieval uncertainty of 2 m s^{-1} or 10%, whichever is greater, with a spatial resolution of 25 × 25 km.
4. Collect space-based measurements of ocean surface wind speeds at all times during the science mission with the following temporal and

spatial sampling: (a) temporal sampling better than 12-hour mean revisit time and (b) spatial sampling 70% of all storm tracks between 35°N and 35°S latitude to be sampled within 24 hours.

5. Conduct a calibration and validation (Cal/Val) program to verify data delivered meets the requirements within individual wind speed bins above and below 20 m s^{-1}.
6. Support the operational hurricane forecast community for assessment of CYGNSS data impacts on numerical prediction of TCs in retrospective studies.

III. Mission Synopsis

The CYGNSS mission schedule is composed of distinct, sequential phases. Phase A defines high level mission requirements and culminates with the system requirements review (SRR). Phase B defines the preliminary design of the mission and the relationship between the mission's requirements and its design. It culminates with the preliminary design review (PDR). Phase C defines the detailed design of the mission—in particular, the flight segment, consisting of the eight observatories and deployment module (DM), and the ground segment, consisting of the data telemetry ground stations, the Mission Operations Center (MOC), the Science Operations Center (SOC), and the NASA Distributed Active Archive Center (DAAC). Phase C culminates in the critical design review (CDR) and the system integration review (SIR). Phase D consists of the flight segment build and test phase, followed by the launch vehicle integration. It culminates in the launch and early on-orbit engineering commissioning. Phase E consists of the on-orbit science mission execution, including science payload calibration, science data product Cal/Val, and engagement with the wider science community of data users. Phase F occurs after the end of on-orbit operations and typically consists of final science algorithm revisions, a last cycle of reprocessing of the mission science data, and final archiving of data products and associated documentation. Figure 2.1 shows a mission timeline, and Subsections A through D describe the launch through decommissioning phases in more detail.

A. Launch

In this phase, the eight CYGNSS satellites are affixed to a DM and shipped to Vandenberg Air Force Base for integration with the Orbital ATK Pegasus three-stage launch vehicle. Once integrated, the Pegasus is attached to the underside of Orbital ATK's L-1011 airplane and performs a ferry flight to Cape Canaveral Air Force Station in Florida. After completing final inspections and checkouts, the L-1011 takes off and flies to the specified drop location off the coast of Florida at an altitude of 39,000 feet for launch. The CYGNSS target orbit is a 510 km altitude at a 35°

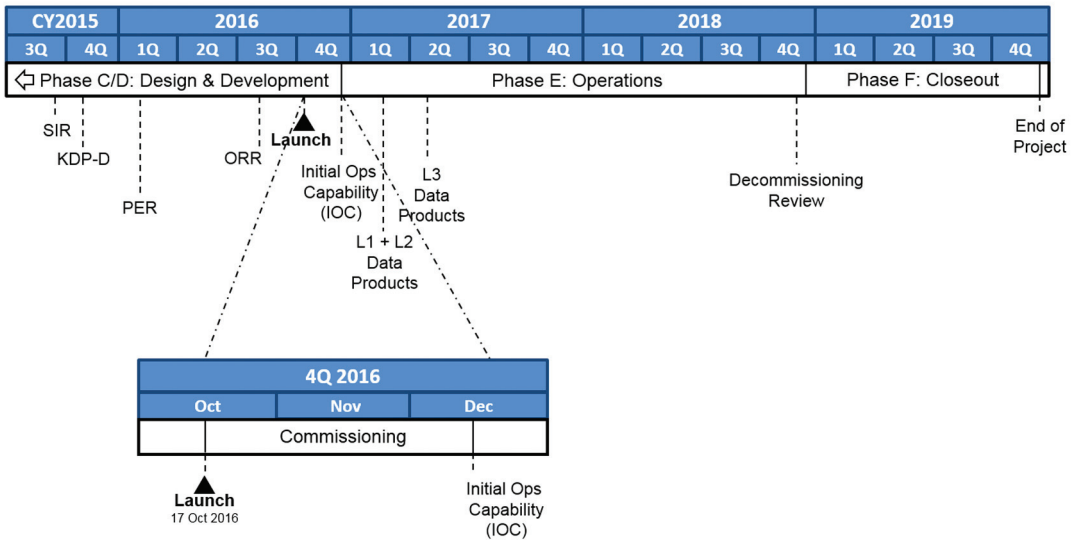

Figure 2.1. CYGNSS mission timeline.

inclination. Nominally, total flight time from drop to stage-three burnout is under eight minutes. The eight observatories are then deployed in opposite pairs off the DM.

B. Commissioning

The commissioning phase is the period of initial operations that includes deployment of solar arrays, checkout of the spacecraft subsystems and payload, and drag maneuvers to spread the constellation into the desired spacing. The baseline constellation configuration will be an even spacing of ~45° between observatories. The science coverage requirement for the mission can be met when the observatories are ≥20° apart from each other. The commissioning phase extends from launch until both the ground elements and the spacecraft and instrument subsystems are fully functional and have demonstrated the required on-orbit performance to begin routine science data collection. The Level 1 requirements call for these activities to be completed within 60 days after launch.

C. Operations

The science operations phase is the period of near-continuous data collection, extending from the end of commissioning for two years. Each observatory is maintained in a nadir pointing attitude, except for brief periods when drag maneuvers are required to maintain the constellation spacing or for potential collision avoidance maneuvers. Nominally, each observatory is contacted once every 48 hours for commanding and data downlinking, an average of four contacts per day for the ground segment. If a sufficient number of observatories are still functioning adequately at the end of the two-year baseline mission duration, the science operations phase may be extended, subject to review and approval by NASA.

Science data products will be made available to the public via NASA's Physical Oceanography Distributed Active Archiving Center (PO.DAAC). CYGNSS is required to deliver the initial Level 1 and 2 data products two months after initial operational capability (IOC) and Level 3 data products four months after IOC. After the initial delivery, all data products will be made publically available within six days of the data being downlinked.

D. Decommissioning

CYGNSS postmission disposal will be accomplished via uncontrolled atmospheric reentry within 25 years of the end of mission. As such, no systems are required to be operational, and there are no plans for any special maneuvers to support the disposal. The micro reaction wheels onboard each observatory will be commanded off at the end of mission.

IV. Mission System Description

In developing the design concepts for the CYGNSS observatories, the systems engineering team has kept in mind ensuring the safety of the observatories without ground intervention. Providing onboard systems that minimize the need to develop time-tagged command sequences for each observatory for routine operations also supports a simplified operational cadence for maintaining the constellation.

A. Launch through Commissioning

Each observatory is deployed with solar arrays stowed. After deployment from the launch vehicle, each observatory transitions automatically through the initial three states to reach the standby mode. Deployment of the solar arrays occurs next. Additional commissioning activities for the observatories will begin once the solar arrays are deployed and will continue for a period of two to four weeks.

Commissioning activities for a CYGNSS DDMI commence once its microsat has completed its commissioning sequence. DDMI commissioning begins and lasts an additional four weeks. During this time, the DDMI operates in two engineering modes, which are used to verify on-orbit performance and tune the onboard DDM generation and subsampling algorithms. At the end of the DDMI commissioning activities, the instrument will be transitioned into its science mode, where it will collect data continuously.

Commissioning activities for the microsats and then the instruments may progress in an interleaved manner. Within a single communication pass, activities will be performed on a single observatory; however, it is not necessary to complete all commissioning tasks on one observatory before progressing to the next observatory in the constellation. Since all observatories are independent, it is also unnecessary to ensure each observatory is at the same "step" in a

commissioning sequence. This independence allows a flexible scheduling approach to be used in setting up commissioning passes and does not delay commissioning activities for all observatories if a single observatory requires extra time while an off-nominal issue is being addressed.

B. Nominal Operations

Upon completion of commissioning activities, the observatories will be transitioned into the "science" mode of operation. At this point, the DDMI is set to science mode for the duration of the mission, except for brief returns to Cal/Val mode performed biannually. In science mode, subsampled DDMs are generated onboard and downlinked with 100% duty cycle.

The observatories are designed to implement nominal observatory operations and science data collection without onboard time-tagged command sequences. With the DDMI in its continuous science mode and the observatory set to maintain all nominal operations without additional commanding, the primary "routine" activity performed on a regular basis is communication with the ground network to downlink the accumulated science and engineering data.

Science and engineering data files are generated, stored onboard, and automatically added into an onboard downlink file list. Retrieval of the science data occurs during communications passes, which are planned to occur at the rate of one pass per observatory every 1.5 to 2 days during the nominal operations period. Onboard microsat data storage provides storage for greater than 10 days of science data, allowing flexibility in pass scheduling and supporting recovery from loss of communications during a pass.

Downlink pass acquisition operations are automated using an onboard automated event recognition (AER) capability. The mission operations team will schedule passes for each observatory, and when the observatory is within range of the scheduled ground antenna asset, the antenna will illuminate the microsat with a Clear Channel communication. Onboard, the AER will be set to switch the microsat transmitter on when the receiver detects the ground network signal. Once the transmitter is enabled, housekeeping telemetry will be transmitted, allowing the ground antenna to synchronize with the microsat. Once lock has been established, a notification of the acquisition status will be relayed to the CYGNSS MOC.

After establishing contact, the following steps are performed:

- Housekeeping data is continuously transmitted by the microsat, received on the ground and flowed to the MOC.
- MOC sends the command to thaw the Consultative Committee for Space Data Systems (CCSDS) File Delivery Protocol (CFDP) engine onboard the microsat.
- MOC sends the CFDP protocol commands associated with the files downlinked during the last pass for this observatory.
- Any incomplete transmissions from the previous pass, based on the protocol messages, are downlinked by the microsat CFDP engine.
- Science and engineering files placed on the downlink list in the microsat since the last pass are transmitted to the ground and collected at the antenna site.
- At the end of the planned pass time, the MOC sends a CFDP freeze command to stop the transmission of files and a transmitter off command.
- The AER system onboard the microsat has a backup transmitter off command that will be triggered by a timer set when the transmitter is turned on to ensure the transmitter is not inadvertently left on for a long period of time.
- Postpass, the collected files are transferred from the antenna site to the Universal Space Network (USN) Network Management Center (NMC), where they can then be transferred to the CYGNSS MOC for processing and distribution.

The plan for CYGNSS operations is to flow the CFDP files from the remote USN antenna sites to the USN NMC after the completion of the pass. This flow decouples the file processing from the real-time flow of the pass, which simplifies the operations and does not levy any bandwidth requirements on the links from the remote antenna sites to the NMC.

Postpass, the files collected during the pass will be flowed to the CYGNSS MOC, where they will be processed through the CFDP engine to create the protocol messages that will be uplinked at the next contact with the observatory. Complete science files will then be transferred to the SOC. Incomplete files

will be saved at the MOC until they can be completed during the next pass with the observatory.

C. Routine Maintenance and Calibration

The majority of postcommissioning operations for CYGNSS will occur using the automated features available in the microsat and in the MOC. However, there will also be routine microsat maintenance and DDMI calibration activities that will occur throughout the operational period of the constellation.

Maintenance activities for the microsat do not need to be scheduled on a specific cadence. Review of microsat systems and positioning information will be used to assess the status of each subsystem as well as the location of each observatory to determine when maintenance activities may be needed. Based on the type of activity, either real-time commanding or time-tagged command sequences can be developed to perform the required activities.

Cal/Val of the DDMI is planned to occur two times per year, nominally before and after hurricane season. Cal/Val activities will be performed using onboard time-tagged command sequencing. Part of the Cal/Val process uses cooperative beacons on the ground, and the time-tag command sequencing allows the team to coordinate instrument activities with the time periods when the beacons will be observable by the observatory.

D. Ground System Overview

The CYGNSS ground system, as shown in Figure 2.2, consists primarily of the MOC; existing USN Prioranet ground stations in Australia, Hawaii, and Santiago, Chile; and the SOC facility. Additional interfaces between the MOC and the microsat engineering team and the DDMI instrument engineering teams are supported. The MOC coordinates operational requests from all facilities and develops long-term operations plans.

Ground Data Network: USN

CYGNSS selected USN for the ground data network due to their experience in autonomously acquiring spacecraft per our baseline approach. Colocation of a backup CYGNSS MOC server at the USN NMC can also be supported.

The observatories within the CYGNSS constellation will be visible to three ground stations within the USN (Hawaii, Australia, and Santiago, Chile) for periods that average 470 to 500 seconds per pass. Each observatory will pass over each of the three ground stations six to seven times each day, thus providing a large pool of scheduling opportunities for communication passes.

The MOC personnel will schedule passes as necessary to support commissioning and operational activities. High priority passes will be scheduled to

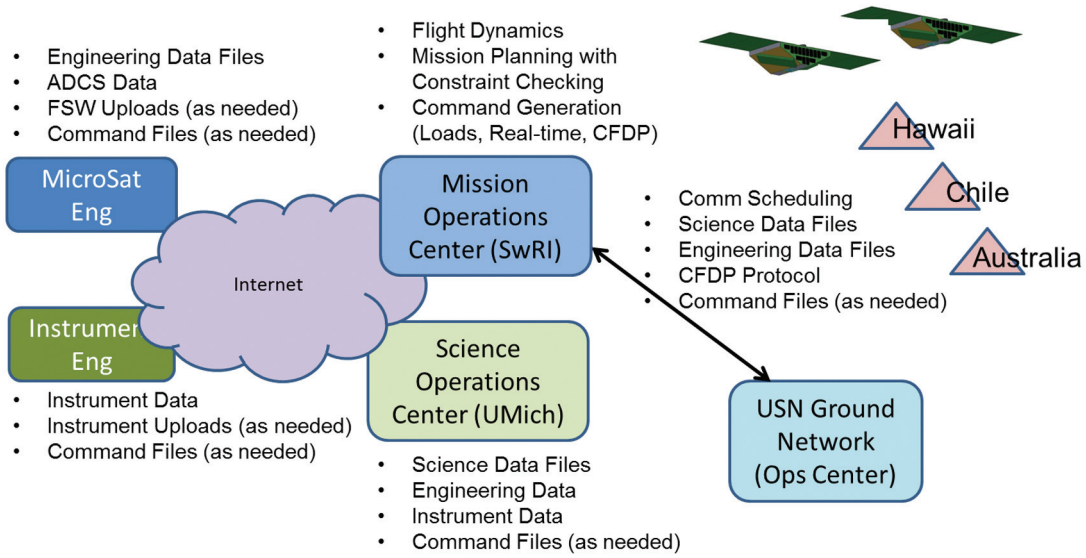

Figure 2.2. Diagram of the CYGNSS ground mission system.

support the observatory solar array deployment for each of the constellation microsats.

For all subsequent stages, the MOC schedules nominal passes for the USN stations for each observatory in the constellation per the USN scheduling process. Each observatory can accommodate gaps in contacts with storage capacity for over 10 days of data with no interruption of science.

Mission Operations Center (MOC)

During the mission, the CYGNSS MOC, located at the SwRI Boulder location, is responsible for the mission planning, flight dynamics, and command and control tasks for each of the observatories in the constellation. A summary of the primary MOC tasks includes

- Coordinating activity requests
- Scheduling ground network passes
- Maintaining the CFDP ground processing engine
- Collecting and distributing engineering and science data
- Tracking and adjusting the orbit location of each observatory in the constellation
- Trending microsat data
- Creating real-time command procedures or command loads required to perform maintenance and calibration activities
- Maintaining configuration of onboard and ground parameters for each observatory

Science Operations Center (SOC)

The CYGNSS SOC, located at UM, will be responsible for the following actions:

- Support DDMI testing and validation both prelaunch and on-orbit.
- Provide science operations planning tools.
- Generate instrument command requests for the MOC.
- Process science data for Levels 0–3.
- Archive Level 0–4 data products, DDMI commands, codes, algorithms, and ancillary data at a NASA DAAC.

Another key aspect to providing cost-effective support for a constellation is to have a set of tools supporting the mission operations team that allows the team to see issues with any single observatory; the tools should also allow the team to view the potential issues or interactions between observatories. The CYGNSS mission operations team has selected a set of tools with features that will allow them to address these issues, as outlined in the following paragraphs.

Command and Control System

The MOC is required to implement a command and control system that can handle all unique aspects of the CYGNSS mission. For uplink, it must support real-time commanding at 2000 bps, including memory load-dump-compare operations. On downlink, it must support ingesting CFDP data, Reed-Solomon decoding, and derandomization and include real-time telemetry display and long-term archival and analysis tools. For the ground segment, the tools need to be able to interface, configure, and monitor the ground network. It is also important that the system is easily deployed, is low in cost, and facilitates use by a team distributed across the country.

The CYGNSS mission chose the Integrated Test and Operations System (ITOS) for its command and control system. ITOS is a suite of software developed by the Real-Time Software Engineering Branch at the Goddard Space Flight Center and supported by the Hammers Company. This government off-the-shelf (GOTS) solution also has zero license costs for NASA missions and runs on inexpensive Linux hardware.

ITOS itself is not uniquely customized from mission to mission; instead mission customization is through database-driven command and telemetry specifications and a small set of configuration files. This obviates the need for additional software development and training. The database includes limit checking and engineering unit configurations as well as highly customizable display pages for monitoring spacecraft data. The ITOS telemetry server can interface across a firewall to a public server that can display telemetry and events remotely via a web browser, which facilitates simple, real-time monitoring of the spacecraft from a geographically diverse mission team.

For the success of the CYGNSS mission, it is critical for the command and control system to be able to define eight unique and concurrent spacecraft and be able to manage and display data unique to each. Though the spacecraft will be identical by design, they will all likely have unique aspects that the ground system

must take into account, including unique command constraints, telemetry conversions, and limit checking. The ITOS tools provide the database elements necessary to support and maintain a constellation configuration.

The CYGNSS team will be using ITOS throughout the spacecraft development, including as the main control system during system integration and environmental testing. This bench-to-flight approach allows for heavy reuse of existing STOL (Spacecraft Test and Operations Language) procedures that will be baselined into the mission operations configuration management system as the standard scripts and processes the team will use to fly the mission.

The CYNGSS Mission Planning System takes inputs from flight dynamics and science activities from the SOC, as well as event files, such as eclipse periods and ground tracks. In addition, it must resolve resource conflicts, such as power load, recorder usage, or oversubscription of a ground antenna resource. The system must also check that planned events do not result in violation of flight constraints—either for a single observatory or for the constellation. Resolving the conflicts, the system can then generate a command load, when required, that is handed off to the command and control system for uplink to the spacecraft.

3. Constellation Design

I. Orbital Elements

The baseline CYGNSS constellation consists of eight observatories dispersed over a common 510 km circular orbit at a 35° inclination angle. The temporal and spatial coverage of the constellation depends on each of these design parameters. A useful measure of sampling performance is the number of three-hour intervals during the lifetime of a TC in which at least one sample is made. A sample is considered made if it is located within 75 nautical miles of the eye. This coverage statistic is estimated using a software simulator in which CYGNSS (or other spaceborne missions) is flown over all TCs recorded during the 2003–2007 Atlantic hurricane seasons. As points of comparison, the three-hour coverage statistics for three heritage ocean wind scatterometers missions are as follows:

- QuikSCAT on NASA SeaWinds: 27.1%
- OSCAT on ISRO OceanSat-2: 23.5%
- ASCAT on EUMETSAT Metop: 16.7%

Applying the same analysis to the CYGNSS baseline design produces a three-hour coverage statistic of 33.6%.

The three-hour coverage statistic reduces to 32.9–32.6% when one of the eight observatories is removed, depending on which one it is. Coverage reduces further, to 32.2–32.8%, when two observatories are removed, illustrating the graceful degradation in performance provided by the CYGNSS constellation should additional observatories fail.

A second statistical measure of sampling performance is the percentage of CYGNSS samples made in a 24-hour interval that are coincident with the complete historical storm track record for the 10-year period between 2000 and 2009. This 24-hour storm coverage statistic is shown in Figure 3.1 as a function of the number of observatories lost from the initial constellation of eight. A coverage statistic of 70%, which is consistent with the coverage that would have been provided by both the OSCAT and ASCAT missions operating as a constellation, meets the mission requirement.

Orbit altitude can affect coverage in competing ways. As altitude increases, the projected antenna footprint on the ground grows, increasing the potential number of observable GPS reflections. Increasing altitude also lengthens the propagation path and lowers received signal strength, thus narrowing the usable solid angle of the antenna pattern. The increase in footprint size would dominate if the number of observable reflections was allowed to grow. However, because the DDMI can simultaneously observe a maximum of only four reflections, coverage does not improve much above an altitude of ~350 km. Coverage begins to decrease due to the longer propagation path above ~550 km. This behavior is illustrated in Figure 3.2. The baseline altitude of 510 km satisfies the mission lifetime requirement while staying within the broad range indicated by this coverage analysis.

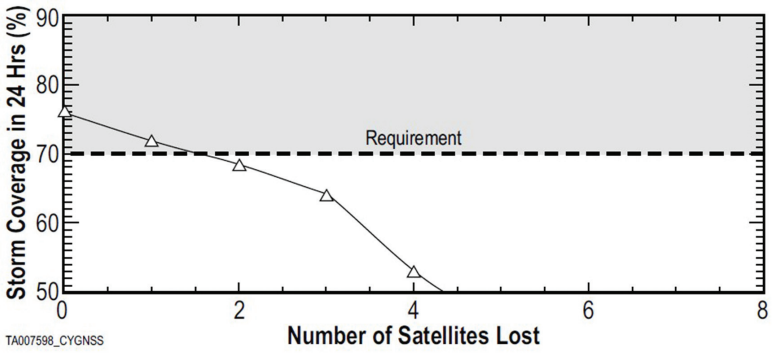

Figure 3.1. Dependence of 24-hour coverage on number of observatories lost. The 70% storm coverage requirement is met by seven or more observatories.

Orbit inclination affects storm coverage in two ways. Very low inclination angles reduce coverage because the prevailing latitudinal "corridors" favored by tropical storms become undersampled or missed altogether. Inclination angles too far above these preferred latitudes also tend to decrease coverage because more time is spent over midlatitude regions with a low probability of TC occurrence. These competing dependencies are shown in Figure 3.3. The baseline mission design of 35° is located at the center of a broad maximum in coverage.

II. Observatory

The CYGNSS observatory is based on a single-string hardware architecture with functional and selective redundancy included for critical areas. It consists of the DDMI and a highly integrated microsatellite. The simple operational nature of the DDMI and science profile allows the microsatellite to be designed for autonomous control during all normal science and communication operations without the need for daily onboard command sequences.

The microsatellite is a three-axis-stabilized, nadir pointed vehicle using a star tracker for primary attitude knowledge and a reaction wheel triad for control. Fixed solar arrays, stowed for launch and then deployed soon thereafter, provide power to the onboard peak power tracking electronics for battery charging. Communication is provided by an S-band transceiver and low-gain patch antennas to provide near 4π steradian communications without interrupting science operations. The vehicle's structure and thermal design is driven by physical accommodation of the DDMI antennas, the solar arrays, and launch configuration constraints.

Microsatellite performance is enabled by key nanosatellite technology, specifically the star tracker and reaction wheels, both provided by Blue Canyon Technologies of Boulder, Colorado. The form-factor, mass, and power requirements of these components are well suited for the highly integrated nature of the CYGNSS observatory. The SwRI avionics, including

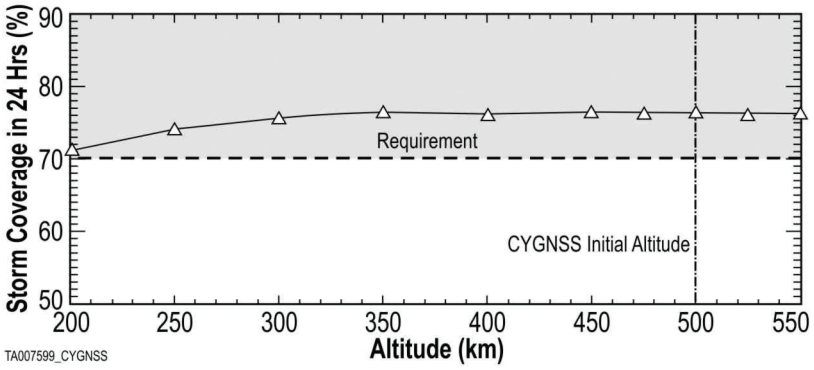

Figure 3.2. Dependence of 24-hour coverage on orbit altitude. The 70% storm coverage requirement is met by a wide range of altitudes. The 510 km baseline altitude meets the mission lifetime requirement.

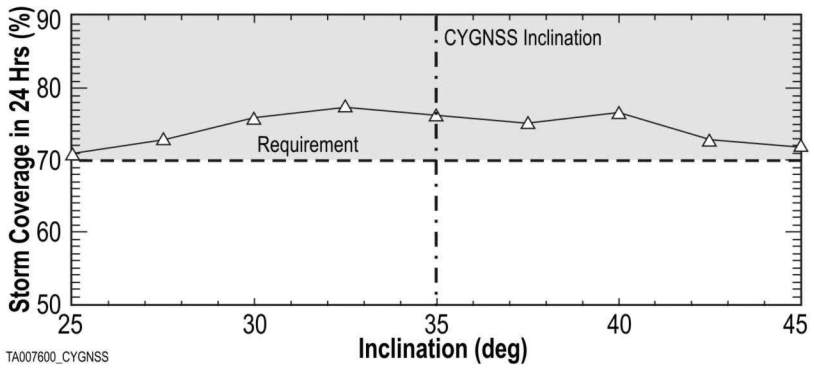

Figure 3.3. Dependence of 24-hour coverage on orbit inclination angle. The 35° baseline inclination is centered in a broad maximum of storm coverage dependence.

the flight computer, S-band transceiver, peak power tracker (PPT), and low voltage power supply, are based on heritage solutions that have been used on more than 20 previous missions. The avionics leverage recent development in high density microelectronics to achieve a packaging volume of a 3U CubeSat, a 4:1 volume reduction.

Each observatory has a 24 kg mass and requires ~37 watts of power. Once deployed, the zenith solar cell array has a span of 176.3 cm and a width of 42.5 cm. The avionics bay has a depth of 18.6 cm. Exploded graphic views of the observatory from three perspectives are shown in Figure 3.4a, b, c.

III. Science Payload

A functional schematic of the CYGNSS science payload, the DDMI, is shown in Figure 3.5. The DDMI performs the following primary tasks:

1. It performs all the core functions of a space GPS receiver, with front-end supporting three single frequency antenna ports.
2. It stores a quantity of raw sampled data from multiple front ends or processed data in its 1 gigabyte solid state data recorder.
3. It has a dedicated field-programmable gate array (FPGA) coprocessor (Virtex 4).

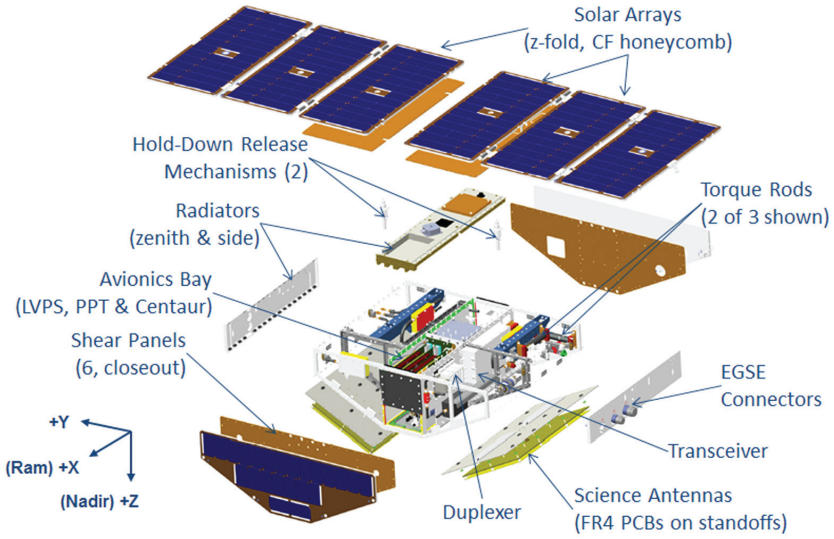

Figure 3.4a. RAM view of a CYGNSS observatory (courtesy of Keith Smith, Southwest Research Institute).

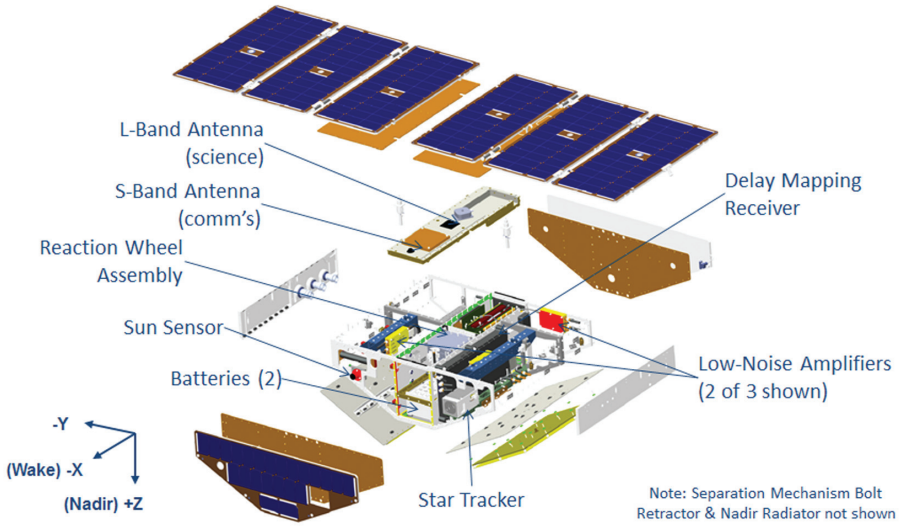

Figure 3.4b. Wake view of a CYGNSS observatory (courtesy of Keith Smith, Southwest Research Institute).

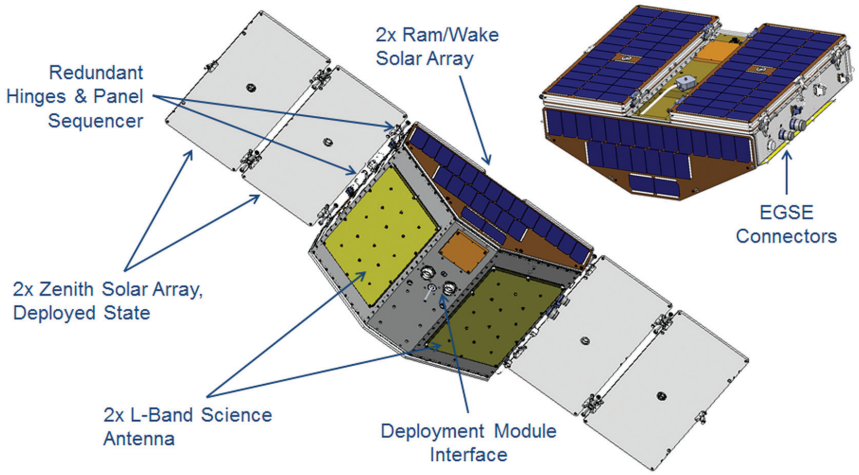

Figure 3.4c. Underside view of a CYGNSS observatory (courtesy of Keith Smith, Southwest Research Institute).

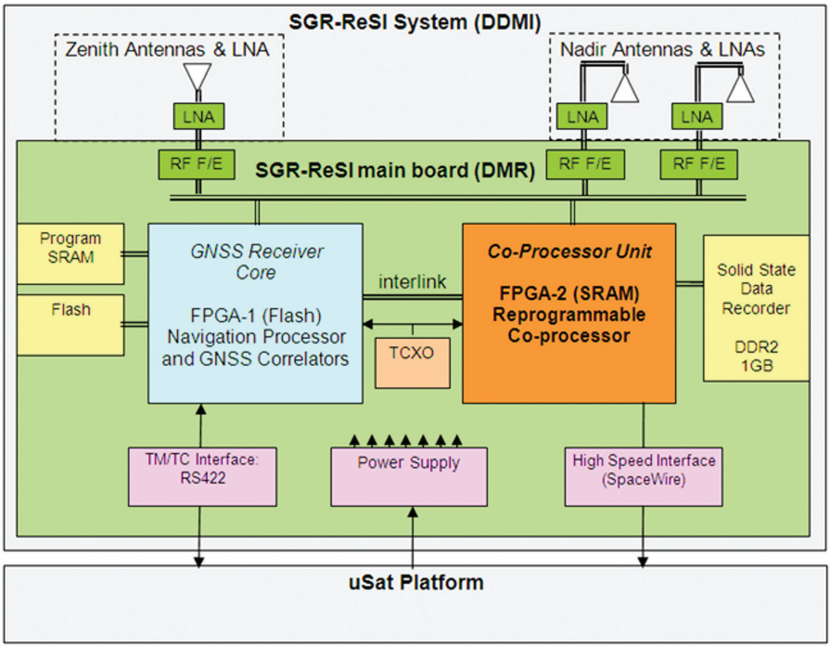

Figure 3.5. DDMI configuration (Unwin et al., 2010).

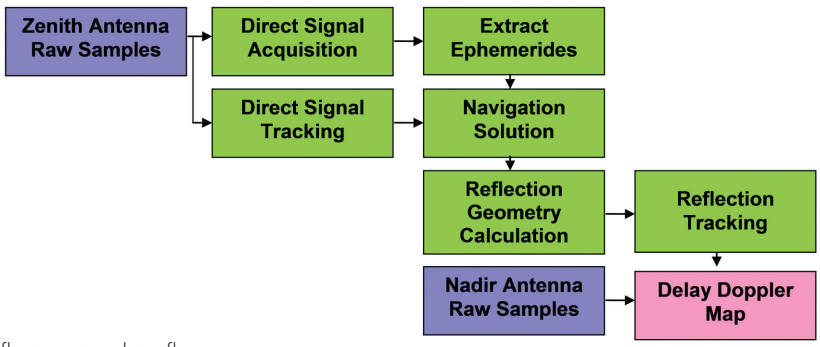

Figure 3.6. GPS reflectometry data flow.

The coprocessor is included for the real-time processing of the raw reflected GPS data into DDMs. For the coprocessor to generate DDMs of the sampled reflected data, it needs to be primed with the PRN (pseudorandom noise) code of the transmitting GPS satellite and the estimated time delay and Doppler of the reflection as seen from the satellite. These are calculated by the processor in conjunction with the main navigation solution; the data flow for this is shown in Figure 3.6. Direct signals (received by the zenith antenna) are used to acquire and track GPS signals. From the broadcast ephemerides, the GPS satellite positions are known. Then, from the geometry of the position of the transmit and receive satellites, the bistatic radar geometry can be calculated.

The processing of the DDM is performed on the coprocessor using data directly sampled from the nadir antenna. Similar to a standard GPS receiver, the local PRN is generated onboard the coprocessor. As an alternative to synchronizing and decoding the reflected signal in a stand-alone manner, the direct signals can be used to feed the navigation data sense and assist the synchronization. The sampled data is multiplied by a replica carrier and fed into a matrix that performs an FFT on a row-by-row basis to form the DDM, achieving in effect a 7000 channel correlator, integrating over 1 millisecond. Each point is then accumulated incoherently over 1000 milliseconds to bring the weak signals out of the noise.

This processing is performed in real-time onboard the satellite, which greatly reduces the quantity of data required to be stored and downlinked. CYGNSS plans to use the DDMI in an autonomous manner generating DDMs at a low data rate continuously, which will provide gap-free measurements of the ocean roughness throughout the tropical oceans.

Reference

Unwin, M., Van Steenwijk, R., Gommenginger, C., Mitchell, C., & Gao, S. (2010, September). The SGR-ReSI—A new generation of space GNSS receiver for remote sensing. In *Proceedings of the 23rd International Technical Meeting of The Satellite Division of the Institute of Navigation (ION GNSS 2010)* (pp. 1061–1067). Portland, OR.

4. Data Product Overview

I. Data Levels

The CYGNSS mission makes four levels of data products available to the public. A brief description of each data product level is given below. A table of the products is also provided in Part II of this section. More detailed information about the processing and the products for each data level is provided in the ATBDs in Sections 5 through 10.

Level 1, 2, and 3 data products are produced in the form of netCDF files and are made available to the public through the NASA Physical Oceanography Data Active Archive Center (PO.DAAC). The maximum data latency from spacecraft downlink to PO.DAAC availability is six days.

A. Level 1 Data

The goal of the Level 1 calibration is to attain DDMs of bistatic radar cross section (BRCS), which will be used to determine the ocean surface wind speeds in proceeding algorithms. The Level 1 calibration consists of two parts. First, the Level 1A calibration converts the individual bins of raw Level 0 DDMs from processed counts into DDMs of received power (P_g) in units of watts. These Level 1A DDMs are provided at a spatial resolution of 17 delay × 11 Doppler bins, corresponding to a surface area of about 50 km^2. Second, the Level 1A DDMs are converted to Level 1B DDMs of BRCS values by unwrapping the forward scattering model and generating two additional data products: one 17 delay × 11 Doppler DDM of unnormalized BRCS values (σ) in units of m^2 and a second 17 delay × 11 Doppler DDM of effective scattering areas (also in units of m^2). Dividing the unnormalized BRCS by the effective scattering area results in σ_0, the normalized bistatic radar cross section (NBRCS). All Level 1 data products are provided at a time resolution of 1 Hz. These data products are generated in such a way as to allow for flexible processing of variable areas of the DDM that correspond to different regions on the surface (Clarizia & Ruf, 2016).

The process of quantifying the error in the Level 1 data products is described in detail in Sections 5 and 7. For Level 1A, errors in the received power in watts, P_g, depend on wind speed. For ocean surface winds below 20 m s^{-1} (corresponding to σ_0 = 20 dB), P_g has a total root sum square (RSS) error of 0.50 dB. For winds above 20 m s^{-1} (corresponding to σ_0 = 12 dB), P_g has an RSS error of 0.23 dB. For the Level 1B product, the total RSS errors for σ (including errors from the Level 1A calibration) are 0.82 dB (for winds below 20 m s^{-1}) and 0.70 dB (for winds above 20 m s^{-1}; Gleason et al., 2016).

Section 5 includes a detailed derivation of the Level 1A calibration and a term-by-term error analysis, and Section 7 includes the derivation of the Level 1B data products and error analysis. This includes analysis related to using only near specular DDM bins to calculate the NBRCS over a DDMA, as used in the baseline Level 2 wind retrieval algorithm.

B. Level 2 Data

The Level 2 mean square slope (MSS) product is the spatially averaged MSS, plus uncertainty, over a 25 × 25 km^2 region centered at the SP. The Level 2 wind speed product is the spatially averaged wind speed, plus uncertainty, over a 25 × 25 km^2 region centered at the SP. Each Level 2 netCDF file contains the wind speeds and the MSS generated by the entire CYGNSS constellation during a single UTC (Coordinated Universal Time) day.

Level 2 MSS

The primary mission of the CYGNSS project is to measure ocean surface winds by fitting the calibrated DDM peak power data to the empirical or modeled geophysical functions. Those functions relate the measured signal parameters directly to surface wind. At the same time, the forward scattering model based on the bistatic radar equation directly relates the DDM to the BRCS, which in its turn can be characterized by the MSS of the ocean surface. Therefore this Level 2 data product will also be available during the CYGNSS mission.

The MSS of the ocean surface is a very important quantity. It is crucial for understanding the physical processes at the air-sea interface and for interpreting altimeter and scatterometer radar backscatter

measurements. The practical needs for global MSS datasets in air-sea interaction research is increasingly apparent—for example, for estimating the dynamics of gas transfer rates across a water boundary layer. MSS measurements also provide an opportunity to verify new model forecasts of hurricane development.

The purpose of Section 8 is to describe the CYGNSS Level 2 MSS algorithms and provide all necessary equations for implementing the algorithm during the mission. It describes the physics of the problem and explains the connection between the BRCS and the MSS and between the MSS and the ocean surface spectrum. It provides a theoretical description of the MSS baseline retrieval algorithm. Since the MSS algorithm relies on the BRCS retrieval, all temporal and spatial resolution criteria developed in the documents for Level 1 are valid here as well.

The issue of the MSS retrieval accuracy is addressed in Section 8, Part IV, "Performance Characterization." The creation of the Level 2 MSS product is contingent on the availability of input observational data (from CYGNSS and ancillary data sources) and accurate estimates of their errors. The accuracy of the Level 2 MSS product is dependent on the accuracy of the BRCS retrieval, the accuracy of the scattering geometry determination (incidence angle), and the accuracy of the Fresnel reflection coefficient estimates. This error analysis of the Level 2 MSS retrieval algorithm is presented at the end of the Section 8.

Level 2 Wind Speed

The Level 2 wind speeds are obtained from two observables known as the DDMA and the leading edge slope (LES; see Section 9, Part I). The observables are calculated from DDMs that derive from the SP selection algorithm over a limited delay and Doppler range to comply with the 25 km spatial resolution requirements for the CYGNSS retrieved winds. In cases where the true resolution is finer than 25 km, time averaging between consecutive observables is applied to further reduce the noise in the observables. An empirical GMF is developed separately for DDMA and LES, relating the observable value to the ground truth matchup winds and the incidence angle, using a training subset of high-quality data (Section 9, Part III). The empirical GMF is then used to estimate the winds from a generic dataset of observables, independent of the training one. In addition, the degree of decorrelation between winds retrieved from DDMA and LES is exploited to derive a MV estimator, which provides improved wind estimates compared to DDMA or LES alone. A system of quality control flags (Section 9, Part IV) is applied to the final wind speed product to remove nonfeasible wind values.

The retrieval algorithm is applied and tested using synthetic DDMs collected over a simulated tropical cyclone with a life cycle of 13 days. The performance and error analysis of the retrieval algorithm (Section 9, Part V) highlights that for those SPs acquired with high enough gain of the receiver antenna, the RMS error meets the CYGNSS requirements on wind speed uncertainty of either 2 m s^{-1} or 10% of the measured wind, whichever is greatest. In particular, the uncertainty is 1.4 m s^{-1} for wind speeds lower than 20 m s^{-1}, and it is 9.2% of the measured wind speed for winds higher than 20 m s^{-1}, for data acquired with range corrected gain (RCG). RCG is defined in Section 9, Part I, and represents a more efficient definition of receiver antenna gain.

The wind speeds retrieved using this algorithm have a spatial resolution of 25 km, and the estimation refers to a time interval between 1 and 5 seconds of data, depending on the amount of time averaging applied. In Section 9, Part V, a comparison of true and retrieved winds is also illustrated for SP transects acquired with sufficient RCG and crossing the eye of simulated hurricanes or areas near the eye with high wind gradients (Clarizia & Ruf, 2016).

C. Level 3 and 4 Data

The Level 3 gridded wind product is surface wind speed, averaged in space and time on a 0.2° latitude, longitude grid. Each Level 3 gridded wind file covers a one-hour time period for the entire CYGNSS constellation.

The Level 4 wind speed for data assimilation product is the surface wind vector analysis field on a basin-wide domain of 9 km grid spacing, in which the assimilation of both conventional data and CYGNSS winds is performed. This product will be computed using NOAA's HWRF model framework. The purpose is to provide an improved gridded surface wind analysis that includes CYGNSS data for community use. Six-hourly HWRF analyses and forecasts will be created for a limited number of Atlantic hurricanes, and the influence of assimilating CYGNSS data will be evaluated. The uncertainty depends on the errors in the observation, model, and assimilation scheme.

II. Table of Data Products

A. Level 1 Data and Metadata Products

The data and metadata contained in the Level 1 netCDF file are shown in Table 4.1. Each Level 1 netCDF file contains the DDMs produced by one CYGNSS observatory during one UTC day and the metadata used to convert from Level 0 (raw telemetry) to Level 1 data products. Note that the time stamp of all values is DDM time, unless otherwise indicated. LNA stands for low noise amplifier, Tx for transmitting, and Rx for receiving.

B. Level 2 Data and Metadata Products

The Level 2 data and metadata were in development during the writing of this handbook. As such, basic products will be listed in Table 4.2, and updates to them should be consulted in future releases of this handbook and in the most current ATBDs.

C. Level 3 and 4 Data and Metadata Products

The Level 3 and 4 data and metadata were in development during the writing of this handbook. As such, basic products will be listed in Table 4.3, and updates to them should be consulted in future releases of this handbook and in the most current ATBDs.

Next, Sections 5–10 provide the reader with relevant excerpts from the ATBDs that describe the physical and mathematical descriptions of the algorithms used in the generation of science data products in more detail. The ATBDs include a description of variance and uncertainty estimates and considerations of calibration and validation, exception control, and diagnostics. Internal and external data flows are also described. Users requiring more information than what is found in this section should consult Sections 5–10, as well as the Appendix, "Ocean Surface Bistatic Scattering Forward Model," found at the end of this handbook.

References

Clarizia, M. P., & Ruf, C. (2016). Wind speed retrieval algorithm for the Cyclone Global Navigation Satellite System (CYGNSS) mission. *Geoscience and Remote Sensing, IEEE Transactions On*. Manuscript in review.

Gleason, S., Ruf, C., Clarizia, M. P., & O'Brien, A. (2016). Calibration and unwrapping of the normalized scattering cross section for the Cyclone Global Navigation Satellite System (CYGNSS). *Geoscience and Remote Sensing, IEEE Transactions On*. doi: 10.1109/TGRS.2015.2502245

Table 4.1. CYGNSS Level 1 data and metadata.

General (1 Hz)	
Number of DDMs	Number of DDMs per sample. Nominal sample rate is 1 Hz.
Spacecraft CCSDS ID	0xF7 = CYGNSS 1 0xF9 = CYGNSS 2 0x2B = CYGNSS 3 0x2C = CYGNSS 4 0x2F = CYGNSS 5 0x36 = CYGNSS 6 0x37 = CYGNSS 7 0x49 = CYGNSS 8 0x0D = not valid 0x0E = engineering-model-01
PO.DAAC spacecraft/mission name	"cyg1" "cyg2" "cyg3" "cyg4" "cyg5" "cyg6" "cyg7" "cyg8" "cygEngModel" "cygDefault" "cygUnknown"
DDM source	0 = end to end simulator 1 = GPS signal simulator 2 = CYGNSS DDMI 3 = source unknown
Time stamps (1 Hz)	
DDM time type	0 = start of DDM sampling period 1 = middle of DDM sampling period 2 = end of DDM sampling period 3 = PVT time
DDM time	DDM sample time stamp. See DDM time type above.
PVT time	Position and velocity time stamp
Attitude time	Spacecraft attitude time stamp
Spacecraft position, velocity, and attitude (1 Hz)	
Spacecraft position at PVT time	Spacecraft position at PVT time, ECEF, m
Spacecraft velocity at PVT time	Spacecraft velocity at PVT time, ECEF, m/s
Spacecraft position	Spacecraft position, ECEF, m
Spacecraft velocity	Spacecraft velocity, ECEF, m/s
Spacecraft attitude at attitude time	Spacecraft attitude at attitude time, roll, pitch, yaw, radians
Spacecraft attitude	Spacecraft attitude, roll, pitch, yaw, radians
Spacecraft subsatellite point latitude	Spacecraft subsatellite point latitude, degrees North (–90 to 90)
Spacecraft subsatellite point longitude	Spacecraft subsatellite point longitude, degrees East (–180 to 180)
Spacecraft WGS84 ellipsoid altitude	Spacecraft height above WGS84 ellipsoid, m
Spacecraft sun angle	The zenith antenna look angle to the sun. Antenna frame elevation and azimuth, degrees.
Zenith antenna boresight direction	ECI unit vector

(*continued*)

Table 4.1. CYGNSS Level 1 data and metadata (continued).

GPS receiver clock (1 Hz)	
GPS receiver clock bias (multiplied by the speed of light)	The difference between the receiver GPS time and the GPS constellation time, m
GPS receiver clock bias rate (multiplied by the speed of light)	The rate at which the GPS receiver clock bias is changing, m/s
GPS receiver clock bias at PVT time (multiplied by the speed of light)	The difference between the receiver GPS time and the GPS constellation time at PVT time, m
GPS receiver clock bias rate at PVT time (multiplied by the speed of light)	The rate at which the GPS receiver clock bias was changing at PVT time, m/s
LNA temperatures (1 Hz)	
Starboard LNA temp	Starboard antenna low noise amplifier temperature, degrees C
Port LNA temp	Port antenna low noise amplifier temperature, degrees C
Zenith LNA temp	Zenith antenna low noise amplifier temperature, degrees C
RF noise channels (1 Hz)	
Starboard noise channel (I^2 + Q^2)	RF noise channel counts
Port noise channel (I^2 + Q^2)	RF noise channel counts
Zenith noise channel (I^2 + Q^2)	RF noise channel counts
1 Hz quality flags	
S-band transmitter powered up	0 = S-Band transmitter was not powered up during the DDM sample time 1 = S-Band transmitter was powered up during the DDM sample time
Large spacecraft attitude error	0 = false 1 = true
1 Hz DDM values	
DDM delay resolution	The delay difference between adjacent DDM bins, chips
DDM Doppler resolution	The Doppler frequency difference between adjacent DDM bins, Hz
DDMI tracking delay offset	The currently commanded delay offset being applied to the DDMI reflectometry channel, chips
DDMI tracking Doppler offset	The currently commanded Doppler frequency offset being applied to the DDMI reflectometry channel, Hz
End of DDM integration time offset	The time between PVT time and the end of the DDM integration period, ns
Per DDM values	
DDMI PRN mode and antenna selection mode	0 = direct signal override (autonomous PRN selection is overridden by command) 1 = beacon (not used) 2 = open loop reflection tracking (autonomous PRN selection)
PRN code	GPS pseudo random noise code, 0..32. 0 indicates channel is idle.
GPS space vehicle number	The GPS space vehicle transmitting PRN code
Antenna	0 = zenith antenna (not used for DDMs) 1 = starboard nadir antenna 2 = port nadir antenna
Additional range to SP	Additional range to SP relative to direct signal, chips
Additional range to SP at PVT time	Additional range to the SP relative to direct signal at PVT time, chips
Zenith signal code phase	Zenith (direct) GPS signal code phase at PVT time, chips

Table 4.1. CYGNSS Level 1 data and metadata (continued).

Per DDM values	
Direct signal power	Zenith (direct) GPS signal power at PVT time, W
Direct signal SNR	Zenith GPS (direct) signal to noise ratio at PVT time, dB
SP Doppler frequency	The SP GPS signal Doppler frequency, Hz
SP relative delay	The SP GPS signal delay calculated relative to the direct signal, chips
SP absolute delay	The SP GPS signal delay calculated from signal path lengths and GPS clock time biases, chips
SP Doppler frequency	The SP GPS Doppler frequency calculated from Tx and Rx velocity, Hz
SP delay error	Difference between the delay of the DDM center bin and the SP absolute delay, chips
SP Doppler error	Difference between the Doppler frequency of the DDM center bin and the SP Doppler frequency, Hz
DMR PRN selection figure of merit	The range corrected gain of the Rx antenna in the direction of the SP. Units: antenna_gain/((R1^2)(R2^2)) * 1e27, where R1 is the distance from the Tx to the SP and R2 is the distance from the Rx to the SP.
Flight software compression algorithm delay shift	The amount of delay introduced by the onboard DDM compression process, chips
Flight software compression algorithm Doppler shift	The amount of Doppler frequency shift introduced by the onboard DDM compression process, Hz
GPS transmitter clock bias (multiplied by the speed of light)	The GPS transmitter clock bias, m
SP latitude	SP latitude, degrees North (–90 to 90)
SP longitude	SP longitude, degrees East (–180 to 180)
SP position	SP position, ECEF, m
SP velocity	SP velocity, ECEF, m/s
SP incidence angle	SP incidence angle, degrees
SP theta angle, orbit frame	The angle from the orbit frame Z axis to the SP, degrees
SP azimuth angle, orbit frame	The angle from spacecraft velocity vector to SP, degrees
SP theta angle, Rx antenna frame	The angle from the Rx antenna Z axis to the SP, degrees
SP azimuth angle, Rx antenna frame	The angle from the Rx antenna X axis to the SP, degrees
Rx antenna gain in the direction of the SP	dB
Tx effective isotropic radiated power in the direction of the SP	W
DDM SNR	DDM signal to noise ratio, dB
Rx to SP range	Distance between the Rx antenna and the SP, m
Tx to SP range	Distance between the Tx antenna and the SP, m
GPS Tx position	The GPS satellite position, ECEF, m
GPS Tx velocity	The GPS satellite velocity, ECEF, m
Time to nearest blackbody reading	Time to the nearest (previous or next) blackbody reading, seconds. Negative values indicate that the nearest blackbody reading occurred before DDM time. Positive values indicate that the nearest block body reading occurred after DDM time.
Sea surface temperature	The estimated sea surface temperature at the SP, degrees C
Sea surface salinity	The estimate sea surface salinity at the SP, parts per thousand

(*continued*)

Table 4.1. CYGNSS Level 1 data and metadata (continued).

Per DDM quality flags	
Overall DDM quality is good	This flag is the OR of several other quality flags. Detailed definition TBD. 0 = Overall quality is not good. 1 = Overall quality is good.
Blackbody DDM	0 = LNA received input from the Rx antenna. 1 = LNA received input from the blackbody load.
DDMI was reconfigured during DDM integration	0 = DDMI was not reconfigured during DDM integration. 1 = DDMI was reconfigured during DDM integration. (DDM is contaminated and invalid.)
Spacewire DDM packet CRC is invalid	The flight software detected a CRC error in the spacewire packet containing this DDM. 0 = CRC is valid. 1 = CRC is not valid.
This is a test DDM	This DDM contains test data generated by the DDMI or the flight software (not a valid DDM). 0 = false 1 = true
DDM channel is idle	0 = Channel is not idle. 1 = Channel is idle. (DDM is not valid.)
Negative signal power In Level 2 DDMA area	Level 1A calibration resulted in at least one bin in the Level 2 DDM Area (DDMA) having a negative power value. 0 = negative signal power not present 1 = negative signal power present
Negative Sigma0 in Level 2 DDMA area	Level 1A calibration resulted in at least one bin in the Level 2 DDM Area (DDMA) having a negative power value. 0 = negative Sigma0 not present 1 = negative Sigma0 present
Low confidence in DDM noise floor estimate	0 = The DDM noise floor is confidence level is high. 1 = The DDM noise floor confidence level is low.
Land present in DDM	0 = false 1 = true
SP over land	0 = false 1 = true
SP over open ocean	0 = false 1 = true
Large step change in DDM noise floor	0 = false 1 = true
Large step change in LNA temperature	0 = false 1 = true
Direct signal in DDM	0 = DDM not contaminated 1 = DDM contaminated by direct GPS signal
Low Rx antenna range corrected gain	0 = false 1 = true
High SP incidence angle	0 = false 1 = true
High cross correlation power present	0 = false 1 = true
Low confidence in GPS EIRP estimate	0 = false 1 = true

Table 4.1. CYGNSS Level 1 data and metadata (continued).

Bin values (per DDM)	
Received power, analog	11 × 17 floats, W
Received power, digital	11 × 17 floats, W
Bistatic radar cross section	11 × 17 floats, m^-2
Ideal scattering area	11 × 17 floats, m^2
Physical scattering area	11 × 17 floats, m^2
Ancillary data version numbers (per netCDF file)	
LNA noise figure parameters version	Version number of the LNA noise figure parameters file
Effective scattering area table version	Version number of effective scattering area lookup table
Ideal scattering area table version	Version number of ideal scattering area lookup table
GPS receiver antenna gain table version	Version number of the GPS receiver antenna gain lookup tables
PRN to SV map version	Version number of GPS PRN to space vehicle number lookup table
GPS EIRP parameters version	Version number of GPS effective isotropic radiated power parameter file
On-orbit antenna RCG maps version	Version number of antenna range corrected gain maps file
Open ocean mask version	Version number of open ocean mask data file
Land mask version	Version number of land mask data file
Level 1 algorithm version	Version number of the Level 1 calibration algorithm

Table 4.2. CYGNSS Level 2 data and metadata.

Level 2 mean square slope (MSS)	
Spatially averaged mean square slopes (plus uncertainty)	Averaged over 25 × 25 km^2 region, centered at the SP, geolocated, in spacecraft time and space coordinates
Level 2 wind speed	
Spatially averaged wind speed (plus uncertainty)	Averaged over 25 × 25 km^2 region, centered at the SP, geolocated, in spacecraft time and space coordinates

Table 4.3. CYGNSS Level 3 and 4 data and metadata.

Level 3 gridded wind product	
Wind speed	Gridded in space and time (0.2° latitude and longitude, 1 hour)
Level 4 wind speed for data assimilation	
Wind speed	Gridded and optimized for observing system experiment data assimilation (optimized spatial and temporal resolution)

5. Level 1A DDM Calibration and Error Analysis

I. Level 1A Calibration Algorithm: Counts to Watts

Individual bins of a DDM generated by the DDMI are measured in raw, uncalibrated units referred to as counts. These counts are linearly related to the total signal power processed by the DDMI. In addition to the ocean surface scattered GPS signal, the total signal includes contributions from the thermal emission by the earth and by the DDMI itself. The power in the total signal is the product of all the input signals, multiplied by the gain of the DDMI receiver. Level 1A calibration converts each bin in the DDM from raw counts to units of watts. A flowchart of the Level 1A calibration procedure is shown in Figure 5.1.

The open ocean calibration (see Section 6, Part I) will occur approximately every orbit and the blackbody calibration will be performed every 60 seconds on-orbit for each nadir science antenna. The routine calibration will be performed at 1 Hz on all DDMs output by the DDMI (four per second). Figure 5.2 illustrates the actions performed and intervals for all the CYGNSS Level 1A calibration steps.

A. Raw Level 0 Delay Doppler Map

The DDM values output from the CYGNSS science instrument will be sent to the CYGNSS spacecraft as arbitrary counts. The count values will be a result of the signal travelling through the various stages of the instrument, which will add a gain to the received power levels. The value of the DDM in arbitrary counts can be linked to the arriving signal power in watts such that

$$C = G\left(P_a + P_r + P_g\right) \tag{5.1}$$

where

- C are the DDM values in counts output from the instrument at each delay/Doppler bin.
- P_a is the thermal noise power generated by the antenna in watts.
- P_r is the thermal noise power generated by the instrument in watts.
- P_g is the scattered signal power at the instrument in watts.
- G is the total instrument gain applied to the incoming signal in counts per watt.

The terms, C and P_g are functions of delay and Doppler, while P_a and P_r are assumed to be independent of the delay Doppler bin in the DDM. Every DDM includes a number of delay bins where signal power is not present and an individual DDM noise floor level can be estimated. These bins physically represent delays above the ocean surface where no GPS signal power is present. These delay and Doppler bins provide an estimate of the DDM noise power, expressed in counts as

$$C_N = G\left(P_a + P_r\right) \tag{5.2}$$

Assuming P_a and P_r are independent of delay and Doppler, the DDM samples above the ocean surface can be used to estimate the noise only contribution to the raw counts.

B. Noise Power Expressions

The input antenna noise can be expressed as

$$P_a = kT_aB_W \tag{5.3}$$

where T_a is the top of the atmosphere brightness temperature integrated over the receive antenna pattern, k is Boltzmann's constant, and $B_W = \frac{1}{T_i} = 1000Hz$ is the signal bandwidth. The bandwidth of the GPS signal at the antenna is determined by the coherent integration processing interval, which is $T_i = 1$ ms.

When the instrument input is switched to the calibration load, the input antenna noise becomes

$$P_B = kT_BB_W \tag{5.4}$$

where P_B and T_B are the noise power and temperature of the instrument blackbody load source.

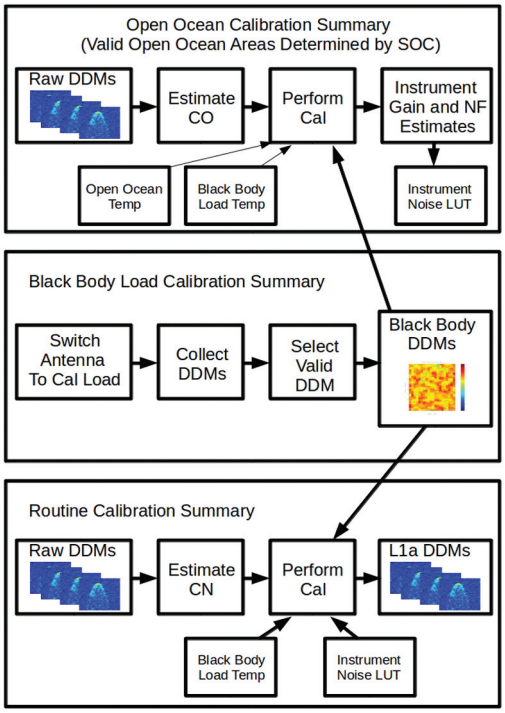

Figure 5.1. Overview of CYGNSS Level 1A calibration. CO is the open ocean measurement in counts, and CN is the individual DDM noise floor estimate. The determination of whether or not a DDM occurs over the open ocean will be performed during ground processing in the Science Operations Center. LUT = lookup table, NF = noise figure, DDM = delay Doppler map, SOC = Science Operations Center. *Reused from Gleason et al. (2016), © 2016 IEEE.*

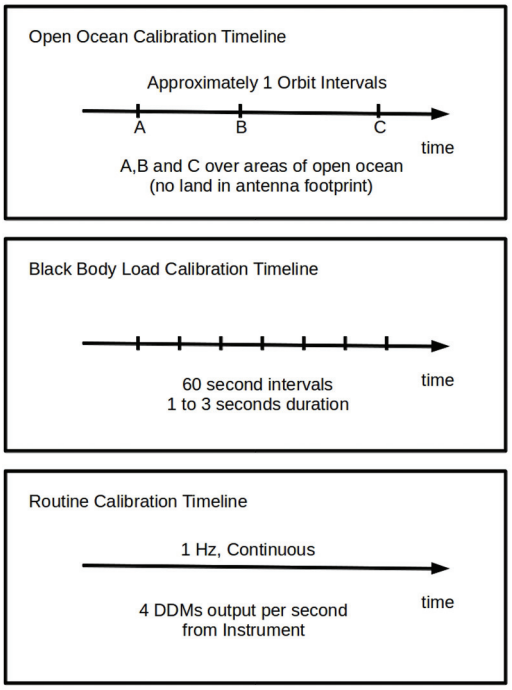

Figure 5.2. CYGNSS Level 1A calibration timing. The open ocean calibration will occur where the Science Operations Center determines there is no land in the antenna footprint. The blackbody calibration interval is configurable, with a default of 60 seconds. The routine calibration is applied to all four 1 Hz DDMs output by the DDMI. *Reused from Gleason et al. (2016), © 2016 IEEE.*

When the instrument input is switched to the external antenna over an area of open ocean with no land in the surface glistening zone, the input antenna cold noise power is

$$P_O = kT_O B_W \quad \textbf{(5.5)}$$

where P_O and T_O are the noise power and brightness temperature over the ocean, respectively. It is possible to estimate the value of T_O using a microwave radiative transfer model forced by climatological environmental conditions or by numerical forecast models, such as GDAS or ECMWF. However, analyses using a radiative transfer model confirm that a single value of T_O = 99.4 K is adequate given our error tolerance (see Section 6, Part II).

The instrument thermal noise power can be expressed as a function of the instrument noise figure:

$$P_r = kT_r B_W = k[(NF - 1)290]B_W \quad \textbf{(5.6)}$$

where P_r and T_r are the instrument noise power and temperature. The receiver noise figure NF is directly related to the instrument noise temperature.

II. Estimating the Instrument Gain and Noise Power over the Open Ocean

At periodic intervals over the receiver orbit the instrument gain (G) and noise power/noise figure (P_r / NF) can be estimated using DDMs collected over the open ocean. This will be as the spacecraft passes over areas where there is no land present in the nadir antenna beam. Open ocean DDMs will be identified in the SOC using a global open ocean mask, which consists of all ocean cover 50 km or farther from the nearest land. (This buffer distance is configurable and can be increased if necessary.) During these intervals, the instrument noise power and gain will be estimated using open ocean noise samples and blackbody load DDMs. The resulting expressions for the Level 0 DDM in counts for the open ocean and blackbody load are

$$C_O = G(P_O + P_r) \quad \textbf{(5.7)}$$

$$C_B = G(P_B + P_r) \quad \textbf{(5.8)}$$

The receiver gain can then be calculated by differencing the average blackbody noise counts and the average open ocean noise counts, resulting in the cancellation of the receiver noise power, P_r, giving us

$$C_O - C_B = G(P_O + P_r) - G(P_B + P_r) = GP_O - GP_B \quad \textbf{(5.9)}$$

We can then solve for the instrument gain:

$$G = \frac{C_O - C_B}{P_O - P_B} \quad \textbf{(5.10)}$$

Finally, substituting Equation 5.10 into Equation 5.7 allows us to solve for the instrument noise power as follows:

$$P_r = \frac{P_O C_B - P_B C_O}{C_O - C_B} \quad \textbf{(5.11)}$$

By rearranging Equation 5.6, the instrument noise figure, NF, can then be estimated from the calculated instrument noise power as

$$NF = \frac{P_r}{k290B_W} + 1 \quad \textbf{(5.12)}$$

More detail on the open ocean calibration can be found in Section 6, Part I.

III. Routine Calibration of Signal Power

The generic instrument DDM in counts is expressed in Equation 5.1, which includes the received signal power, P_g. These DDMs will be generated by the instrument every second and will be corrected by the estimated noise floor using Equation 5.2, such that we are left with a signal-only DDM:

$$C_g = C - C_N = GP_g \quad \textbf{(5.13)}$$

Subsequently the instrument gain at the collection time of this DDM can be calculated using the current estimate of the blackbody load noise temperature, T_B, and the last (corrected) open ocean calibration estimate of the instrument noise power, P_r. This is achieved by rearranging Equation 5.13 into an expression of the instrument gain and setting this equal to the instrument gain estimated directly from the blackbody load DDM calculated from Equation 5.8:

$$G = \frac{C - C_N}{P_g} = \frac{C_B}{P_B + P_r} \quad \textbf{(5.14)}$$

where

C_B is the mean count value of the last blackbody load DDM.
P_B is the estimated blackbody load noise power estimated using the last thermistor temperature reading near the load itself in the LNA and Equation 5.4.
P_r is the last estimate of the instrument noise power, estimated from a noise figure versus temperature lookup table (LUT) and validated during the open ocean calibration sequence.

A. Generating the Level 1A Data Product

The routine calibration assumes that the gain, G; antenna noise temperature, T_a; and the instrument noise power, P_r, remain constant over the combined collection interval for Equation 5.1 (DDM to be calibrated), Equation 5.2 (noise floor estimate for the DDM being calibrated), and Equation 5.8 (the blackbody load noise DDM). By substituting Equation 5.14 into Equation 5.13 and solving for the signal power term, P_g, we arrive at the final Level 1A calibration:

$$P_g = \frac{(C - C_N)(P_B + P_r)}{C_B} \quad \textbf{(5.15)}$$

B. Consideration of Time and Temperature Dependencies

All the terms in Equation 5.15 are collected at slightly different times than the actual science measurements themselves, and during these time intervals, it is possible that the noise temperatures can vary slightly from the measurement time. Each of the terms in the Level 1A calibration equation is addressed below with regard to this time difference:

1. C—The science measurement is made once per second and provides the reference time for all the other parameters.
2. C_N—The noise measurements for each science DDM are made at delays above the ocean surface, which are only on the order of a handful of microseconds from the time of the science measurement.
3. P_B—The blackbody target power is determined from a physical temperature sensor measured at 1 Hz and near enough in time to the 1 Hz science measurements that the physical temperature will not have changed significantly between the thermistor reading and the science measurement.
4. P_r—The receiver noise power is derived from open ocean measurements that may have been made minutes or hours apart from the science measurement. During this time, it is possible that the instrument noise temperature will have changed. How this is mitigated is described below.
5. C_B—The blackbody target measurement is made within 30 seconds of the science measurement and close enough in time that the receiver gain noise figure has not changed significantly.

One term in Equation 5.15, the receiver noise power, P_r, is derived from measurements that may have been made minutes or possibly hours apart from the science measurements. As such, it is possible that P_r has changed in that time. In order to address this, a temperature dependent LUT will be used to correct P_r. The LUT will be indexed by the readings of the same physical temperature sensor used to track the blackbody target temperature. The dependence of P_r on temperature will initially be characterized in prelaunch environmental testing, and the first flight LUT will be derived from those test data. Once in orbit, open ocean measurements will be used to validate P_r using Equation 5.11. As open ocean data are assembled over a range of physical temperatures, the LUT will be validated and, if necessary, updated in orbit.

C. Quality Control Flags

The Level 1A data product will include a set of quality control flags designed to indicate potential problems with the data. These flags, the parameters from which they are derived, and the default threshold values are listed in Table 5.1. Each of the quality control flags is briefly described below.

1. *Negative signal power in DDMA*. The delay Doppler map area (DDMA) is used for Level 2 wind speed retrievals and consists of three delay bins and five Doppler bins. This flag will be

Table 5.1. Level 1A quality control flags summary (OO stands for open ocean; TBD are values to be determined; DDMA stands for delay Doppler map area).

Flag	*Derived from*	*Threshold*	*Comment*
Negative signal power in DDMA	Output of Level 1A calibration algorithm	0 watts	$C - C_N < 0$
S/C S-Band transmitter on	S/C housekeeping telemetry	On/off	Possible power leakage into Level 1A DDM noise level
LNA temperature change since last BB calibration	LNA thermistor	TBD	Possible larger than expected error in P_B estimate
Open ocean DDM flag	Ground-based open ocean mask	Mask	Flag presence of land in DDM
Potentially high cross correlation power present	Number of PRNs in view	TBD	Detect bias in noise floor estimate
Low confidence in OO noise temperature	Ground-based model	TBD	Do not use DDM for open ocean calibration
Radio frequency interference (RFI) flag	Noise floor	TBD	Possible internal or external RFI present

set if the Level 1A calibration resulted in any of these bins having negative power values.

2. *S-Band transmitter on*. During spacecraft downlink operations, there is a possibility of power leaking into the nadir antennas and biasing the noise floor estimation. This flag will be set for individual DDMs whenever the S-band transmitter was on while the DDM was taken.
3. *LNA temperature change since last blackbody load calibration*. The blackbody load calibration will be performed every 60 seconds. This flag will indicate a larger than expected temperature change in the LNA since the last blackbody calibration.
4. *Open ocean DDM flag*. Will indicate that there is no land within 50 km of measurement location. When not set, the absence of this flag indicates the presence of land in the DDM glistening zone, allowing users to filter out contaminated DDM bins during higher level processing.
5. *Low confidence in open ocean noise temperature*. If the modeled value of the open ocean noise temperature is suspected to have larger than normal errors, this flag will be set.
6. *Radio frequency interference (RFI) flag*. If unusual statistics are observed in the DDM noise floor, this is an indication that an internal (to the instrument or spacecraft) or external RFI noise source is biasing the DDM noise floor estimate.

IV. Error Analysis of the Level 1A Calibration Algorithm

The Level 1A data product consists of observed signal power, P_g (in watts), over a range of delay steps and Doppler frequencies. This error analysis concentrates on the uncertainties present in the CYGNSS Level 1A calibration algorithm. Each uncertainty in the Level 1A calibration algorithm will be considered an independent uncorrelated error source. The method for this error analysis is based on that presented in Jansen et al. (1995) for a microwave radiometer. The errors in the Level 1A calibration can be broken into two parts: the estimation of the instrument noise performed during the open ocean calibration sequence, P_r, and the routine second by second calibration of the science DDM, P_g. The error analysis included here is based on the method proposed in Janssen et al. (1995).

A. Error Analysis in Open Ocean Instrument Noise Calibration

Equation 5.11 for the calculation of the instrument noise power is repeated below:

$$P_r = \frac{P_O C_B - P_B C_O}{C_O - C_B} \tag{5.16}$$

The total error in the estimate of the instrument noise power, P_r, is the RSS of the individual errors

Table 5.2. Open ocean instrument noise calibration errors (dB).

Error term	*N1 = 5120 (2 DDMs)*	*Comment*
$E(P_B)$	0.05	Blackbody load power error $\Delta T_B = 2°$
$E(P_O)$	0.07	Open ocean power error $\Delta T_B = 2°$
$E(C_B)$	0.18	Blackbody noise floor estimate, counts
$E(C_O)$	0.10	Open ocean noise floor estimate, counts
Total RSS error (ΔP_r)	0.23	LUT errors and Equation 5.17

contributed by the independent terms of Equation 5.16, expressed as

$$\Delta P_r = \left[\sum_{i=1}^{4} E^2(q_i)\right]^{1/2} \quad \textbf{(5.17)}$$

where the partial derivatives of the individual errors terms can be expressed as

$$E(q_i) = \left| \frac{\partial P_r}{\partial q_i} \right| \Delta q_i \quad \textbf{(5.18)}$$

The individual error quantities are defined as $q_1 = P_B$, $q_2 = P_O$, $q_3 = C_B$, and $q_4 = C_O$. The 1-sigma uncertainties in these quantities are expressed as Δq_i. Using Equation 5.16 and Equation 5.18 to evaluate the partial derivative error terms, we obtain

$$E(P_B) = \frac{C_O}{C_B - C_O} \Delta P_B \quad \textbf{(5.19)}$$

$$E(P_O) = \frac{C_B}{C_B - C_O} \Delta P_O \quad \textbf{(5.20)}$$

$$E(C_B) = \frac{P_O C_O - 2P_O C_B + P_B C_O}{(C_B - C_O)^2} \Delta C_B \quad \textbf{(5.21)}$$

$$E(C_O) = \frac{P_B C_B - 2P_B C_O + P_O C_B}{(C_B - C_O)^2} \Delta C_O \quad \textbf{(5.22)}$$

The error magnitudes for each of these terms can be approximated as follows. The blackbody load P^B and open ocean P^O power can be broken down to their respective temperatures such that

$$P^B = kT^B B_W \quad \textbf{(5.23)}$$

$$P^O = kT^O B_W \quad \textbf{(5.24)}$$

This results in the following expressions for changes in noise power due to uncertainties in the blackbody and open ocean reference temperatures:

$$\Delta P_B = k\Delta T_B B_W \quad \textbf{(5.25)}$$

$$\Delta P_O = k\Delta T_O B_W \quad \textbf{(5.26)}$$

where ΔT_B and ΔT_O are the blackbody load and open ocean temperature 1-sigma errors.

The 1-sigma errors in the observed noise powers, ΔC_O and ΔC_B, vary as a function of the number of noise samples collected to estimate the average power level as

$$\Delta C_B = std(\vec{C}_B^{N_1}) \quad \textbf{(5.27)}$$

$$\Delta C_O = std(\vec{C}_O^{N_1}) \quad \textbf{(5.28)}$$

Where $\vec{C}_B^{N_1}$ and $\vec{C}_O^{N_1}$ are noise samples vectors of length N_1. Given 20 noise samples in every DDM Doppler row, a full DDM corresponds to 2560 noise samples.

Quantitative values for each of the error components listed above and the total RSS for open ocean calibration using two full DDMs and instrument noise power estimates using a LUT only are shown in Table 5.2.

B. Instrument Noise Power Estimation Using a LUT

It will be necessary to estimate the change in instrument noise power between open ocean calibrations due to LNA temperature fluctuations. This will be done using a LUT derived from measured characteristics of the LNA gain and noise figure characteristics as a function of temperature. Preliminary thermal testing of the LNA noise figure performance as a function

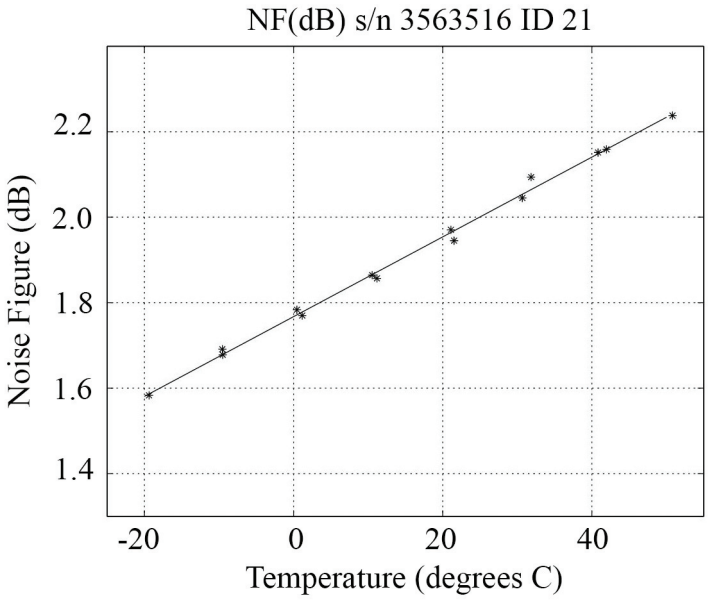

Figure 5.3. Measured noise figure performance of a CYGNSS LNA over 13 thermal cycles. Results shown over the temperature the LNA is expected to see based on S/C level thermal modeling.

of temperature over several thermal cycles indicates relatively good predictability and repeatability of the LNA gain and noise figure.

The temperature of the LNA is read at 1 Hz and the value of the instrument noise figure is retrieved from a LUT generated from prelaunch testing. The LUT is then updated on orbit using instrument noise floor estimates performed at sufficient intervals to track slow changes in the LNA performance. The instrument noise figure from the LUT is related to the instrument noise power using Equation 5.12, where the instrument noise power can be calculated from the noise figure as

$$P_r = k(NF - 1)290B_W \tag{5.29}$$

C. Error Analysis in Routine Signal Power Estimation

Equation 5.15 for the routine calculation of the calibrated signal power is repeated below:

$$P_g = \frac{(C - C_N)(P_B + P_r)}{C_B} \tag{5.30}$$

The total error in the estimate of the signal power, P_g, is the RSS of the individual errors contributed by the independent terms of Equation 5.30, expressed as

$$\Delta P_g = \left[\sum_{i=1}^{5} E^2(p_i)\right]^{1/2} \tag{5.31}$$

where the partial derivatives of the individual errors terms can be expressed as

$$E(p_i) = \left|\frac{\partial P_g}{\partial p_i}\right| \Delta p_i \tag{5.32}$$

The individual error quantities are defined as $p_1 = C$, $p_2 = C_N$, $p_3 = P_B$, $p_4 = P_r$, and $p_5 = C_B$. The 1-sigma uncertainties in these quantities are expressed as Δp_i. Using Equation 5.30 and Equation 5.32 to evaluate the partial derivative error terms, we obtain

$$E(C) = \frac{P_B + P_r}{C_B}\Delta C \tag{5.33}$$

$$E(C_N) = \frac{P_B + P_r}{C_B}\Delta C_N \tag{5.34}$$

$$E(P_B) = \frac{C - C_N}{C_B}\Delta P_B \tag{5.35}$$

$$E(P_r) = \frac{C - C_N}{C_B}\Delta P_r \tag{5.36}$$

Table 5.3. Routine Level 1A signal power calibration errors (dB). In both wind cases, the noise floor was computed using 52 rows (20 pixels per row) of noise pixels. ***Reused from Gleason et al. (2016), © 2016 IEEE.***

Error term	*Low winds, σ_0 = 20*	*High winds, σ_0 = 12*	*Comment*
$E(C)$	0.002	0.01	Quantization error
$E(C_N)$	0.10	0.14	Noise floor power error, counts
$E(P_B)$	0.01	0.01	Blackbody load power error $\Delta T_B = 2°$
$E(P_r)$	0.49	0.17	Instrument noise error
$E(C_B)$	0.06	0.06	Blackbody noise floor estimate, counts
Total RSS error	0.50	0.23	Equation 5.31

$$E(C_B) = \frac{(C - C_N)(P_B + P_r)}{C_B^2}\Delta C_B \qquad \textbf{(5.37)}$$

where the error terms can be calculated from the following:

ΔC —The error inherent in the Level 0 DDMs from the instrument is due to the quantization error in the raw DDM bins. From the CYGNSS DDM compression algorithm, each DDM bin will be quantized over a range of nine bits, resulting in an error of $\frac{1}{2^9}$.

ΔC_N —The error in the estimate of the DDM noise floor (from DDM samples above the ocean surface) is a function of the number of noise samples taken and can be expressed as

$$\Delta C_N = std(\vec{C}_N^{N_2}) \qquad \textbf{(5.38)}$$

where $\vec{C}_N^{N_2}$ is a noise samples vector of length N_2. Given 20 noise samples in every DDM Doppler row, a half of a full DDM corresponds to 64 rows or 1280 samples.

ΔP_B can be calculated from Equation 5.25, ΔP_r is the RSS errors from the open ocean calibration, and ΔC_B can be calculated from Equation 5.27. Quantitative values for each of the error components listed above and the RSS total for both wind retrieval regions are shown in Table 5.3. The below 20 m s^{-1} wind analysis assumed a σ_0 value of 20 dB, while the above 20 m s^{-1} regions assumed a σ_0 of 12 dB. Table 5.3 reflects that in order to accurately determine the DDM noise floor, C_N, it is desirable to have at least half a DDM of noise samples.

Table 5.3 shows the estimated Level 1A errors for winds at or below 20 m s^{-1}, as well as winds above 20 m s^{-1}. The estimated σ_0 for 20 m s^{-1} winds is 20 dB.

V. Zenith Level 1A Calibration Algorithm: Counts to Watts

The zenith Level 1A calibration converts the zenith direct channel signal counts to watts. These counts are linearly related to the direct noise and direct signal power processed by the DDMI. The total signal includes contributions from the deep space background noise and internal instrument noise generated by the DDMI itself. The power in the received signal is multiplied by the total gain of the DDMI receiver. The direct signal value in counts is related to the arriving signal power in watts by

$$C^z = G\left(P_a^z + P_r^z + P_g^z\right) \qquad \textbf{(5.39)}$$

where C^z is the tracked zenith direct signal value in counts output from the delay mapping receiver (DMR) navigation channel, P_a^z is the antenna noise power generated by the zenith space-looking antenna in watts, P_r^z is the instrument thermal noise power added by the instrument zenith channel in watts, P_g^z is the tracked zenith signal power in watts, and G is the total instrument gain applied to the incoming direct signal in counts per watt.

Noise information is calculated separately using a dedicated noise channel on the DMR. The noise can be expressed as

$$C_N^z = G\left(P_a^z + P_r^z\right) \qquad \textbf{(5.40)}$$

where C_N^z is the output of the zenith noise channel in counts.

A. Zenith Antenna Noise Power Expressions

The zenith LNA calibration switch selects between the zenith antenna and a blackbody target as the source of the input signal. When switched to the zenith antenna, the signal will consist of both the thermal emission from deep space and the direct GPS signal. The zenith calibration will be performed only when the deep space model indicates that the zenith antenna is oriented toward deep (cold) space.

$$P_a^z = P_{DS} = kT_{DS}B_W \quad \textbf{(5.41)}$$

where P_{DS} and T_{DS} are the noise power and antenna beam-integrated brightness temperature of deep space. The value of T_{DS} is the deep space brightness temperature integrated over the zenith antenna derived from a model, k is Boltzmann's constant, and $B_W = \frac{1}{T_i} = 1000\ \text{Hz}$ is the processed signal bandwidth. The bandwidth of the processed GPS signal at the antenna is determined by the coherent integration processing interval, which is $T_i = 1$ ms. When the zenith calibration switch is directed to the blackbody target, the thermal noise power entering the DDMI zenith channel becomes

$$P_B^z = kT_B^z B_W \quad \textbf{(5.42)}$$

where P_B^z and T_B^z are the blackbody load noise power and effective temperature of the instrument blackbody load source, respectively. The thermal noise power of the DDMI zenith channel can be expressed as a function of the noise figure of the zenith LNA as

$$P_r^z = kT_r^z B_W = k[(NF - 1)290]B_W \quad \textbf{(5.43)}$$

where P_r^z and T_r^z are the instrument noise power and noise temperature for the zenith antenna channel, respectively. The zenith LNA noise figure is determined from the prelaunch derived LUT and is used to calculate the instrument noise power using Equation 5.43.

B. Estimating Direct Signal Power Levels

The routine zenith signal power calibration will be performed whenever the zenith antenna is oriented toward deep space, as determined by the model. The direct signal power will be calculated from Equation 5.39 directly as follows:

$$P_g^z = \frac{C^z}{G} - P_r^z - P_a^z = \frac{C^z}{G} - P_r^z - P_{DS} \quad \textbf{(5.44)}$$

where

1. C^z is the direct signal counts, provided for every GPS satellite being used to generate a DDM measurement.
2. G is the total instrument gain, including the LNA gain, all cascaded front-end gain stages, and processing gain. This will be determined from a prelaunch generated LUT, which will be updated on orbit using the periodic zenith blackbody calibration described below.
3. P_r^z is the instrument noise power calculated from the instrument noise figure versus temperature LUT and Equation 5.43. The noise figure LUT of the zenith channel will be updated on orbit during the blackbody calibration described below.
4. P_{DS} is the deep space noise power calculated using Equation 5.41, derived from a model. The model will determine when the zenith antenna is pointed at deep space and estimate the expected deep space noise temperature T_{DS}.

C. Zenith Blackbody Calibration

The blackbody load input on the zenith antenna will only be switched on occasionally (on the order of weeks). This is due to the disruption the switch causes in the instrument navigation and corresponding DDM generation. However, during these occasional blackbody load switches, we will be able to make on-orbit estimates of the zenith channel total system gain, G, and noise figure, NF, which are used in the direct power calculation of Equation 5.44. The total instrument gain can be estimated by differencing the deep space noise counts and the blackbody noise counts, where each is represented as

$$C_B^z = G(P_B^z + P_r^z) \quad \textbf{(5.45)}$$

$$C_{DS} = G(P_{DS} + P_r^z) \quad \textbf{(5.46)}$$

Differencing the above two equations gives us

$$C_{DS} - C_B^z = GP_{DS} - GP_B^z \quad \textbf{(5.47)}$$

which can be solved for the instrument total system gain,

$$G = \frac{C_{DS} - C_B^z}{P_{DS} - P_B^z} \quad \textbf{(5.48)}$$

Subsequently, substituting Equation 5.48 into Equation 5.46 gives an estimate of the instrument noise power as

$$P_r^z = \frac{P_{DS}C_B^z - P_B^z C_{DS}}{C_{DS} - C_B^z} \quad \textbf{(5.49)}$$

where

P_{DS} is the deep space noise power calculated from the model.

C_{DS} is the deep space noise counts from the zenith noise channel when the antenna input is selected and the antenna is oriented toward deep space.

P_B^z is the blackbody noise power calculated using Equation 5.42 using the zenith LNA physical temperature T_B^z.

C_B^z is the blackbody load noise counts from the zenith noise channel when the LNA is switched to the blackbody load.

This estimate of the instrument noise power, P_r^z, can then be used to estimate the instrument LNA noise figure LUT entry by solving for NF in Equation 5.43 as

$$NF = \frac{P_r^z}{290kB_W} + 1 \quad \textbf{(5.50)}$$

D. Conclusions and Discussion

The above algorithm is very similar to the nadir antenna DDM calibration with a couple of notable exceptions:

1. The open ocean calibration used to update the instrument noise power and gain tables has been replaced by the deep space calibration. In the case of the deep space calibration, a model is used to determine when the CYGNSS observatory is pointed towards deep space, and the corresponding antenna brightness temperature T_{DS} is used to calculate the input antenna noise power, P_{DS}. P_{DS} is then used in a direct calculation of the direct signal power P_g^z.
2. The blackbody load on the zenith antenna is switched in at a significantly slower rate than during the routine nadir calibration. For this reason, it is used only to periodically check and validate the gain and noise figure LUTs.

References

Gleason, S., Ruf, C., Clarizia, M. P., & O'Brien, A. (2016). Calibration and unwrapping of the normalized scattering cross section for the Cyclone Global Navigation Satellite System (CYGNSS). *Geoscience and Remote Sensing, IEEE Transactions On*. doi: 10.1109/TGRS.2015.2502245

Janssen, M., Ruf, C. S., & Keihm, S. J. (1995). TOPEX/Poseidon Microwave Radiometer (TMR). II. Antenna pattern correction and brightness temperature algorithm. *Geoscience and Remote Sensing, IEEE Transactions On, 33*(1), 138–146. doi: 10.1109/36.368214

6. Additional Level 1 Calibration Procedures

I. Open Ocean Calibration

A. Algorithm Theoretical Basis for Open Ocean Calibration

In describing the open ocean calibration, it is instructive to briefly review the fundamental goal of the overall Level 1A calibration as described in Section 5 (and as taken from Gleason et al., 2016). The bins of the DDM are acquired at a time resolution of 1 Hz in uncalibrated units of counts (C). The purpose of the Level 1A calibration is to (a) convert counts to units of power (P) in watts and (b) remove unwanted noise. Regarding (a), counts are linearly related to power by the instrument gain (G) and can be converted to power once G is known. Regarding (b), the desired scattered GPS signal power (P_g) is accompanied by thermal emission from the ocean/atmosphere (P_a) and also from the instrument itself (P_r), both of which constitute noise power that must be removed to isolate the scattered signal power, P_g.

Thermal emission from the instrument results in an instrument noise temperature (T_r) that lowers the signal-to-noise ratio. T_r is related (but not equal) to the instrument's physical temperature ($T_{r\,phys}$), and this relationship is initially established during the prelaunch period under controlled laboratory conditions where a LUT mapping $T_{r\,phys}$ to T_r is created over a range of T_r values (Figure 6.1).

Using this LUT (hereafter LUT_{Tr}), measured values of $T_{r\,phys}$ can be directly converted to T_r, which can then be expressed as an instrument noise power (P_r) by use of the Rayleigh-Jeans approximation for long wavelengths. The resulting relationship is

$$P_r = kT_rB_W \tag{6.1}$$

where k is Boltzmann's constant, and B_W is the receiver effective noise bandwidth. T_r is also directly related to the numeric value of NF, which is a measure of the decline in the signal-to-noise ratio as the signal passes through the LNA:

$$T_r = \frac{P_r}{kB_W} = 290(NF - 1) \tag{6.2}$$

Earlier in Section 5, P_r was combined with a noise power from an onboard blackbody calibration load (P_B) in order to determine the instrument gain (G):

$$P_B = kT_BB_W \tag{6.3}$$

$$C_B = G(P_B + P_r) \tag{6.4}$$

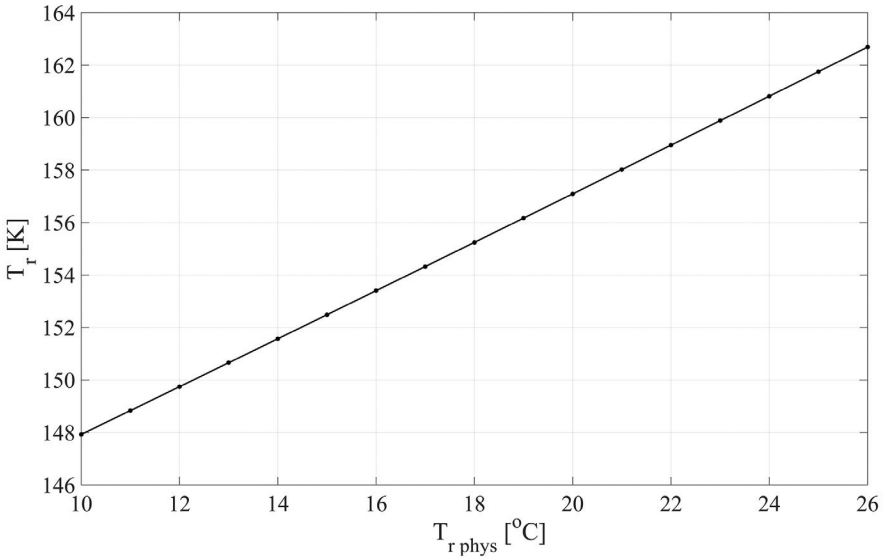

Figure 6.1. Relationship between $T_{r\,phys}$ versus T_r, for a range of $T_{r\,phys}$ from 10°C to 26°C.

Here, T_B is the temperature of the blackbody load, and C_B are counts measured when the instrument input is switched from the external antenna to the blackbody calibration load. The relationship between $P_B + P_r$ and C_B is illustrated conceptually in Figure 6.2.

From here, measurements of the total noise in counts (C_N) from samples of the DDM well away from the specular point and diffuse scattering regions (i.e., a region of the DDM where P_g is negligibly small, Figure 6.3) can be combined with G to determine P_g. Refer to Section 5 for more details.

An issue that arises is that the dependence of T_r on $T_{r\,phys}$ as defined in the LUT_{Tr} (Figure 6.1) may drift over the life of the spacecraft due to, for example, bombardment by high level solar radiation and/or energized ions. When this occurs, T_r (and thus P_r) as derived from the LUT_{Tr} will no longer be able to provide reliable values of G and P_g. The purpose of the open ocean calibration is to evaluate whether or not the original relationship between T_r and $T_{r\,phys}$ has changed—and to what extent. To do so requires a method for obtaining T_r by means other than the originally prescribed LUT_{Tr}. This can be achieved by acquiring the cold thermal noise power from the ocean/atmosphere (P_O) whenever the spacecraft has no land within its nadir antenna beam:

$$P_O = kT_O B_W \tag{6.5}$$

In Equation 6.5, T_O is the antenna temperature or nadir science antenna beam averaged brightness temperature of the Earth over the open ocean. Evaluation of an L-band radiative transfer model (RTM) revealed that a constant value of T_O = 99.4 K for all time and locations may be sufficient for the calibration (see Part II of this section). Therefore, a LUT for values of T_O with a resolution of 1° × 1° latitude and longitude will be generated for each month (hereafter LUT_{TO}) and initially populated solely with the value 99.4 K. From T_O, the value for P_O is easily obtained from Equation 6.5.

Next, we obtain the relationship between counts and gain for the open ocean calibration:

$$C_O = G(P_O + P_r) \tag{6.6}$$

This is similar to Equation 6.4, except now the noise counts (C_O) and noise power (P_O) are from over the open ocean, rather than from the blackbody load. Here the value C_O is taken from the same region of the DDM as C_N shown in Figure 6.3. Next, taking the difference between Equations 6.6 and 6.4 results in the cancellation of P_r, which allows one to rearrange and solve for G:

$$C_O - C_B = G(P_O + P_r) - G(P_B + P_r) \tag{6.7}$$

$$C_O - C_B = GP_O + GP_r - GP_B - GP_r \tag{6.8}$$

$$G = \frac{C_O - C_B}{P_O - P_B} \tag{6.9}$$

Substitution of Equation 6.9 into 6.6 allows one to arrive at an expression for P_r:

$$P_r = \frac{P_O C_B - P_B C_O}{C_O - C_B} \tag{6.10}$$

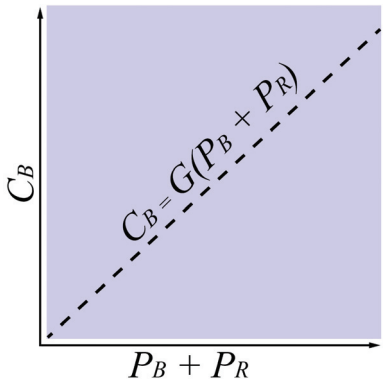

Figure 6.2. Conceptual diagram of the relationship between $P_B + P_r$ versus C_B, where the slope of the dashed line is the instrument gain (G).

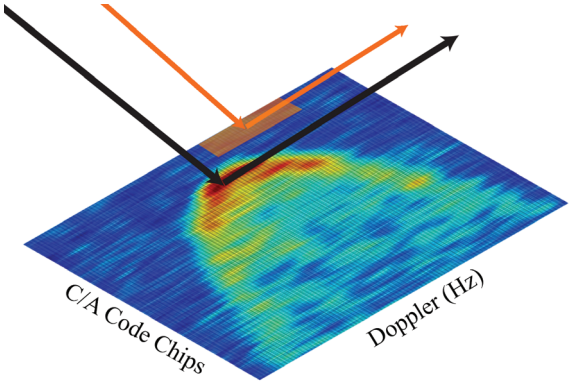

Figure 6.3. Orange shading and arrows indicate the region of the DDM where C_N is obtained. Black arrows indicate the signal at the specular reflection point.

With this value of P_r, one returns to Equation 6.2 in order to obtain T_r. From a range of values of T_r, a new relationship between T_r and $T_{r\ phys}$ can be derived. The existing LUT_{Tr} describing the relationship between T_r and $T_{r\ phys}$ will be revised if there is a statistically significant indication by the most recent open ocean analysis that it has changed (Figure 6.4). This process is described in more detail in Subsection B.

B. Algorithm Specification

The eight CYGNSS spacecraft will obtain 4 DDMs each second. These 1 Hz DDM measurements will be taken from specular reflection points that lie within the nadir antenna beams. Given that there are two downward looking antennas on each spacecraft and each antenna has its own receiver noise temperature, it will be important to distinguish which DDM was measured by which antenna, since each antenna will require its own calibration. Furthermore, the instrument input will be switched to the internal blackbody load every 30 s (current default), so there will be expected gaps in the time sequence of DDMs during these intervals. Additionally, open ocean measurements of C_O can only be acquired when no land is within the field of view, so the availability of C_O will be restricted. Required inputs to the open ocean calibration are defined below and described in Table 6.1.

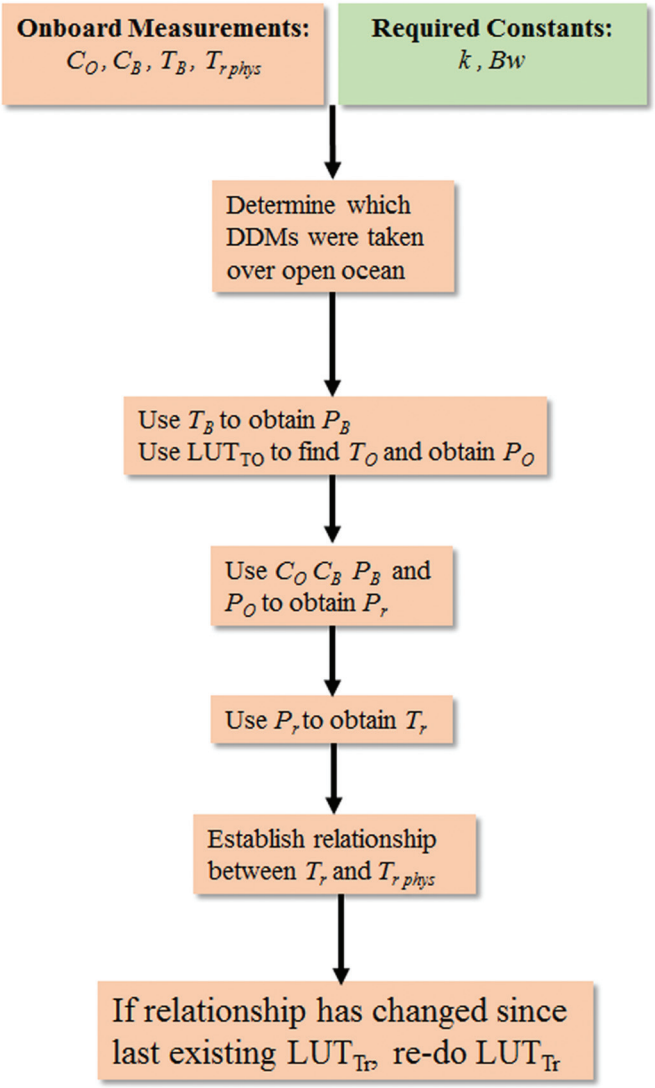

Figure 6.4. Flowchart showing the steps in the open ocean calibration used to estimate T_r. Part B gives a more detailed explanation of this procedure.

Input Definitions

Measured variables and constants:

C_O = counts while viewing the Earth, made from the science DDMs in regions with no scattered GPS signal present
C_B = counts when viewing the internal blackbody load
T_B = physical and brightness temperature of the blackbody load measured with the onboard temperature sensor
$T_{r\ phys}$ = physical temperature of the LNA from the temperature sensor
k = Boltzmann's constant
B_W = signal bandwidth
T_O = nadir science antenna beam averaged brightness temperature of Earth (over the ocean)

Required outputs are defined below and described in Table 6.2.

Output Definitions

P_r = noise power from the instrument
T_r = noise temperature from the instrument

To perform the calibration requires obtaining the input variables from Table 6.1 over a prescribed acquisition period. From this block of data, all input variables coming from each nadir antenna (2 for each of the 8 satellites; i.e., 16 antennas) must be treated separately. This results in 16 matrices of input variables. The following steps are performed on each matrix from each acquisition period:

Step 1. A filter will be applied to the DDMs to determine which are adequate for processing.
Step 2. For the DDMs retained after Step 1, isolate the input variables from Table 6.1 for each antenna.
Step 3. From those input variables, collect all counts from the blackbody load (C_B) and all corresponding counts made over the open ocean (C_O) for each antenna. Note that C_O will have been acquired every 1 s, while C_B will be taken less frequently (every 30 s is the current default). It is necessary to cluster the data so that each value of C_O is associated with the correctly corresponding value of C_B.
Step 4. Insert the measured values of T_B into Equation 6.3 to obtain P_B.

Table 6.1. Required inputs for the open ocean calibration. First column is the input variable as described above, second column is the source for obtaining that value (or the value if it is constant), third column is the units of the variable, and fourth column is the periodicity at which the measurement is obtained.

Input variable	*Source*	*Units*	*Periodicity*
C_O	DDMI	counts	1 s (when over ocean)
C_B	DDMI	counts	30 s
T_B	temp. sensor	°C	30 s
$T_{r\ phys}$	temp. sensor	°C	1 s
k	$1.3806488 \times 10^{-23}$	$W\ K^{-1}\ Hz^{-1}$	n/a (constant)
B_W	1000	Hz	n/a (constant)
T_O	LUT_{TO}	K	monthly

Table 6.2. Required outputs from the open ocean calibration. First column is the output variable as described above, second column is the equation from this document needed to obtain that value, and third column is the units of the value.

Output variable	*Equation*	*Units*
P_r	6.10	W
T_r	6.2	K

Step 5. Use a monthly LUT_{TO} to obtain T_O. The LUT_{TO} will have a resolution of 1° × 1° latitude and longitude and initially will be populated with the prescribed value of T_O = 99.4 K, as determined from analysis of the RTM (see Part II of this section). Insert T_O into Equation 6.5 to obtain P_O.

Step 6. Using C_B, C_O, P_B, and P_O, apply Equation 6.10 to obtain P_r.

Step 7. Using P_r, apply Equation 6.2 to get T_r. Note that there will be a new value of T_r for every science DDM.

Step 8. Compare the relationship between T_r to the values of $T_{r\ phys}$ over the range of values of T_r to determine if the relationship from the last existing LUT_{Tr} significantly differs from the new relationship.

Step 9. If the relationship in the last existing LUT_{Tr} is significantly different from the newly derived relationship for any given antenna, then a new LUT_{Tr} must be adopted. This new LUT_{Tr} will be used until future calibrations indicate that it must be replaced once again.

II. Radiative Transfer Model (RTM)

Top of atmosphere open ocean brightness temperature (*TB*) was determined via a radiative transfer model (RTM). Top of atmosphere *TB* is calculated as follows:

$$TB = e^{-\tau}(1-\varepsilon)TB_{DN} + e^{-2\tau}(1-\varepsilon)TB_{COS} + TB_{UP} + e^{-\tau}\varepsilon T_{SFC} \quad \textbf{(6.11)}$$

where $e^{-\tau}$ is the total atmosphere transmissivity, ε is the surface emissivity, TB_{DN} and TB_{UP} are the downwelling and upwelling *TB*, TB_{COS} is the cosmic microwave background *TB*, and T_{SFC} is the physical ocean surface temperature. Analysis of the atmosphere absorption models of Rosenkranz (1998), Rosenkranz (1993), and Liebe et al. (1992) revealed that at the CYGNSS frequency, TB_{DN} = 2.0060 K, TB_{UP} = 2.0053 K, and $\tau = 7.6 \times 10^{-3}$ Np, with very small variability. Slant path dependence on TB_{DN} and TB_{UP} is parameterized using sec(θ), where θ is the earth incidence angle. The surface emissivity model is based on Reul et al. (2012), Elsaesser (2006), and Meissner and Wentz (2004).

Using environmental inputs from the National Centers for Environmental Prediction (NCEP) Climate Forecast System Reanalysis (CFSR), *TB* is calculated for the open ocean. After *TB* is calculated for all points in the CYGNSS antenna pattern, all values of *TB* are weighted by the antenna pattern and integrated over the solid angle to obtain the antenna temperature (*TA*). We found that this *TA* integration limits the RMS error of *TA* to 0.7 K over time and space—if we were to use a single mean *TA* value for the open ocean calibration process. Since this RMS error is less than the 2 K accuracy requirement, the open ocean *TA* value used for T_O is 99.4 K for all instances in time and open ocean space. For each month, a LUT_{TO} with a spatial resolution of 1° × 1° latitude and longitude will be populated initially with T_O = 99.4 K for all fields (see Table 6.1 in Part I of this section). In the event that this value requires adjustment, this LUT_{TO} will be modified accordingly.

III. Zenith Antenna Calibration: Milky Way Filter Procedure

Occasionally, an absolute power calibration of the zenith antenna will be performed, for which looks at the cold sky are required. Care must be taken to note when the antenna boresight direction approaches that of the sun or the galactic plane of the Milky Way, both of which can result in higher brightness temperatures than cold space. While determination of the solar location is relatively straightforward, determining the location of the galactic plane of the Milky Way requires an ancillary dataset compiled from radio astronomy surveys. These data are a map of L-band effective brightness temperatures of the sky (Le Vine and Abraham, 2004) and are available as binary files in Section 1.2 on the following page (Dinnat et al., 2010): http://oceancolor.gsfc.nasa.gov/AQUARIUS/DinnatEtAl2010/. The data are in Earth centered inertial (ECI) J2000 coordinates, and each pixel is 0.25° × 0.25° (Figure 6.5). In this coordinate system, the horizontal axis is right ascension (α), which is similar to longitude except that it is measured as a continuous angle in the equatorial plane from the position of the vernal equinox (see Figure 6.7). The vertical axis is declination (δ), which is equivalent to latitude (negative values are in the southern hemisphere and 0 marks the equator).

Since the zenith antenna integrates pixels over a solid angle, it is appropriate to employ a weighted Gaussian filter to smooth the original brightness

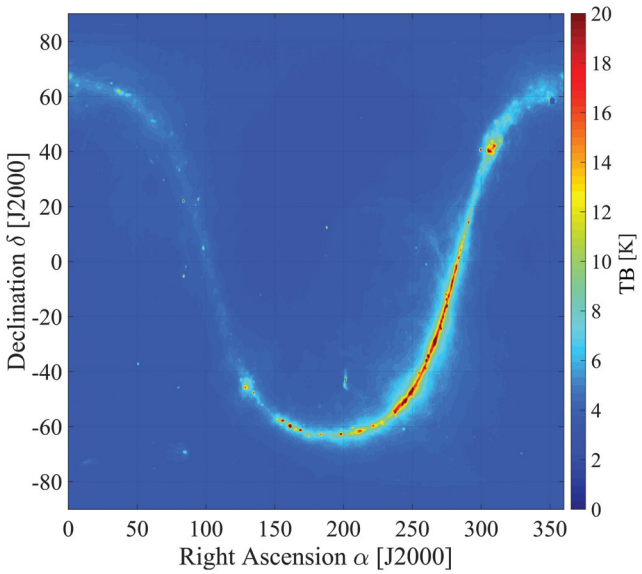

Figure 6.5. Raw values of L-band *TB* from Dinnat et al. (2010, see their Figure 6 on the website). The brighter values are the galactic plane of the Milky Way. Values of α and δ are in degrees.

temperature values. The two-dimensional Gaussian kernel used for smoothing the data is a matrix, $G_{x,y}$, defined as

$$G_{x,y} = \frac{1}{2\pi\sigma^2} e^{\frac{(-x^2-y^2)}{2\sigma^2}} \quad \textbf{(6.12)}$$

Here, x and y have 81 values that range from –40 to +40 pixels, with zero as their mean (center) value. The value σ is set equal to 10 pixels. By definition, this means that the full width half maximum (*FWHM*) is

$$FWHM = 2\sigma\sqrt{2ln2} \quad \textbf{(6.13)}$$

which, for $\sigma = 10$ pixels, provides a *FWHM* of 23.55 pixels or 5.89° (since each pixel is 0.25° square). The Gaussian kernel $G_{x,y}$ is then normalized via

$$F_{x,y} = \frac{G_{x,y}}{\sum_{x=1}^{81}\sum_{y=1}^{81} G_{x,y}} \quad \textbf{(6.14)}$$

where $\sum_{x=1}^{81}\sum_{y=1}^{81} G_{x,y}$ is, of course, the sum of all values in the matrix $G_{x,y}$ (note that if the coefficient $1/2\pi\sigma^2$ is used in Equation 6.12, this normalization is unnecessary). Then, for every pixel i in the matrix of raw data *TB*, we define a submatrix $A_{x,y}$ of size x by y, centered at i. All values in the submatrix $A_{x,y}$ are then multiplied by all the corresponding values in the matrix $F_{x,y}$ to provide a weighted matrix, $C_{x,y}$:

$$C_{x,y} = A_{x,y} \times F_{x,y} \quad \textbf{(6.15)}$$

Next, the center pixel value $A_{x,y}(i)$ is replaced by the sum of all values in the matrix $C_{x,y}$:

$$A_{x,y}(i) = \sum_{x=1}^{81}\sum_{y=1}^{81} C_{x,y} \quad \textbf{(6.16)}$$

The procedure is applied to all points in the original matrix *TB* until they are each replaced by the smoothed values in a new matrix *TBS*. To contend with pixels near the edge of the map in Figure 6.5, the map is replicated in the appropriate orientation on all sides of the original matrix of *TB* values.

The next step involves defining a threshold temperature above which values are considered to be within the galactic plane of the Milky Way. A histogram of the smoothed brightness temperatures (*TBS*) reveals that the most probable temperature value is about 3.64 K (Figure 6.6).

Adding half a degree Kelvin provides a threshold of 4.14 K, on either side of which lies a region of high and low temperature values. The high temperatures to the right of the threshold are considered "bright" values within the galactic plane of the Milky Way.

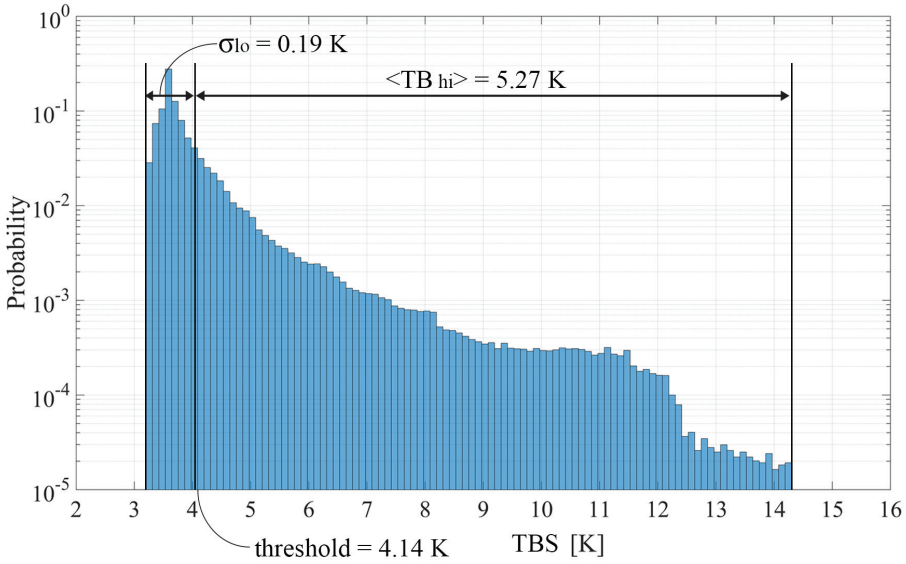

Figure 6.6. Histogram of *TBS* as described in the text. Sample size is 1,038,961 values, and bin size is 100.

The mean of those high values, $<TB_{hi}>$, is 5.27 K. The low temperatures to the left of the threshold are acceptable regions of "cold sky." The standard deviation of those cold values, σ_{lo}, is 0.19 K.

In order to evaluate how much the bright pixels contaminate the antenna for any given look direction, the zenith antenna boresight direction is first defined using Cartesian unit position vectors in the ECI J2000 coordinate system, $\mathbf{V}_B$ (Figure 6.7). Similar vectors are used to locate all Milky Way values ($\mathbf{V}_M$) and all cold sky values ($\mathbf{V}_C$). To obtain Cartesian (x, y, and z) coordinates from coordinates of α and δ in Figure 6.5, we employ

$$x = r\cos(\delta)\cos(\alpha) \tag{6.17}$$

$$y = r\cos(\delta)\sin(\alpha) \tag{6.18}$$

$$z = r\sin(\delta) \tag{6.19}$$

where r is a magnitude of unity. Note that in Figure 6.7, $\mathbf{V}_B$ assumes a perfect spacecraft attitude. In practice, small deviations in attitude will be considered, such that $\mathbf{V}_B$ may differ slightly from the ideal vector in Figure 6.7.

Next, all angles between $\mathbf{V}_B$ and every $\mathbf{V}_M$ and $\mathbf{V}_C$ vector are evaluated. These angles are denoted Υ_M and Υ_C, where the subscripts $_M$ and $_C$ stand for Milky Way and cold sky, respectively. All values of Υ_M and Υ_C that are less than 90° are flagged as being within the antenna's view and are denoted as Γ_M and Γ_C. Then the cosines of all Γ_M and Γ_C are evaluated in order to weight their significance owing to antenna gain. This is because when Υ is small, it is closer to the boresight direction and therefore it has more impact on the antenna (e.g., for a value of Υ close to 0°, $\mathbf{V}_B$ would be almost parallel to $\mathbf{V}_M$ in Figure 6.7). In addition, since the map projection in Figure 6.5 is equirectangular, pixels at high latitudes (nearing δ = –90 or +90) will be overrepresented. Therefore we also scale Γ_M and Γ_C by the cosine of their declination. Thus, for any given look direction $\mathbf{V}_B$, the following sums are evaluated for the Milky Way and the cold sky:

$$\Psi_M = \sum_{i=1}^{N_M} \cos(\Gamma_{Mi})\cos(\delta_{Mi}) \tag{6.20a}$$

$$\Psi_C = \sum_{i=1}^{N_C} \cos(\Gamma_{Ci})\cos(\delta_{Ci}) \tag{6.20b}$$

where N_M and N_C are the number of Milky Way (Γ_M) and cold sky (Γ_C) angles within the antenna's view, respectively. Next, a ratio, Ω, is generated such that

$$\Omega = \frac{\Psi_M}{\Psi_M + \Psi_C} \tag{6.21}$$

This ratio provides a robust evaluation of how much the Milky Way contaminates the antenna view as

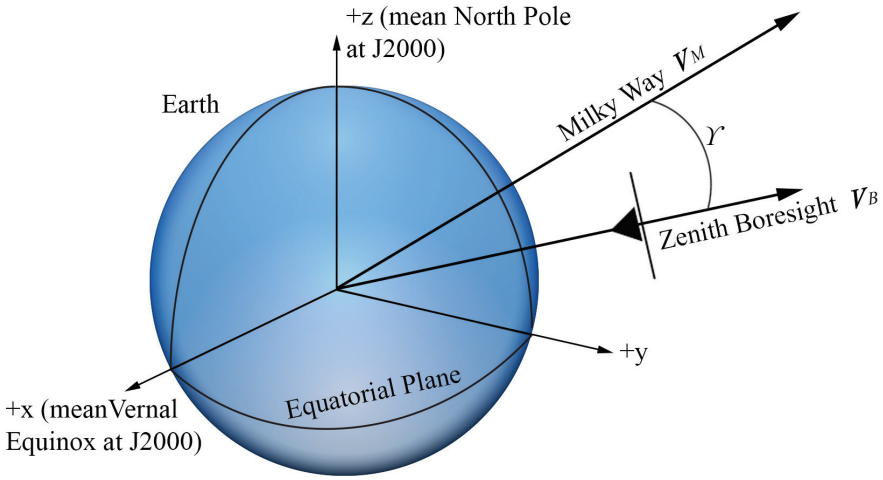

Figure 6.7. Diagram showing the relationship between position vectors V_B and V_M (V_C not shown for clarity).

compared to the total sky (Milky Way plus cold sky). The ratio Ω is more reliable than a simple measure of the fraction of Milky Way points in view, which gives equal weight to values that are far from the boresight direction and does not consider how much of the cold sky is also impacting the same view. To put Ω into context with the actual values of *TBS*, Ω is multiplied by the value $<TB_{hi}>$ to attain units of degrees Kelvin:

$$\beta = \Omega \times \langle TB_{hi} \rangle \quad \textbf{(6.22)}$$

For any given look direction, higher (lower) values of β imply that the Milky Way (cold sky) has a greater impact on the antenna. In Figure 6.8, curves of β for values of declination (δ) ranging from −45 to +45 are plotted at right ascension α = 180°. The look directions associated with where β is lowest are optimal to perform the zenith antenna calibration, provided that the spacecraft is also on the night side of the Earth (i.e., the sun is not in view). To decide how low the values of β must be for them to be acceptable, a threshold of $3\sigma_{lo}$ is employed. Therefore, in Figure 6.8, all look directions that correspond to α = 180° and δ = +10 to +45 would be considered uncontaminated by the Milky Way.

By evaluating β for the range of δ = −45 to +45 at every α (0 to 360°), a LUT indicating whether or not these look directions are contaminated by the Milky Way is generated. Figure 6.9 shows the results plotted on the celestial map. This LUT is employed in the Level 1 algorithm to flag look directions that are not available for zenith antenna calibration owing to the brightness of the galactic plane of the Milky Way. Look directions that are not contaminated by the Milky Way are then evaluated to determine if their time of occurrence was night or day, so that instances where the sun is in view can also be eliminated for calibration.

References

Dinnat, E. P., Le Vine, D. M., Abraham, S., & Floury, N. (2010). Map of sky background brightness temperature at L-band. Retrieved from http://oceancolor.gsfc.nasa.gov/AQUARIUS/DinnatEtAl2010/

Elsaesser, G. S. (2006). *A parametric optimal estimation retrieval of the non-precipitating parameters over the global oceans* (Doctoral dissertation, Colorado State University).

Gleason, S., Ruf, C., Clarizia, M. P., & O'Brien, A. (2016). Calibration and unwrapping of the normalized scattering cross section for the Cyclone Global Navigation Satellite System (CYGNSS). *Geoscience and Remote Sensing, IEEE Transactions On*. doi: 10.1109/TGRS.2015.2502245

Le Vine, D. M., & Abraham, S. (2004). Galactic noise and passive microwave remote sensing from space at L-band. *Geoscience and Remote Sensing, IEEE Transactions On*, *42*(1), 119–129. doi: 10.1109/TGRS.2003.817977

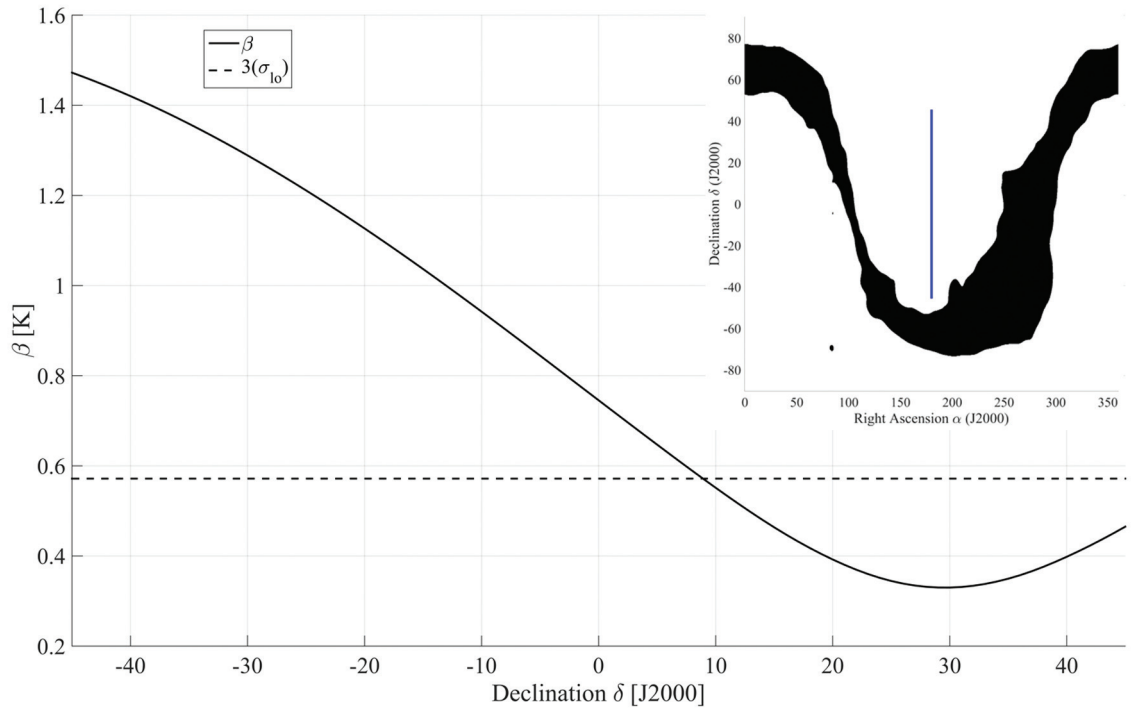

Figure 6.8. Sample plot of β for values of declination $\delta = -45$ to $+45$, at right ascension $\alpha = 180°$. The solid curve represents values of β. The black dashed line represents the threshold of $3\sigma_{lo}$. Values of β below the threshold are uncontaminated by the Milky Way. The inset shows these values of β with respect to the Milky Way. (Black values are the galactic plane.)

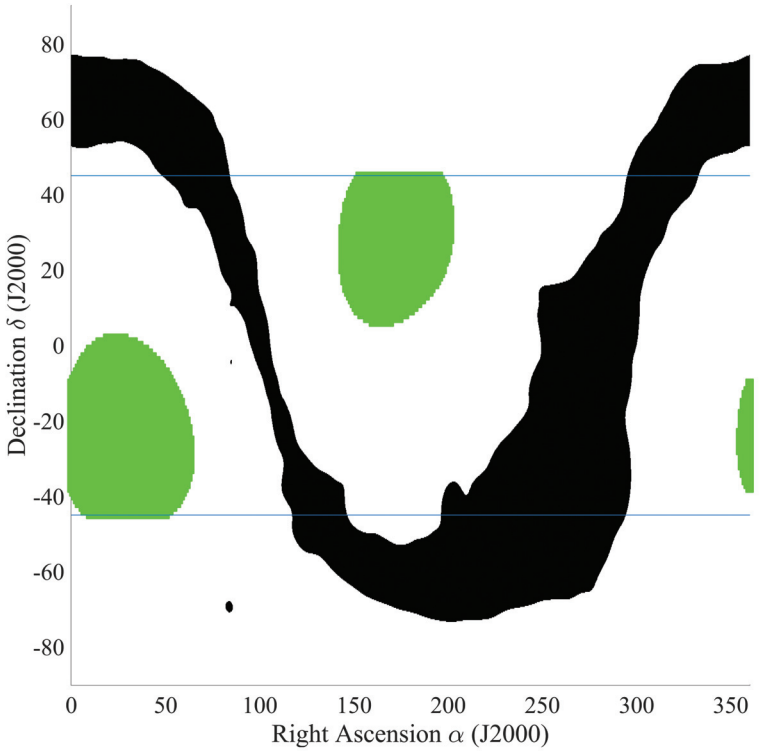

Figure 6.9. Celestial map with green squares indicating which coordinates are acceptably free of contamination by the galactic plane of the Milky Way. The two horizontal lines are the ±45° latitude lines.

Liebe, H. J., Rosenkranz, P. W., & Hufford, G. A. (1992). Atmospheric 60-GHz oxygen spectrum: New laboratory measurements and line parameters. *Journal of Quantitative Spectroscopy and Radiative Transfer*, *48*(5), 629–643. doi: 10.1016/0022-4073(92)90127-P

Meissner, T., & Wentz, F. J. (2004). The complex dielectric constant of pure and sea water from microwave satellite observations. *Geoscience and Remote Sensing, IEEE Transactions On*, *42*(9), 1836–1849. doi: 10.1109/TGRS.2004.831888

Reul, N., Tenerelli, J., Chapron, B., Vandemark, D., Quilfen, Y., & Kerr, Y. (2012). SMOS satellite L-band radiometer: A new capability for ocean surface remote sensing in hurricanes. *Journal of Geophysical Research: Oceans (1978–2012)*, *117*(C2). doi: 10.1029/2011JC007474

Rosenkranz, P. W. (1993). Absorption of microwaves by atmospheric gases. In M. A. Janssen (Ed.), *Atmospheric Remote Sensing by Microwave Radiometry* (pp. 37–79). New York, NY: John Wiley & Sons. Retrieved from http://hdl.handle.net/1721.1/68611

Rosenkranz, P. W. (1998). Water vapor microwave continuum absorption: A comparison of measurements and models. *Radio Science*, *33*(4), 919–928. doi: 10.1029/98RS01182

7. Level 1B Calibration and Error Analysis

I. Level 1B Calibration Approach

The Level 1B calibration is performed after the Level 1A calibration and will use external metadata to convert the Level 1A mapped power in watts to a DDM map of BRCS values and a corresponding map of normalization areas. This calibration will be done for every DDM and requires the following information at the time every science DDM is collected:

1. The CYGNSS satellite GPS time, position, and velocity in the Earth centered, Earth fixed (ECEF) reference frame.
2. The GPS satellite position and velocity in the ECEF reference frame.
3. Detailed knowledge of the CYGNSS nadir antenna gain patterns.
4. Attitude information of the CYGNSS spacecraft.
5. Information on the GPS satellite transmit power and antenna gain derived from the CYGNSS direct signal power measurements.

II. Summary of Forward Model Used in Level 1B Calibration

A full expression for the GPS scattered signal power has been previously derived and published by Zavorotny and Voronovich (2000), shown in Equation 7.1. A full derivation of the forward scattering model is included in the appendix at the end of this handbook. The original representation has been slightly modified in form and variables:

$$P_{g,\hat{\tau},\hat{f}} = \frac{P^T \lambda^2}{(4\pi)^3} \iint_A \frac{G^T_{x,y} \sigma_{0\,x,y} G^R_{x,y}}{(R^R_{x,y})^2 (R^T_{x,y})^2 L_{a1} L_{a2}} \Lambda^2_{\hat{\tau};x,y} S^2_{\hat{f};x,y} \, dxdy \quad \textbf{(7.1)}$$

where $P_{g,\hat{\tau},\hat{f}}$ is the coherently processed scattered signal power, in watts; P^T is the GPS satellite transmit power and $G^T_{x,y}$ is the GPS satellite antenna gain; $G^R_{x,y}$ is the CYGNSS satellite receiver antenna gain; $R^T_{x,y}$ and $R^R_{x,y}$ are the transmitter to surface and surface to receiver ranges, respectively; L_{a1} and L_{a2} are atmospheric losses to and from the surface; $\sigma_{0\,x,y}$ is the NBRCS; λ is the GPS signal carrier wavelength (~19 cm); $\Lambda_{\hat{\tau};x,y}$ is the GPS signal spreading function in delay and $S_{\hat{f};x,y}$ is the frequency response of the GPS signal; and A is the surface integration area, covering the region of diffuse scattering for each delay Doppler bin. The scattered signal power is processed using 1 millisecond coherent integration intervals over a range of relative delays $\hat{\tau}$ and Doppler frequencies $\hat{f}$, followed by 1 second of noncoherent averaging.

By performing the surface integration, the above expression can be simplified using the effective values (indicated by an overbar) of several variables in each bin under the integrand of Equation 7.1, at each delay/Doppler bin:

$$P_{g,\hat{\tau},\hat{f}} = \frac{P^T \lambda^2 \bar{G}^T_{\hat{\tau},\hat{f}} \bar{\sigma}_{0\,\hat{\tau},\hat{f}} \bar{G}^R_{\hat{\tau},\hat{f}} \bar{A}_{\hat{\tau},\hat{f}}}{(4\pi)^3 (\bar{R}^R_{\hat{\tau},\hat{f}})^2 (\bar{R}^T_{\hat{\tau},\hat{f}})^2 \bar{L}_{a1} \bar{L}_{a2}} \quad \textbf{(7.2)}$$

where $\bar{G}^R_{\hat{\tau},\hat{f}}$ is the receiver antenna gain at each delay/Doppler bin, $\bar{R}^T_{\hat{\tau},\hat{f}}$ and $\bar{R}^R_{\hat{\tau},\hat{f}}$ are the range losses at each delay/Doppler bin, and $\bar{A}_{\hat{\tau},\hat{f}}$ is the effective surface scattering area at each delay/Doppler bin.

III. Level 1B Calibration Algorithm: Watts to Sigma0

The Level 1A calibrated DDM represents the received surface signal power in watts over a range of time delays and Doppler frequencies. Before any geophysical parameters can be estimated, these power values must be corrected for non-surface-related terms by inverting the forward model shown in Equation 7.2, based on the familiar radar equation. The CYGNSS Level 1B calibration generates two data products associated with each Level 1A DDM: (1) a bin-by-bin calculation of the surface BRCS, σ (not normalized by scattering area), and (2) bin-by-bin values of the effective scattering areas. These two products will allow users to normalize values of σ to values of σ_0 over configurable surface extents using the effective scattering area of each DDM bin. The values of sigma are corrected for effects of the transmit and receive antennas, range losses, and other non-surface-related parameters. The effective scattering areas are calculated based on the measurement-specific reflection geometry and include the

GPS specific delay and Doppler spreading functions. An overview of the CYGNSS Level 1B calibration is shown in Figure 7.1.

A. Expression for BRCS

The final expression for the Level 1B DDM can be derived from the expression of the signal forward model, shown in Equation 7.2, by solving for the scattering cross section term, $\bar{\sigma}_0$. As the Level 1B sigma product will not be normalized, we have removed $\bar{A}$ from Equation 7.2 and replaced the NBRCS $\bar{\sigma}_0$ with the unnormalized BRCS $\bar{\sigma}$. The resulting expression for $\bar{\sigma}$ is

$$P_{\hat{\tau},\hat{f}}^{L1b} = \bar{\sigma}_{\hat{\tau},\hat{f}} = \frac{P_{g,\hat{\tau},\hat{f}}(4\pi)^3 L_{a1} L_{a2} I_{\hat{\tau},\hat{f}}}{P^T \lambda^2 G_{SP}^T G_{SP}^R R_{SP}^{Total}} \tag{7.3}$$

where the individual terms in Equation 7.3 are as follows:

1. $P_{g,\hat{\tau},\hat{f}}$ is the Level 1A calibrated signal power at a specific delay $(\hat{\tau})$ and Doppler $(\hat{f})$ bin.
2. R_{SP}^{Total} is the total range loss from the transmitter to the surface and the surface to the receiver at the SP. When using a relatively small area of the DDM near the SP, this value can be approximated as the total range from the transmitter to the SP to the receiver. This term is included in the denominator as it is calculated as a loss $R^{Total} = \frac{1}{(R^R)^2}\frac{1}{(R^T)^2}$.
3. L_{a1} and L_{a2} are the estimated atmospheric loss corrections from the transmitter to the surface and surface to receiver, respectively.
4. $I_{\hat{\tau},\hat{f}}$ is an additional term used to correct for losses introduced by the DDMI. These include the 2-bit sampling correction and possibly a roll-off correction in the outer Doppler bins due to processing losses inherent in the zoom transform correlator of the instrument (Jales, 2013).
5. P^T and G_{SP}^T are the GPS satellite transmit power and antenna gain at the SP. These values are estimated as part of mapping the GPS satellite effective isotropic radiated power (EIRP) pattern of the GPS transmitters.
6. G_{SP}^R is the receiver antenna gain at the SP. When using a relatively small area of the DDM near the SP, this value can be approximated as the receiver antenna gain at the SP.

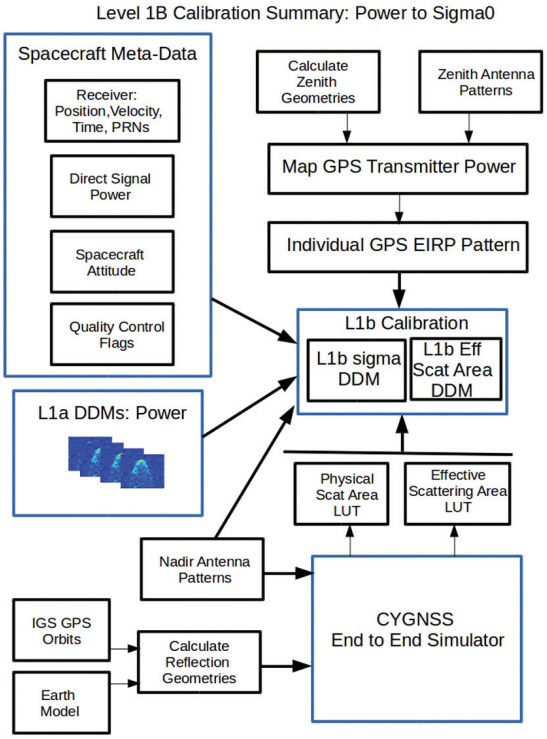

Figure 7.1. Overview of CYGNSS Level 1B calibration. *Reused from Gleason et al. (2016), © 2016 IEEE.*

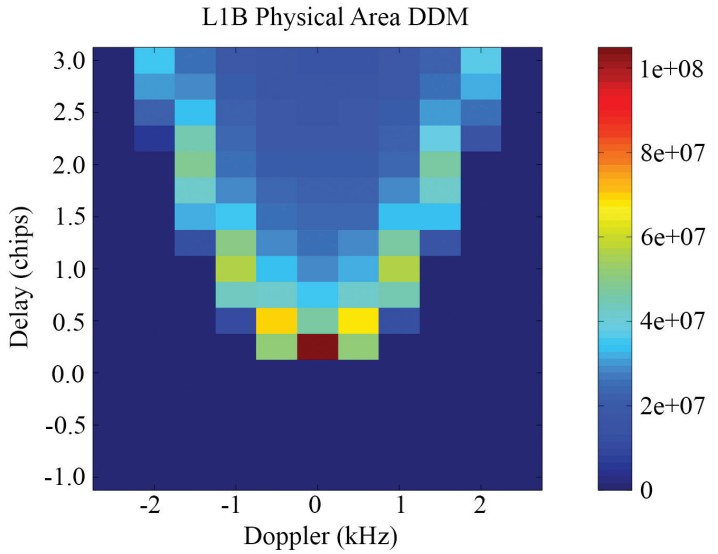

Figure 7.2. Physical scattering area (m^2) for a typical DDM reflection geometry. Note that delays before the SP and delays at and ahead of SP at increasing Doppler do not correspond to any physical surface region. ***Reused from Gleason et al. (2016), © 2016 IEEE.***

B. Calculating Effective and Physical Scattering Areas

A single delay Doppler bin will contain the captured scattered power from a distinct physical region on the ocean surface. For each delay Doppler bin in the DDM, this region will vary both in actual physical size (on the ground surface area) and effective area (including GPS spreading functions). The GPS ambiguity functions (in both delay and Doppler) increase the effective area of each delay Doppler bin, causing power to be "spread" into adjacent delay and Doppler bins from outside the geometry determined physical scattering area. These functions change the overall processed power observed. The physical area of each DDM bin can be calculated as follows:

$$A_{\hat{\tau},\hat{f}} = \iint_A dxdy \qquad \textbf{(7.4)}$$

An example of the physical scattering area for a typical DDM is shown in Figure 7.2. Note that points up to and before the SP bin (i.e., at delays shorter than the SP delay) have no physical surface scattering area. The power received in the bins before the SP is due to power being spread into these bins by the GPS ambiguity functions from physical areas near the SP. The effective surface scattering area for each delay/Doppler bin is expressed as the ambiguity function weighted surface integration:

$$\bar{A}_{\hat{\tau},\hat{f}} = \iint_A \Lambda^2_{\hat{\tau};x,y} S^2_{\hat{f};x,y} dxdy \qquad \textbf{(7.5)}$$

where the delay spreading function, $\Lambda_{\hat{\tau};x,y}$, and the Doppler spreading function, $S_{\hat{f};x,y}$, are integrated over the physical surface corresponding to each individual delay/Doppler bin. Figure 7.3 shows the effective scattering area DDM corresponding to the physical scattering areas illustrated in Figure 7.2.

Initial analysis has shown that when only using a relatively small area of the DDM (corresponding to approximately a 25 km^2 area on the surface, which we refer to in this analysis as the delay Doppler map area, or DDMA), it is sufficient to approximate the receive antenna gain, range loss terms, and the GPS transmit antenna power and gain using constant values calculated at the SP. However, it is recommended that if larger DDMs are used for parameter retrieval at delay and Doppler bins more than 25 km distant from the SP, then an improved correction factor for the receiver antenna gain and range loss terms should be applied, which account for the surface variations of these parameters over the region of interest.

C. Calculating a NBRCS

The bin-by-bin sum of scattering cross sections $\left(\bar{\sigma}_{total}\right)$ and the bin-by-bin sum of effective scattering areas $\left(\bar{A}_{total}\right)$ can be combined to calculate an effective

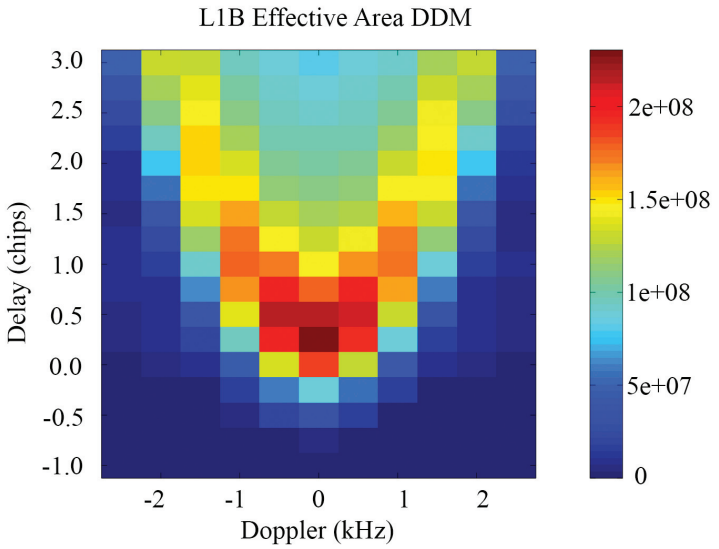

Figure 7.3. Effective scattering area (m^2) corresponding to the physical scattering area shown in Figure 7.2. This DDM of effective scattering area is a key output product of the Level 1B calibration, which allows users to calculate σ_0. *Reused from Gleason et al. (2016), © 2016 IEEE.*

NBRCS value, $\bar{\sigma}_0$, over selected regions of the DDM. The resulting expression for $\bar{\sigma}_0$ is

$$\bar{\sigma}_0 = \frac{\bar{\sigma}_{total}}{\bar{A}_{total}} = \frac{\sum_{i=1}^{N}\sum_{j=1}^{M}\bar{\sigma}_{\tau_i,f_j}}{\sum_{i=1}^{N}\sum_{j=1}^{M}\bar{A}_{\tau_i,f_j}} \quad \textbf{(7.6)}$$

where N and M represent the DDM bins for delay and Doppler, respectively, used in calculating both the scattering cross section and effective scattering area DDMs. During initial testing and validation of the algorithms, including using the end-to-end simulator (E2ES, a model designed to artificially simulate DDMs using orbit estimates and modeled winds) to generate 13-day Nature Run DDM sets (O'Brien et al., 2016) to test the Level 2 wind retrieval algorithms, a 3×5 area corresponding to $N = 3, M = 5$ centered at the SP was used to calculate $\bar{\sigma}_0$. This region corresponds roughly to a 25 km^2 surface resolution, often less, enabling averaging of consecutive DDMs during retrievals (Clarizia & Ruf, 2016; Clarizia et al., 2014).

D. Generating GPS Transmit Power and Antenna Gain LUT

The GPS transmit power, P_T, and transmit antenna gain, G_T, can be estimated using a parameterized model of the GPS antenna pattern and a locus of measurements over the entire bottom sphere of the GPS antenna pattern using direct signal power measurements from the receiver zenith antenna. The baseline GPS antenna patterns will be based on the patterns released in Marquis (2013). The theoretical GPS antenna patterns will be generated based on the antenna designs published in Marquis (2013) and in Czopek and Shollenberger (1993).

With the off-boresight angle (θ) and azimuth angles (ϕ) calculated relative to the GPS satellite frame of reference, the GPS transmitter EIRP (including the GPS transmit power P_T and antenna gain G_T) can be estimated using the radar equation and indexed as follows:

$$EIRP^a = (P_T^l G_T^l)(\theta,\phi) = \frac{P_d^l R_D^2 (4\pi)^2}{G_D \lambda^2} \quad \textbf{(7.7)}$$

where P_d^l is the received direct signal power from the satellite, l, R_D is the direct signal range, G_D is the zenith antenna gain, and λ is the GPS L1 wavelength.

E. Quality Control Flags

The Level 1B data product will include a set of quality control flags designed to indicate to users potential problems with the data. These flags, the parameters they are derived from, and the default threshold values are listed in Table 7.1.

Table 7.1. Level 1B quality control flags summary. C/A = course acquisition; ADCS = attitude determination and control system.

Flag	*Derived from*	*Threshold*	*Comment*
Reconfiguration during DDM	DDMI flag	On/off	On indicates invalid DDM
Blackbody/science DDM	DDMI flag	Switch state	Indicates type of DDM
Direct signal in DDM	Ground-based analysis	Within compressed DDM extent	Due to aliasing of the C/A code period
Low RCG	RCG	TBD	Low power signals due to antenna gain and range losses
High incidence angle	θ	60°	Region of different scattering properties
Large spacecraft attitude error	Spacecraft roll, pitch, yaw	TBD	Possible ADCS
High atmospheric activity	Ground-based data and models	TBD	Could affect DDM
GPS antenna gain not confidently estimated	GPS EIRP uncertainty	TBD	Due to gaps or errors in GPS transmitter model
Physically impossible value for σ in DDM	In area near DDM center	TBD	Possible calibration anomaly

1. *Reconfiguration during DDM.* This flag is set by the instrument when a configuration change occurs during the 1 second DDM integration interval. During calibration events, this flag will be set to indicate that the DDM is a mixture of the antenna and blackbody load inputs and should not be used.
2. *Blackbody/science DDM.* This flag reflects the state of the blackbody calibration switch. The switch will indicate either the external antenna (science mode) or the blackbody load as the current input source.
3. *Direct signal in DDM.* This flag will be generated in the SOC by analyzing the reflection geometry to determine if the direct signal delay and Doppler fall in the same range as the DDM used in Level 2 wind retrievals.
4. *Low RCG.* This flag indicates a DDM where the RCG is below a required threshold (which therefore may not meet the wind speed retrieval requirements). This flag is used to indicate a possible weak signal due to low antenna gain and range losses.
5. *High incidence angle.* Reflection geometries resulting in incidence angles greater than a threshold will be flagged.
6. *Large spacecraft attitude error.* This flag will be set if the spacecraft attitude determination algorithm indicates that the spacecraft is outside its nominal attitude requirement.
7. *High atmospheric activity.* Used to flag potential adverse atmospheric conditions in the signal path that could degrade the quality of the DDM.
8. *Low confidence in GPS EIRP.* This flag will be set by the SOC if the model of the GPS transmitter at a given geometry is not well determined.
9. *Physically impossible value of σ in DDM.* When this conditions occurs, it will be flagged to indicate a possible problem in the Level 1 calibration algorithm.

IV. Error Analysis of the Level 1B Calibration Algorithm

The Level 1B data product consists of the BRCS over a range of delay steps and Doppler frequencies. This error analysis concentrates on the uncertainties present in CYGNSS Level 1B calibration algorithm. Each uncertainty in the Level 1B calibration algorithm will be considered an independent uncorrelated error source. The method for this error analysis is based on that presented in Janssen et al. (1995) for a microwave radiometer.

Table 7.2. Error allocations for the receiver antenna gain. ADCS = attitude determination and control system. *Reused from Gleason et al. (2016), © 2016 IEEE.*

Error term	*Error magnitude*	*Comment*
Spacecraft pointing knowledge	0.9 deg (1 σ)	From ADCS analysis (with star tracker)
Star tracker optical/mechanical boresight misalignment	0.4 deg (1 σ)	Rough estimate from mechanical analysis
Star tracker to nadir antenna misalignment	0.4 deg (1 σ)	Rough estimate from mechanical analysis
Mechanical-electrical nadir antenna boresight misalignment	0.5 deg (1 σ)	Expected antenna calibration accuracy
Repeatability of antenna gain	0.2 dB (1 σ)	Based on 18 FM antenna pattern measurements
Antenna pattern uncertainty	0.25 dB (1 σ)	Expected antenna calibration accuracy
RSS (1 σ) antenna gain error	0.43 dB	From Monte Carlo simulation

In order to assess the error in the NBRCS, $\bar{\sigma}_0$, expressed in Equation 7.6, Equation 7.3 has been normalized by the effective scattering area and considered for DDM bins in a region (within the DDMA) near the SP such that

$$\bar{\sigma}_{0,\,DDMA} = \frac{P_{g,DDMA}(4\pi)^3 L_{a1} L_{a2} I}{P^T \lambda^2 G^T_{SP} G^R_{SP} R^{Total}_{SP} A_{DDMA}} \tag{7.8}$$

The total error in the Level 1B DDM is the RSS of the individual errors contributed by the independent terms of Equation 7.8. This is expressed as

$$E(q_i) = \left| \frac{\partial \bar{\sigma}_{0,\,DDMA}}{\partial q_i} \right| \Delta q_i \tag{7.9}$$

where the errors terms are $q_1 = P_g$, $q_2 = L_{a12}$, $q_3 = R^R$, $q_4 = R^T$, $q_5 = P_T$, $q_6 = G^T$, $q_7 = G^R$, and $q_8 = A$, respectively. The partial derivatives of the individual errors terms can be expressed as

$$E(P_{g,DDMA}) = \frac{(4\pi)^3 (R^R_{SP})^2 (R^T_{SP})^2 L_{a1} L_{a2}}{P^T \lambda^2 G^T_{SP} G^R_{SP} A_{DDMA}} \Delta P_{g,DDMA} \tag{7.10}$$

$$E(L_{a12}) = \frac{P_{g,DDMA}(4\pi)^3 (R^R_{SP})^2 (R^T_{SP})^2}{P^T \lambda^2 G^T_{SP} G^R_{SP} A_{DDMA}} \Delta L_{a12} \tag{7.11}$$

$$E(R^R_{SP}) = \frac{2P_{g,DDMA}(4\pi)^3 (R^R_{SP})(R^T_{SP})^2 L_{a12}}{P^T \lambda^2 G^T_{SP} G^R_{SP} A_{DDMA}} \Delta R^R_{SP} \tag{7.12}$$

$$E(R^T_{SP}) = \frac{2P_{g,DDMA}(4\pi)^3 (R^R_{SP})^2 (R^T_{SP}) L_{a12}}{P^T \lambda^2 G^T_{SP} G^R_{SP} A_{DDMA}} \Delta R^T_{SP} \tag{7.13}$$

$$E(P_T) = \frac{P_{g,DDMA}(4\pi)^3 (R^R_{SP})^2 (R^T_{SP})^2 L_{a12}}{\left(P^T\right)^2 \lambda^2 G^T_{SP} G^R_{SP} A_{DDMA}} \Delta P_T \tag{7.14}$$

$$E(G^T) = \frac{P_{g,DDMA}(4\pi)^3 (R^R_{SP})^2 (R^T_{SP})^2 L_{a12}}{P^T \lambda^2 (G^T)^2 G^R_{SP} A_{DDMA}} \Delta G^T \tag{7.15}$$

$$E(G^R) = \frac{P_{g,DDMA}(4\pi)^3 (R^R_{SP})^2 (R^T_{SP})^2 L_{a12}}{P^T \lambda^2 G^T_{SP} (G^R_{SP})^2 A_{DDMA}} \Delta G^R \tag{7.16}$$

$$E(A) = \frac{P_{g,DDMA}(4\pi)^3 (R^R_{SP})^2 (R^T_{SP})^2 L_{a12}}{P^T \lambda^2 G^R_{SP} G^T_{SP} (A_{DDMA})^2} \Delta A_{DDMA} \tag{7.17}$$

The error analysis was performed for both the below 20 m s^{-1} wind case (assuming a σ_0 of 20 dB) and greater than 20 m s^{-1} wind case (assuming a σ_0 of 12 dB) to fully understand the possible errors in both wind retrieval groups. Initially, the errors due to the receiver antenna gain, G_R, were estimated using a Monte Carlo simulation. The simulation was run using the error estimates listed in Table 7.2 as input conditions, and then the 1 σ error statistics of the antenna gain were calculated as a function of antenna gain magnitude.

Errors for the remaining terms of the Level 1B calibration were arrived at using best estimates. Table 7.3 shows the resulting error values used for the low wind and high wind cases, respectively.

Subsequently, the rolled-up Level 1 calibration error can be estimated using the equations above, which consist of taking the RSS of all of the individual error terms, including the total error estimate from the Level 1A calibration (Table 7.4).

Table 7.3. Level 1B calibration error analysis input parameters. *Reused from Gleason et al. (2016), © 2016 IEEE.*

Error term	*Error magnitude*	*Comment*
ΔP_g	0.50/0.23 dB	From Level 1A error analysis (low winds, σ_0 = 20/high winds, σ_0 = 12), see Section 5, Table 5.3
ΔL_{a12}	0.04 dB	Based on approximate L-Band attenuations
ΔR^R	~1000 meters	Determined by reflection geometry
ΔR^T	~1000 meters	Determined by reflection geometry
$\Delta P_T + \Delta G^T$	0.4 dB	GPS Tx EIRP error
ΔG^R	0.43 dB	From Monte Carlo simulation, Table 7.2
ΔA	0.2 dB	Determined by reflection geometry

Table 7.4. Level 1B calibration algorithm errors (dB). *Reused from Gleason et al. (2016), © 2016 IEEE.*

Error term	*Level 1B error, dB, for low winds, less than 20 m s^{-1}*	*Level 1B error, dB, for high winds, greater than 20 m s^{-1}*	*Comment*
$E(P_g)$	0.50	0.23	Level 1A calibration error
$E(L_{a12})$	0.04	0.04	Total atmospheric modeling error
$E(R^R) + E(R^T)$	0.01	0.01	Total range error
$E(P_T) + E(G^T)$	0.40	0.40	GPS transmitter EIRP error
$E(G^R)$	0.43	0.43	Receiver antenna gain error
$E(A)$	0.20	0.20	Effective scattering area error
Margin	0.20	0.20	
Total RSS Level 1B error	0.82	0.70	

References

Clarizia, M. P., & Ruf, C. (2016). Wind speed retrieval algorithm for the Cyclone Global Navigation Satellite System (CYGNSS) mission. *Geoscience and Remote Sensing, IEEE Transactions On*. Manuscript in review.

Clarizia, M. P., Ruf, C. S., Jales, P., & Gommenginger, C. (2014). Spaceborne GNSS-R minimum variance wind speed estimator. *Geoscience and Remote Sensing, IEEE Transactions On*, *52*(11), 6829–6843. doi: 10.1109/TGRS.2014.2303831

Czopek, F. M., & Shollenberger, S. (1993, September). Description and performance of the GPS Block I and II L-Band antenna and link budget. In *Proceedings of the 6th International Technical Meeting of the Satellite Division of The Institute of Navigation (ION GPS 1993)* (pp. 37–43). Salt Lake City, UT.

Gleason, S., Ruf, C., Clarizia, M. P., & O'Brien, A. (2016). Calibration and unwrapping of the normalized scattering cross section for the Cyclone Global Navigation Satellite System (CYGNSS). *Geoscience and Remote Sensing, IEEE Transactions On*. doi: 10.1109/TGRS.2015.2502245

Jales, P. (2013). *GNSS-R algorithm implementation technical note*. Internal document, Surrey Satellite Technology Ltd.

Janssen, M., Ruf, C. S., & Keihm, S. J. (1995). TOPEX/Poseidon Microwave Radiometer (TMR). II. Antenna pattern correction and brightness temperature algorithm. *Geoscience and Remote Sensing, IEEE Transactions On*, *33*(1), 138–146. doi: 10.1109/36.368214

Marquis, W. (2013). *The GPS block IIR/IIR-M antenna panel pattern*. Internal document publically released, Lockheed Martin.

O'Brien, A., Gleason S., Johnson J., & Ruf, C. (2016). The end-to-end simulator for the cyclone GNSS (CYGNSS) mission. Manuscript in preparation.

Zavorotny, V. U., & Voronovich, A. G. (2000). Scattering of GPS signals from the ocean with wind remote sensing application. *Geoscience and Remote Sensing, IEEE Transactions On*, *38*(2), 951–964. doi: 10.1109/36.841977

8. Level 2 Mean Square Slope Retrieval

I. Introduction

The primary mission of the CYGNSS project is to collect measurements of ocean surface winds through variations in the direct versus reflected GPS signals. It will be achieved through fitting the calibrated data obtained by the eight CYGNSS microsatellite observatories to the empirical or modeled functions that relate the measured signal parameters (e.g., the DDM peak power) to surface wind. At the same time, such an ocean surface characteristic as the MSS will be also available.

Within the framework of the scattering model adopted here, the MSS can be related directly to the NBRCS σ_0. On the other hand, the bistatic radar equation allows connecting σ_0 to the calibrated estimates of power for each delay/Doppler bin through the instrument calibration algorithm. The algorithm theory is based on the details of the instrument processing chain hardware and firmware, a model of the received signal power model (Zavorotny & Voronovich, 2000), and estimates of the external and internally generated noise power. The purpose of this document is to describe the CYGNSS Level 2 MSS algorithms and provide all necessary equations for implementing the algorithm during the mission. Subsection A provides science background and objectives. It explains the need for ocean MSS. Part II describes the physics of the problem and explains the connection between the NBRCS and the MSS and between the MSS and the ocean surface spectrum. Part III provides an overview of the MSS retrieval algorithm.

A. Science Background and Objectives

The MSS of the ocean surface is a very important quantity. It is crucial for understanding the physical processes at the air-sea interface and for interpreting altimeter and scatterometer radar backscatter measurements (Jähne et al., 1987; Wu, 1990; Liu et al., 1997; Walsh et al., 1998; Chapron et al., 2000; Liu et al., 2000). The need for global MSS datasets in air-sea interaction research is increasingly apparent. Indeed, the presence of waves significantly enhances gas transfer rates across a water boundary layer. The transfer rates correlate well with the MSS of the waves. It has been observed in laboratory conditions that gas transfer velocities significantly increase at the onset of surface wave generation (Jähne et al., 1987).

The need for ocean MSS is also evident in satellite radiometry, specifically for salinity measurements (Font et al., 2004; Guimbard et al., 2012). At L-band, the brightness temperature of the ocean surface depends equally on three surface parameters: the sea surface salinity, the sea surface temperature, and the sea state, which is responsible for the deviations of the brightness temperature with respect to the flat sea model. To estimate the sea roughness effect on brightness temperature, various models driven either directly by 10 m height wind speed, U_{10}, or by the significant wave height (SWH) have been tried without significant success. With the advent of the GPS bistatic radar technique, which uses L-band signals, the idea has been proposed to measure L-band limited MSS to provide sea surface roughness estimates for L-band radiometric measurements of ocean salinity (Font et al., 2004; Guimbard et al., 2012).

II. Physics of the Problem

A. Connection between the Bistatic Radar Cross Section and the MSS

According to the forward model based on the bistatic radar equation adopted for the case of the GPS scattered signals, the DDM emerges as a result of the integration of the product of several factors over a certain ocean surface area. One of those factors is the BRCS σ_0, which describes the effect of ocean surface roughness. In the geometric optics (GO) limit of the Kirchhoff approximation (KA), this term is represented by the following expression (Bass & Fuks, 1979; Barrick, 1968):

$$\sigma_0 = \pi \left|\Re\right|^2 \left(q / q_z\right)^4 P\left(-q_\perp / q_z\right) \qquad \textbf{(8.1)}$$

where $\vec{q}$ is the scattering vector that can be regarded as a function of the coordinate $\vec{\rho}$ in the mean surface plane; and $\Re$ is the complex Fresnel coefficient, which depends on signal polarization state, a complex dielectric constant of the reflecting medium, ε, and the local incidence angle. In the case of GPS

bistatic radar, the reflected signal is LHCP. The factor $P(\vec{s})$ in Equation 8.1 is the probability density function (PDF) of large scale "smoothed" surface slopes. The adjective "smoothed" implies that very small scale components of the surface spectrum (of the order of several tens of centimeters) are filtered out. This is a consequence of using in this technique 0.2 m long L-band waves, which obey the geometric-optics limit of the KA. In order to sense all surface scales, one would need to use 1 mm (or shorter) electromagnetic (EM) waves.

It is believed that for linear surface gravity waves, the slope PDF $P(\vec{s})$ can be approximated by the anisotropic bivariate Gaussian distribution (Zavorotny & Voronovich, 2000; Elfouhaily et al., 2002; Soulat, 2004), which for the case of wind directed along the *x*- or *y*-axis is

$$P(\vec{s}) = \frac{1}{2\pi\sqrt{mss_x mss_y(1-b_{x,y}^2)}} \exp\left[-\frac{1}{2(1-b_{x,y}^2)}\left(\frac{s_x^2}{mss_x} - 2b_{x,y}\frac{s_x s_y}{\sqrt{mss_x mss_y}} + \frac{s_y^2}{mss_y}\right)\right] \quad \textbf{(8.2)}$$

where mss_x and mss_y are MSSs of the sea surface for two orthogonal components, one along the wind direction and another is across it; and $b_{x,y}$ is the correlation coefficient between two slope components. Upon substitution of Equation 8.2 into 8.1, we obtain an algebraic expression that connects the MSS components with the NBRCS, σ_0:

$$\sigma_0(\vec{q}) = \frac{|\Re|^2 (q/q_z)^4}{2\sqrt{mss_x mss_y(1-b_{x,y}^2)}} \exp\left[-\frac{1}{2q_z^2(1-b_{x,y}^2)}\left(\frac{q_x^2}{mss_x} - \frac{2b_{x,y}q_x q_y}{\sqrt{mss_x mss_y}} + \frac{q_y^2}{mss_y}\right)\right] \quad \textbf{(8.3)}$$

B. Connection between the MSS and the Surface Elevation Spectrum

By definition, the MSS components are introduced as

$$mss_{x,y} = \left\langle s_{x,y}^2 \right\rangle = \iint_{\kappa<\kappa_*} \kappa_{x,y}^2 \Psi(\vec{\kappa}) d^2\kappa \quad \textbf{(8.4)}$$

$$b_{x,y} = \left\langle s_x s_y \right\rangle / \sqrt{mss_x mss_y} \quad \textbf{(8.5)}$$

$$\left\langle s_x s_y \right\rangle = \iint_{\kappa<\kappa_*} \kappa_x \kappa_y \Psi(\vec{\kappa}) d^2\kappa \quad \textbf{(8.6)}$$

Therefore, two MSS components, mss_x and mss_y, are determined solely by the wave-number integral from the ocean elevation spectrum $\Psi(\vec{\kappa})$ times $\kappa_{x,y}^2$. This product is called a slope spectral density. The limit of integration at low wave numbers is κ_*, which plays a role as the "smoothing" filter that is related to the EM wavelength and the angle of incidence. There are some indications that the actual PDF of slopes does not exactly follow a Gaussian shape at their tails (Cardellach & Ruis, 2008). In terms of the glistening zone, it implies that this departure affects the periphery of the zone. However, for the conditions of the CYGNSS mission, most of the contribution to the signal comes from the peak area of the PDF of slopes. Frequently, when it is not possible to measure each of two orthogonal components, the total MSS is used:

$$mss = \left\langle s^2 \right\rangle = \left\langle s_x^2 \right\rangle + \left\langle s_y^2 \right\rangle = mss_x + mss_y = \iint_{\kappa<\kappa_*} \kappa^2 \Psi(\vec{\kappa}) d^2\kappa \quad \textbf{(8.7)}$$

In the case of global winds, the model spectrum $\Psi(\vec{\kappa})$ proposed by Elfouhaily et al. (1997) is widely used. An example of the Elfouhaily et al. (1997) slope spectrum taken along the wind direction is shown in Figure 8.1.

This empirical model describes deep-water waves driven by winds of constant direction under diverse wave-age (often called "fetch") conditions. This model has two input parameters, the local wind speed at 10 m height, U_{10}, and the wave age, or fetch. It was designed to agree with in situ observations of the first sun-glint-derived wave slope measurements of Cox and Munk (1954), made several decades ago.

For conditions when the surface can be described by the Elfouhaily et al. (1997) spectrum (assuming that the fetch is known), it is possible to retrieve the wind U_{10} from the CYGNSS measurement. At the same time, the retrieval of the total MSS is available as a by-product of the wind retrieval. In some cases, the total MSS retrieval may be the only product that has a high level of validity. This may occur when sea roughness cannot be described solely by the local wind (e.g., in the presence of unknown swell, currents, surfactants) so the surface cannot be described by the Elfouhaily et al. (1997) spectrum or its proxy. For example, if swell is present that does not interact with the waves driven by the local wind, then the total spectrum of the wave will be

$$\Psi_{tot}(\vec{\kappa}) = \Psi_{wind}(\vec{\kappa}) + \Psi_{swell}(\vec{\kappa}) \quad \textbf{(8.8)}$$

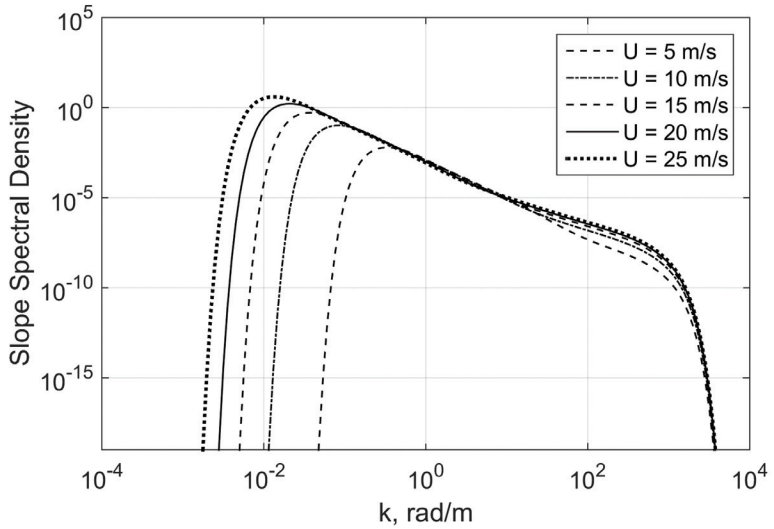

Figure 8.1. Ocean surface slope spectrum from Elfouhaily et al. (1997), taken along the wind direction.

And the total MSS component will obey the equation

$$mss_{x,y,tot} = mss_{x,y,wind} + mss_{x,y,swell} \quad \textbf{(8.9)}$$

As was pointed out above, the MSS that determines the BRCS through the PDF of slopes is not a full-wave slope. Even though the sea surface contains wave harmonic components both longer and shorter than the L-band electromagnetic waves, the short waves can be disregarded in a process of forward quasi-specular reflection under the GO approximation. Therefore, the full surface spectrum should be cut off at the high end of wave numbers. There are various choices of cutoff wave number κ_*, which are discussed in the Appendix, "Ocean Surface Bistatic Scattering Forward Model."

III. Retrieval Algorithm Overview

A. Theoretical Description

Since the regime of CYGNSS measurements does not allow one to distinguish between the along- and crosswind directions, we assume that $mss_y = mss_x = mss/2$, and $b_{x,y}^2 = 0$. Then the expression for the bistatic radar cross section from Equation 8.3 simplifies:

$$\sigma_0(\vec{q}) = \frac{|\Re|^2}{mss}\left(\frac{q}{q_z}\right)^4 \exp\left(-\frac{q_\perp^2}{q_z^2 mss}\right) \quad \textbf{(8.10)}$$

Factors containing components of the scattering vector $\vec{q}$ can be expressed through local (at the point of reflection) incidence and scattering angles, θ_1 and θ_2 (see Figure 8.2).

$$\left(\frac{q}{q_z}\right)^2 = \frac{2(1-\sin\theta_1\sin\theta_2\cos\varphi+\cos\theta_1\cos\theta_2)}{(\cos\theta_1+\cos\theta_2)^2} \quad \textbf{(8.11)}$$

$$\frac{q_\perp^2}{q_z^2} = \frac{(\sin\theta_2\cos\varphi-\sin\theta_1)^2+\sin^2\theta_2\sin^2\varphi}{(\cos\theta_1+\cos\theta_2)^2} \quad \textbf{(8.12)}$$

In principle, MSS can be retrieved from Equation 8.10 for any combination of incident and scattering angles θ_1 and θ_2 (and azimuthal scattering angle φ) by solving a transcendental equation:

$$\log mss - \frac{q_\perp^2}{q_z^2 mss} - \log\left[|\Re|^2\left(\frac{q}{q_z}\right)^4\right] + \log\sigma_0(\vec{q}) = 0\,. \quad \textbf{(8.13)}$$

However, more beneficial would be to use $\sigma_0(\theta)$ in the specular direction where $\theta_1 = \theta_2 = \theta$ and $\varphi = 0$. Then Equation 8.10 simplifies to

$$\sigma_0(\theta) = \frac{|\Re(\theta)|^2}{mss} \quad \textbf{(8.14)}$$

The Fresnel reflection coefficient of the ocean surface, $\Re$, is evaluated in the nominal specular direction described by the incidence angle θ.

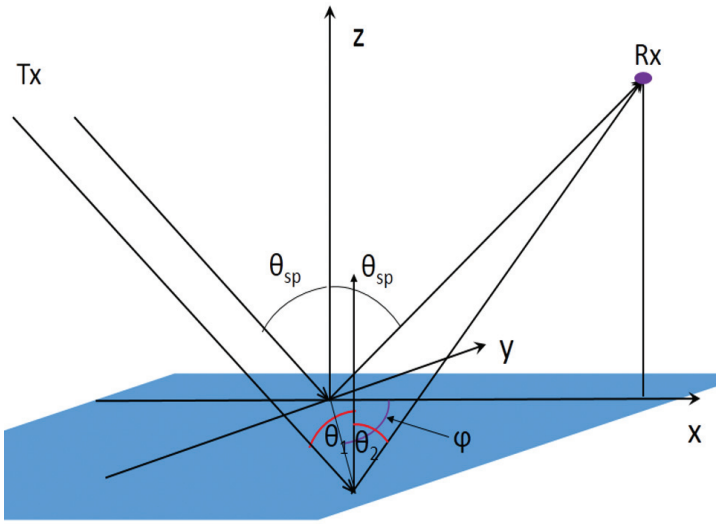

Figure 8.2. Geometry of quasi-specular scattering.

B. Baseline Algorithm

In Section 7, Equation 7.3 was obtained, which expresses NBRCS σ_0 through available calibrated measured power values from the Level 1A calibration described elsewhere and parameters of the system. This equation can be rewritten here as

$$\sigma_0 = \alpha \overline{P}^{Sig}_{\hat{\tau},\hat{f}} \tag{8.15}$$

where α is a coefficient that depends on various geometric, transmitter, and receiver parameters:

$$\alpha = \frac{(4\pi)^3 R_T^2 R_R^2 L^1_{atm} L^2_{atm}}{P_T T_i^2 \lambda^2 G_T G_R \chi_{\hat{\tau},\hat{f}}} \tag{8.16}$$

where

1. $\overline{P}^{Sig}_{\hat{\tau},\hat{f}}$ is the calibrated Level 1A DDM, as a function of delay and frequency.
2. R_T is the GPS transmitter to SP path length, calculated using the international GNSS service (IGS) positions of the GPS satellites and estimated SP location.
3. R_R is the SP to CYGNSS satellite path length, calculated using the positions of the CYGNSS spacecraft and estimated SP location.
4. L^1_{atm} and L^2_{atm} are the atmospheric losses as the signal travels from the GPS satellite to the surface and from the surface to the receiver, respectively. These terms will be estimated on the ground using a propagation model at the GPS signal transmit frequency.
5. P_T is the GPS transmit signal power and is estimated using the absolute power of the direct signal.
6. T_i is the coherent time integration.
7. λ is the signal wavelength.
8. G_T is the GPS antenna gain for the reflection geometry. This will be calculated using a model of the GPS antenna gain pattern generated using power measurements from the direct signal. The above two terms will be estimated together as a single combined quantity.
9. G_R is the CYGNSS nadir antenna gain, which is a function of reflection geometry and spacecraft orientation. This term will be estimated using a prelaunch calibration of the antenna pattern and the reflection viewing geometry.
10. $\chi_{\hat{\tau},\hat{f}}$ is the effective scattering area for the delay Doppler (DD) bin at $\hat{\tau},\hat{f}$. This area will be estimated based on the delay Doppler surface geometry calculated using modules within the CYGNSS E2ES.

Details for the calculation of each of the above terms are described in Section 7.

For the CYGNSS geometry and system parameters, the coefficient $\alpha \approx 10$ at $\theta = 35^\circ$ for the DDM bin with $\hat{\tau} = 0$, $\hat{f} = 0$, which corresponds to a nominal

SP on the surface. The MSS estimation algorithm is found by solving for MSS in Equation 8.14, or

$$mss = \frac{\left|\Re(\theta)\right|^2}{\sigma_0(\theta)} \quad \textbf{(8.17)}$$

where $\Re$ is the Fresnel reflection coefficient evaluated at the incidence angle of the SP for a given complex dielectric constant of the ocean surface ε. Thus the MSS estimation error is determined by uncertainties of several parameters entering Equation 8.17. Two leading parameters are NBRCS, σ_0, provided by the Level 1 DDM calibration algorithm (Section 7), and the absolute value squared of the Fresnel reflection coefficient, $\left|\Re(\theta)\right|^2$. In turn, the Fresnel reflection coefficient is determined by the complex dielectric constant, ε, of the ocean surface and the incidence angle at the SP. Estimation of ε requires knowledge of the sea surface temperature and salinity. Related uncertainties will be analyzed in the next subsection.

IV. Performance Characterization

A. Accuracy

If we put aside the issue of geophysical variability of the MSS of ocean waves, the accuracy of the MSS retrieval based on Equation 8.17 is determined by the uncertainty in two factors entering Equation 8.17: NBRCS σ_0 taken in the specular direction and the absolute value squared of the Fresnel reflection coefficient of the flat ocean surface, $\left|\Re(\theta)\right|^2$, also taken in the specular direction. An analysis of the uncertainty in σ_0 is presented in Section 7.

Let us first start with estimation of accuracy of the reflection coefficient. In the case of LHCP, the expression for the complex Fresnel reflection coefficient $\Re$ at the interface between air and a medium (in our case, seawater) with a complex dielectric permittivity, ε, is

$$\Re(\theta) = \frac{1}{2}\left[\frac{\varepsilon\cos\theta - \sqrt{\varepsilon - \sin^2\theta}}{\varepsilon\cos\theta + \sqrt{\varepsilon - \sin^2\theta}} - \frac{\cos\theta - \sqrt{\varepsilon - \sin^2\theta}}{\cos\theta + \sqrt{\varepsilon - \sin^2\theta}}\right] \quad \textbf{(8.18)}$$

where θ is the local incidence (or reflection) angle. We performed calculations of $\left|\Re(\theta)\right|^2$ for a range of incidence angles θ and various values of water temperature and salinity, which are the two most important driving parameters of the complex dielectric permittivity ε of seawater. The latter can be calculated using either the Klein and Swift model (Klein & Swift, 1977; Ulaby et al., 1986) or Meissner and Wentz model (Meissner & Wentz, 2004). Those models for the seawater permittivity rely on L-band measurements. They are close enough to each other at those frequencies, and no other models have been shown more reliable (Ellison et al., 1998). The analytical expressions for ε as a function of radio frequency, water temperature T, and salinity S for the Klein and Swift model is given in the appendix to this section. The radio frequency of the received signals for CYGNSS is known with high accuracy. It is the L1-band frequency that is equal to 1.57542 GHz. Figures 8.3a and 8.3b demonstrate the dependence of both the real and imaginary parts of the dielectric permittivity of ocean water (ε' and ε'', respectively) on water temperature and salinity.

Therefore, the retrieval of MSS depends on sea surface temperature (SST) and sea surface salinity (SSS). Analyses reveal that the changes in SSS and SST over time and space are small enough that using a single value of $\left|\Re(\theta)\right|^2$ maintains an acceptable error tolerance (Figure 8.4). Therefore, LUTs for monthly and zonal averaged Fresnel coefficients, at a $1° \times 1°$ resolution, are used for the derivation of MSS (see Figure 8.5).

B. Error Analysis of the Level 2 MSS Retrieval Algorithm

The creation of the Level 2 MSS product is contingent on the availability of input observational data (from CYGNSS and ancillary data sources) and accurate estimates of their errors. The accuracy of the Level 2 MSS product is dependent on the accuracy of the NBRCS σ_0 retrieval, the accuracy of the scattering geometry determination (incidence angle), and the accuracy of the Fresnel reflection coefficient estimates. It should be remembered that this algorithm is built upon two basic assumptions: validity of the GO limit of the KA and validity of the Gaussian PDF of slopes. At very rough surface conditions, such as in the hurricane wind maximum areas, both of these assumptions may be violated. These scenarios would require an independent calibration and validation of the MSS by using collocated and simultaneous in situ measurements of the MSS. In some circumstances, this may be impractical.

The expression for generating the Level 2 MSS data product is given by Equation 8.17. The equation

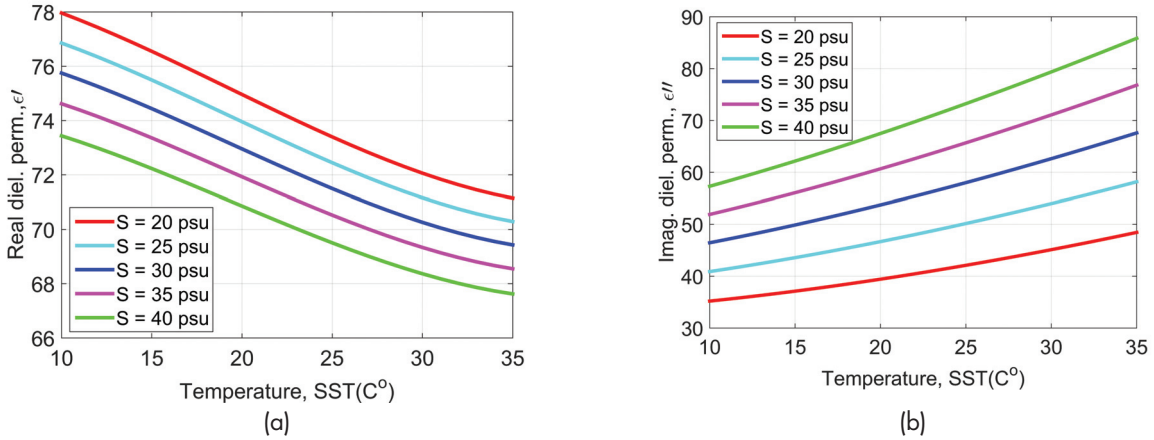

Figure 8.3. Dependence of both real and imaginary parts of dielectric permittivity of ocean water (ε' and ε'', respectively) on water temperature and salinity.

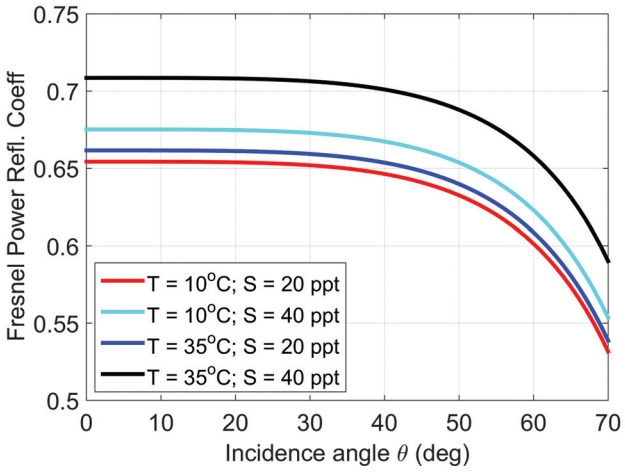

Figure 8.4. Dependence of $|\Re(\theta)|^2$ on incidence angle for a wide range of temperatures and salinities, calculated using the Klein and Swift model (Klein & Swift, 1977; Ulaby et al., 1986).

is repeated below with the reflection coefficient from Equation 8.18:

$$mss = \frac{|\Re(\theta)|^2}{\sigma_0(\theta)} \tag{8.19}$$

Each uncertainty in the Level 2 MSS retrieval algorithm will be considered as an independent uncorrelated error source. The total error in the Level 2 MSS retrieval is the RSS of individual errors contributed by the independent variable of Equation 8.19. For relative MSS error, we have

$$\frac{\Delta mss}{mss} = \left[\sum_{i=1}^{4} E^2(p_i)\right]^{1/2} \tag{8.20}$$

where the error variables are $p_1 = \sigma_0(\theta)$, $p_2 = \theta$, $p_3 = T$, $p_4 = S$. The individual errors $E(p_i)$ can be expressed via partial derivatives as

$$E(p_i) = \frac{1}{mss}\left|\frac{\partial mss}{\partial p_i}\right|\Delta p_i \tag{8.21}$$

One can specify the error for each of these variables:

$$E(\sigma_0) = \frac{|\Re|^2}{\sigma_0}\left|\frac{\partial mss}{\partial \sigma_0}\right|\Delta\sigma_0 = \frac{\Delta\sigma_0}{\sigma_0} \tag{8.22}$$

$$E(\theta) = \frac{|\Re|^2}{\sigma_0}\left|\frac{\partial mss}{\partial \theta}\right|\Delta\theta = \frac{1}{|\Re|^2}\left|\frac{\partial |\Re|^2}{\partial \theta}\right|\Delta\theta \tag{8.23}$$

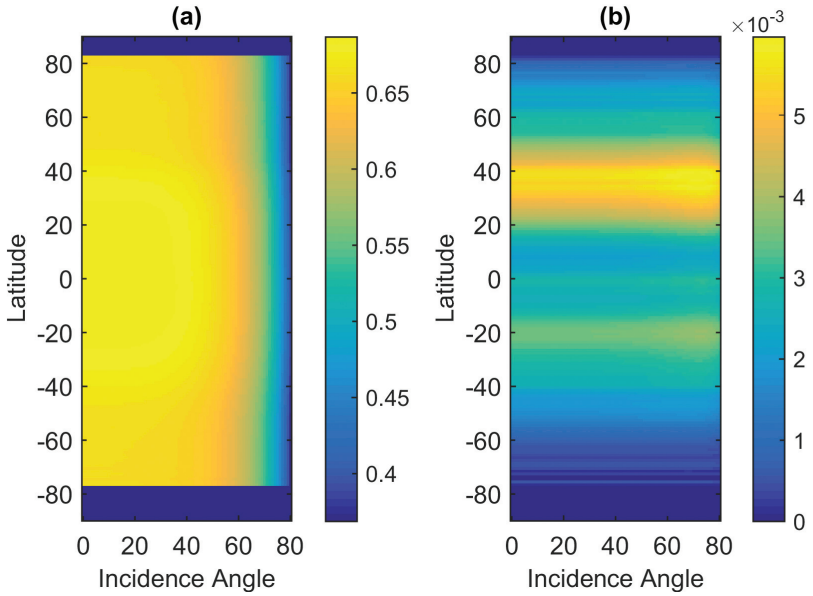

Figure 8.5. (a) Average (zonal and seasonal) Fresnel reflection coefficient $|\Re(\theta)|^2$; (b) standard deviation (zonal and seasonal) of $|\Re(\theta)|^2$.

$$E(T) = \frac{|\Re|^2}{\sigma_0}\left|\frac{\partial mss}{\partial T}\right|\Delta T = \frac{1}{|\Re|^2}\left|\frac{\partial|\Re|^2}{\partial T}\right|\Delta T \qquad \textbf{(8.24)}$$

$$E(S) = \frac{|\Re|^2}{\sigma_0}\left|\frac{\partial mss}{\partial S}\right|\Delta S = \frac{1}{|\Re|^2}\left|\frac{\partial|\Re|^2}{\partial S}\right|\Delta S \qquad \textbf{(8.25)}$$

To estimate $E(\sigma_0)$, empirically derived values for σ_0 and $\Delta\sigma_0$, based on tests under different wind speeds, are employed. The error estimates for σ_0 also include uncertainties related to the antenna gain model, the LNA noise model, the GPS transmitter model, and so on. For details, see Section 7. Therefore, we use

σ_0 = 20 dB (100) and $\Delta\sigma_0$ = 0.82 dB (1.21), for U_{10} < 20 m s^{-1}

σ_0 = 12 dB (15.85) and $\Delta\sigma_0$ = 0.70 dB (1.17), for U_{10} > 20 m s^{-1}

Partial derivatives of $|\Re|^2$ in Equations 8.23 to 8.25 are computed numerically because the analytical derivation is not practical due to a complicated dependence of $|\Re|^2$ over the arguments θ, T, and S. Examples of such computations are shown in Figures 8.6 to 8.8.

Figure 8.6a represents $\frac{1}{|\Re|^2}\left|\frac{\partial|\Re|^2}{\partial T}\right|$ as a function of incidence angle θ for a range of sea surface temperatures T between 10°C and 35°C and for a fixed sea surface salinity S = 40 psu. Figure 8.6b shows $\frac{1}{|\Re|^2}\left|\frac{\partial|\Re|^2}{\partial S}\right|$ as a function of incidence angle θ for a range of sea surface salinities S between 10 and 40 psu and for a fixed sea surface temperature T = 35°C. Analogously, Figures 8.7a and 8.7b represent respectively the dependence of $\frac{1}{|\Re|^2}\left|\frac{\partial|\Re|^2}{\partial\theta}\right|$ on temperature and salinity at fixed salinity and temperature for a range of incidence angles θ. And, finally, Figures 8.8a and 8.8b show cuts of functions $\frac{1}{|\Re|^2}\left|\frac{\partial|\Re|^2}{\partial S}\right|$ and $\frac{1}{|\Re|^2}\left|\frac{\partial|\Re|^2}{\partial T}\right|$ along parameters such

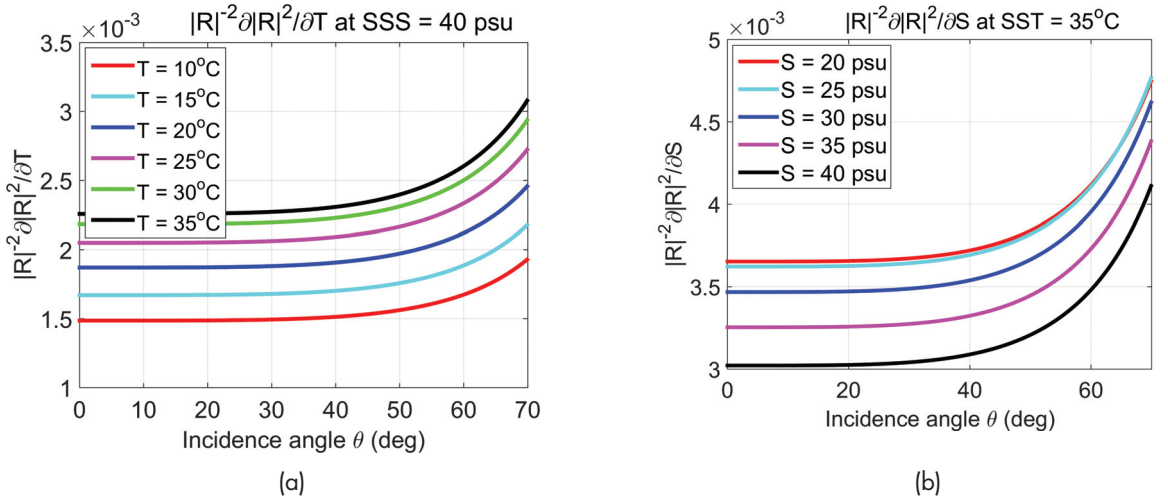

Figure 8.6. Relative partial derivatives of $|\Re|^2$ over temperature and salinity as a function of incidence angle.

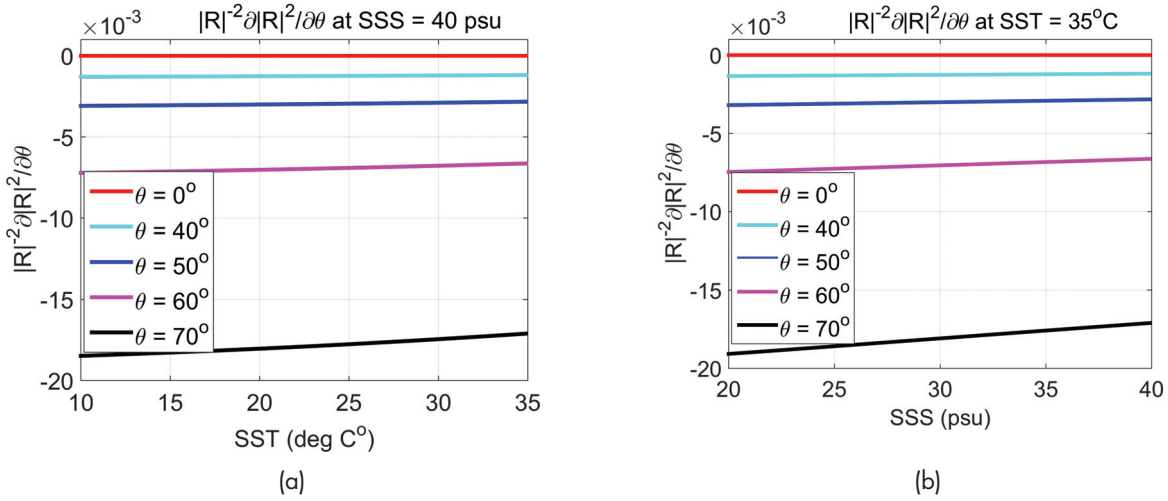

Figure 8.7. Relative partial derivative of $|\Re|^2$ over incidence angle as a function of temperature and salinity.

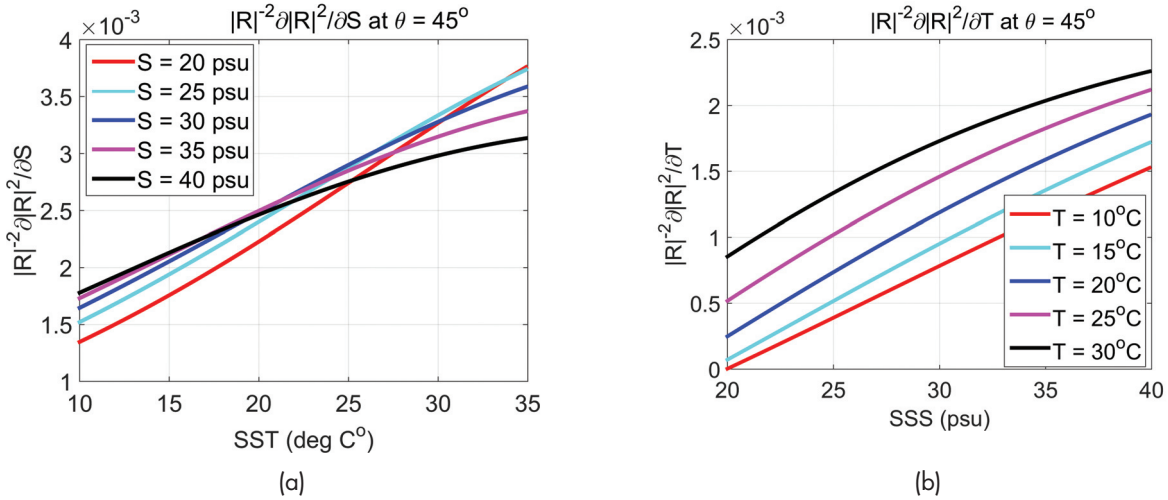

Figure 8.8. Relative partial derivative of $|\Re|^2$ over temperature and salinity.

as temperature and salinity, keeping other parameters constant. All these plots give an idea of the relative magnitudes of values of quantities entering Equations 8.22 to 8.25. To obtain values of respective errors, $E(\sigma_0)$, $E(\theta)$, $E(T)$, and $E(S)$, one needs to input errors for $\Delta\sigma_0$, $\Delta\theta$, ΔT, and ΔS. In the following tables, we present results of calculations of the relative MSS error, $\frac{\Delta mss}{mss}$, based on Equations 8.20 to 8.25, for some limiting values of the parameters involved.

For Tables 8.1 and 8.2, we used some reasonable values for input errors shown in the header of the table. One can see that the relative MSS error for $U_{10} < 20$ m s^{-1}, and for the range of incidence angles between 0 and 70°, lies within 1.7%, and within 7.5% for higher winds. The maximum relative MSS errors increase to 3% and 7.7%, respectively, if a more conservative estimate is taken for the input errors shown in the header of Tables 8.3 and 8.4. The following conclusions can be drawn from these numbers. For winds below 20 m s^{-1}, the MSS error is relatively low but it is more sensitive to the input SST and SSS errors, whereas for higher winds, the MSS error is higher but less sensitive to the input SST and SSS errors.

Table 8.1. Relative MSS error ($U_{10} < 20$ m s^{-1}, $\Delta\sigma_0 = 1.21$, $\Delta\theta = 0.5°$, ΔT = 0.5°C, ΔS = 2 psu).

Parameters	$\theta = 0°$	$\theta = 35°$	$\theta = 70°$
SSS = 20 psu, SST = 10°C	$1.24 \cdot 10^{-2}$	$1.24 \cdot 10^{-2}$	$1.58 \cdot 10^{-2}$
SSS = 40 psu, SST = 10°C	$1.26 \cdot 10^{-2}$	$1.26 \cdot 10^{-2}$	$1.59 \cdot 10^{-2}$
SSS = 20 psu, SST = 35°C	$1.41 \cdot 10^{-2}$	$1.41 \cdot 10^{-2}$	$1.81 \cdot 10^{-2}$
SSS = 40 psu, SST = 35°C	$1.36 \cdot 10^{-2}$	$1.36 \cdot 10^{-2}$	$1.70 \cdot 10^{-2}$

Table 8.2. Relative MSS error ($U_{10} > 20$ m s^{-1}, $\Delta\sigma_0 = 1.17$, $\Delta\theta = 0.5°$, ΔT = 0.5°C, ΔS = 2 psu).

Parameters	$\theta = 0°$	$\theta = 35°$	$\theta = 70°$
SSS = 20 psu, SST = 10°C	$7.42 \cdot 10^{-2}$	$7.42 \cdot 10^{-2}$	$7.42 \cdot 10^{-2}$
SSS = 40 psu, SST = 10°C	$7.42 \cdot 10^{-2}$	$7.42 \cdot 10^{-2}$	$7.43 \cdot 10^{-2}$
SSS = 20 psu, SST = 35°C	$7.45 \cdot 10^{-2}$	$7.45 \cdot 10^{-2}$	$7.48 \cdot 10^{-2}$
SSS = 40 psu, SST = 35°C	$7.44 \cdot 10^{-2}$	$7.44 \cdot 10^{-2}$	$7.46 \cdot 10^{-2}$

Table 8.3. Relative MSS error ($U_{10} < 20$ m s^{-1}, $\Delta\sigma_0 = 1.21$, $\Delta\theta = 1°$, ΔT = 1°C, ΔS = 5 psu).

Parameters	$\theta = 0°$	$\theta = 35°$	$\theta = 70°$
SSS = 20 psu, SST = 10°C	$1.37 \cdot 10^{-2}$	$1.38 \cdot 10^{-2}$	$2.42 \cdot 10^{-2}$
SSS = 40 psu, SST = 10°C	$1.49 \cdot 10^{-2}$	$1.50 \cdot 10^{-2}$	$2.48 \cdot 10^{-2}$
SSS = 20 psu, SST = 35°C	$2.19 \cdot 10^{-2}$	$2.21 \cdot 10^{-2}$	$3.28 \cdot 10^{-2}$
SSS = 40 psu, SST = 35°C	$1.95 \cdot 10^{-2}$	$1.96 \cdot 10^{-2}$	$2.95 \cdot 10^{-2}$

Table 8.4. Relative MSS error ($U_{10} > 20$ m s^{-1}, $\Delta\sigma_0 = 1.17$, $\Delta\theta = 1°$, ΔT = 1°C, ΔS = 5 psu).

Parameters	$\theta = 0°$	$\theta = 35°$	$\theta = 70°$
SSS = 20 psu, SST = 10°C	$7.44 \cdot 10^{-2}$	$7.44 \cdot 10^{-2}$	$7.46 \cdot 10^{-2}$
SSS = 40 psu, SST = 10°C	$7.47 \cdot 10^{-2}$	$7.47 \cdot 10^{-2}$	$7.50 \cdot 10^{-2}$
SSS = 20 psu, SST = 35°C	$7.65 \cdot 10^{-2}$	$7.66 \cdot 10^{-2}$	$7.81 \cdot 10^{-2}$
SSS = 40 psu, SST = 35°C	$7.58 \cdot 10^{-2}$	$7.58 \cdot 10^{-2}$	$7.71 \cdot 10^{-2}$

C. Overall Uncertainty

Above we considered errors in determining the MSS due to thermal and speckle noise, assuming that the MSS remains constant within the scene. This is only part of the uncertainty in the MSS retrieval. There are other factors that can add to the overall uncertainty.

There are factors related to the variability of the transmit signal and of the parameters of the receiving system. All of them can be boiled down to an uncertainty in the coefficient α introduced above in Equations 8.15 to 8.16. The coefficient is needed to calculate MSS from σ_0, measured in the specular direction. The uncertainty in the physical and technical parameters composing it can be eliminated, or significantly reduced, by calibration procedures or by ancillary measurements. These procedures are described in Section 7.

First, the most important uncertainty is in the spatial variability of the MSS field. Even given a homogenous wind field, which is an input for the MSS, the wave statistics can be affected by limited fetch, swell, currents, surfactants, and bathymetry. If the scales of this spatial variability are smaller than or close to the spatial resolution of the system, this factor can affect the accuracy of the MSS retrieval.

Our retrieval algorithm is based on Equation 8.17, which, in turn, is based on the radar bistatic equation and diffusive rough surface described by the GO limit of the KA and Gaussian PDF of surface slopes (Zavorotny & Voronovich, 2000). This equation and underlying EM scattering model work well for a broad range of surface conditions, but of course, they have their own limitations. If diffraction effects become important, this model can be augmented by the small slope approximation (SSA; Voronovich & Zavorotny, 2014). For the case of very small MSS (<0.003, which correspond to very weak winds, $U < 3$ m s^{-1}), the bistatic radar equation should be augmented by an additional coherent term (Zavorotny et al., 2014). The case of very steep and breaking waves can be challenging for the MSS retrieval based on either GO or the SSA, but in this case, the notion of the MSS itself becomes questionable.

References

Barrick, D. E. (1968). Relationship between slope probability density function and the physical optics integral in rough surface scattering. *Proceedings of the IEEE*, *56*(10), 1728–1729. doi: 10.1109/PROC.1968.6718

Bass, F. G., & Fuks, I. M. (1979). *Wave scattering from statistically rough surfaces* (Vol. 93). Elmsford, NY: Pergamon.

Cardellach, E., & Rius, A. (2008). A new technique to sense non-Gaussian features of the sea surface from L-band bi-static GNSS reflections. *Remote Sensing of Environment*, *112*(6), 2927–2937. doi:10.1016/j.rse.2008.02.003

Chapron, B., Kerbaol, V., Vandemark, D., & Elfouhaily, T. (2000). Importance of peakedness in sea surface slope measurements and applications. *Journal of Geophysical Research Oceans*, *105*(C7), 17195–17202. doi: 10.1029/2000JC900079

Cox, C., & Munk, W. (1954). Measurement of the roughness of the sea surface from photographs of the sun's glitter. *Journal of the Optical Society of America*, *44*(11), 838–850. doi: 10.1364/JOSA.44.000838

Elfouhaily, T., Chapron, B., Katsaros, K., & Vandemark, D. (1997). A unified directional spectrum for long and short wind-driven waves. *Journal of Geophysical Research-Oceans*, *102*(C7), 15781–15796. doi: 10.1029/97JC00467

Elfouhaily, T., Thompson, D. R., & Linstrom, L. (2002). Delay-Doppler analysis of bistatically reflected signals from the ocean surface: theory and application. *Geoscience and Remote Sensing, IEEE Transactions On*, *40*(3), 560–573. doi: 10.1109/TGRS.2002.1000316

Ellison, W., Balana, A., Delbos, G., Lamkaouchi, K., Eymard, L., Guillou, C., & Prigent, C. (1998). New permittivity measurements of seawater. *Radio Science*, *33*, 639–648. doi: 10.1029/97RS02223

Font, J., Lagerloef, G. S., Le Vine, D. M., Camps, A., & Zanifé, O. Z. (2004). The determination of surface salinity with the European SMOS space mission. *Geoscience and Remote Sensing, IEEE Transactions On*, *42*(10), 2196–2205. doi: 10.1109/TGRS.2004.834649

Guimbard, S., Gourrion, J., Portabella, M., Turiel, A., Gabarró, C., & Font, J. (2012). SMOS semi-empirical ocean forward model adjustment.

Geoscience and Remote Sensing, IEEE Transactions On, *50*(5), 1676–1687. doi: 10.1109/TGRS.2012.2188410

Jähne, B., Münnich, K. O., Bösinger, R., Dutzi, A., Huber, W., & Libner, P. (1987). On the parameters influencing air-water gas exchange. *Journal of Geophysical Research: Oceans (1978–2012)*, *92*(C2), 1937–1949. doi: 10.1029/JC092iC02p01937

Klein, L., & Swift, C. T. (1977). An improved model for the dielectric constant of sea water at microwave frequencies. *Antennas and Propagation, IEEE Transactions On*, *25*(1), 104–111. doi: 10.1109/TAP.1977.1141539

Liu, Y., Su, M. Y., Yan, X. H., & Liu, W. T. (2000). The mean-square slope of ocean surface waves and its effects on radar backscatter. *Journal of Atmospheric and Oceanic Technology*, *17*(8), 1092–1105. doi: 10.1175/1520-0426(2000)017<1092:TMSSOO>2.0.CO;2

Liu, Y., Yan, X. H., Liu, W. T., & Hwang, P. A. (1997). The probability density function of ocean surface slopes and its effects on radar backscatter. *Journal of Physical Oceanography*, *27*(5), 782–797. doi: 10.1175/1520-0485(1997)027<0782:TPDFOO>2.0.CO;2

Meissner, T., & Wentz, F. J. (2004). The complex dielectric constant of pure and sea water from microwave satellite observations. *Geoscience and Remote Sensing, IEEE Transactions On*, *42*(9), 1836–1849. doi: 10.1109/TGRS.2004.831888

Soulat, F. (2004). *Sea surface remote sensing with GNSS and sunlight reflections* (Doctoral dissertation, Universitat Politecnica de Catalunya).

Ulaby, F. T, Moore, R. K., & Fung, A. K. (1986). *Microwave remote sensing: Active and passive* (Vol. 3). Norwood, MA: Artech House.

Voronovich, A. G., & Zavorotny, V. U. (2014). Full-polarization modeling of monostatic and bistatic radar scattering from a rough sea surface. *Antennas and Propagation, IEEE Transactions On*, *62*(3), 1362–1371. doi: 10.1109/TAP.2013.2295235

Walsh, E. J., Vandemark, D. C., Friehe, C. A., Burns, S. P., Khelif, D., Swift, R. N., & Scott, J. F. (1998). Measuring sea surface mean square slope with a 36-GHz scanning radar altimeter. *Journal of Geophysical Research: Oceans (1978–2012)*, *103*(C6), 12587–12601. doi:10.1029/97JC02443

Wu, J. (1990). Mean square slopes of the wind-disturbed water surface, their magnitude, directionality, and composition. *Radio Science*, *25*(1), 37–48. doi: 10.1029/RS025i001p00037

Zavorotny, V. U., & Voronovich, A. G. (2000). Scattering of GPS signals from the ocean with wind remote sensing application. *Geoscience and Remote Sensing, IEEE Transactions On*, *38*(2), 951–964. doi: 10.1109/36.841977

Zavorotny, V. U., Gleason, S., Cardellach, E., & Camps, A., (2014). Tutorial on remote sensing using GNSS bistatic radar of opportunity. *Geoscience and Remote Sensing, IEEE Magazine*, *2*(4), 8–45. doi: 10.1109/MGRS.2014.2374220

Appendix: Klein-Swift Ocean Dielectric Model

According to the empirical model of Klein and Swift (1977), the real and imaginary parts of the dielectric constant of seawater at microwave frequencies are, respectively,

$$\mathrm{Re}\,\varepsilon = \varepsilon_\infty + \left(\varepsilon_s - \varepsilon_\infty\right) / \left(1 + \omega^2\tau^2\right) \tag{8.26}$$

and

$$\mathrm{Im}\,\varepsilon = \omega\tau\left(\varepsilon_s - \varepsilon_\infty\right) / \left(1 + \omega^2\tau^2\right) + \sigma / \varepsilon_0\omega \tag{8.27}$$

Here, $\omega = 2\pi f \cdot 10^9$ is the radian frequency (radians per second), and f is frequency in GHz. $\varepsilon_0 = 8.854 \cdot 10^{-12}$ is the dielectric permittivity of free space in farads per meter. $\varepsilon_\infty = 4.9$ is the dielectric permittivity of water at infinite frequency; $\varepsilon_s = a\varepsilon_{sT}$ is the static dielectric constant, where

$$a = 1 + 1.613 \cdot 10^{-5} TS - 3.656 \cdot 10^{-3} S + 3.210 \cdot 10^{-5} S^2 - 4.232 \cdot 10^{-7} S^3 \tag{8.28}$$

$$\varepsilon_{sT} = 87.134 - 1.949 \cdot 10^{-1} T - 1.276 \cdot 10^{-2} T^2 + 2.491 \cdot 10^{-4} T^3 \tag{8.29}$$

$\sigma = \sigma_0 \exp\left(-\Delta\beta\right)$ is the ionic conductivity in mhos per meter, where

$$\sigma_0 = S(0.182521 - 1.46192 \cdot 10^{-3} S + 2.09324 \cdot 10^{-5} S^2 - 1.28205 \cdot 10^{-7} S^3) \quad \textbf{(8.30)}$$

and $\Delta = 25 - T$.

$$\beta = 2.033 \cdot 10^{-2} + 1.266 \cdot 10^{-4} \Delta + 2.464 \cdot 10^{-6} \Delta^2 - S(1.849 \cdot 10^{-5} - 2.551 \cdot 10^{-7} \Delta + 2.551 \cdot 10^{-8} \Delta^2) \quad \textbf{(8.31)}$$

Here, S is seawater salinity in parts per thousand, T is seawater temperature in °C. $\tau = b\tau_0$ is the relaxation time in seconds, where

$$b = 1 + 2.282 \cdot 10^{-5} ST - 7.638 \cdot 10^{-4} S - 7.760 \cdot 10^{-6} S^2 + 1.105 \cdot 10^{-8} S^3 \quad \textbf{(8.32)}$$

and

$$\tau_0 = 1.768 \cdot 10^{-11} - 6.086 \cdot 10^{-13} T + 1.104 \cdot 10^{-14} T^2 - 8.111 \cdot 10^{-17} T^3 \quad \textbf{(8.33)}$$

9. Level 2 Wind Speed Retrieval Algorithm

The Level 2 wind speed retrieval algorithm described here is a revised and improved version of the algorithm illustrated in Clarizia et al. (2014). While the overall approach remains the same (i.e., regression-based wind retrieval using GMFs), the present algorithm contains a number of improvements to the calculation of the observables, as well as to the actual retrieval method (Clarizia & Ruf, 2016). The basic steps for the Level 2 retrieval algorithm can be summarized as follows:

1. Two DDM "observables," the DDMA and the LES, are derived from Level 1B DDMs of BRCS and DDMs of scattering area, which are generated as explained in Gleason (2014).
2. A population of simulated samples produced by the CYGNSS Project E2ES (a model designed to artificially simulate DDMs using orbit estimates and modeled winds), applied to a 13-day NR of TC and background wind fields, is split into training and test subsets, using odd and even minutes of sample time.
3. A statistical inversion algorithm is trained using the training data subset, by constructing an empirical GMF from measured and truth matchups.
4. Debiasing is applied to wind retrievals produced by the DDMA and LES observables.
5. The test data subset is mapped to retrieved wind speed using a MV estimator.
6. Time averaging is applied to consecutive samples to produce a consistent 25 km spatial resolution data product, whenever it is appropriate to do so (the appropriate level of averaging depends on the incidence angle of the sample).
7. Samples with effective field of view (EFOV) above the spatial resolution requirement are removed (EFOV filter).
8. The performance of the retrieval algorithm is evaluated, in terms of RMS error between the true wind and the retrieved wind.

Steps 2, 3, 7, and 8 represent new additions to the previous (prerelease) version of the retrieval algorithm. They significantly improve the overall performance, as will be shown later. Each step is described in detail in the subsequent paragraphs.

I. DDM Observables: DDMA and LES

Here we present a definition of the observables we use for our retrieval algorithm, along with the overall set of DDMs from which they are calculated, and the Level 1B corrections applied to the DDMs. The DDMs used have all been simulated under realistic conditions, using the CYGNSS E2ES.

A. Definition of Delay-Doppler Map Average (DDMA)

The DDMA is the average of the Level 1B DDM of the NBRCS over a given delay/Doppler range window around the SP. The DDMA exploits the DDM region that is most sensitive to varying wind speed, namely the scattered power at and around the SP. Notably, the DDMA has the advantage of mitigating the effect of noise by averaging the power over the area around the SP, rather than the power value at the single SP pixel. An illustration of a DDM simulated with the CYGNSS E2ES, and a qualitative example of the area where the DDMA is calculated (shown as the "black box"), is shown in Figure 9.1.

The DDMA is calculated from the DDM after the additive noise floor has been removed. The noise floor is estimated from the DDM in a region where there is no signal (i.e., at delay values just before the SP and before entering the horseshoe shape) and is subtracted from each DDM pixel. The noise floor is computed as the average of the DDM over a number of delay rows where no signal is present (i.e., averaged across all the Doppler frequency bins at delay values before the presence of a scattered signal from the Earth's surface appears).

B. Definition of Leading Edge Slope (LES)

The LES (previously called delay waveform slope, or DWS, in Clarizia & Zavorotny, 2015) is the slope of the leading edge of the integrated delay waveform (IDW). IDWs are obtained as the incoherent

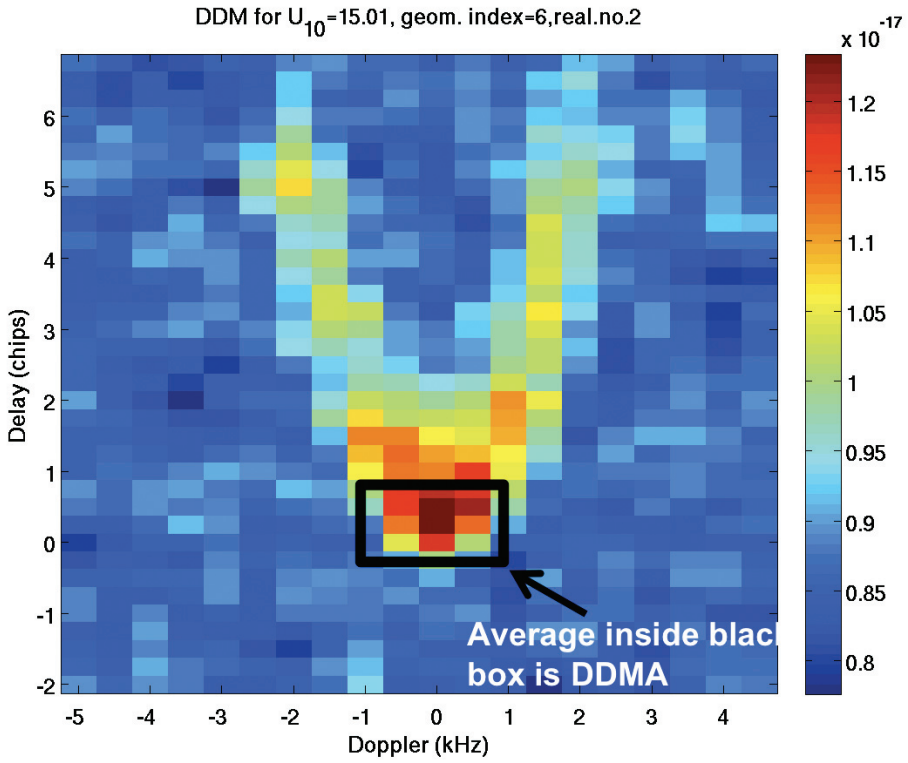

Figure 9.1. A simulated DDM and the DDM area where the DDMA is calculated.

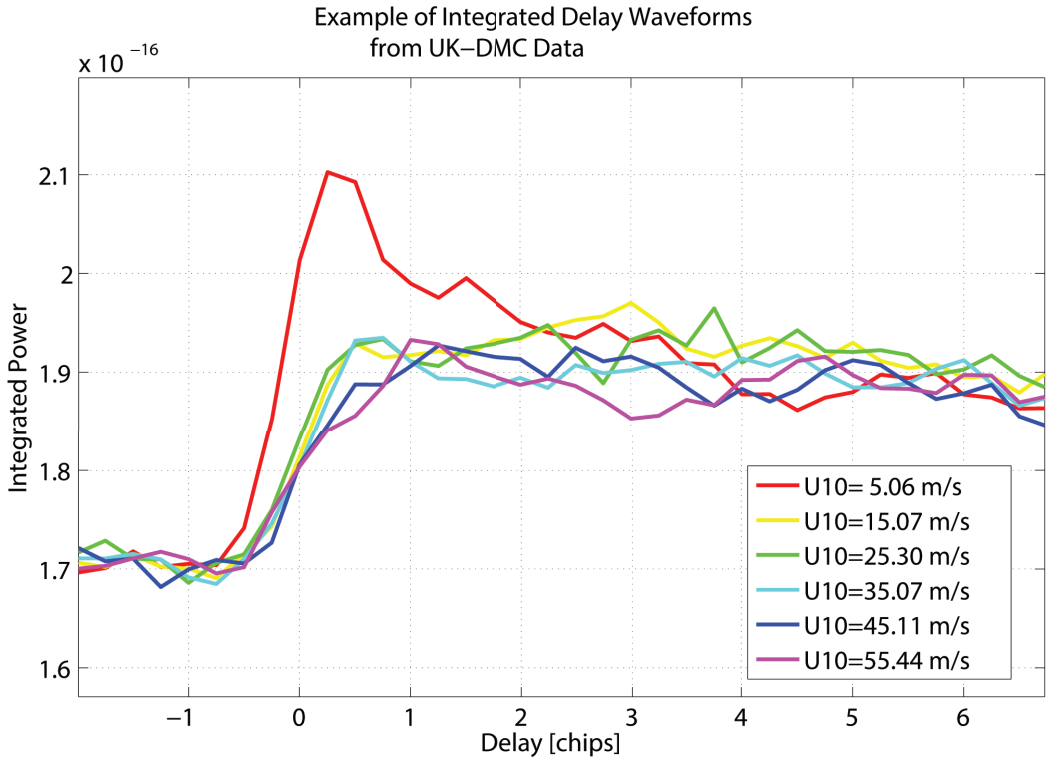

Figure 9.2. IDWs computed from DDMs simulated using different wind speeds.

integration of DDMs of NBRCS in the Doppler dimension over a range of Doppler frequencies. An illustration of IDWs, and how the slope of their rising edge differs for different wind speeds, is illustrated in Figure 9.2.

The DDMA is computed in practice as the average of the Level 1B DDM of BRCS over a selected DD window, divided by the average of the DDM of scattering area over the same window. Similarly, the LES is calculated as the slope of IDWs obtained from Level 1B DDMs of BRCS, divided by the average of DDMs of scattering area. The slope is determined using a least-squares fit of the IDW within the delay window to a linear expression. Both the DDMs of BRCS and the DDMs of scattering area are output from the Level 1B calibration, as described in Gleason (2014).

C. 13-Day NR Dataset

The dataset used to develop and test the Level 2 wind speed retrieval algorithm is a very large set of simulated DDMs collected from all the CYGNSS observatories over a time frame of 13 days, during which a full life cycle of a TC has been simulated using the ECMWF/WRF NR model (Nolan et al., 2013). The NR model generates physically realistic, long-lived storms with a very fine grid spacing (1 km reporting interval; ~4 km spatial resolution), a very high frequency output (1 output every 6 minutes, over a standard 13-day total run), and it outputs the complete set of ocean and atmosphere state variables. An example of four snapshots of the TC, spaced 6 hours apart, is shown in Figure 9.3. These are data grids of 480 × 480 km.

Figure 9.4 shows the histogram of the wind speeds for the four snapshots illustrated in Figure 9.3.

The wind distribution is not uniform and exhibits a very strong peak between 20 m s^{-1} and 30 m s^{-1} in all cases. This represents the wind distribution of a realistic TC. A plot of the locations of the inner core of the simulated TC, registered every three hours, is shown in Figure 9.5, along with plots of minimum surface pressure and peak wind speed. The TC is simulated from July 29, 2005, up until August 10, 2005, and the maximum winds are registered in August 3 and 4. A plot of the 25 × 25 km spatially averaged wind speeds from the full 13-day NR is shown in Figure 9.6.

D. Generation of DDMs and Level 1B Observables

A large set of DDMs was obtained using a realistic 13-day TC scenario generated with the NR model and using realistic geometries for the eight CYGNSS observatories, generated through orbital simulations.

A DDM was generated for each second of acquired data and for those SPs acquired during an overpass of the satellites on the TC, resulting in more than two million DDMs. Each DDM is therefore characterized by different incidence angles and antenna gains at the SP. The altitude of the transmitter and receiver for the four geometries is respectively ~20,200 km and ~500 km, and the transmitter antenna gain is assumed to be constant and equal to 13 dB. Each DDM was also associated with a simulated ground truth wind, computed as the 25 × 25 km spatial average of the wind simulated from the NR.

DDMs are simulated using the CYGNSS E2ES. The E2ES simulates DDMs using an advanced implementation of the Zavorotny-Voronovich model (Zavorotny & Voronovich, 2000), to which thermal noise and speckle noise are added. Furthermore, the simulated NBRCS accounts for the nonuniformity of the wind field across the 100 × 100 km spatial area that is used to generate the DDM. A detailed description of the E2ES can be found in O'Brien (2014). Two examples of simulated Level 1A DDMs, for low wind speed (5 m s^{-1}) and for high wind speed (40 m s^{-1}), from the CYGNSS E2ES are shown in Figure 9.7.

The delay and Doppler resolution for the simulated DDMs is respectively 0.25 chips and 500 Hz. The delay axis extends from −2 chips to 6.75 chips, whereas the Doppler axis spans −5 kHz to 4.5 kHz.

The Level 1B DDM is generated by calibrating the Level 1A data, as described in Section 7, and then a DDMA and LES observable are computed for each of them. A very important aspect for this computation is the delay and Doppler range, over which the observables are computed. The choice of the delay and Doppler ranges is a trade-off between the improvement in SNR that results from averaging more samples of the diffusely scattered signal in the glistening zone, versus the improvement in spatial resolution that results from limiting the extent of the glistening zone included in the average. For CYGNSS, the baseline spatial resolution requirement for retrieved winds is 25 × 25 km, constraining the extent of the usable

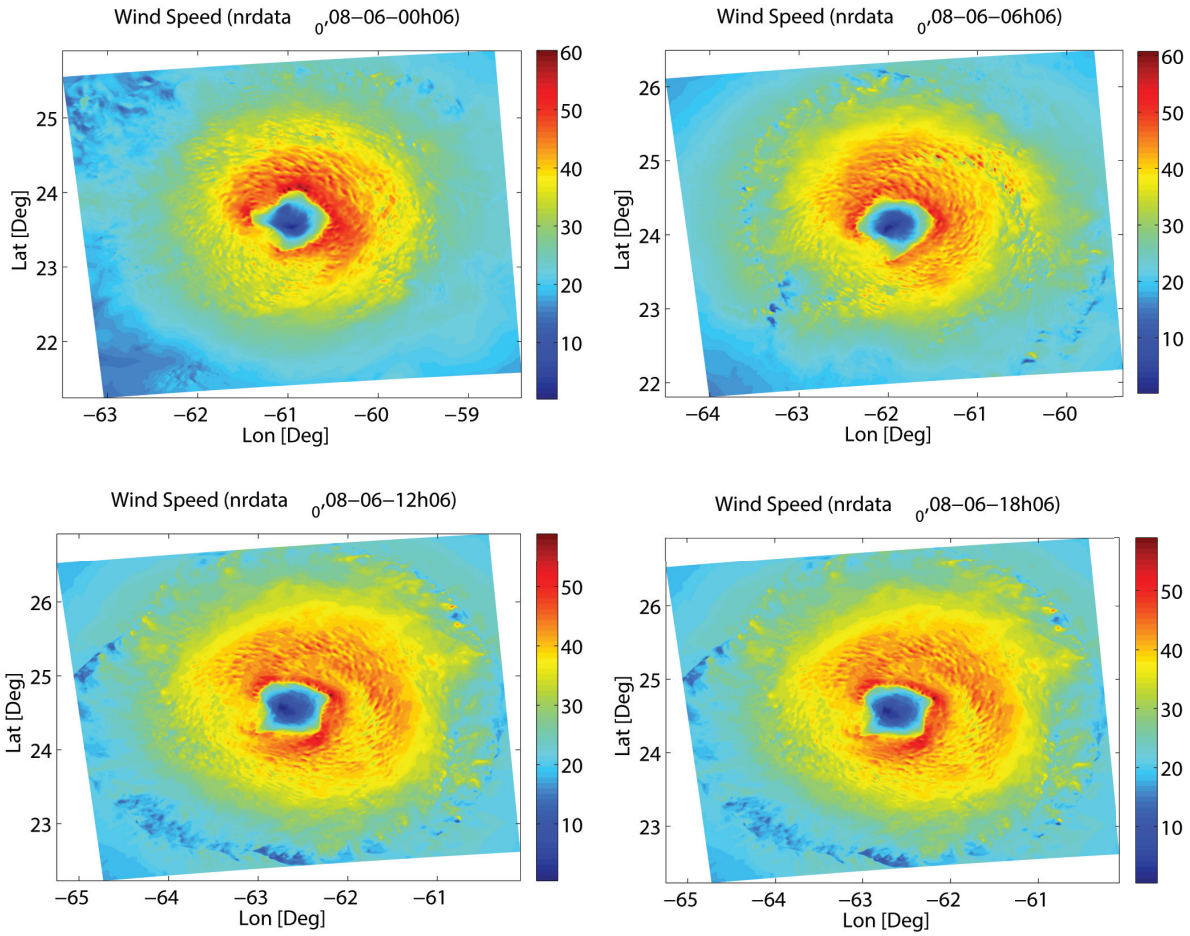

Figure 9.3. Snapshots of simulated realistic TCs from the NR model.

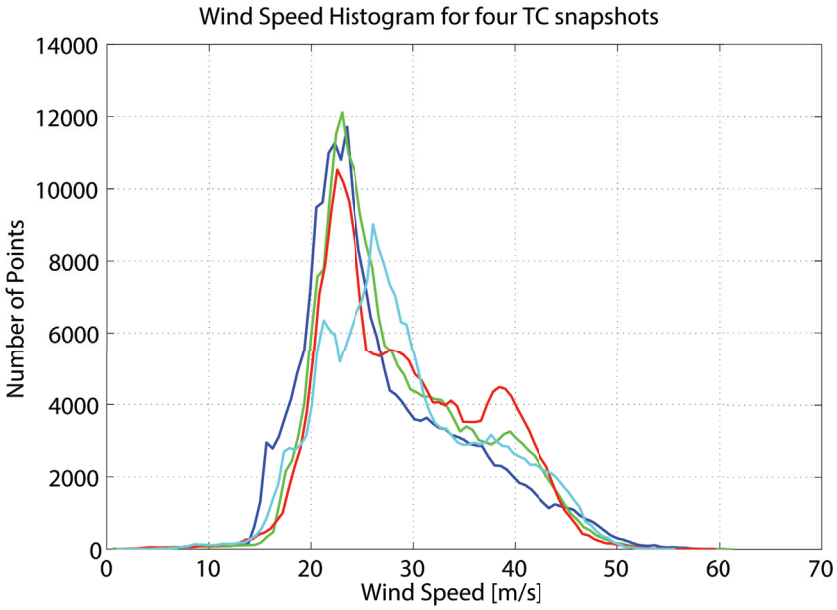

Figure 9.4. Wind speed histograms for the four TC snapshots.

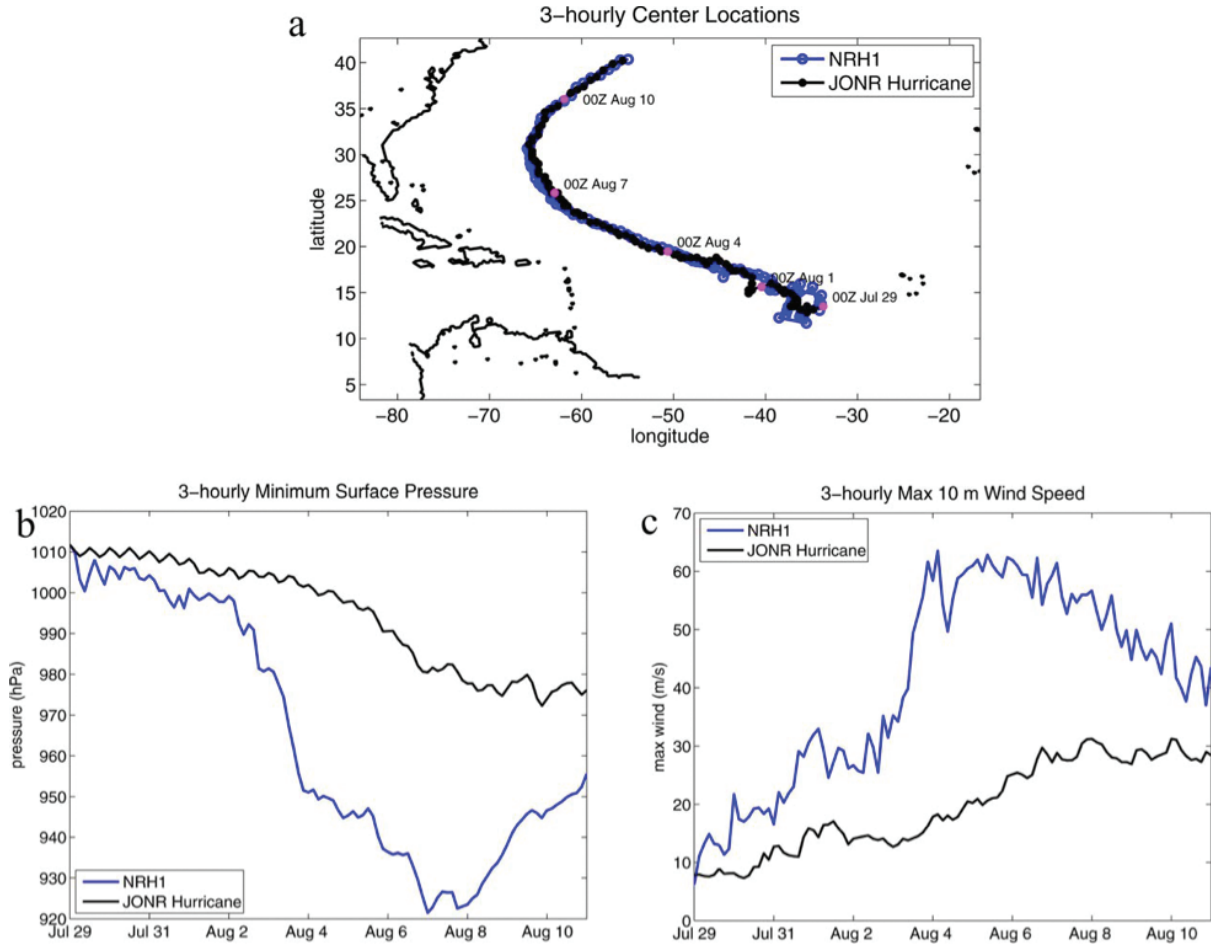

Figure 9.5. Illustration of three hourly center locations of the simulated TC (top), and plots of three hourly minimum surface pressure (bottom left) and maximum wind speed (bottom right) for the 13-day NR simulation considered for this study. NRH1 are the values by the NR numerical model, whereas JONR are the values estimated by the US Navy's Office of Naval Research's hurricane prediction center. The NR shows higher winds and a lower pressure depression due to its higher spatial and temporal resolution. *Reused from Nolan et al. (2013), © American Geophysical Union (John Wiley and Sons, Inc.), 2013.*

DDM. Figure 9.8 illustrates two examples of the dependence of delay and Doppler range on spatial resolution. Note that the iso-range ellipses become closer to each other as the delay increases; furthermore, they widen and stretch out with increasing incidence angles without changing their orientation, so the geometrical parameter that mostly influences the configuration of the iso-delay lines is the incidence angle. In the case of iso-Doppler lines, the spacing between them also increases with increasing incidence angle, but they are also strongly affected by the velocity vectors of the transmitter and above all of the receiver, which change their orientation.

Figure 9.9 shows curves of the square root of the instantaneous field of view (IFOV) versus the incidence angle, for different delay ranges. Samples within a delay of +/− 1 chip with respect to the SP contain some fraction of the scattered power from the SP pixel, due to convolution with the Woodward ambiguity function (WAF). For this reason, we incorporate the first sample at an earlier delay (–0.25 chip) than the SP into all observables. The longest delay included in the observable will set the IFOV, defined here as the physical area within the largest iso-range ellipse. It is clear from Figure 9.9 that in order to maintain a 25 × 25 km resolution requirement for all usable measurement geometries (as set by angle of incidence), the delay range must be limited to [–0.25, 0.25]. The dashed magenta line shows the 25 km limit on the square root of the IFOV.

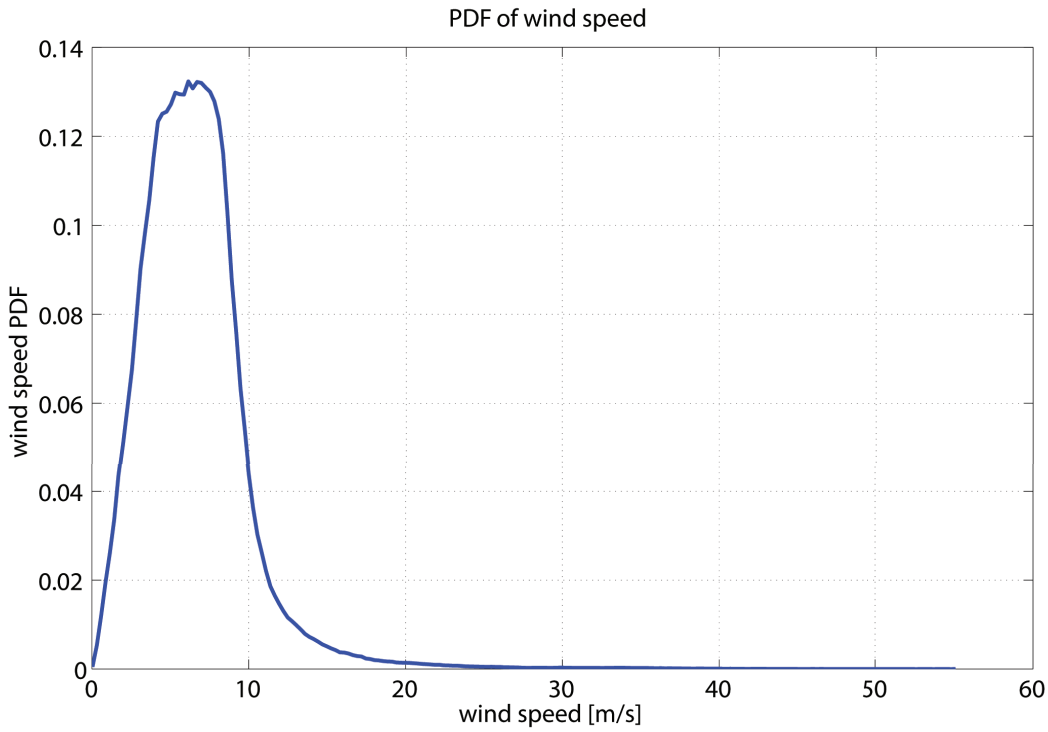

Figure 9.6. PDF of 25 × 25 km spatially averaged wind speeds from the full 13-day NR. *Reused from Clarizia & Ruf (2016), © 2016 IEEE.*

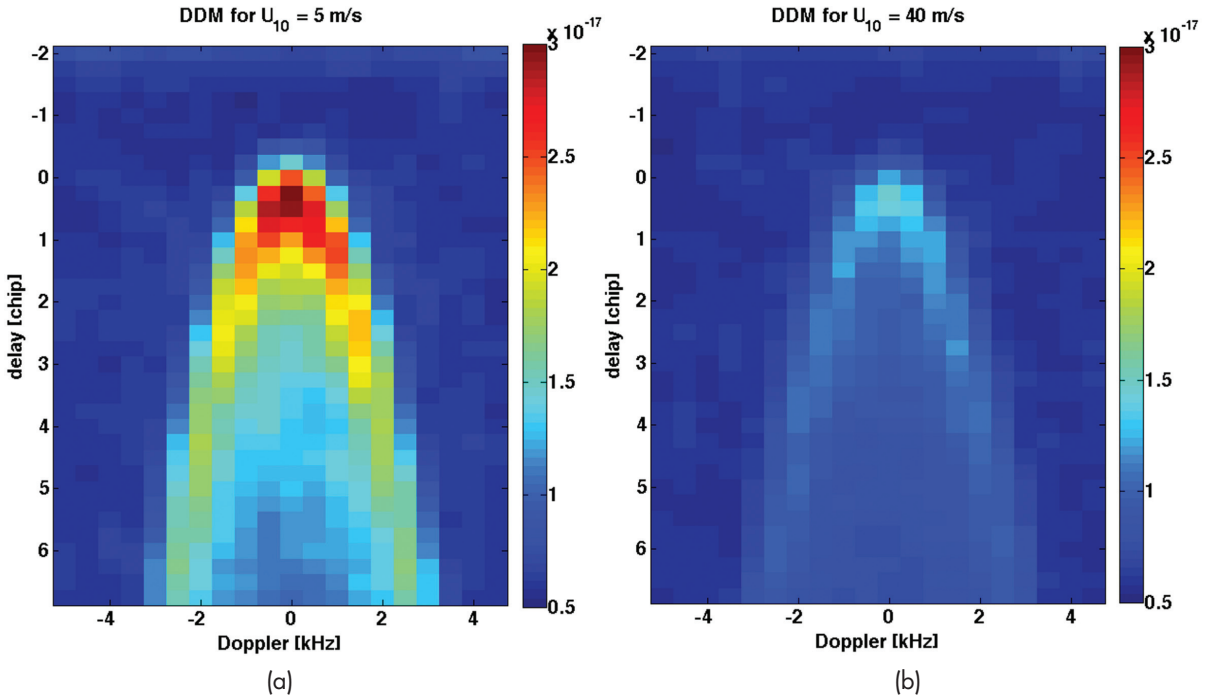

Figure 9.7. (a) DDM simulated with the E2ES, using geometry 2, baseline configuration, and a wind speed of 5 m s^{-1}. (b) DDM simulated using geometry 4, baseline configuration, and a wind speed of 40 m s^{-1}.

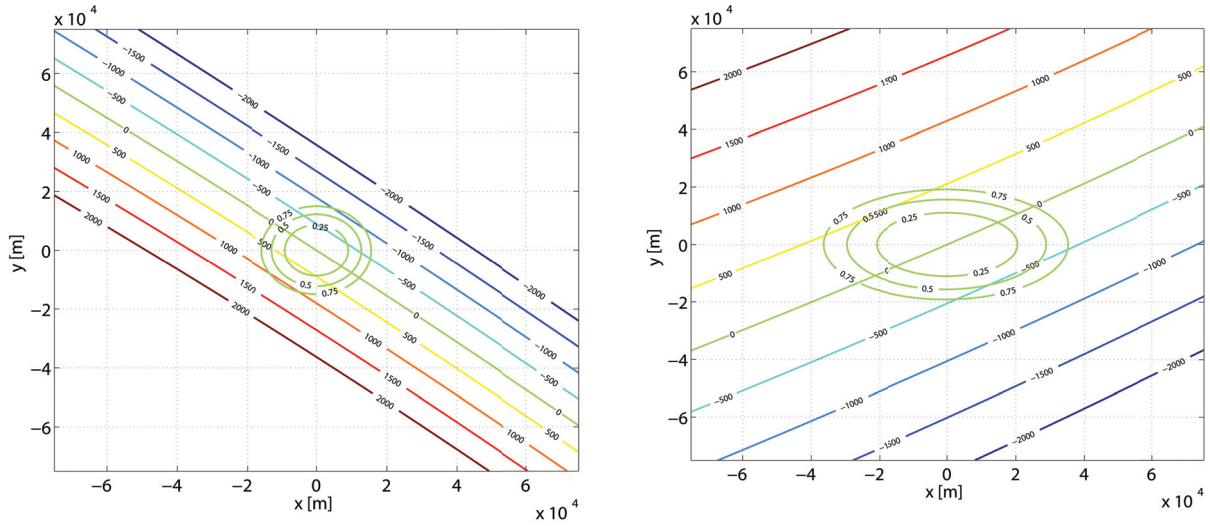

Figure 9.8. Iso-delay and iso-Doppler lines for an incidence angle of 16.5° (left) and of 57.6° (right). *Reused from Clarizia & Ruf (2016), © 2016 IEEE.*

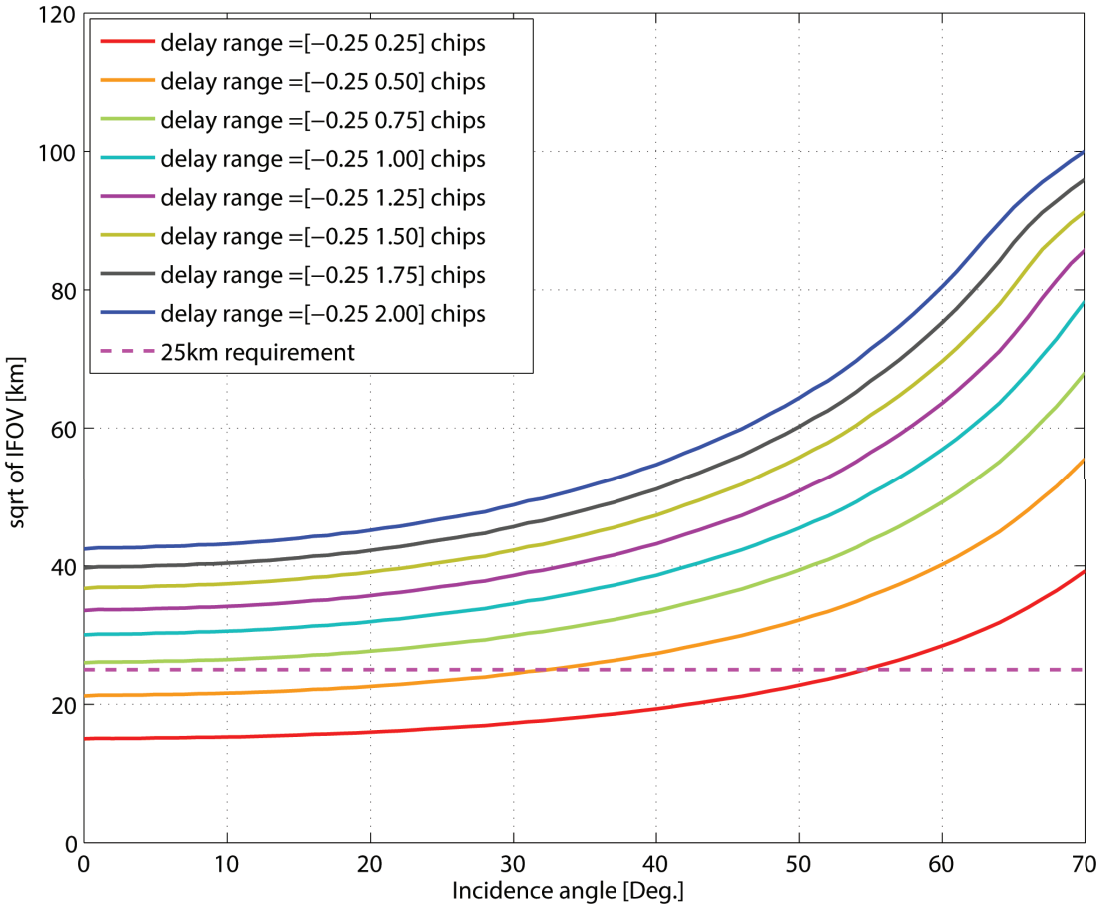

Figure 9.9. Illustration of curves of square root of IFOV versus incidence angle, for a variety of delay ranges. The dashed magenta line shows the 25 km requirement. *Reused from Clarizia & Ruf (2016), © 2016 IEEE.*

Having selected the delay range, the Doppler range has to be chosen such that the iso-Doppler lines will not truncate some of the scattered signal within the largest iso-delay ellipse (0.25 chips). The Doppler range should not be wide enough to include reflections from the ocean surface that lie entirely outside the maximum delay ellipse, either. In such a case, measurements at all delays would contain only noise without adding more signal, serving only to decrease the SNR of the observable. The Doppler range is therefore selected to satisfy the following two conditions:

- Iso-Doppler lines are the closest possible to the iso-delay line selected.
- Iso-Doppler lines are always outside the iso-delay line selected.

The Doppler range satisfying the above conditions will depend on the particular geometry (incidence angle and velocity vectors), as illustrated in Figure 9.8. However, the dependence of IFOV on the maximum Doppler range is weak, as it is illustrated in Figure 9.10, where curves of square root of IFOV versus incidence angle are shown for a single delay range and a number of different Doppler ranges. It is interesting to observe that the first case of Doppler range of (–250 250) Hz is different from the others—and noisier, since the very small Doppler range chops off part of the area within the iso-delay ellipse at 0.25 chips. Instead, small differences are observed for the other cases, mostly at lower incidence angles. At higher incidence angles, the iso-Doppler lines stretch out more rapidly than the iso-delay lines and tend to fall quickly

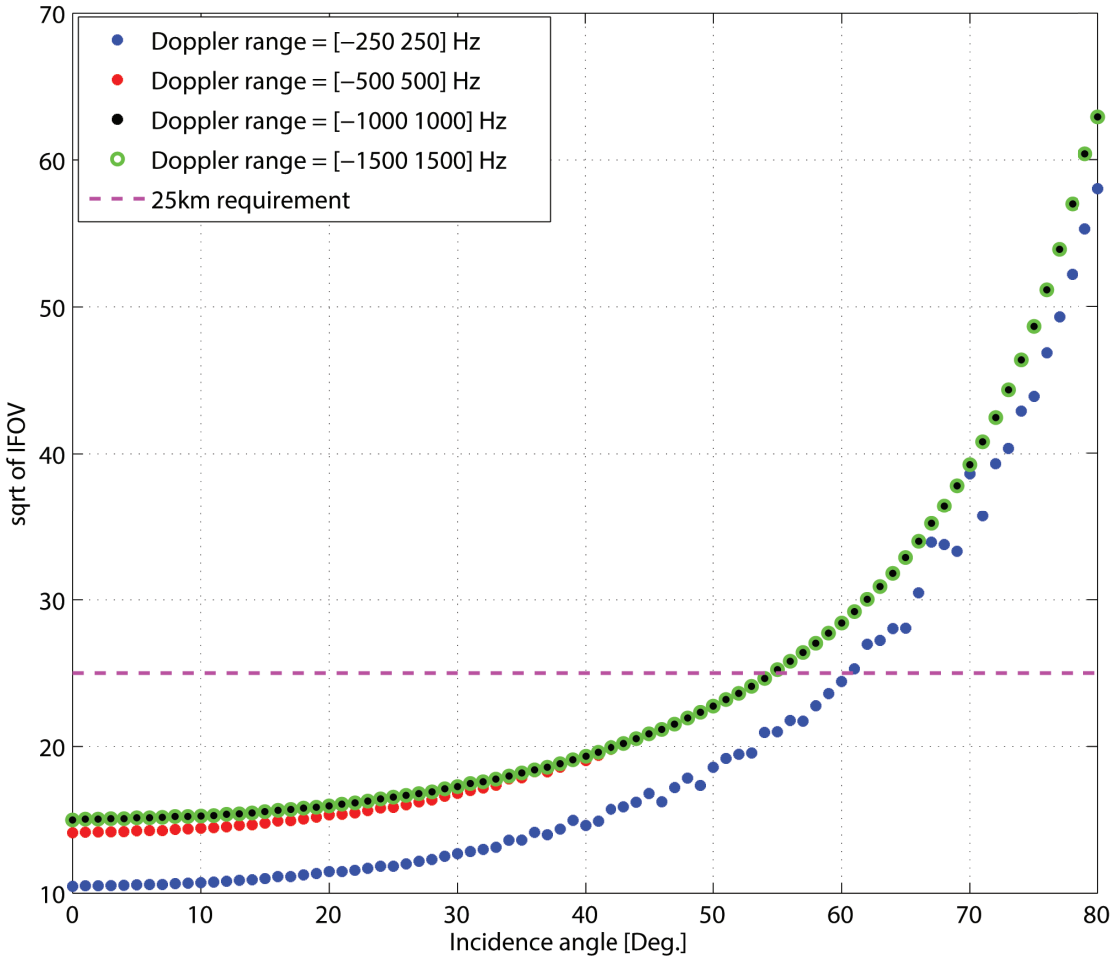

Figure 9.10. Illustration of curves of square root of IFOV versus incidence angle, for a fixed delay range of (–0.25 0.25) chips and different Doppler ranges. The dashed magenta line shows the 25 km requirement. *Reused from Clarizia & Ruf (2016), © 2016 IEEE.*

outside the 0.25 iso-delay ellipse. The IFOV at higher incidence angles is thus entirely determined by the delay range. Furthermore, there is no difference in the IFOV between the (–1000 1000) Hz Doppler range and the (–1500 1500) Doppler range, suggesting that these iso-Doppler lines fall outside the 0.25 chip iso-delay lines for all geometries.

A Doppler range of (–1000 1000) Hz was selected based upon these considerations. This choice has then been confirmed by applying the full Level 2 retrieval algorithm to DDMA observables computed using the three different Doppler ranges. The Doppler range of (–1000 1000) was verified as providing the lowest RMS error among the three (Figure 9.11).

Note that in this case only the physical area included in the iso-delay and iso-Doppler lines is considered. Several additional factors need to be taken into account in order to properly relate the delay and Doppler ranges to the spatial region. These include the following: First, the spatial boundaries defined by lines of constant iso-delay and iso-Doppler do not conform to a fixed distance from the SP. An effective spatial resolution based, for example, on equal area coverage needs to be defined. The SP is not centered in the iso-delay ellipse. Second, the WAF and Doppler filter impulse response define weighted response functions for the contribution of different regions of the delay/Doppler domain to the measurements. These weightings should also be accounted for by a suitable definition of the effective spatial resolution. Third, multiple samples of the DDM can be averaged together in ground processing to reduce measurement noise. This will produce spatial smearing in the direction of motion of the SP. Each of these factors will be included in a more complete definition of the spatial resolution, which is currently under development. The DDMA and LES are therefore computed using a delay range of (–0.25 0.25) chips and a Doppler range of (–1000 1000) Hz, and they are referred to as Level 1A observables, since they represent the very first stage of the retrieval algorithm and are not corrected for any antenna or geometrical affects.

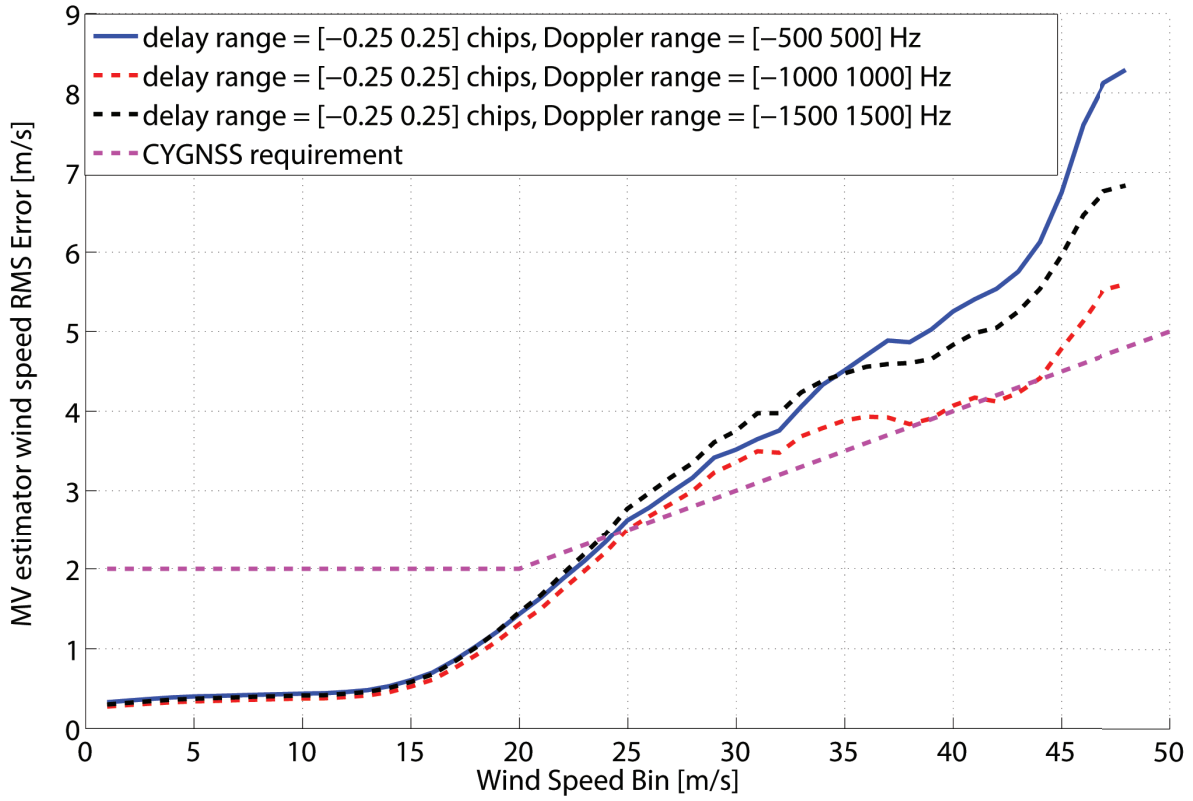

Figure 9.11. Curves of RMS error as a function of wind speed, obtained for a fixed delay range, and three different Doppler ranges, using only samples with receiver antenna gain higher than 10 numeric. The lowest RMS error is provided by the Doppler range of (–1000 1000) Hz.

A filter is applied to remove the noisiest observable based upon a minimum value for the RCG. RCG is defined as the receiver antenna gain, multiplied by the range losses, at the SP, as follows:

$$RCG = \frac{G_{RX}^{SP}}{\left(R_0^{SP} R^{SP}\right)^2} \quad \textbf{(9.1)}$$

The RCG represents an improved definition of gain, which takes into account both the effect of the receiver antenna and the effect of the attenuation due to range losses. It will be used to filter data with low, medium, or high gain and analyze different results for different data types. Typical values of low, medium, and high RCG are respectively $3{\cdot}10^{-27}$, $10{\cdot}10^{-27}$, and $20{\cdot}10^{-27}$. For brevity, we will often refer to RCG values of 3, 10, and 20, omitting the 10^{-27} term. Figures 9.12 and 9.13 plot the Level 1B DDMA and LES observables against the ground truth wind speeds, with an RCG higher than 20, thus representing data with very low noise.

II. Overview of Level 2 Wind Speed Retrieval Algorithm

The overall approach of the wind speed retrieval algorithm is similar to the one presented in Clarizia and Zavorotny (2015), with some additional steps in the data processing that improve the final performance. The retrieval algorithm follows a statistical inversion approach using an empirical GMF derived from the true wind matchups against their respective DDM observable. Each observable is individually used to estimate a wind speed (Clarizia & Zavorotny, 2015). However, compared to Clarizia and Zavorotny (2015), the GMF used here is a function of not only wind speed but also incidence angle. This is due to the dependence existing between the Level 1B observables and the incidence angle, which has been observed in Level 1B observables simulated without thermal noise and speckle. This can be found in the equation of the NBRCS (see Zavorotny & Voronovich, 2000). Two approaches exist to deal with such dependence: one is to remove the incidence angle dependence from the Level 1B observables (the so-called Level 2A correction) and another is to generate the GMF function such that it accounts for the incidence angle dependence. While both approaches work quite well with simulated data, the second approach is preferred since it is consistent with scatterometry where GMFs are functions of wind speed and incidence angle. In general, GMFs can be functions of a number of other parameters (including wind direction, azimuth angle, dielectric properties of the sea, etc.), with a dominant dependence on wind speed and incidence angle. For this reason, it is desirable to model and incorporate these dependencies in the GMF, rather than trying to remove them from the observables. The steps taken to develop each retrieval algorithm are as follows:

1. All available DDM observables and the corresponding collocated ground truth winds and incidence angle are assembled.
2. An empirical 2D GMF, function of both wind speed and incidence angle, is constructed from the matchups using least squares regression analysis.
3. The GMF is used as the basis for the mapping from DDM observable to estimated wind speed.
4. The RMS difference between the estimated wind and the NDBC ground truth wind speed is computed as the RMS error in the retrieval.

As already mentioned, this type of wind retrieval algorithm is often used in scatterometry and synthetic aperture radar (SAR), where empirical GMFs are derived from a large collocation study between observed measurements and in situ buoy and/or NWP model data. Similarly, CYGNSS will make use of a large dataset of collocated wind speed information from different sources (including buoys, model outputs, aircraft measurements, and satellite crossovers) to construct a robust empirical GMF model for each observable. In order to work with independent datasets for the inversion algorithm training and for the performance evaluation of the algorithm itself, we split the full 13-day NR data into two subsets: one including all the data with an odd minute in their time stamp and another with an even minute in their time stamp. The choice of separating the datasets based on their odd and even minutes is commonly adopted in these cases when two independent datasets need to be created. The odd minute dataset is used to train the LUT, which is used to estimate the winds, and the even minute dataset is used to assess the performances of the algorithm in terms of RMS error.

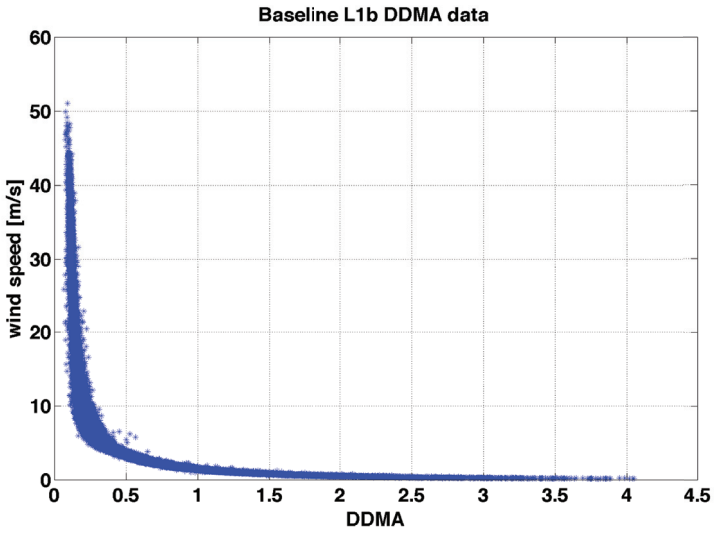

Figure 9.12. Illustration of ground truth wind speeds versus Level 1B DDMA, for RCG > 20.

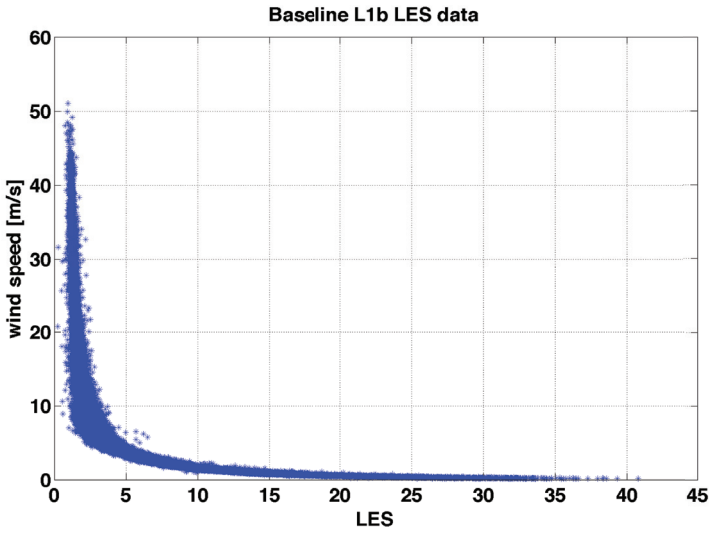

Figure 9.13. Illustration of simulated ground truth wind speeds versus Level 1B LES, for RCG > 20.

III. Generation of Geophysical Model Function

For each observable, the training data are formed as the Level 1B observable, computed over a delay range of (–0.25 0.25) chips and a Doppler range of (–1000 1000) Hz, to which the SP selection algorithm has been applied. Only data with sufficiently high enough RCG are selected for LUT generation, and in our case, we have used a RCG threshold of 20. The derivation of a full 2D GMF, a function of both wind speed and incidence angle, was in this case made difficult by the lack of enough available samples, particularly at certain ranges of incidence angles. An alternative approach was used here, which is described in the following steps:

1. The dependence of the observables on the incidence angle is preestimated, using observables computed from noise-free DDMs (the so-called Level 2A correction).
2. A unique GMF is derived for all the samples to map the selected observables against their simulated ground truth wind speed, which is true wind speed from the NR, spatially averaged over an area of 25 x 25 km, centered at the SP.

3. A number of different, sufficiently small incidence angle intervals are considered, and the GMF obtained in step 2 is scaled according to the Level 2A correction developed in step 1. This produces a one-dimensional GMF for each incidence angle interval. This represents our final 2D GMF, which is a function of both wind speed and incidence angle.

This method, which represents a simplified but approximate way to derive a full 2D GMF, will then be replaced by the more appropriate approach of deriving the 2D GMF entirely from the samples, once a high enough number of simulated storms are made available. The following subsections describe in detail each of the steps listed above.

A. Level 2A Correction

The Level 2A correction represents the correction for the dependence on the incidence angle θ_i, which is not eliminated by the Level 1B corrections. After the Level 1B corrections, a dependence on θ_i of the DDM of scattered power remains in the equation for the radar cross section, $\sigma_0(\vec{r})$, which according to the model by Zavorotny and Voronovich (2000), can be written as

$$\sigma_0(\vec{r},\,\theta_i) = \frac{\pi\left|\Re(\theta_i)\right|^2 q^4(\vec{r},\,\theta_i)}{q_z^4(\vec{r},\,\theta_i)} f_q(\mathrm{s}) \qquad \textbf{(9.2)}$$

and it depends on the Fresnel reflection coefficient $\Re$, and on the PDF $f_q(\ldots)$ of the sea surface slopes, the latter defined as $\mathrm{s} = -\mathrm{q}_\perp/q_z = \left[-q_x/q_z, -q_y/q_z\right]$. The vector $\mathrm{q} = \left[q_x,\, q_y,\, q_z\right]$ is known as the scattering vector, namely the bisector of the angle formed by the transmitter point on surface and receiver point on surface ranges. Assuming a Gaussian PDF for the sea surface slopes, it can be expressed as follows:

$$f_q\left[\frac{-\mathrm{q}_\perp(\vec{r},\,\theta_i)}{q_z(\vec{r},\,\theta_i)}\right] = \frac{1}{2\pi\sqrt{\sigma_x^2\sigma_y^2}}\exp\left[-\frac{s_x^2}{2\sigma_x^2} - \frac{s_y^2}{2\sigma_y^2}\right] \qquad \textbf{(9.3)}$$

where σ_x^2 and σ_y^2 are the mean square slopes along the *x* and *y* direction (for simplicity, here we are not accounting for any effect of the wave direction in the PDF). If we consider all the terms in Equation 9.2 to be approximately constant within the scattering area contributing to the observables and equal to the value at the SP, then the *x*- and *y*- component of the scattering vector are null, and Equation 9.2 becomes

$$\sigma_0(\vec{r},\,\theta_i) = \frac{\pi\left|\Re(\theta_i)\right|^2 q_z^4(\vec{r},\,\theta_i)}{2\pi\sqrt{\sigma_x^2\sigma_y^2}\,q_z^4(\vec{r},\,\theta_i)} = \frac{\left|\Re(\theta_i)\right|^2}{2\sqrt{\sigma_x^2\sigma_y^2}} \qquad \textbf{(9.4)}$$

In other words, the dependence on the incidence angle remains only contained in the Fresnel reflection coefficient (Equations 36–39 in Zavorotny & Voronovich [2000]), and thus it would be sufficient to correct for $\Re$ to eliminate such dependence. A plot of $\sigma_0(\vec{r})$ at the SP versus incidence angle is shown in Figure 9.14.

Unfortunately, compensating for the effect of $\Re$ is not sufficient to fully eliminate the dependence of $\sigma_0(\vec{r})$ on θ_i. This is shown in Figure 9.15, where a set of DDMAs from noise-free simulated DDMs has been generated for a number of different realistic CYGNSS geometries, corresponding to different incidence angles. Both Level 1B DDMA and Level 2A DDMA are illustrated in Figure 9.15 versus the incidence angle, where Level 2A DDMA have been obtained by simply dividing the Level 1B DDMA value by the squared module of $\Re$ for the specific incidence angle.

Figure 9.15 shows a dependence on incidence angle that remains after the modeled dependence on $\Re$ has been removed. This suggests that the assumption of all the terms in Equation 9.2 being constant and equal to their values at the SP is not accurate enough. We have therefore developed an empirical correction for the Level 1B DDMA, representing the trend shown in Figure 9.15 (bottom). We are also investigating an analytical or semianalytical model for this incidence angle dependence. Once each curve in Figure 9.15 (bottom) has been normalized by their approximate value at θ_i = 0°, the dependence of LIB DDMA on incidence angle is not found to be dependent on wind speed. We then fit a power curve in the form of $y(\theta) = a\theta^b + c$ to the normalized function by determining the coefficients *a*, *b*, and *c*. The normalized curves and the best-fit power curve are shown in Figure 9.16.

This function has then been used to model the dependence of the DDMA on the incidence angle. The same procedure has been applied to LES data, and the final coefficients for the power fit have been found

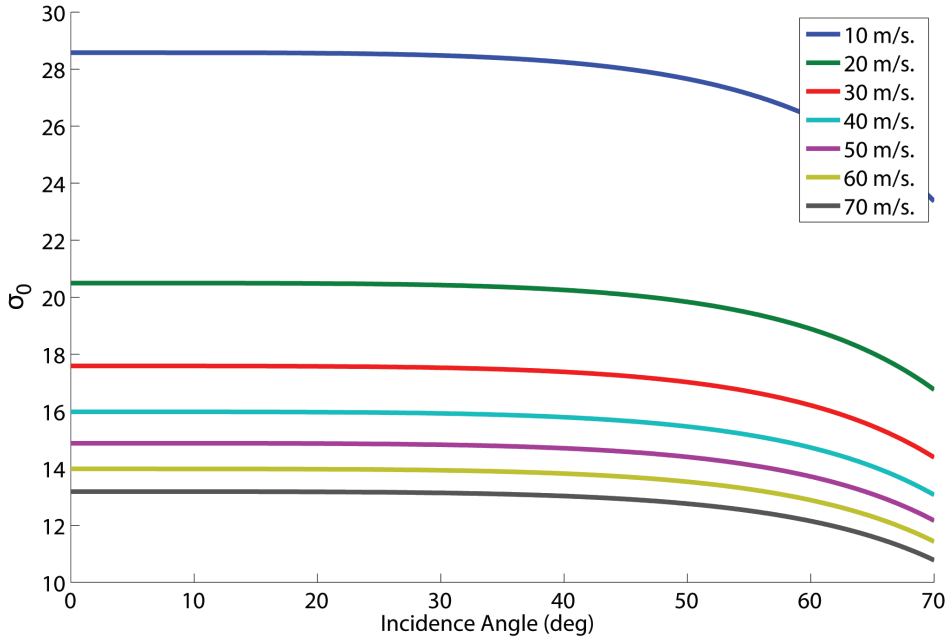

Figure 9.14. Curves of $\sigma_0\left(\vec{r}_{SP}\right)$ versus incidence angle, for different wind speed values.

to be the same as for the DDMA. The final expression to derive the Level 2A observables is therefore

$$OBS_{L2A} = \frac{OBS(\theta)_{L1B}}{y(\theta)} \qquad \textbf{(9.5)}$$

where OBS stands for the observable and $y(\theta)$ is the power fit shown in Figure 9.16. Figure 9.17 shows the Level 2A DDMA, where the Level 2A correction has been now implemented through the use of the power fit mentioned above and where the dependence on the incidence angle has been eliminated.

B. Derivation of GMF from All Samples

The GMF is computed in the form of a LUT of DDMA values corresponding to the 25 × 25 km spatially averaged wind values and must be a monotonic curve fitting the whole cloud of samples covering the expected range of wind speeds and smooth enough to allow accurate interpolation. A discrete LUT was used, rather than an empirical function of some assumed form. It was derived using a tapered approach to the bin widths, starting with very small bin widths for very low or very high winds, since those are the wind ranges with the smallest number of samples. Then the bin widths gradually increase towards medium winds (i.e., toward wind ranges with the highest number of samples). The LUT function is constructed by assigning a single wind speed to each wind bin, computed as an average with a triangle weighting of all the true winds falling within that bin (*y*-axis). The same type of weighted average is used to assign the corresponding DDMA values (*x*-axis). A smoothing filter is finally applied to the LUT, to make sure it is a monotonic function. The training data and LUT for both DDMA and LES samples are shown in Figure 9.18.

C. GMF Scaling Using Level 2A Correction

The dependence of the GMF on incidence angle is explicitly accounted for in the retrieval algorithm by adding a second dimension to the LUT indexed by incidence angle. We use the Level 2A correction to scale the GMF obtained at an incident angle of 0° to generate a different GMF for each incidence angle interval. We divide the total incidence angle range (from 0.1° to 80°) into 800 intervals of 0.1° each, and we derive a GMF for each interval by applying inversely the Level 2A correction as follows:

$$GMF(\theta) = GMF^{*} \cdot y(\theta) \qquad \textbf{(9.6)}$$

where GMF^{*} is the total GMF described in Subsection B and $y(\theta)$ is the Level 2A correction. The $GMF(\theta)$ resulting from Equation 9.6 is shown for six incidence

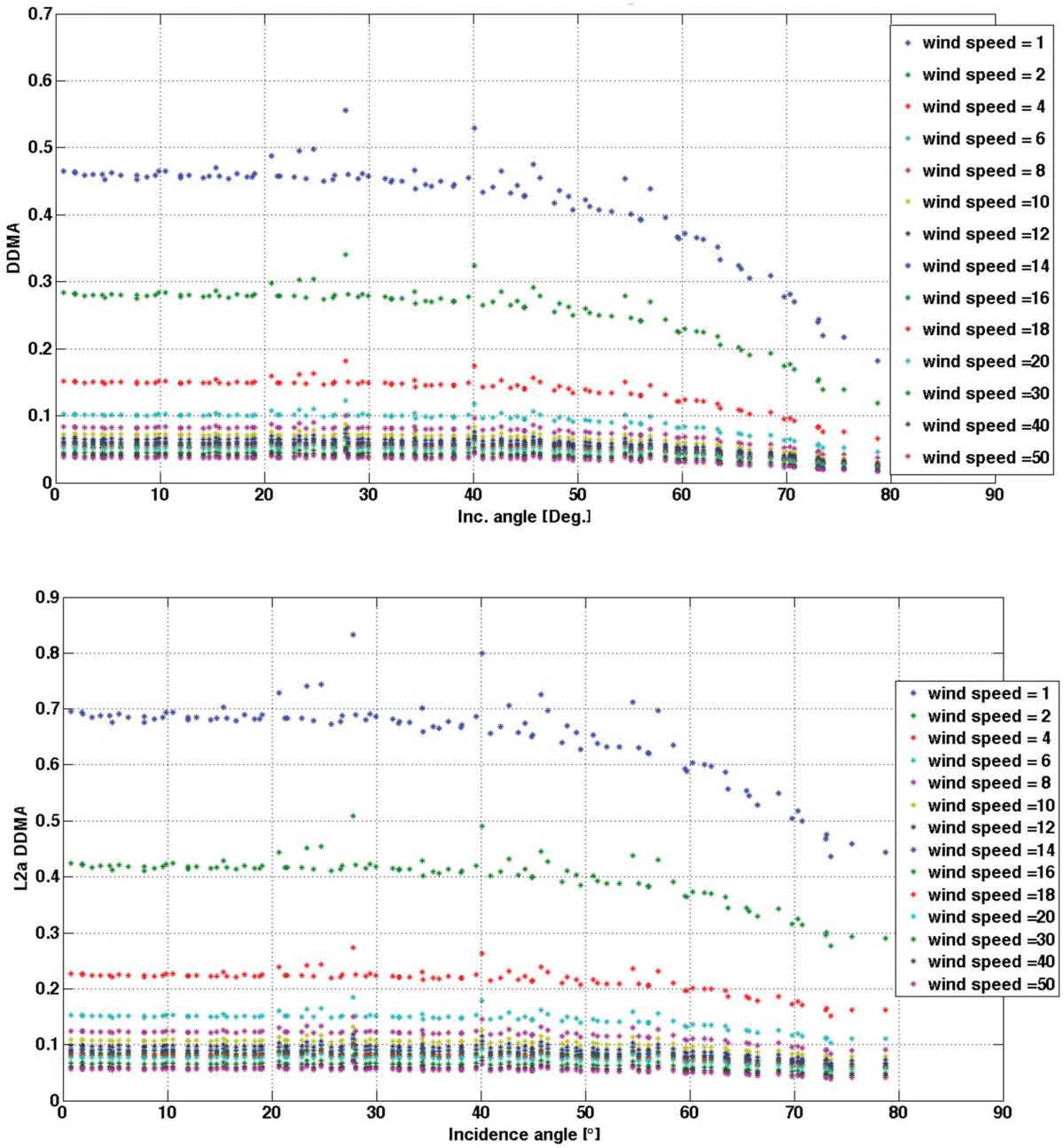

Figure 9.15. Plot of noise-free Level 1B (top) and Level 2A (bottom) DDMA, versus incidence angle, obtained from noise-free DDMs simulated using the E2ES. The different colors refer to different wind speeds. In this case, the Level 2A correction has been implemented by simply compensating for the effect of the Fresnel reflection coefficient (i.e., by considering the curves in Figure 9.14). *Reused from Clarizia & Ruf (2016), © 2016 IEEE.*

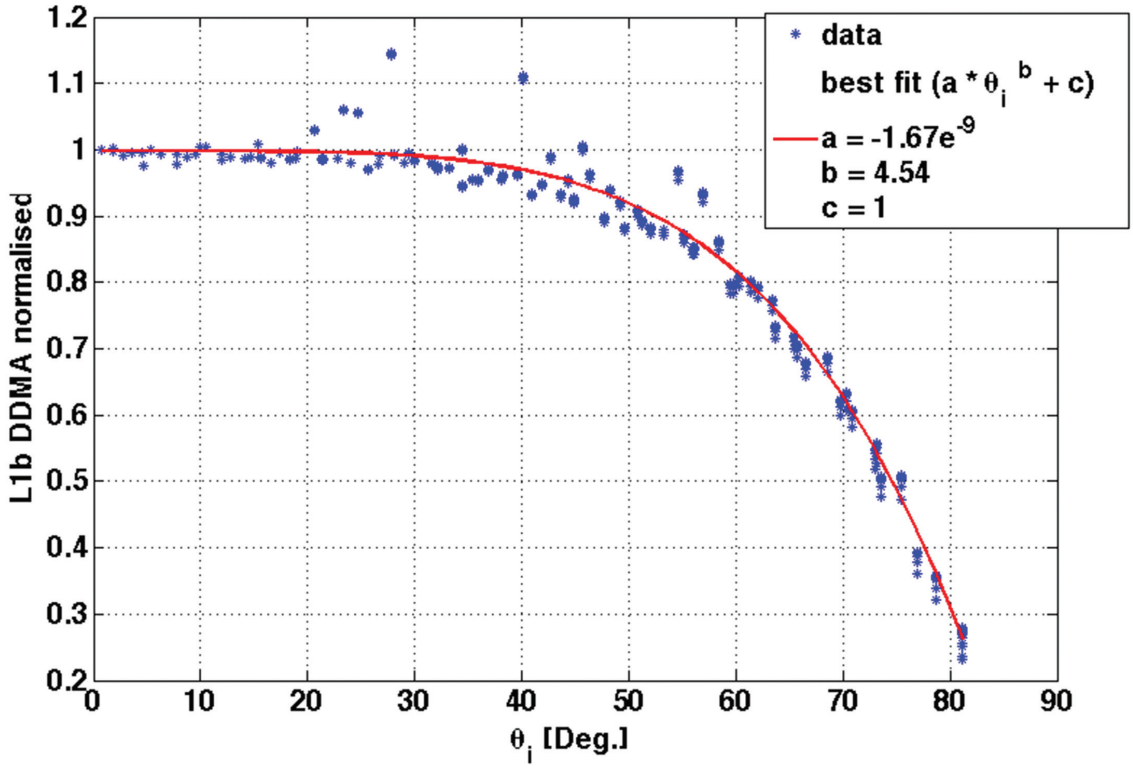

Figure 9.16. Normalized DDMA versus incidence angle curves, with superimposed best-fit power function (dashed black line). *Reused from Clarizia & Ruf (2016), © 2016 IEEE.*

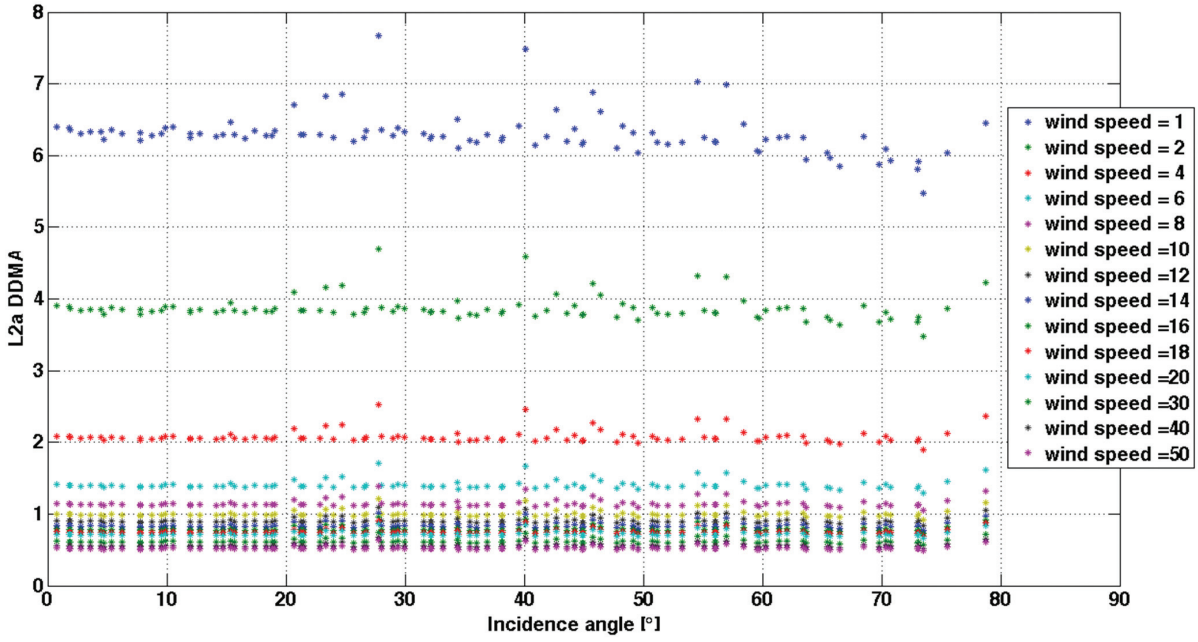

Figure 9.17. Noise-free Level 2A DDMA, versus incidence angle, obtained from noise-free DDMs simulated using the E2ES. The different colors refer to different wind speeds. The Level 2A correction has been developed empirically using the curves in Figure 9.15 and Figure 9.16. *Reused from Clarizia & Ruf (2016), © 2016 IEEE.*

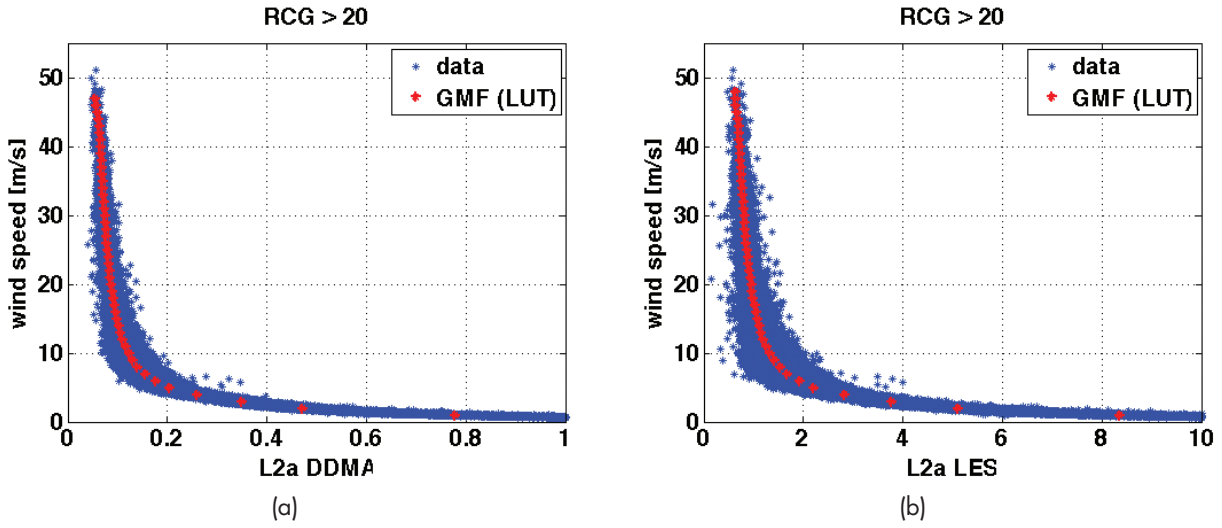

Figure 9.18. Simulated ground truth wind speeds versus Level 2A DDMA (a) and Level 2A LES (b) training data, shown as blue points and selected with RCG > 20. The LUT derived from the data is shown as red points. *Reused from Clarizia & Ruf (2016), © 2016 IEEE.*

angle intervals together with the samples belonging to that interval in Figure 9.19. The six incidence angle intervals span the range of 0° to 55°, since this is the range satisfying constraints from the EFOV filter (explained later). The agreement between samples (blue) and GMFs (red) is good in all cases, expect for the last range of incidence angles (bottom right of Figure 9.19). This is only due to the fact that the strongest changes in the sample distribution with respect to incidence angle occur at the highest incidence angle values, hence at these incidence angles, a GMF obtained from only the central 0.1° incidence angle interval is no longer well representative of all the samples within a 5° incidence angle interval. Note however that the wind retrieval process bins the samples into 800 different intervals (not just 6) and makes use of all the 800 GMFs.

D. Wind Estimation Using the LUT Function

The winds are now estimated using the performance evaluation dataset, namely the subset of data from the 13-day NR with even minutes in their time stamp. For each point of the performance evaluation dataset (either DDMA or LES), a wind speed is estimated using the LUT function for the incidence angle of the sample point. The estimation is done through interpolation, when the observable value falls within the range of values spanned by the LUT, and through extrapolation outside of such range. The interpolation algorithm is given by (referring to DDMA):

$$\hat{U} = U_k + \alpha(DDMA - DDMA_k)$$
$$\alpha = (U_{k+1} - U_k) / (DDMA_{k+1} - DDMA_k) \quad \textbf{(9.7)}$$

where DDMA is the measurement, $\hat{U}$ is the wind estimated from DDMA, the pair of values $(U_k, DDMA_k)$ are the y and x coordinates of the LUT point whose DDMA value (x coordinate) is immediately below the measurement, and the pair of values $(U_{k+1}, DDMA_{k+1})$ are the y and x coordinates of the LUT whose DDMA value is immediately above the measurement.

The mathematical expression for estimating the wind through extrapolation is given by

$$\hat{U} = U_k + \alpha_{ext}(DDMA - DDMA_k) \quad \textbf{(9.8)}$$

where $\hat{U}$ is the wind value estimated through extrapolation and α_{ext} is the slope estimated though linear fitting of the first or last two points in the LUT, depending on which edge the sample lies.

E. Debiasing of Wind Retrievals

At this point, we have for each observable a true wind and an estimated wind obtained following the method described in the previous paragraph. One extra task to be accomplished is to check and remove any potential biases in the estimated winds. This is

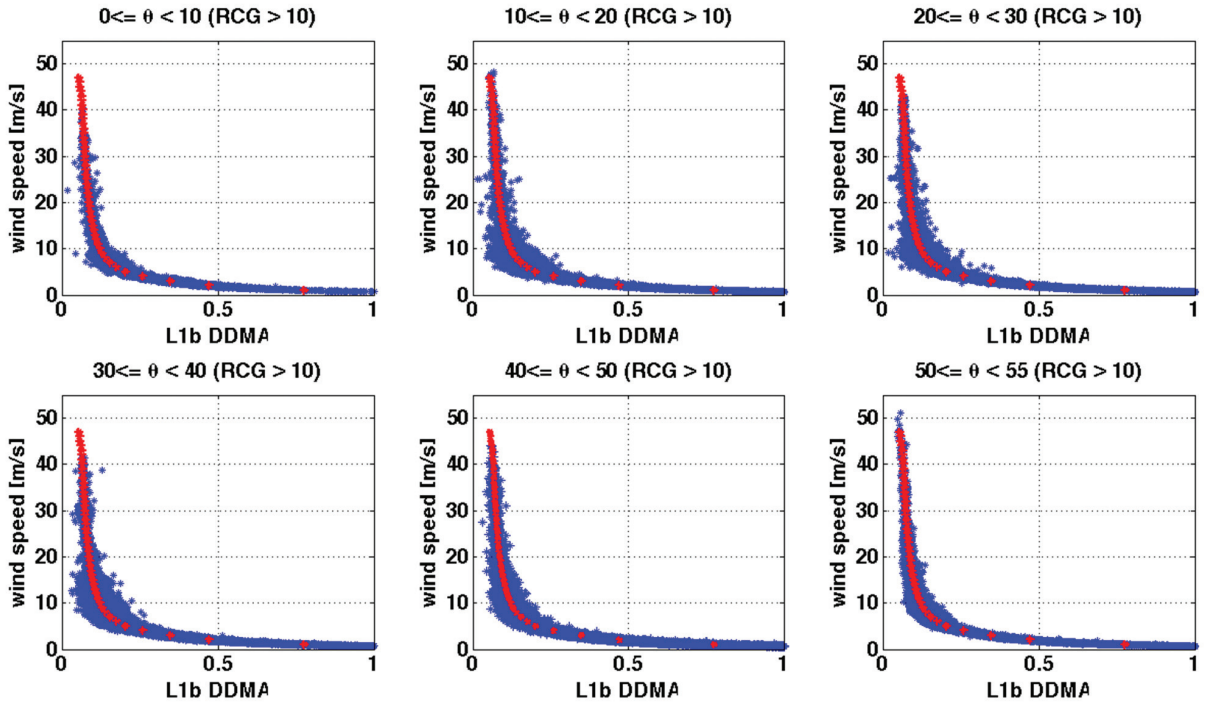

Figure 9.19. Scatter plot of DDMA samples versus wind speed (blue), for six different incidence angle intervals (left to right, top to bottom): (0°–10°), (10°–20°), (20°–30°), (30°–40°), (40°–50°), and (50°–55°). The red stars show the GMF corresponding to the 0.1° incidence angle interval at the center of the interval considered (e.g., the GMF for the [4.95°–5.05°] interval is shown for the samples belonging to the [0°–10°] interval and so on). *Reused from Clarizia & Ruf (2016), © 2016 IEEE.*

done by rebinning again the true winds with a given bin width (in our case, we have chosen the bin width to be 3 m s^{-1}) and for each bin calculating the bias as follows:

$$bias\left(U_{10(c)}^{i}\right) = \frac{1}{N_k^i}\sum_{k=1}^{N_k^i}\left[\hat{u}^k - u^k\right] \tag{9.9}$$

where the hat indicates the estimated quantity (as opposed to the true quantity), $\hat{U}_{10(c)}^{i}$ represents the center of the ith wind speed bin, and k is the index of all the samples falling within the ith bin (from 1 to N_k^i). Once the bias is calculated for each bin, it is then removed (i.e., subtracted) from all the wind estimates that fall within that bin. The bias between estimations and simulated ground truth turned out to be quite small, so debiasing is a useful operation but not crucial.

F. Wind Speed MV Estimator

The wind speed estimates from DDMA and LES can be combined together to produce an MV estimator. A MV estimator exploits the degree of decorrelation between the errors in the individual estimates to minimize the RMS error in its wind speed estimate. The advantage of such an estimator lies in the fact that its RMS error will always be better than or equal to the lowest RMS error in the retrieved wind speeds among the individual observables. The lower the correlation between errors in pairs of individual estimators, the better the RMS error performance of the MV estimator. The MV estimator is built as a linear combination of the original estimators, as shown in Clarizia et al. (2014):

$$u_{MV} = \mathbf{m}\cdot\mathbf{u} \tag{9.10}$$

where $\mathbf{u}$ is the vector of individual estimates and $\mathbf{m}$ is the vector of coefficients. The coefficients are obtained by requiring that the MV estimator be unbiased (i.e., the expected value of its retrieval is equal to the true quantity to be estimated) and by minimizing its variance. The derivation of the coefficients for the estimator is explained in Clarizia et al. (2014). The coefficients are given by

$$\mathbf{m} = \left(\sum_{i=1}^{N}\sum_{j=1}^{N} c_{i,j}^{-1}\right)\mathbf{C}^{-1}\mathbf{1} \tag{9.11}$$

where $\mathbf{1}$ is a vector of ones, $\mathbf{C}^{-1}$ is the inverse of the covariance matrix between the individual retrieval errors, and $c_{i,j}^{-1}$ are its elements. The variance of the MV estimator is given by

$$\sigma_{MV}^2 = \left(\sum_{i=1}^{N}\sum_{j=1}^{N} c_{i,j}^{-1}\right)^{-1} \tag{9.12}$$

The MV estimator requires knowledge of the covariance matrix of the individual retrieval errors. The covariance is estimated empirically from the retrieval errors and can be factored into two component matrices as

$$\mathbf{C} = \mathbf{SRS} \tag{9.13}$$

where $\mathbf{S}$ is a diagonal matrix of standard deviations of the retrieval errors for each observable (i.e., the square root of the diagonal elements of the covariance matrix) and $\mathbf{R}$ is the matrix of correlation coefficients, whose elements are always between −1 and 1. The covariance matrix could be estimated from all the retrieval errors; however, a further improvement in the final performances is obtained when a different covariance matrix is estimated for different ranges of RCG. This happens because the correlation between retrievals from the two observables decreases for noisier data characterized by lower RCG and consequently lower SNR. This will then allow the MV estimator to contribute more to the performance improvement right for those data where the performances are worse due to a lower RCG; so in a sense, the MV approach will help where it is needed most.

Table 9.1 shows the covariance and correlation coefficient matrices for five different RCG intervals. It can be noticed that the correlation coefficients between DDMA and LES retrievals are the lowest for the lowest RCG range, and as expected, they gradually increase as the RCG increases.

A scatter plot of true versus estimated MV winds for RCG > 10 is shown in Figure 9.20. The MV estimated winds match quite well the true ones.

G. Performance Figure of Merit

The performances of the MV estimator are compared to the DDMA and LES alone in a more quantitative way, in the form of wind speed RMS error curves as a function of the wind speed bin. The RMS for the *i*th wind speed bin is calculated as

$$RMS\left(U_{10(c)}^{\ i}\right) = \sqrt{\frac{1}{N_k^i}\sum_{k=1}^{N_k^i}\left[\hat{u}_{(ub)}^k - u^k\right]^2} \tag{9.14}$$

where $\hat{u}_{(ub)}^k$ is the estimated unbiased wind speed. RMS error curves have been calculated over a wind speed range of 1 m s^{-1} to 48 m s^{-1}, considering a bin width of ± 10 m s^{-1}, and with a 1 m s^{-1} bin step. A plot of the RMS error values versus the central wind value of the wind speed bin is shown for the three cases in Figure 9.21. Here only the retrievals from samples with RCG > 10 have been retained

Table 9.1. Covariance matrices (C) and correlation coefficient matrices (R) between winds retrieved from DDMA and from LES for four different RCG intervals.

$C_1 = \begin{bmatrix} 108.1522 & 17.2250 \\ 17.2250 & 207.8095 \end{bmatrix}$	$R_1 = \begin{bmatrix} 1.0000 & 0.1149 \\ 0.1149 & 1.0000 \end{bmatrix}$	3*10^–27 <= RCG < 5*10^–27
$C_1 = \begin{bmatrix} 37.5061 & 6.9362 \\ 6.9362 & 95.0033 \end{bmatrix}$	$R_1 = \begin{bmatrix} 1.0000 & 0.1162 \\ 0.1162 & 1.0000 \end{bmatrix}$	5*10^–27 <= RCG < 10*10^–27
$C_1 = \begin{bmatrix} 5.9796 & 1.1326 \\ 1.1326 & 15.7289 \end{bmatrix}$	$R_1 = \begin{bmatrix} 1.0000 & 0.1168 \\ 0.1168 & 1.0000 \end{bmatrix}$	10*10^–27 <= RCG < 20*10^–27
$C_1 = \begin{bmatrix} 0.7807 & 0.3144 \\ 0.3144 & 1.4212 \end{bmatrix}$	$R_1 = \begin{bmatrix} 1.0000 & 0.2985 \\ 0.2985 & 1.0000 \end{bmatrix}$	RCG >= 20*10^–27

for the RMS error calculation. For convenience, the CYGNSS baseline 2 m s^{-1} / 10% requirement is also shown as a magenta dashed line. The significant improvement in the retrieval algorithm performances due to the MV estimator is clearly visible.

H. Time Averaging

An extra processing step that contributes to improving the performances by reducing the RMS error is to apply time averaging to the collected data. Looking again at Figure 9.10, it can be seen that for a range of incidence angles, the IFOV of the collected samples is below the spatial resolution requirement of 25 km. For all these cases, it is possible to average a number of consecutive samples in time to achieve the spatial resolution limit of 25 km. The maximum number of samples that can be averaged can be easily calculated using some simplifications. Since the SP is moving on the surface at about 6 km s^{-1}, an EFOV can be defined for each sample as follows:

$$EFOV = \sqrt{\sqrt{IFOV}\cdot\left[\sqrt{IFOV}+(n-1)\cdot l\right]} \qquad l \approx 6\ km \quad \textbf{(9.15)}$$

where IFOV is the instantaneous FOV of the sample, l indicates the SP displacement on the surface per second (6 km), and n is the total number of samples to average. Imposing an EFOV equal to 25 km and solving for n, we obtain:

$$n = \frac{EFOV^2}{6\sqrt{IFOV}} - \frac{\sqrt{IFOV}}{6} + 1 \quad \textbf{(9.16)}$$

A plot of the values of n versus incidence angles for two different delay ranges, and using an EFOV limit of 25 km, is shown in Figure 9.22. The value n

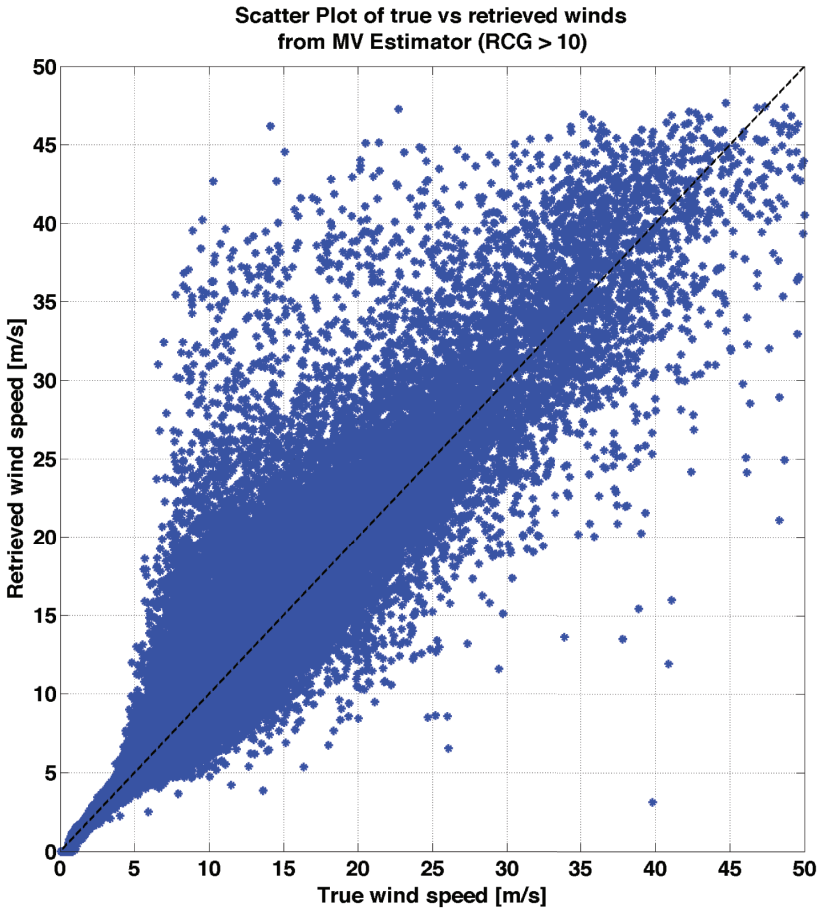

Figure 9.20. Scatter plot of retrieved wind speeds using the MV estimator versus simulated ground truth wind speeds, for those samples with RCG > 10. These have been computed from the performance evaluation dataset. *Adapted from Clarizia & Ruf (2016), © 2016 IEEE.*

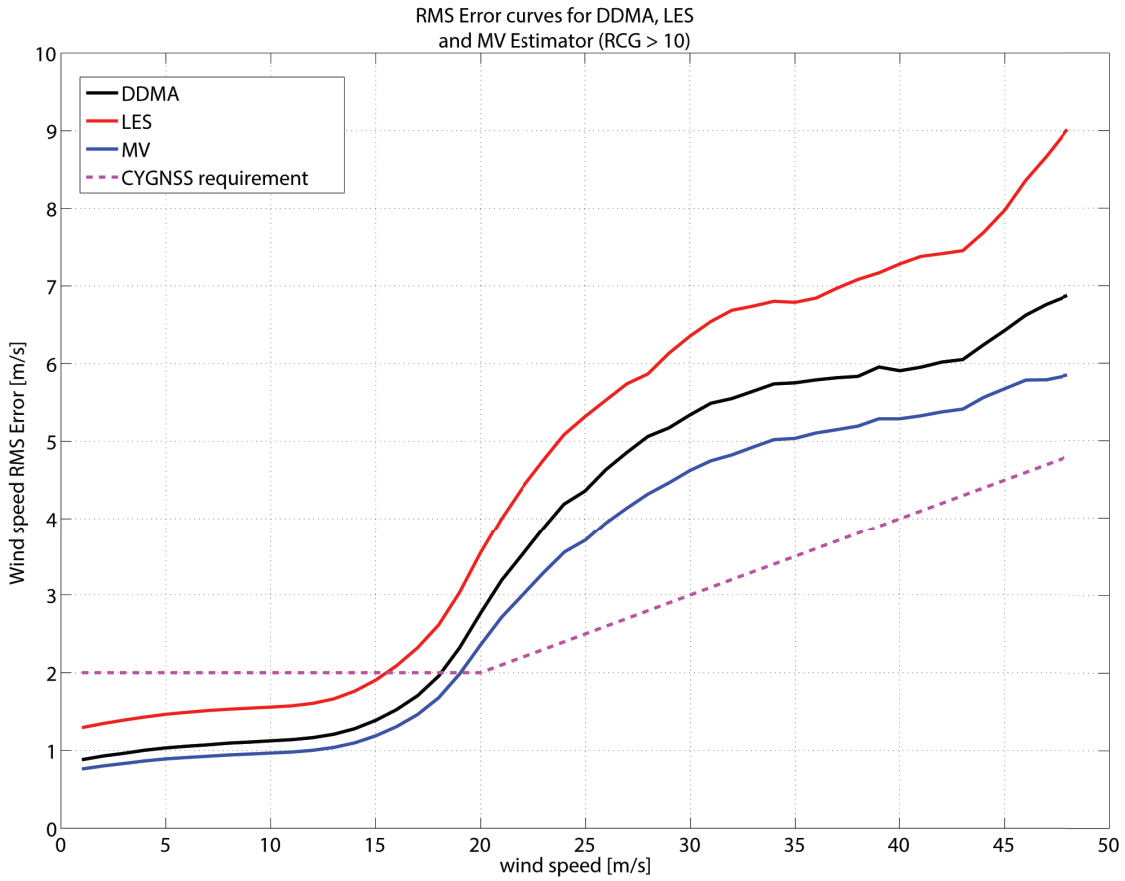

Figure 9.21. RMS error between true and retrieved wind speed, as a function of the true wind speed, for retrievals from DDMA, LES, and MV estimator. The CYGNSS baseline 10% requirement is also shown for comparison. *Adapted from Clarizia & Ruf (2016), © 2016 IEEE.*

has been rounded to the lowest integer value in order to make sure that the 25 km requirement is never violated.

This function can be then used to know, for each incidence angle, the number of samples that can be averaged if a 25 km requirement on the spatial resolution must be met. Of course, the calculation of n uses simplified assumptions and does not take into account several aspects, like the real trajectory of the SP on the surface or the real shape of the IFOV, which is ideally assumed to be a square in Equation 9.16 but depends instead on the configuration of the iso-delay and iso-Doppler lines at the ranges selected for the computation of the observables. However, these simplifications are valid enough to allow a reliable estimation of the number of samples to be averaged together. Figure 9.10 also highlights that in principle two different approaches to time averaging are possible:

1. Average of the values of the observables
2. Average of the retrieved winds

Furthermore, it is possible to choose one of the following:

a. Use of shorter delay ranges (noisier observables) with a longer time averaging
b. Use of longer delay ranges (less noisy observables) with a shorter time averaging

Each of the four combinations has been tested, and the best performances have been obtained using (1) and using (a). The choice of (1) rather than (2) can be explained by the change in slope of the LUTs shown in Figure 9.18. The slope of the LUTs changes more quickly as the wind increases, and therefore at high winds, a small error in the observable would translate into a big error in the retrievals. Hence

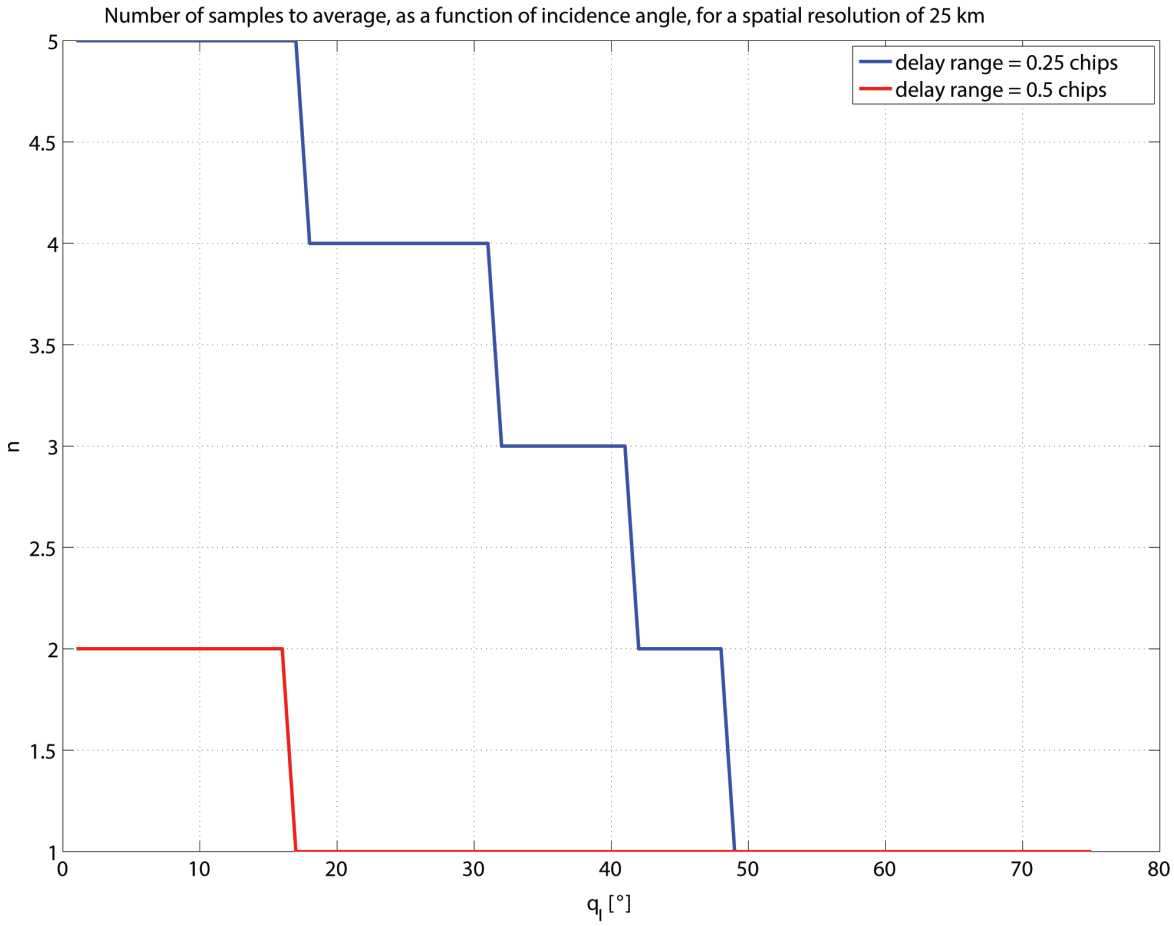

Figure 9.22. Number of samples to average, as a function of the incidence angle θ_i, for two different delay ranges. The blue curve, corresponding to a delay range of (0 0.25) chips, is the one of interest. *Reused from Clarizia & Ruf (2016), © 2016 IEEE.*

averaging the observables helps reduce the noise in the observable itself and translates into more accurate wind estimates.

The choice of (a) instead of (b) simply indicates that increasing the time averaging mitigates the noise in the observables more than computing the observables over a wider delay window. Some graphical examples of time averaging are illustrated in Figure 9.23, where the different SP tracks for a single CYGNSS observatory are shown as blue crosses, the sample considered for time averaging is shown in red, and the consecutive samples to be averaged together with the red one are highlighted with black circles.

The scatter plot of true versus retrieved winds using the MV estimator, before and after time averaging of the observables, is shown in Figure 9.24. Note that the LUTs used to retrieve winds from time averaged DDMA and LES observables have not been recomputed and are the same as those shown in Figure 9.18. A plot of the RMS error before and after time averaging is shown in Figure 9.25, which highlights the further improvement in the algorithm performances when time averaging is used.

I. IFOV Filter

A final processing step needed in the retrieval algorithm is to filter out all those retrievals whose IFOV or EFOV does not meet the requirements on spatial resolution. The 25 km spatial resolution requirement, shown as a dashed magenta line in Figure 9.10, highlights that all the samples acquired with an incidence angle greater than ~54.5° do not fulfill the requirement, since their EFOV (or IFOV) is higher than 25 km and therefore needs to be discarded. This last

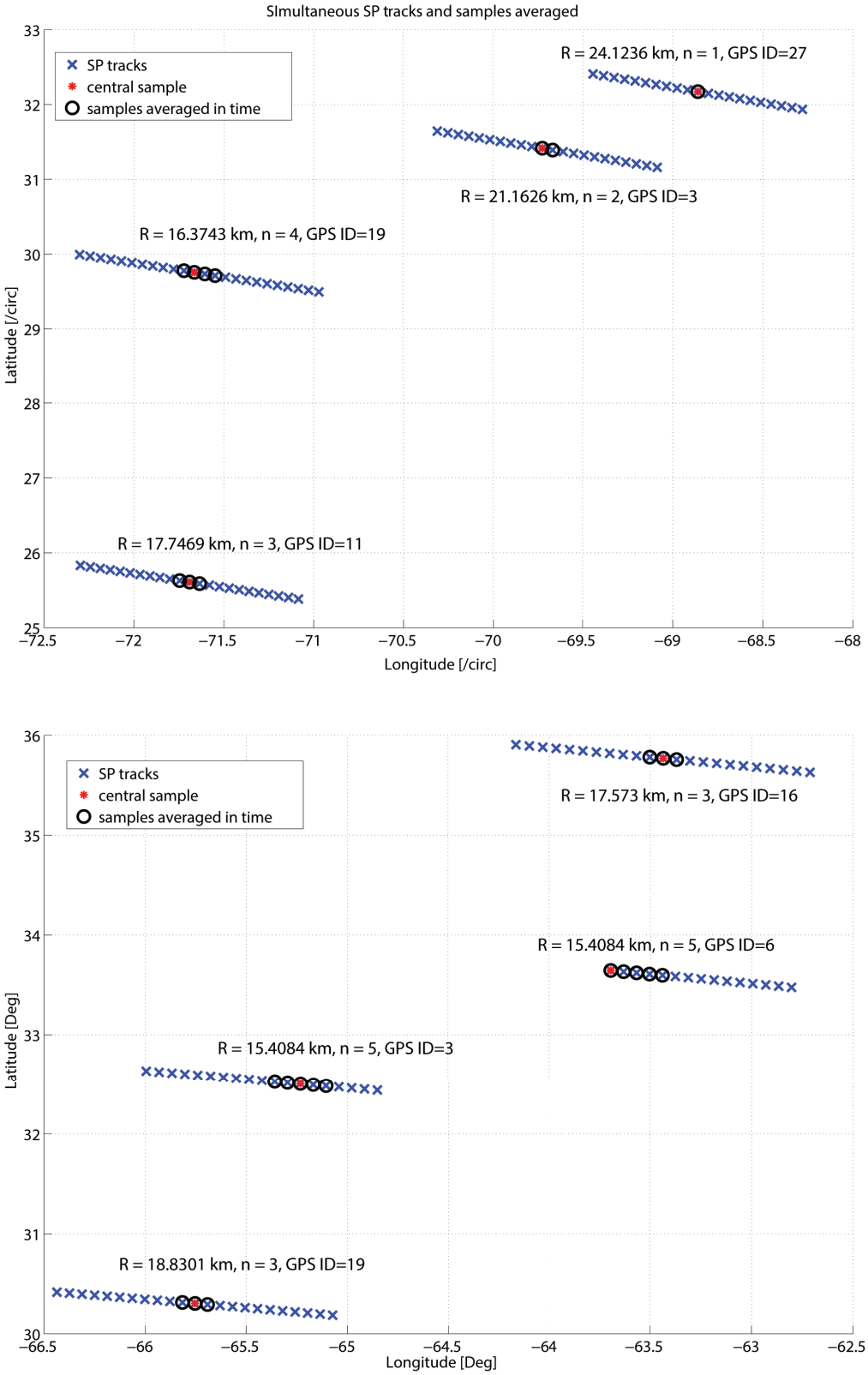

Figure 9.23. Two graphical illustrations of how the time averaging algorithm works for four simultaneous SP tracks acquired by a single CYGNSS observatory. *Reused from Clarizia & Ruf (2016), © 2016 IEEE.*

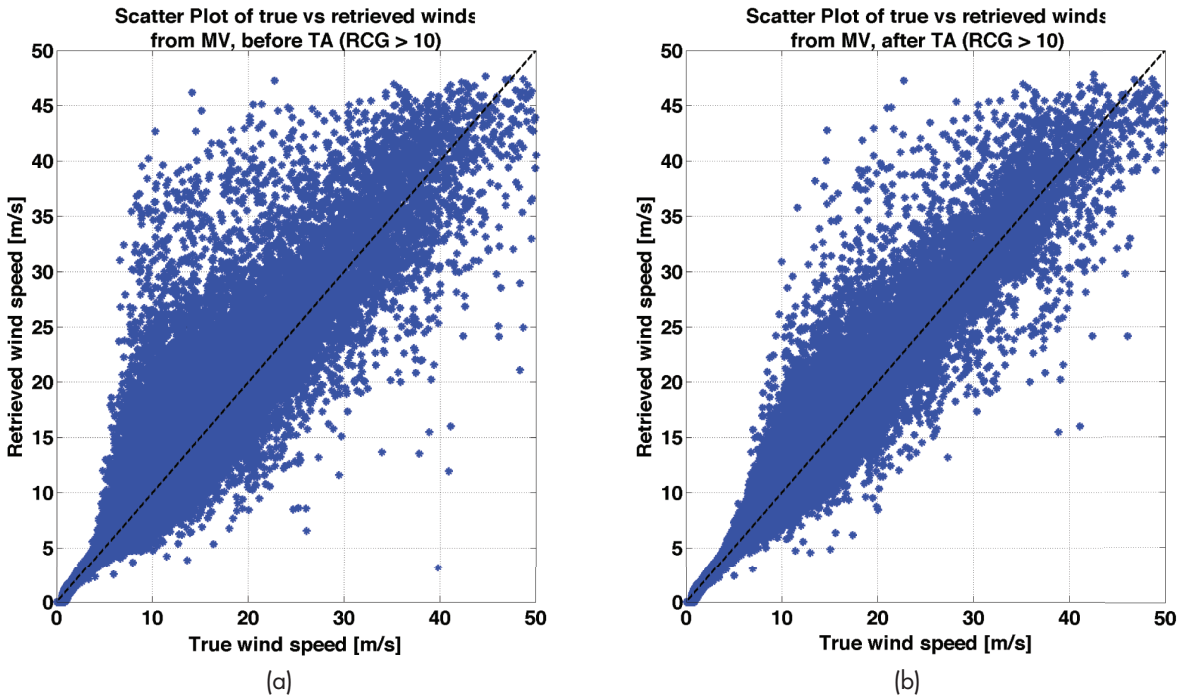

Figure 9.24. Scatter plot of MV true versus retrieved winds before (a) and after (b) time averaging (TA), for samples with RCG > 10. *Adapted from Clarizia & Ruf (2016), © 2016 IEEE.*

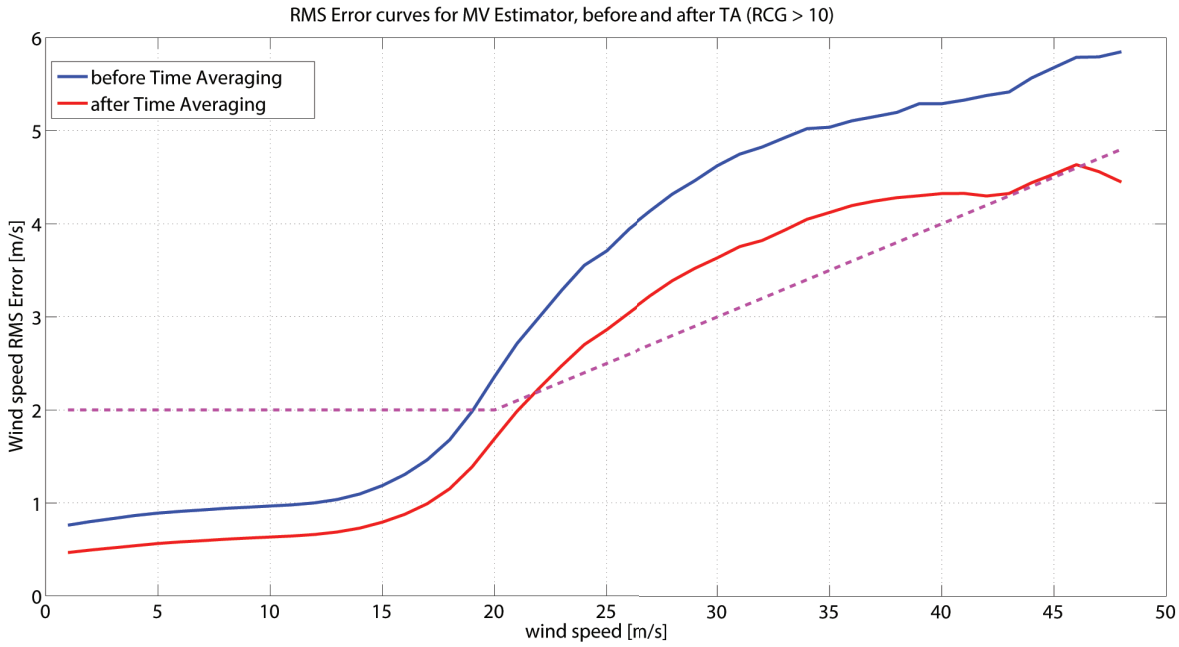

Figure 9.25. RMS error curves before and after time averaging (TA), for RCG > 10.

filter applied to the retrievals also contributes to improving the final RMS error, as shown in Figure 9.26. The improvement is particularly strong when a low RCG threshold is used, suggesting that samples with high incidence angles also tend to have a low RCG, and discarding them improves the quality of the final set of observables and hence of the retrievals. However, filtering out these samples implies a reduction in the final coverage. The reduction in the total number of samples from the full 13-day NR expressed as percentage is shown with respect to different RCG thresholds in Table 9.2.

IV. Quality Control Flags in the Retrieval Algorithm

Each Level 2 wind speed estimate is derived from one or more Level 1B DDMs. The number of DDMs can be greater than 1 due to the time integration used to generate a Level 2 product with a 25 km resolution. The number of DDMs can vary because the mapping from delay and Doppler intervals to spatial extent varies depending on measurement geometry.

The quality flags associated with each of the DDMs used to create a particular Level 2 wind speed estimate are used in two ways by this Level 2 algorithm. The "Overall DDM Quality Is Good" flag is defined in the Level 1B ATBD (Gleason, 2014) as

- Overall DDM quality is good. (This flag is the OR of several other quality flags. TBD: detailed description, 0 = Overall quality is not good, 1 = Overall quality is good)

This flag is used to select which DDMs are used by the Level 2 algorithm. If the flag is set to 0 (not good), then the DDM is not used. In case all DDMs that would have been used are flagged as not good, no Level 2 wind speed data product is output.

There are a number of other relevant quality flags associated with each DDM (Gleason, 2014). They are listed in Table 9.3.

Each of these quality flags is tracked in the Level 2 algorithm, and rolled-up versions are included as Level 2 quality flags. The rolled-up version counts how many of the DDMs used by a particular Level 2 wind speed estimate have one of these flags set. Specifically, the Level 2 quality flags are defined in Table 9.4.

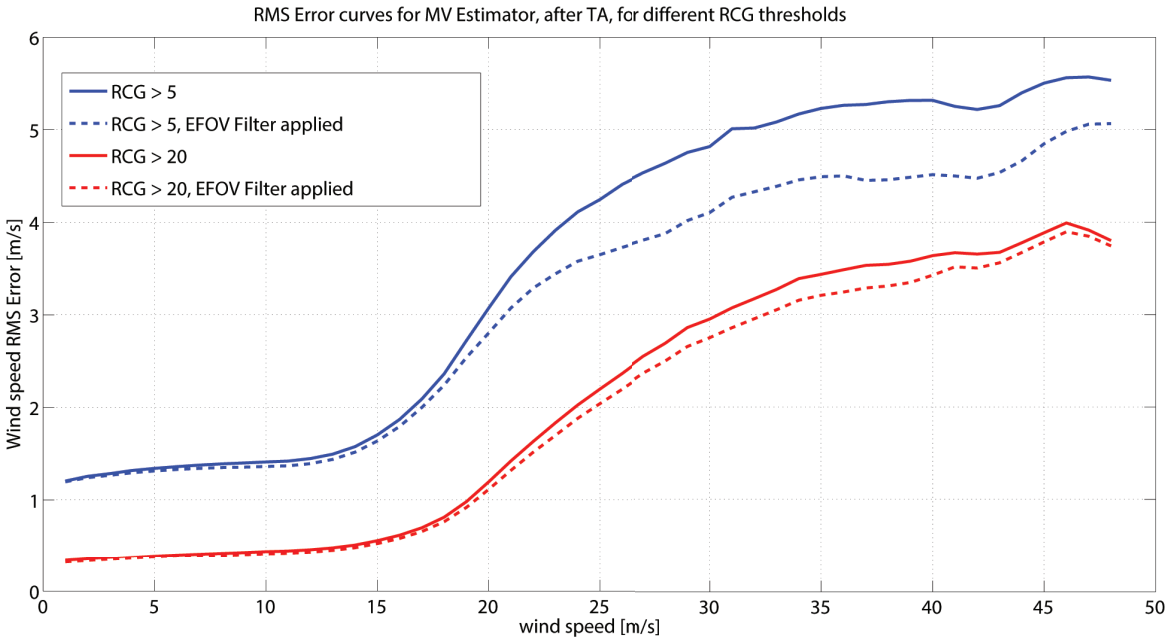

Figure 9.26. RMS error curves after time averaging (TA), with (dashed line) and without (continuous line) EFOV filter, for two different RCG thresholds. *Adapted from Clarizia & Ruf (2016), © 2016 IEEE.*

In addition to the rolled-up version of Level 1B quality flags, quality flags are also produced based on the Level 2 wind speed estimate itself. There are two classes of these flags: nonfatal and fatal. Nonfatal flags indicate wind speed values that may be nonphysical but are explainable as caused by outlier realizations of the noise processes that are inherent in the GNSS-R measurement process. The Level 2 data are flagged in this case but are retained and output in order to prevent statistical biasing of the wind speed distributions generated. Fatal errors are caused by extremely nonphysical wind speed values that could not be simply explained by expected measurement noise processes. These values are not output as Level 2 wind speed data products.

The nonfatal Level 2 quality flags are defined in Table 9.5. The fatal Level 2 quality flags are defined in Table 9.6. If either fatal Level 2 quality flag is set, the wind speed value should not be output as a Level 2 data product for use by subsequent (e.g., Level 3 and 4) algorithms.

V. Results and Performances for 25 km Spatial Resolution

Here we present an overview of the algorithm performances when the CYGNSS baseline 25 km spatial resolution requirement is considered.

Wind speed RMS error curves as a function of the true wind speed, for different RCG thresholds, are shown in Figure 9.27, along with the baseline requirement on the RMS error. The different RCG thresholds are used to determine spatial coverage statistics. From Figure 9.27, we can conclude that while

Table 9.2. Reduction in the number of samples when EFOV filter is applied, for different cases of different RCG thresholds. *Adapted from Clarizia & Ruf (2016), © 2016 IEEE.*

RCG threshold	*Number of samples*	*Number of samples with* $\theta_i > 54.5°$	*% reduction on number of samples*
RCG > 3	2,029,070	397,193	29.6%
RCG > 5	1,830,639	297,216	16.2%
RCG > 10	1,418,675	175,384	12.4%
RCG > 20	1,201,712	73,135	6.1%

Table 9.3. Quality flags associated with each DDM.

Flag	*Flag values*
Large spacecraft attitude error	0 = false, 1 = true
Negative signal power in Level 2 DDMA area	Level 1A calibration resulted in at least one bin in the Level 2 DDMA having a negative power value
Negative Sigma0 in Level 2 DDMA area	Level 1A calibration resulted in at least one bin in the Level 2 DDMA having a negative power value
Low confidence in DDM noise floor estimate	0 = false, 1 = true
Low confidence in open ocean noise floor estimate	0 = false, 1 = true
Low confidence in open ocean noise temperature estimate	0 = false, 1 = true
Land present in DDM	0 = false, 1 = true
SP over open ocean	0 = false, 1 = true
Large step change in DDM noise floor	0 = false, 1 = true
Large step change in LNA temperature	0 = false, 1 = true
Direct signal in DDM	0 = false, 1 = true
Low Rx antenna range corrected gain	0 = false, 1 = true
High SP incidence angle	0 = false, 1 = true
High cross correlation power present	0 = false, 1 = true
Low confidence in GPS EIRP estimate	0 = false, 1 = true

requirements are reasonably met in all cases for low wind speeds (i.e., lower than ~15 m s^{-1}), an RCG higher than 10 is the minimum one that meets the requirements at wind speeds higher than ~15 m s^{-1}.

A slightly different way to look at the RMS error is presented in Figure 9.28, where the curves represent the relative RMS error (i.e., the RMS error divided by the true wind speed at the center of each bin).

The RMS error performances are also shown with respect to different RCG intervals, in Figure 9.29. The different RCG intervals are of interest since they have been used to fine-tune the retrieval covariance, which is ultimately used for assimilating CYGNSS data into the forecast models. In this case, the RMS error is much worse for the first three cases, since each interval no longer contains clean samples with

Table 9.4. Level 2 quality flags. N = # of DDMs used for which the flag was set to 1 = true, unless noted otherwise.

Flag	*Flag values*
Large spacecraft attitude error	*N*
Negative signal power In Level 2 DDMA area	*N* = # of DDMs used for which the Level 1A calibration resulted in at least one bin in the Level 2 DDMA having a negative power value
Negative Sigma0 in Level 2 DDMA area	*N* = # of DDMs used for which the Level 1A calibration resulted in at least one bin in the Level 2 DDMA having a negative power value
Low confidence in DDM noise floor estimate	*N*
Low confidence in open ocean noise floor estimate	*N*
Low confidence in open ocean noise temperature estimate	*N*
Land present in DDM	*N*
SP over open ocean	*N*
Large step change in DDM noise floor	*N*
Large step change in LNA temperature	*N*
Direct signal in DDM	*N*
Low Rx antenna range corrected gain	*N*
High SP incidence angle	*N*
High cross correlation power present	*N*
Low confidence in GPS EIRP estimate	*N*

Table 9.5. Nonfatal Level 2 quality flags.

Flag	*Flag values*
Nonfatal negative wind speed quality flag	0 = wind speed is nonnegative; 1 = wind speed is negative and greater than or equal to –5 m s^{-1}
Nonfatal high wind speed quality flag	0 = wind speed is less than or equal to 70 m s^{-1}; 1 = wind speed is greater than 70 m s^{-1} and less than 100 m s^{-1}

Table 9.6. Fatal Level 2 quality flags.

Flag	*Flag values*
Fatal negative wind speed quality flag	0 = wind speed is nonnegative; 1 = wind speed is negative and less than –5 m/s
Fatal high wind speed quality flag	0 = wind speed is less than 100 m/s; 1 = wind speed is greater than or equal to 100 m/s

high RCG values (as in the case of RCG thresholds), which were highly contributing to the performance improvement. The last case (RCG > 20), shown as a green line, is identical to that shown in Figure 9.27.

Table 9.7 and Table 9.8 illustrate the absolute average RMS error for all cases with true wind speeds lower than 20 m s^{-1} and respectively for different RCG thresholds and different RCG intervals. In Table 9.7, we notice that the requirements of an RMS error below 2 m s^{-1} is well satisfied for a RCG threshold as low as five, whereas in Table 9.8, requirements are only satisfied when 10 < RCG < 20.

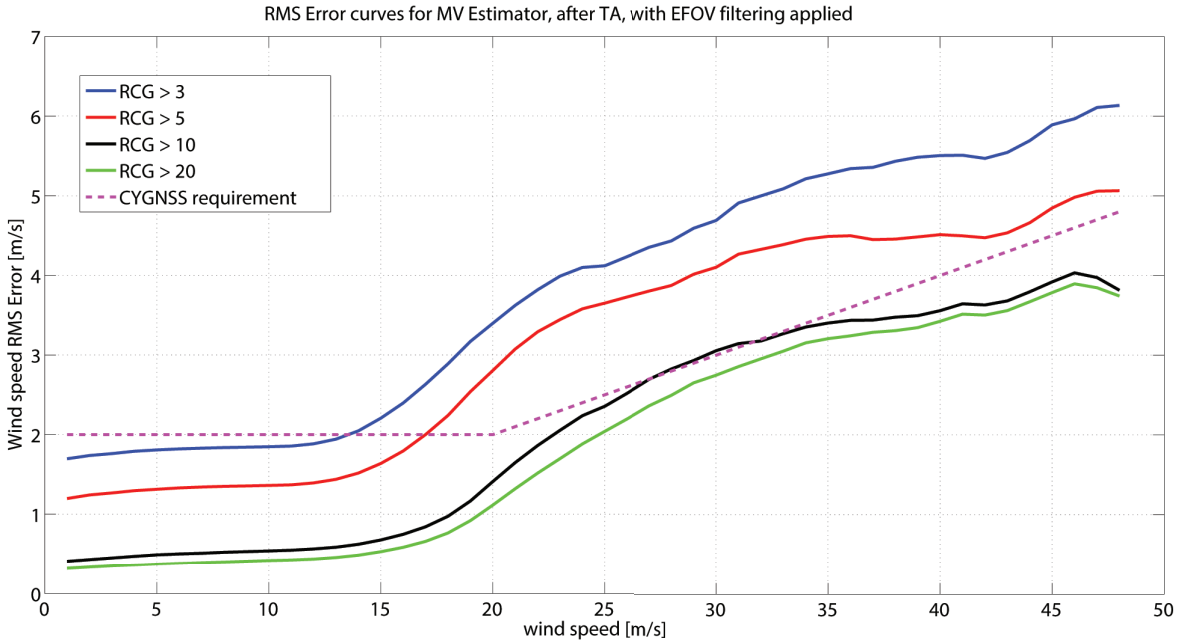

Figure 9.27. Final RMS error curves versus true wind speed for four different RCG thresholds. *Adapted from Clarizia & Ruf (2016), © 2016 IEEE.*

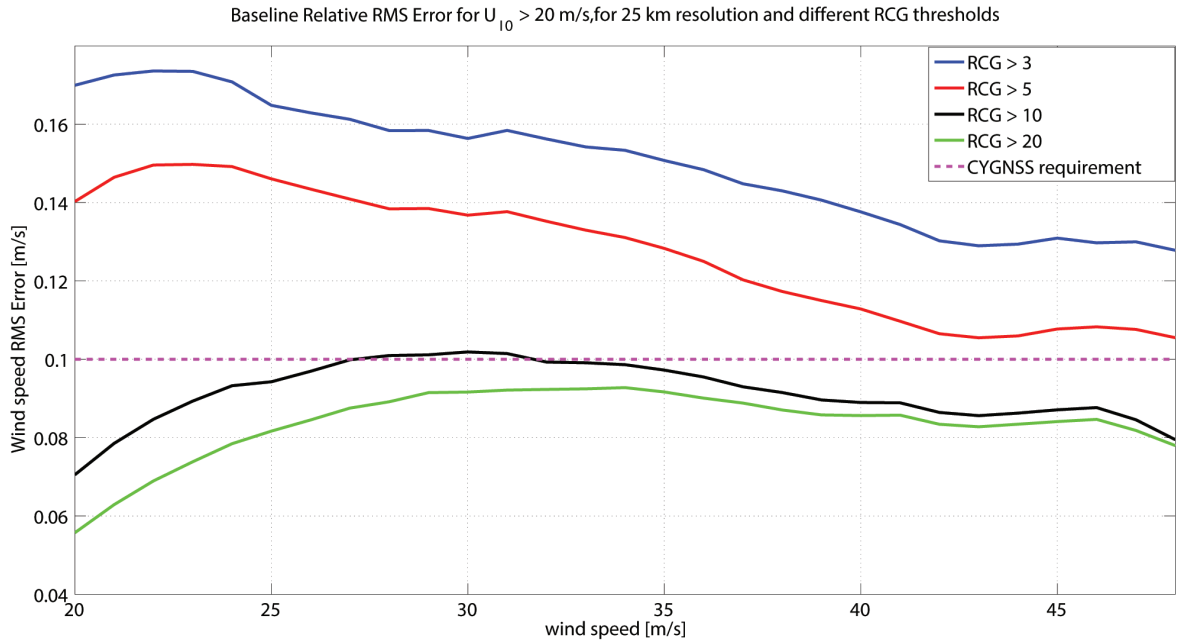

Figure 9.28. Relative RMS error curves versus true wind speed, for four different RCG thresholds. *Adapted from Clarizia & Ruf (2016), © 2016 IEEE.*

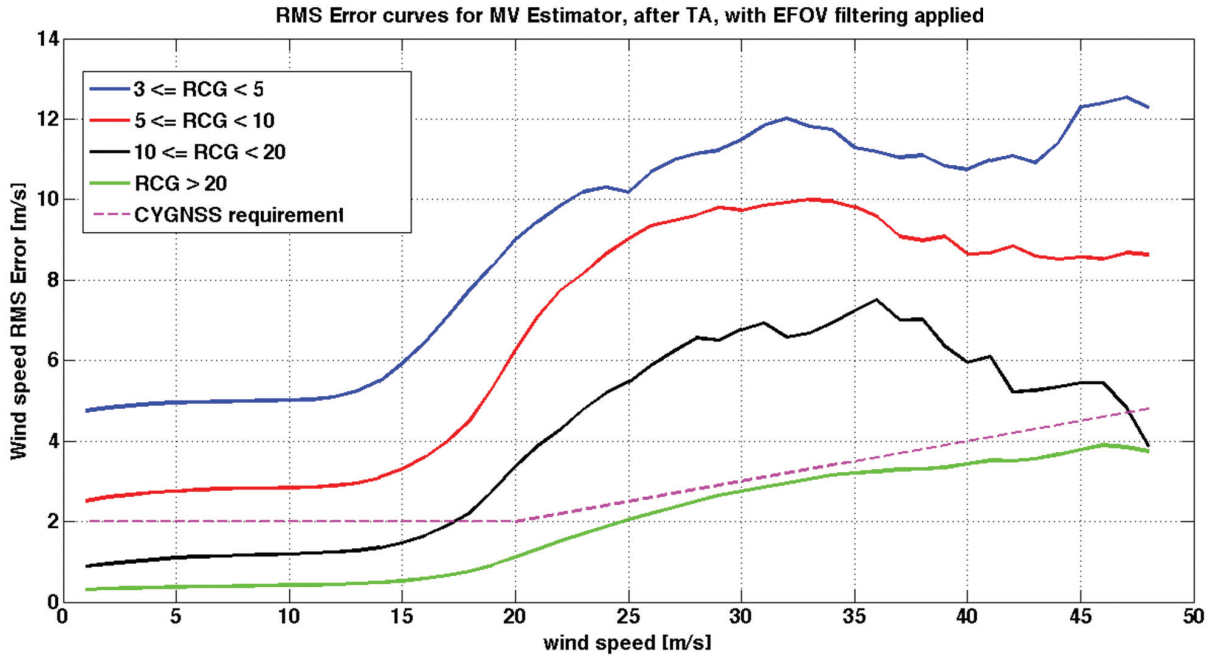

Figure 9.29. Final RMS error curves versus true wind speed, for four different RCG intervals. *Adapted from Clarizia & Ruf (2016), © 2016 IEEE.*

Tables 9.9 and 9.10 show instead the relative average RMS error for true wind speeds higher than 20 m s^{-1} and again respectively for different RCG thresholds and different RCG intervals. The relative average RMS error is calculated as illustrated in the following two equations:

$$RMS_{REL} = \int_{v>20} \overline{RMS}(v) f_v(v \mid H)\, dv \qquad \textbf{(9.17.a)}$$

$$\overline{RMS}_{REL}\left(U^i_{10(c)}\right) = RMS_{REL}\left(U^i_{10(c)}\right) / U^i_{10(c)} \qquad \textbf{(9.17.b)}$$

where $f_v(v \mid H)$ is the conditional PDF of the true wind speeds, with H representing the condition of wind higher than a given threshold (in this case, higher than 20 m s^{-1}).

The RMS error in Table 9.9 and Table 9.10 is shown for both a single wind speed threshold (i.e., all winds higher than 20 m s^{-1}) and for different wind speed intervals. Table 9.9 highlights that the minimum RCG threshold required to meet the baseline requirements for winds higher than 20 m s^{-1} is 10, consistently with what has been shown in Figure 9.27 and Figure 9.28. It also shows that the RMS error decreases with increasing wind speed, probably because the wind at the center of each bin (i.e., the denominator in Equation 9.17b) increases more rapidly than the increase in the absolute RMS error (i.e., the numerator in Equation 9.17b).

A. Some Examples of Retrieved versus True Winds

In this last section, we present some comparisons of true and retrieved winds, for five cases characterized by different RCG values. A plot of the true wind speeds versus RCG, for all the 13-day NR data, is shown in Figure 9.30.

From this plot, we have selected five different SP tracks of 60 seconds each that can be easily identified in the plot, which reach high enough wind speeds. The five cases are also highlighted in Figure 9.30, and it can be noticed that while the first three are in the high RCG range, the last two cases correspond instead to medium RCG values. Plots of the true and retrieved wind speeds versus second number, for cases from 1 to 5, are shown in Figure 9.31. In some cases (e.g., case 1) the retrievals match the true winds very well, and this is generally true for the first three cases of high RCG values. The latter two cases show instead that the error between the two is much higher.

Table 9.7. Summary of performances for winds lower than 20 m s^{-1}, for different RCG thresholds. *Adapted from Clarizia & Ruf (2016), © 2016 IEEE.*

Res = 25 km U_{10} < 20 m/s	**RCG > 3 * 10^{-27} Absolute RMS Err [m/s]**	**RCG > 5 * 10^{-27} Absolute RMS Err [m/s]**	**RCG > 10 * 10^{-27} Absolute RMS Err [m/s]**
Average RMS Error	1.8977	1.4041	0.5730

Table 9.8. Summary of performances for winds lower than 20 m s^{-1}, for different RCG intervals. *Adapted from Clarizia & Ruf (2016), © 2016 IEEE.*

Res = 25 km U_{10} < 20 m/s	**3 * 10^{-27} <= RCG < 5 * 10^{-27} Absolute RMS Err [m/s]**	**5 * 10^{-27} <= RCG < 10 * 10^{-27} Absolute RMS Err [m/s]**	**10 * 10^{-27} <= RCG < 20 * 10^{-27} Absolute RMS Err [m/s]**
Average RMS Error	5.3467	2.9983	1.2184

Table 9.9. Summary of performances for winds higher than 20 m s^{-1}, for different RCG thresholds and different wind speed ranges. *Adapted from Clarizia & Ruf (2016), © 2016 IEEE.*

Res = 25 km U_{10} > 20 m/s	**RCG > 5 * 10^{-27} Rel. RMS Err [%]**	**RCG > 10 * 10^{-27} Rel. RMS Err [%]**	**RCG > 20 * 10^{-27} Rel. RMS Err [%]**
Average RMS Error	14.0%	**9.2%**	**7.9%**
Av. RMS Error for 20 m/s <= U10 < 30 m/s	16.3%	11.9%	10.4%
Av. RMS Error for 30 m/s <= U10 < 40 m/s	12.2%	9.7%	9.3%
Av. RMS Error for U10 >= 40 m/s	8.6%	6.4%	6.2%

Table 9.10. Summary of performances for winds higher than 20 m s^{-1}, for different RCG intervals and different wind speed ranges. *Adapted from Clarizia & Ruf (2016), © 2016 IEEE.*

Res = 25 km U_{10} > 20 m/s	**3 * 10^{-27} <= RCG < 5 * 10^{-27} Rel. RMS Err [%]**	**5 * 10^{-27} <= RCG < 10 * 10^{-27} Rel. RMS Err [%]**	**10 * 10^{-27} <= RCG < 20 * 10^{-27} Rel. RMS Err [%]**
Average RMS Error	40.1%	32.7%	20.1%
Av. RMS Error for 20 m/s <= U10 < 30 m/s	42.8%	38.2%	26.9%
Av. RMS Error for 30 m/s <= U10 < 40 m/s	45.7%	29.5%	22.1%
Av. RMS Error for U10 >= 40 m/s	47.3%	20.7%	9.3%

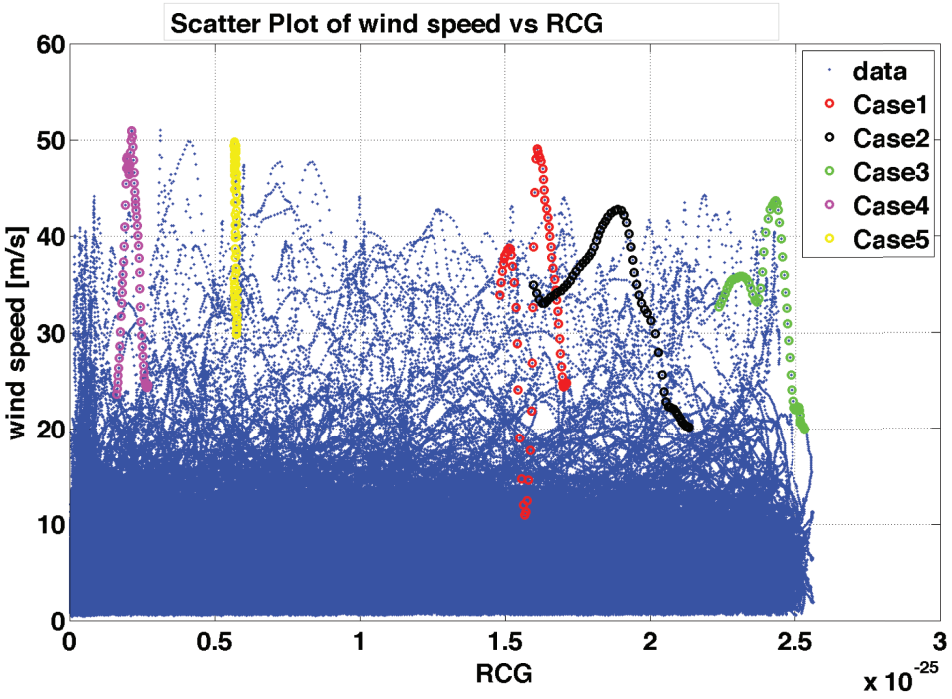

Figure 9.30. Plot of true wind speed versus RCG, for all the data from the 13-day NR simulation.

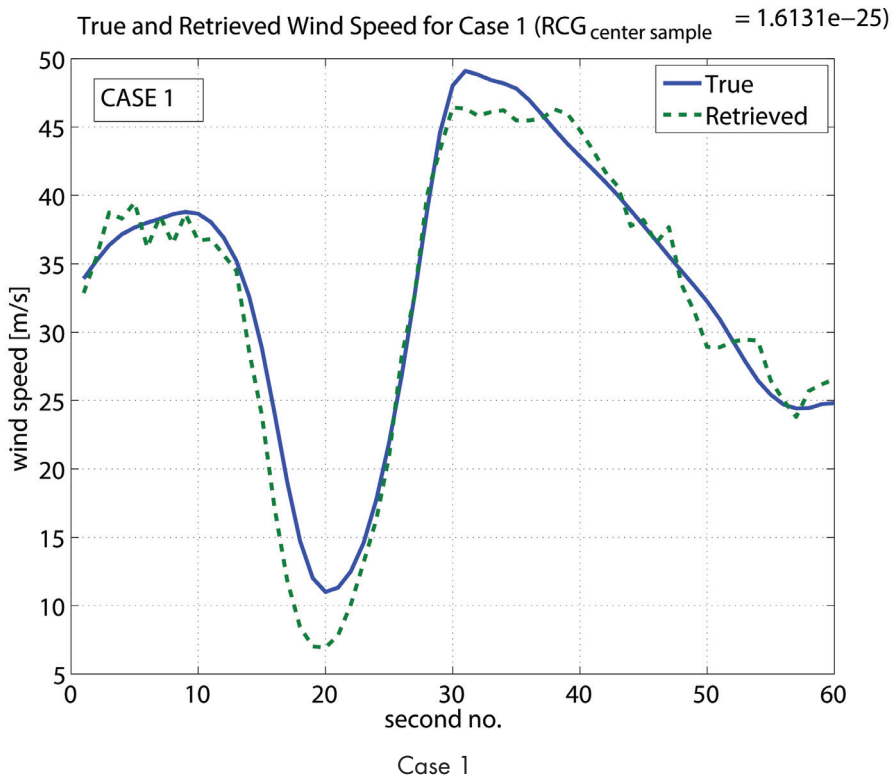

Figure 9.31. Illustration of true and retrieved wind speeds, versus second number, for 5 cases of 60-second acquisition each. (Continued on next page.) *Reused from Clarizia & Ruf (2016), © 2016 IEEE.*

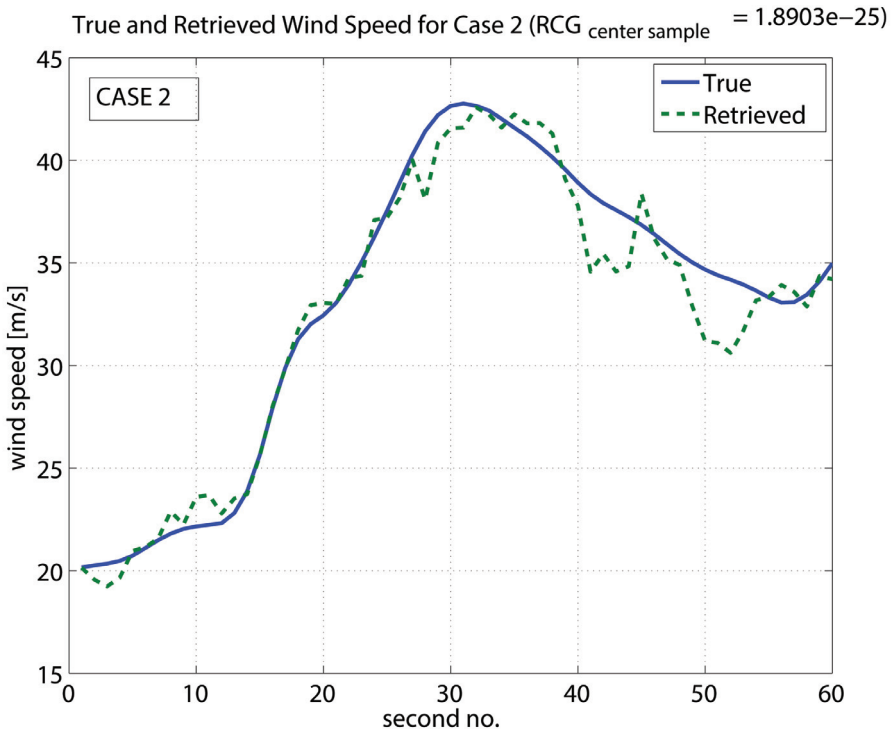

Case 2

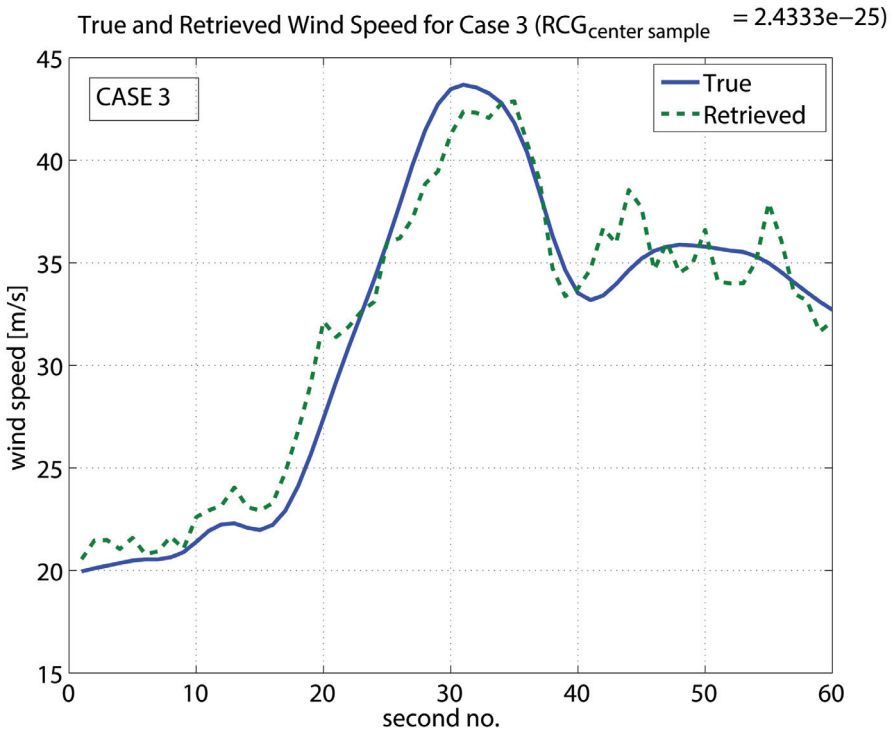

Case 3

Figure 9.31. Illustration of true and retrieved wind speeds, versus second number, for 5 cases of 60-second acquisition each. (Continued on next page.) *Reused from Clarizia & Ruf (2016), © 2016 IEEE.*

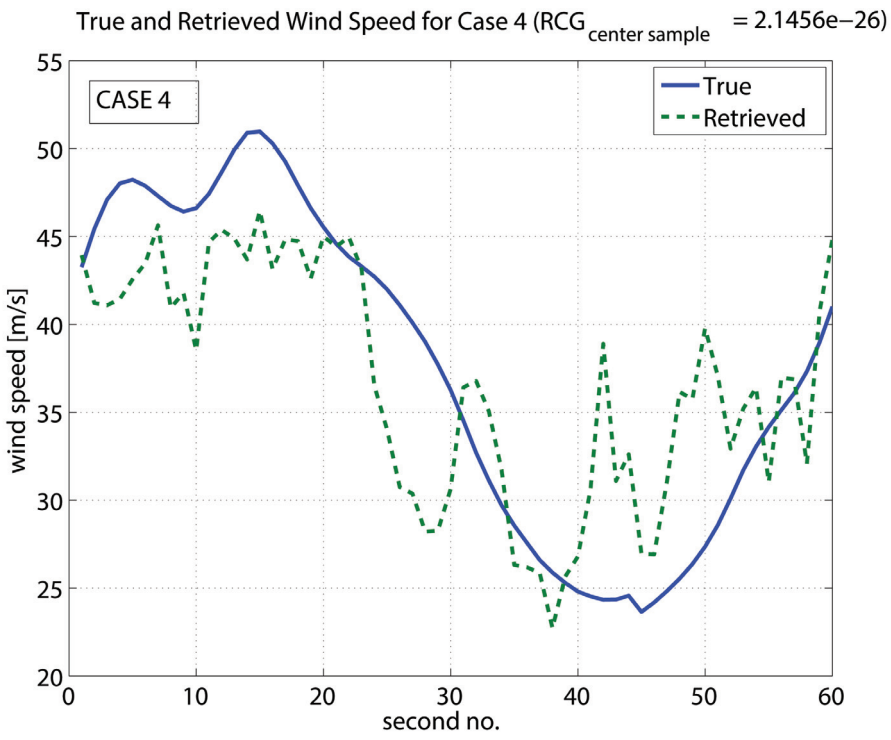

Case 4

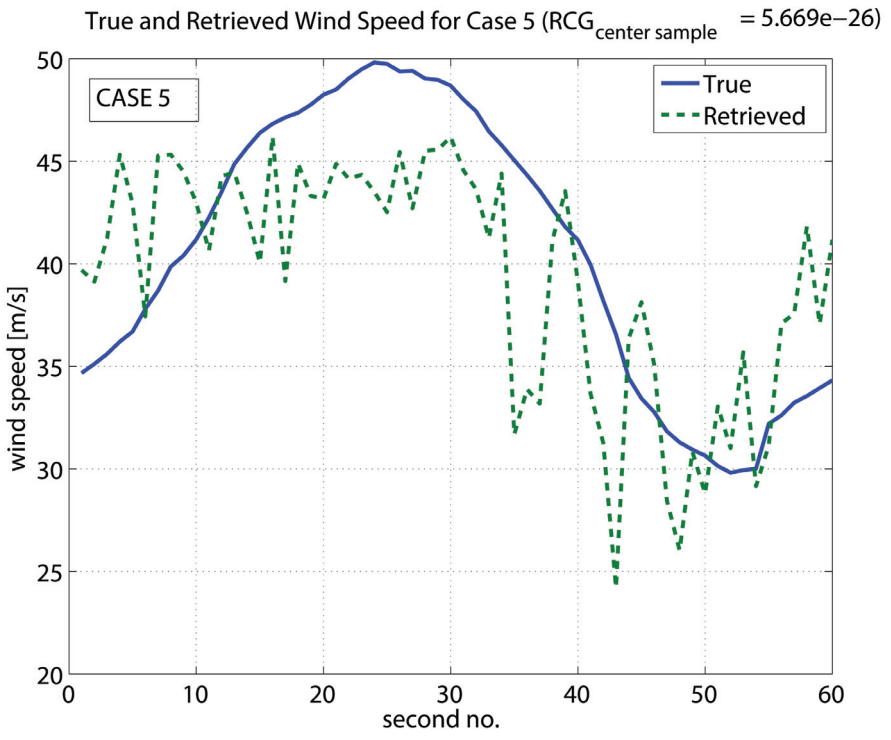

Case 5

Figure 9.31. Illustration of true and retrieved wind speeds, versus second number, for 5 cases of 60-second acquisition each. (Continued from previous page.) *Reused from Clarizia & Ruf (2016), © 2016 IEEE.*

Table 9.11. Summary of performances for the CYGNSS retrieval algorithm.

Res = 25 km	RCG Threshold	Avg RMS Retrieval Error	24 hr Spatial Coverage
U_{10} < 20 m/s	> 5e-27	1.40 m/s	79.6% (8 s/c) 75.0% (7 s/c)
U_{10} > 20 m/s	> 10e-27	9.2%	69.6% (8 s/c) 64.8% (7 s/c)

VI. Summary and Conclusions

A MV wind speed estimator is constructed using two observables derived from the DDMs. The observables exploit properties of the DDM that respond to variations in the ocean surface wind speed. The observables are the DDMA and the LES. A wind retrieval algorithm is first developed individually for each observable using an empirical GMF that is derived by linear regression of the observable against simulated ground truth wind speeds. The MV estimator is constructed as a linear combination of the wind estimates from each observable. It shows improved performance, in terms of RMS difference between estimated and ground truth wind, compared to the retrieval by each individual observable. The improvement is not large because the correlation between observables is high. However, what partial decorrelation does exist is fully exploited by the MV estimator to lower the overall RMS error.

Other processing steps, in addition to the use of an MV estimator, include the following:

- Observable DD range, selected based on spatial resolution
- Level 2A corrections
- Use of Level 2A correction to derive a GMF for every incidence angle interval
- Wind speed MV estimator using RCG-dependent covariance matrix
- Time averaging
- EFOV filter

The general performances of the retrieval algorithm for the CYGNSS baseline spatial resolution requirement of 25 × 25 km have been presented and characterized using RCG thresholds and RCG intervals and for the two distinct cases of wind speed lower than 20 m s^{-1} and higher than 20 m s^{-1}. The main conclusions are summarized in Table 9.11, where the final retrieval error is illustrated for the two RCG thresholds that allow it to meet the mission requirements for low and high wind speed. The 24-hour spatial coverage corresponding to that RCG threshold selection is also reported.

References

Clarizia, M. P., & Ruf, C. (2016). Wind speed retrieval algorithm for the Cyclone Global Navigation Satellite System (CYGNSS) mission. *Geoscience and Remote Sensing, IEEE Transactions On*. Manuscript in review.

Clarizia, M. P., Ruf, C. S., Jales, P., & Gommenginger, C. (2014). Spaceborne GNSS-R minimum variance wind speed estimator. *Geoscience and Remote Sensing, IEEE Transactions On*, *52*(11), 6829–6843. doi: 10.1109/TGRS.2014.2303831

Clarizia M. P., & Zavorotny V. (2015, November). *Algorithm theoretical basis document: Level 2 wind speed retrieval* (No. 148-0138, Revision 2, Change 2). Unpublished internal document, University of Michigan.

Gleason, S. (2014, December). *Algorithm theoretical basis document: Level 1b DDM calibration* (No. 148-0137, Revision 1). Unpublished internal document, University of Michigan.

Nolan, D. S., Atlas, R., Bhatia, K. T., & Bucci, L. R. (2013). Development and validation of a hurricane nature run using the joint OSSE nature run and the WRF model. *Journal of Advances in Modeling Earth Systems*, *5*(2), 382–405. doi: 10.1002/jame.20031

O'Brien, A. (2014, January). *End-to-end simulator technical memo* (No. 148-0123, Revision 0, Initial Release). Unpublished internal document, University of Michigan.

Zavorotny, V. U., & Voronovich, A. G. (2000). Scattering of GPS signals from the ocean with wind remote sensing application. *Geoscience and Remote Sensing, IEEE Transactions On*, *38*(2), 951–964. doi: 10.1109/36.841977

Appendix: Level 1B Corrections for Leading Edge Slope

We can show that the Level 1B correction for DDMA is given by

$$DDMA_{L1B} = C_F \cdot DDMA_{L1A}$$
$$C_F = \frac{\left(R_0^{SP} R^{SP}\right)^2}{G_{RX}^{SP} A_{DDMA}} \quad \textbf{(9.18)}$$

where R_0^{SP} (R^{SP}) is transmitter (receiver) range, G_{RX}^{SP} is receiver gain, and A_{DDMA} is physical scattering area. The following demonstrates that the same correction applies to the LES—namely,

$$LES_{L1B} = C_F \cdot LES_{L1A}$$
$$C_F = \frac{\left(R_0^{SP} R^{SP}\right)^2}{G_{RX}^{SP} A_{DDMA}} \quad \textbf{(9.19)}$$

The LES from Level 1A DDMs of scattered power is obtained through linear regression of the rising edge of the IDWs, and the equation for the slope from the simple linear regression method is

$$LES_{L1A}(\Delta\tau, \Delta f) = \frac{\sum_{m=1}^{M} \tau_m y_m - \frac{1}{M}\sum_{m=1}^{M}\tau_m \sum_{m=1}^{M} y_m}{\sum_{m=1}^{M}\tau_m^2 - \frac{1}{M}\left(\sum_{m=1}^{M}\tau_m\right)^2} \quad \textbf{(9.20)}$$

where τ_m is the delay and the x value of the IDW and y_m is the y value of the IDW derived from the Level 1A DDM, which can be expressed as

$$y_m = \sum_{n=1}^{N} \overline{Y}(\tau_m, f_n) \quad \textbf{(9.21)}$$

In principle, the Level 1B LES should be computed from DDMs whose pixels are Level 1B corrected individually:

$$LES_{L1B}(\Delta\tau, \Delta f) = \frac{\sum_{m=1}^{M} \tau_m \hat{y}_m - \frac{1}{M}\sum_{m=1}^{M}\tau_m \sum_{m=1}^{M} \hat{y}_m}{\sum_{m=1}^{M}\tau_m^2 - \frac{1}{M}\left(\sum_{m=1}^{M}\tau_m\right)^2} \quad \textbf{(9.22)}$$

$$\hat{y}_m = \sum_{n=1}^{N} C_F(\tau_m, f_n) \cdot \overline{Y}(\tau_m, f_n) \quad \textbf{(9.23)}$$

where $\hat{y}_m$ is the y value of the IDW from the Level 1B DDM. If C_F is assumed constant as in the case of the DDMA (and for the reasons explained previously), it can be factored out of the summation as follows:

$$\hat{y}_m = C_F \cdot \sum_{n=1}^{N} \overline{Y}(\tau_m, f_n) = C_F \cdot y_m \quad \textbf{(9.24)}$$

and the final equation for the Level 1B LES becomes

$$LES_{L1B}(\Delta\tau, \Delta f) = C_F \cdot \frac{\sum_{m=1}^{M} \tau_m y_m - \frac{1}{M}\sum_{m=1}^{M}\tau_m \sum_{m=1}^{M} y_m}{\sum_{m=1}^{M}\tau_m^2 - \frac{1}{M}\left(\sum_{m=1}^{M}\tau_m\right)^2} = \quad \textbf{(9.25)}$$
$$C_F \cdot LES_{L1A}(\Delta\tau, \Delta f)$$

10. Level 3 and 4 Wind Speed Science Data Products

I. Level 3 Gridded Wind Speed

A. Summary

This section describes the algorithm and data processing implementation used to produce a CYGNSS Level 3 gridded wind speed science data product. The algorithm uses as its input the mission baseline Level 2 wind speed science data product, which provides its wind speed values at the time and location at which the measurements were made (i.e., in sensor-specific latitude, longitude, and time coordinates) for each of the eight observatories in the CYGNSS constellation and for each of the four bistatic radar channels on each observatory. This Level 3 gridded product combines all 8 × 4 = 32 wind speed measurements made by the CYGNSS constellation each second, sorts them into a uniform (latitude, longitude, time) grid, and reports certain statistics of the samples in each bin (e.g., number, mean value), together with a compilation of the quality flags set for each of the samples in the bin.

B. Algorithm Objectives

The objective of this algorithm is to produce a gridded wind speed science data product that is uniformly sampled in latitude, longitude, and time. This Level 3 product is generated from the full set of Level 2 wind speed samples produced by the constellation of observatories. In addition to a best estimate of the mean ocean surface wind speed within any particular bin, the algorithm also produces statistics of the wind speed that are derived from the population of samples of the Level 2 wind speed made by the constellation within that bin. A compilation of the quality flags associated with the population of individual Level 2 wind speed samples is also produced.

C. Input Data Description

The input data required by this algorithm are listed here. All relevant quality flags associated with the Level 1B BRCS data that are used to produce the Level 2 wind speed data products are included as inputs. These quality flags (Gleason, 2014) are shown in Table 10.1. The relevant input products required from the Level 2 wind speed algorithm (Clarizia & Zavorotny, 2015) are shown in Table 10.2.

D. Algorithm Production Overview

The binning algorithm produces a minimum variance estimate of the mean wind speed in the bin over the spatial and temporal intervals specified by the bin's boundaries. This is done using an inverse variance weighted average of all Level 2 samples of the wind speed that were made within the bin. Specifically, for bin boundaries Lat_{min}, Lat_{max}, Lon_{min}, Lon_{max}, T_{min}, and T_{max}, let S be the set of all Level 2 samples of the wind speed satisfying the following conditions:

$$S = \{\mathrm{Sample}_i \mid \mathrm{Lat}_{min} \le \mathrm{Lat}_i < \mathrm{Lat}_{max};\ \mathrm{Lon}_{min} \le \mathrm{Lon}_i < \mathrm{Lon}_{max};\ T_{min} \le T_i < T_{max}\} \quad \textbf{(10.1)}$$

where the ith sample has bin coordinates (Lat_i, Lon_i, T_i). Sort all Level 2 wind speed samples, together with their uncertainties, that are in S. The uncertainties are the estimated standard deviations of the wind speed estimates. The Level 3 wind speed estimate for that bin is given by

$$u_{L3}(S) = \frac{\sum_{i \in S} u_i \sigma_i^{-2}}{\sum_{i \in S} \sigma_i^{-2}} \quad \textbf{(10.2)}$$

where u_i is the ith Level 2 minimum variance wind speed in S and σ_i is its uncertainty. The uncertainty (i.e., standard deviation) in u_{L3} is given by

$$\sigma_{L3} = \sqrt{\frac{1}{\sum_{i \in S} \sigma_i^{-2}}} \quad \textbf{(10.3)}$$

Relevant quality flags from the Level 2 wind speed algorithm are compiled into an aggregate set of quality flags for the Level 3 wind speed produced here. The wind-speed-dependent quality flags are shown

in Table 10.3. For each flag, a value N will be prescribed, which is the number of samples in S for which the threshold in column two is met.

Table 10.4 shows the rolled-up versions of the quality flags produced by the Level 1B DDM algorithm. For each flag, a value M will be prescribed, which is the number of samples in S for which the threshold in column two is met.

E. Output Data Product Description

The following output data values will be available:

- u_{L3} = The minimum variance estimate of the mean wind speed averaged over the time and space intervals defined by Equation 10.1 for a particular bin, as given by Equation 10.2 (units of m s^{-1})

Table 10.1. Quality flags from Level 1B BRCS data that are used for Level 1 wind speed data products.

Flag	*Flag values*	*Comment*
Large spacecraft attitude error	0 = false, 1 = true	
Overall DDM quality	0 = poor, 1 = good	This is the OR of other quality flags; TBD: detailed description.
Negative signal power in Level 2 DDMA		At least one bin in Level 2 DDMA has a negative power value.
Negative Sigma0 in Level 2 DDMA		At least one bin in Level 2 DDMA has a negative power value.
Low confidence in DDM noise floor estimate	0 = false, 1 = true	
Low confidence in open ocean noise floor estimate	0 = false, 1 = true	
Low confidence in open ocean noise temperature estimate	0 = false, 1 = true	
Land present in DDM	0 = false, 1 = true	
Specular point over open ocean	0 = false, 1 = true	
Large step change in DDM noise floor	0 = false, 1 = true	
Large step change in LNA temperature	0 = false, 1 = true	
Direct signal in DDM	0 = false, 1 = true	
Low Rx antenna range corrected gain	0 = false, 1 = true	
High specular point incidence angle	0 = false, 1 = true	
High cross correlation power present	0 = false, 1 = true	
Low confidence in GPS EIRP estimate	0 = false, 1 = true	

Table 10.2. Input products from Level 2 wind speed algorithm.

Flag	*Flag values*
MV wind speed estimate	
Uncertainty in MV wind speed estimate	
Negative wind speed quality flag	0 = nonnegative, 1 = negative
The >70 m s^{-1} wind speed quality flag	0 = <70 m s^{-1}, 1 = >70 m s^{-1}

Table 10.3. Wind-speed-dependent quality flags.

Flag	*Flag values*
Fatal negative wind speed quality flag	1 = wind speed less than −5 m s^{-1}
Fatal high wind speed quality flag	1 = wind speed greater than 100 m s^{-1}
Nonfatal negative wind speed quality flag	1 = wind speed between −5 m s^{-1} and 0
Nonfatal high wind speed quality flag	1 = wind speed between 70 m s^{-1} and 100 m s^{-1}

- σ_{L3} = The standard deviation of u_{L3} for a particular bin, as given by Equation 10.3 (units of m s^{-1})
- S = The number of samples used to calculate u_{L3}

The output data quality flags are presented in Table 10.5.

F. Algorithm Configuration Parameter Values

The principle configuration parameters for this algorithm are the latitude, longitude, and time boundaries of the bins. The bins are uniformly spaced every 0.2° in latitude from −40°N to +40°N, every 0.2° in longitude from 0 to 360°E and every 1 hour in time. Specifically,

- Lat_{min} = −40°, −39.8°,…, +39.8°N latitude
- Lat_{max} = −39.8°, −39.6°,…, +40°N
- Lon_{min} = 0°, 0.2°,…, 359.8°E
- Lon_{max} = 0.2°, 0.4°,…, 360.0°E
- T_{min} = (year, day of year, 0 hr UTC), (yr, DOY, 1 hr UTC),…, (yr, DOY, 23 hr UTC)
- T_{max} = (year, day of year, 1 hr UTC), (yr, DOY, 2 hr UTC),…, (yr, DOY, 24 hr UTC)

II. Level 4 Wind Speed for Data Assimilation

A. Science Background and Objectives

The Level 4 product described in this section is the surface wind vector analysis field on a basin-wide domain of 9 km grid spacing, in which the assimilation of both conventional data and CYGNSS winds is performed. This product will be computed using NOAA's operational HWRF model framework, incorporating the Hybrid Ensemble Kalman Filter / Gridpoint Statistical Interpolation Data Assimilation Scheme (hereafter referred to as "Hybrid"). The influence of assimilating CYGNSS wind speed data on HWRF analyses and forecasts of Atlantic hurricanes will be evaluated for a limited number of storms.

Need for Ocean Surface Winds

Consistent oceanic surface wind data of high quality and high temporal and spatial resolution are required to understand and predict the large scale air-sea interactions that influence both the atmosphere and ocean. Such observations are needed to drive ocean models and surface wave models; calculate surface fluxes of heat, moisture, momentum, and CO_2; provide initial data and verification data for atmospheric models; and construct surface climatologies.

Table 10.4. Rolled-up versions of quality flags from Level 1B DDM algorithm.

Flag	*Flag values*
Large spacecraft attitude error	1 = true
Negative signal power In Level 2 DDMA area	At least one bin in the Level 2 DDMA has a negative power value
Negative Sigma0 in Level 2 DDMA area	At least one bin in the Level 2 DDMA has a negative power value
Low confidence in DDM noise floor estimate	1 = true
Low confidence in open ocean noise floor estimate	1 = true
Low confidence in open ocean noise temperature estimate	1 = true
Land present in DDM	1 = true
Specular point over open ocean	1 = true
Large step change in DDM noise floor	1 = true
Large step change in LNA temperature	1 = true
Direct signal in DDM	1 = true
Low Rx antenna range corrected gain	1 = true
High specular point incidence angle	1 = true
High cross correlation power present	1 = true
Low confidence in GPS EIRP estimate	1 = true

Table 10.5. Quality flags for the output data. N and M are the number of samples that meet the condition described in column 2; lat = latitude; lon = longitude.

Flag or condition	*Flag values*
Overall Level 3 wind speed quality	0 = poor, 1 = good
Fatal negative wind speed quality flag	*N* = # of wind speed samples in the lat, lon boundary of *S* but not included in *S* because wind speed is less than –5 m s^{-1}
Fatal high wind speed quality flag	*N* = # of wind speed samples in the lat, lon boundary of *S* but not included in *S* because the wind speed is greater than 100 m s^{-1}
Nonfatal negative wind speed quality flag	*N* = # of wind speed samples in *S* for which the = wind speed is between –5 m s^{-1} and 0
Nonfatal high wind speed quality flag	*N* = # of wind speed samples in *S* for which the wind speed is between 70 m s^{-1} and 100 m s^{-1}
Negative signal power In Level 2 DDMA	*M* = # of DDM samples in *S* where at least one bin in the Level 2 DDMA has a negative power value
Negative Sigma0 in Level 2 DDMA	*M* = # of DDM samples in *S* where at least one bin in the Level 2 DDMA has a negative power value
Large spacecraft attitude error	# of true DDM samples
Low confidence in DDM noise floor estimate	# of true DDM samples
Low confidence in open ocean noise floor estimate	# of true DDM samples
Low confidence in open ocean noise temperature estimate	# of true DDM samples
Land present in DDM	# of true DDM samples
Specular point over open ocean	# of true DDM samples
Large step change in DDM noise floor	# of true DDM samples
Large step change in LNA temperature	# of true DDM samples
Direct signal in DDM	# of true DDM samples
Low Rx antenna range corrected gain	# of true DDM samples
High specular point incidence angle	# of true DDM samples
High cross correlation power present	# of true DDM samples
Low confidence in GPS EIRP estimate	# of true DDM samples

Surface wind stress provides the most important forcing of the ocean circulation, while the fluxes of heat, moisture, and momentum across the air-sea boundary are important factors in the formation, movement, and modification of water masses and the intensification of storms near coasts and over the open oceans (Atlas, 1987). In addition, air-sea interaction plays a major role in theories of ENSO and the 50-day oscillation, as well as in the initiation and maintenance of heat waves and drought and other persistent anomalies (Wolfson et al., 1987; Atlas et al., 1993).

Surface wind data are also important for the analysis and forecasting of high-impact weather events, such as tropical cyclones (Atlas et al., 2001). Data of sufficient quality can be used to estimate the intensity (maximum sustained wind speed) in hurricanes and the spatial extent of TC force and hurricane force winds around the center.

Earlier Satellite Instruments

Prior to the launch of satellites capable of determining surface wind from space, observations of surface winds were provided primarily by ships and buoys. While these in situ observations are extremely useful, they also have severe spatial and temporal limitations and are generally not adequate for global applications. For example, reports of surface wind by ships

are often of poor accuracy, cover only very limited regions of the world's oceans, and occur at irregular intervals in time and space. Buoys, while of higher accuracy, have extremely sparse coverage. Due to these deficiencies, analyses of surface wind that do not include space-based data can misrepresent atmospheric flow over large regions of the global oceans, and this contributes to the poor calculation of wind stress and sensible and latent heat fluxes in these regions.

In response to the wind blowing across it, the ocean surface responds on many wavelengths. This response provides a mechanism for the microwave remote sensing of ocean surface wind from space. The active sensing of the radar backscatter of centimeter-scale capillary waves allows the retrieval of ocean surface wind vectors with some directional ambiguity. The Seasat, ERS-1/2, NSCAT, QuikSCAT, and ASCAT scatterometers were designed to take advantage of this phenomenon, but the time periods for which scatterometer data alone are available are still limited and not sufficient for studies of interannual variability and climate change. Seasat data are available for only the third quarter of 1978 (Atlas et al., 1987). ERS-1/2 scatterometer data, with more limited coverage, are available from 1992 to 2011 but are severely limited past January 2001. The NASA Scatterometer (NSCAT) provided data from fall 1996 through Spring 1997. SeaWinds on QuikSCAT was launched in July 1999 and operated until November 2009. SeaWinds on ADEOS2 functioned from April to October 2003. ASCAT on MetOp-A overlaps with most of the last two years of QuikSCAT and continues to the present. Passive microwave remote sensing of the ocean surface also has the capability of retrieving ocean surface winds through the response of the microwave emissivity to the surface roughness. Four passive instruments, the Scanning Multichannel Microwave Radiometer (SMMR), the Special Sensor Microwave Imager (SSMI), the TRMM Microwave Imager (TMI), and the Advanced Microwave Scanning Radiometer (AMSR), have provided ocean surface wind speed data. SSMI provides the longest and most continuous record of satellite surface wind observations over the oceans.

CYGNSS Measurement Requirements Specific to This Algorithm

The Level 2 ocean surface wind speeds retrieved by CYGNSS are used as inputs to this algorithm.

B. Algorithm Overview

Algorithm Objectives

The main objective is to improve gridded ocean surface wind fields via state-of-the-art assimilation of the CYGNSS wind speed data. These gridded fields represent a blended product of the measurements and a basin-scale configuration of the HWRF model (Gopalakrishnan et al., 2013).

Algorithm Production Overview

First, NOAA's operational version of the data assimilation system will be implemented. At the time of writing (2015), the data assimilation algorithm at NOAA's NCEP is a "Hybrid" three-dimensional variational and ensemble Kalman filter technique (Hamill et al., 2011). Following the CYGNSS launch, the influence of assimilating CYGNSS wind speeds on HWRF analyses and forecasts of a limited number of Atlantic hurricanes will be evaluated using observing system experiments (OSEs).

C. Input Data Description

Level 2 Retrieved Winds

The required data are CYGNSS Level 2 wind speed retrievals, together with error estimates (including correlated observation errors if appropriate).

Ancillary Data

All *in situ observations* that are assimilated into NOAA's operational hurricane data assimilation system will be included. These include observations from ships and buoys, the rawinsonde network over land, and dropwindsondes released from hurricane hunter aircraft.

All *satellite observations* that are assimilated into NOAA's operational hurricane data assimilation system will be included. These include atmospheric motion wind vectors, scatterometer winds, passive infrared, and microwave radiances.

Operational *global model analyses* will be used to provide boundary conditions.

Output Data Product Description

The Level 4 products will be created for a limited number of hurricanes in the Atlantic Basin. Blended

analyses of surface wind speed and direction at 9 km horizontal grid spacing will be created utilizing the basin-scale HWRF, at a frequency of every 6 hours through cycled data assimilation.

D. Physics of the Problem

Data Assimilation

Data assimilation represents the melding of observational data with a "first guess" field to produce a theoretically optimal new "analysis" field. The first guess, or background field, is normally a short-range forecast (or ensemble of forecasts) of a few hours, integrated forward from a previous analysis. In addition to the observations and background fields themselves, their respective error covariance matrices are prescribed. Based on linear least squares estimation theory or maximum likelihood theory, the minimum error variance estimate of the analysis is then produced as a weighted linear combination of the observations and background field. A conventional, widely used method is the three-dimensional variational method (3D-Var; Parrish & Derber 1992), which has until recently been used at NOAA through NCEP's Gridpoint Statistical Interpolation assimilation scheme (GSI; Kleist et al. 2009). Over the past decade, ensemble Kalman filters (EnKF) have become increasingly widespread in full-physics atmospheric models. In contrast to 3D-Var, which provides temporally stationary and spatially isotropic background error covariance information, the EnKF uses several independent ensemble forecasts (typically 30–100 members) to create anisotropic, flow-dependent error covariance information that is pertinent to the weather system of interest. For the Level 4 wind analysis fields to be created here, a Hybrid of the GSI and EnKF, following Hamill et al. (2011), will be used.

Hurricane Model

NOAA's operational hurricane prediction system will be available for use. The HWRF is currently available on a basin-scale domain, and it is anticipated that by the time of the CYGNSS launch, a domain with a horizontal grid spacing of 9 km will be ready for use for preparation of the Level 4 wind analysis fields. The modeling system has undergone several upgrades to its physics parameterizations, as described in Gopalakrishnan et al. (2013).

E. Analysis Algorithm

Theoretical Description

The Hybrid data assimilation scheme employed in NCEP operations incorporates ensemble perturbations directly into the variational cost function to be minimized per Equation 10.4:

$$J(x_f', \alpha) = \beta_f \frac{1}{2}(x_f')^T B^{-1}(x_f') + \beta_e \frac{1}{2}(\alpha)^T L^{-1}(\alpha) + \frac{1}{2}(y_o' - Hx_f')^T R^{-1}(y_o' - Hx_f') \quad \textbf{(10.4)}$$

The state vector x'_f represents the background (or first guess) field provided by a short-range HWRF forecast. The matrix containing the corresponding background ensemble perturbations is represented by α. β_f and β_e are the weighting coefficients for the fixed (3D-Var) covariance B and ensemble covariance $\alpha\alpha^T$, respectively, and L is the correlation matrix that represents localization on the ensemble perturbations. R is the observation error covariance matrix, and y_o represents the vector of observations assimilated. H is the observation operator, which operates on the first guess field. β_f and β_e represent weighting coefficients for the fixed and ensemble covariance respectively, and they satisfy Equation 10.5:

$$\frac{1}{\beta_f} + \frac{1}{\beta_e} = 1 \quad \textbf{(10.5)}$$

The total analysis increment, which represents the sum of the increment from the fixed covariance and the ensemble-based covariance, is given by Equation 10.6:

$$x_t' = x_f' + \sum_{k=1}^{K} \left(\alpha_k \circ x_k^e \right) \quad \textbf{(10.6)}$$

where x_k^e represents the kth ensemble perturbation and α_k is the "extended control variable."

This analysis increment is added to the background (first guess) field to provide the new analysis field. The analysis field of wind vectors at the ocean surface is the Level 4 product.

Processing and Data Flow

The operational analysis fields are available at NCEP. They are produced via the assimilation of all conventional in situ and satellite data described in Subsection C. CYGNSS data are not assimilated.

These analysis fields will be referred to as the "control." They will be routinely downloaded from NCEP.

The next step in the OSE is to use the identical version of the Hybrid to assimilate not only the conventional data but also CYGNSS wind speed data. The background ensemble perturbations α will be produced from a short-range (6-hour) HWRF ensemble forecast, which is integrated forward from ensemble initial conditions. The "quality control" algorithm at NCEP will be used on all the ingested data including CYGNSS, via comparisons with neighboring observations and their departure from the background ensemble. Following the preparation of the observations and assignment of their errors (from input files with fixed values), the Hybrid data assimilation will then be performed, resulting in a three-dimensional analysis field comprising all physical meteorological variables in HWRF. The Level 4 product is the surface wind vector analysis field on a basin-wide domain of 9 km grid spacing, in which the assimilation of both the conventional data and CYGNSS winds is performed.

Practical Considerations

The creation of the Level 4 surface wind product is contingent on the availability of input observational data (from CYGNSS and ancillary data sources) and estimates of their errors. Global model fields are required for boundary conditions, and the latest version of the HWRF model is required. The accuracy of the Level 4 surface wind product is dependent on the number of ensemble members in the Hybrid data assimilation and therefore the available computing capacity (number of nodes, disk space, memory).

F. Performance Characterization

Accuracy

The fit of the Level 4 surface wind fields to collocated available data types will be computed before and after the assimilation. In other words, the observations minus background (O-B) statistics will be tabulated, together with the observations minus analysis (O-A) statistics and the analysis increment (A-B). In addition, statistics on the quality control, and patterns in which the observational data are rejected, will be compiled.

The impact of assimilating CYGNSS data on HWRF analyses and forecasts of hurricanes will be quantified. The following metrics will be employed:

- Central position (track) of hurricane
- Maximum surface wind speed (intensity) of hurricane
- Radius of gale-force winds (34 kt or 17 m s^{-1})
- Radius of 50 kt winds (25 m s^{-1})
- Radius of hurricane force winds (64 kt or 33 m s^{-1})
- Azimuthally averaged wind speed
- Wave number 1 and wave number 2 components of wind speed
- Integrated kinetic energy (IKE)

These measures will be evaluated with respect to the following:

- NHC best track (track, intensity, wind radii)
- Analyses will be verified against independent observations not assimilated.
- HWRF forecasts will be evaluated with respect to observations, including CYGNSS wind speed and aircraft observations where available.
- Forecast wind fields will be verified against subsequent HWRF analyses.

Error metrics include the absolute error, RMS error, and overall bias.

Overall Uncertainty

The methodology to estimate errors in the product will be similar to that reported in Hoffman et al. (2013), which follows the diagnostics of Desroziers et al. (2005). Assuming that the analysis field is optimal, the background, observation, and analysis error covariances are estimated in observation space through computation of the aforementioned increments O-B, O-A, and A-B.

Prelaunch Test Procedures

Prior to launch, observing system simulation experiments (OSSEs) will be performed in which simulated CYGNSS data sampled from a nature run (NR; Nolan et al., 2013) are assimilated into HWRF using the Hybrid data assimilation technique. Evaluations of the surface wind analysis products and of the HWRF forecasts will be conducted using the NR as "truth."

On-Orbit Validation

Validation will be performed through collocations with independent data and computations of the impact of CYGNSS data on the analysis fields.

References

Atlas, R. (1987). The role of oceanic fluxes and initial data in the numerical prediction of an intense coastal storm. *Dynamics of Atmospheres and Oceans*, *10*(4), 359–388. doi: 10.1016/0377-0265(87)90025-X

Atlas, R., Busalacchi, A. J., Ghil, M., Bloom, S., & Kalnay, E. (1987). Global surface wind and flux fields from model assimilation of Seasat data. *Journal of Geophysical Research: Oceans (1978–2012)*, *92*(C6), 6477–6487. doi: 10.1029/JC092iC06p06477

Atlas, R., Hoffman, R. N., Leidner, S. M., Sienkiewicz, J., Yu, T. W., Bloom, S. C., … & Jusem, J. C. (2001). The effects of marine winds from scatterometer data on weather analysis and forecasting. *Bulletin of the American Meteorological Society*, *82*(9), 1965–1990. doi: http://dx.doi.org/10.1175/1520-0477(2001)082<1965:TEOMWF>2.3.CO;2

Atlas, R., Wolfson, N., & Terry, J. (1993). The effect of SST and soil moisture anomalies on GLA model simulations of the 1988 US summer drought. *Journal of Climate*, *6*(11), 2034–2048. doi: http://dx.doi.org/10.1175/1520-0442(1993)006<2034:TEOSAS>2.0.CO;2

Clarizia, M. P., & Zavorotny, V. (2015, November). *Algorithm theoretical basis document: Level 2 wind speed retrieval* (No. 148-0138, Revision 2, Change 2). Unpublished internal document, University of Michigan.

Desroziers, G., Berre, L., Chapnik, B., & Poli, P. (2005). Diagnosis of observation, background and analysis-error statistics in observation space. *Quarterly Journal of the Royal Meteorological Society*, *131*(613), 3385–3396. doi: 10.1256/qj.05.108

Gleason, S. (2014, November). *Algorithm theoretical basis document: Level 1b DDM calibration* (No. 148-0137, Revision 1, Change 0). Unpublished internal document, University of Michigan.

Gopalakrishnan, S. G., Marks Jr., F., Zhang, J. A., Zhang, X., Bao, J. W., & Tallapragada, V. (2013). A study of the impacts of vertical diffusion on the structure and intensity of the tropical cyclones using the high-resolution HWRF system. *Journal of the Atmospheric Sciences*, *70*(2), 524–541. doi: http://dx.doi.org/10.1175/JAS-D-11-0340.1

Hamill, T. M., Whitaker, J. S., Kleist, D. T., Fiorino, M., & Benjamin, S. G. (2011). Predictions of 2010's tropical cyclones using the GFS and ensemble-based data assimilation methods. *Monthly Weather Review*, *139*(10), 3243–3247. doi: 10.1175/MWR-D-11-00079.1

Hoffman, R. N., Ardizzone, J. V., Leidner, S. M., Smith, D. K., & Atlas, R. (2013). Error estimates for ocean surface winds: Applying Desroziers diagnostics to the cross-calibrated, multiplatform analysis of wind speed. *Journal of Atmospheric and Oceanic Technology*, *30*(11), 2596–2603. doi: http://dx.doi.org/10.1175/JTECH-D-13-00018.1

Kleist, D. T., Parrish, D. F., Derber, J. C., Treadon, R., Wu, W. S., & Lord, S. (2009). Introduction of the GSI into the NCEP global data assimilation system. *Weather and Forecasting*, *24*(6), 1691–1705. doi: http://dx.doi.org/10.1175/2009WAF2222201.1

Nolan, D. S., Atlas, R., Bhatia, K. T., & Bucci, L. R. (2013). Development and validation of a hurricane nature run using the joint OSSE nature run and the WRF model. *Journal of Advances in Modeling Earth Systems*, *5*(2), 382–405. doi: 10.1002/jame.20031

Parrish, D. F., & Derber, J. C. (1992). The National Meteorological Center's spectral statistical-interpolation analysis system. *Monthly Weather Review*, *120*(8), 1747–1763. doi: http://dx.doi.org/10.1175/1520-0493(1992)120<1747:TNMCSS>2.0.CO;2

Wolfson, N., Atlas, R., & Sud, Y. C. (1987). Numerical experiments related to the summer 1980 US heat wave. *Monthly Weather Review*, *115*(7), 1345–1357. doi: http://dx.doi.org/10.1175/1520-0493(1987)115<1345:NERTTS>2.0.CO;2

11. Data Science Calibration and Validation

The CYGNSS Cal/Val plan consists of prelaunch and postlaunch activities starting in Phase A and continuing through launch and commissioning through the end of the mission (Phase E). The prelaunch objectives of the Cal/Val program include

- Acquire instrument specifications necessary for the characterization of CYGNSS Level 1 L-Band sensor products.
- Acquire and process data with which to calibrate, test, and improve models and algorithms used for retrieving CYGNSS science data products.
- Develop and test the infrastructure and protocols for postlaunch validation; this includes establishing an in situ observation strategy for the postlaunch phase.

The postlaunch objectives of the Cal/Val program are to

- Verify and improve the performance of the sensor and science algorithms.
- Validate the accuracy of the science data products.
- Validate the utility of CYGNSS wind products in the marine forecasting and warning environment.

I. Overview of Validation Methodology

A. Background

In developing the Cal/Val plan for CYGNSS, there are useful precedents and experiences to consider. The Committee on Earth Observation Satellites (CEOS) Working Group on Calibration and Validation (WGCV; see http://calvalportal. ceos.org) has established standards that can provide a starting point for CYGNSS. There are also the Cal/Val approaches that have been extensively utilized for satellite microwave scatterometers and radiometers that will be leveraged.

A useful reference in developing a validation plan is the CEOS Hierarchy of Validation (http://lpvs.gsfc.nasa.gov) posted by the CEOS Land Product Validation subgroup:

Stage 1. Product accuracy is assessed from a small (typically <30) set of locations and time periods by comparison with in situ or other suitable reference data.

Stage 2. Product accuracy is estimated over a significant set of locations and time periods by comparison with reference in situ or other suitable reference data. Spatial and temporal consistency of the product and similar products has been evaluated over globally representative locations and time periods. Results are published in the peer-reviewed literature.

Stage 3. Uncertainties in the product and its associated structure are well quantified from comparison with reference in situ or other suitable reference data. Uncertainties are characterized in a statistically robust way over multiple locations and time periods representing global conditions. Spatial and temporal consistency of the product and with similar products has been evaluated over globally representative locations and periods. Results are published in the peer-reviewed literature.

Stage 4. Validation results for stage 3 are systematically updated when new product versions are released and as the time series expands.

For satellite ocean wind remote sensing, the Stage 1 validation would typically involve collocating measurements with numerical weather model wind fields. This allows a relatively large number of collocation measurements to be obtained in a short amount of time. The differences between the model and measured winds can generally be considered random, and the mean retrieval accuracy can be readily determined for winds from about 5 to 20 m s^{-1}. The model winds are generally not reliable enough to properly validate very low or very high wind speeds. The remaining stages are applicable, and a validation program would be expected to transition through these stages over the mission life span.

B. CYGNSS Cal/Val Approach

The primary objectives of the Cal/Val effort are to characterize the forward model, evaluate the performance of each sensor, evaluate the retrieval algorithm(s), and evaluate the retrieved wind speeds. The first step in this process is collocating various "truth" data with the CYGNSS data. These "truth" data include numerical model output parameters, GPS dropsondes, other satellite data (ASCAT, ScatSat, RapidScat, WindSat, AMSR2, etc.), and aircraft-based measurements. The next steps involve statistical analyses of the collocation database. The GMF (see Section 9 for details) is characterized, and any unexpected artifacts or trends are analyzed. The collocation database is also used to evaluate measurement performance relative to the instrument characteristics and measurement geometry for each sensor. The wind speed retrieval algorithms are analyzed, and their strengths and weaknesses are defined. Quality control flags are developed based upon these analyses and are included with the final product files provided to the end users. Another facet of the wind speed retrieval validation will be in the context of the operational forecasting environment and evaluation of the CYGNSS wind speed product performance by marine forecasters. This type of validation has proven to be invaluable for other satellite data in revealing performance characteristics that are not readily apparent from standard statistical analyses.

C. Prelaunch Activities

Prior to launch, CYGNSS wind speed retrieval performance will be analyzed utilizing simulated CYGNSS retrievals from the E2ES, a model designed to artificially simulate DDMs using orbit estimates and modeled winds. The simulated CYGNSS retrievals are derived from high-resolution numerical weather model nature runs and from simulated CYGNSS measurements from actual TCs during 2010–2011, derived from realistic high-resolution model wind fields from the HWRF model. A total of 43 storms were run through the E2ES, which included everything from tropical depressions (TDs) to TSs and category 4 strength hurricanes (H1 to H4) from the Atlantic and Eastern Pacific basins (Table 11.1). These storms are also plotted geographically in Figure 11.1.

The prelaunch GMF was developed for the two CYGNSS observables of DDMA and LES. This GMF is a function of wind speed and incidence angle and is provided in a tabulated form for wind speeds 0–55 m s^{-1} and 0–80° incidence angles. The GMF was trained utilizing wind speeds on a 25 × 25 km spatial grid and using measurements with a receiver antenna gain greater than 15 km^{-4}. Figure 11.2 displays the current prelaunch DDMA and LES GMFs.

The launch of TechDemoSat-1 on July 8, 2014, provided an additional prelaunch opportunity to investigate space-based GPS bistatic radar measurements of the ocean surface and prepare for the launch of CYGNSS. The SGResi instrument utilizes a receiver that is very similar in design to those that will be used by CYGNSS. While the measurement geometry is different and the dataset limited, these measurements will provide valuable insights and experience in preparation for the CYGNSS postlaunch Cal/Val activities.

D. CYGNSS Data Quality Flag Development

The development of a proper data quality flag is an important part of the Cal/Val process. The quality flag not only helps guide end users on proper product utilization, but it also is required to properly characterize the wind retrieval performance. The CYGNSS prelaunch data quality flag development will utilize the retrieved winds from the DDMA (U_{10_DDMA}) and LES (U_{10_LES}) GMF, which are provided separately. The winds retrieved from the DDMA and from the LES GMFs are combined to generate a MV estimator (U_{10_MV}):

$$U_{10\_MV} = k_0 U_{10\_DDMA} + k_1 U_{10\_LES} \quad \textbf{(11.1)}$$

Table 11.1. Storms evaluated through the E2ES.

	TD	*TS*	*H1*	*H2*	*H3*	*H4*
Atlantic	1	14	3	0	3	6
Pacific	3	3	4	1	1	4
Total	4	17	7	1	4	10

There is one pair of MV coefficients for each RCG interval that is defined, where RCG is the receiver gain normalized by the range from the specular point to the receiver and transmitter. The error probability of the MV wind speed (U_{10_MV}) will be computed as a function of U_{10_DDMA} and U_{10_LES} such that

$$\text{Prob}_{err}[\text{abs}(U_{10\_MV} - U_{10\_HWRF}) > 2\ I\{U_{10\_DDMA}, U_{10\_LES}, \text{RCG\_range}\}] \quad \textbf{(11.2)}$$

The U_{10_DDMA} and U_{10_LES} values that are outside of the valid ranges of the GMFs will be excluded (i.e., valid range: DDMA = [0.012, 0.704], LES = [0.112, 7.548]).

A three-dimensional probability of error LUT is then created as a function of U_{10_DDMA}, U_{10_LES}, and RCG range with a 0.5 m s^{-1} bin size for wind speeds ranging from 0 to 60 m s^{-1} and the four RCG ranges, <5, [5, 10], [10, 20], and >20. The LUT will be trained using all the storm data from the Atlantic and East Pacific 2010–2011 database.

E. High Wind Speed Validation

Utilizing numerical weather model winds allows for a large number of collocations to be obtained in a relatively short amount of time. Statistically, this permits us to characterize the wind speed performance over a certain range of wind speeds with some confidence. Typically this wind speed range is from about 3 m s^{-1} to approximately 20 m s^{-1}. While the hurricane models can provide wind speeds up to category 5 strength, and even global models provide wind speeds higher than 20 m s^{-1}, the number of collocations is not statistically significant enough to make any robust conclusions.

For validation and performance assessment at the higher wind speeds, other comparison data is required.

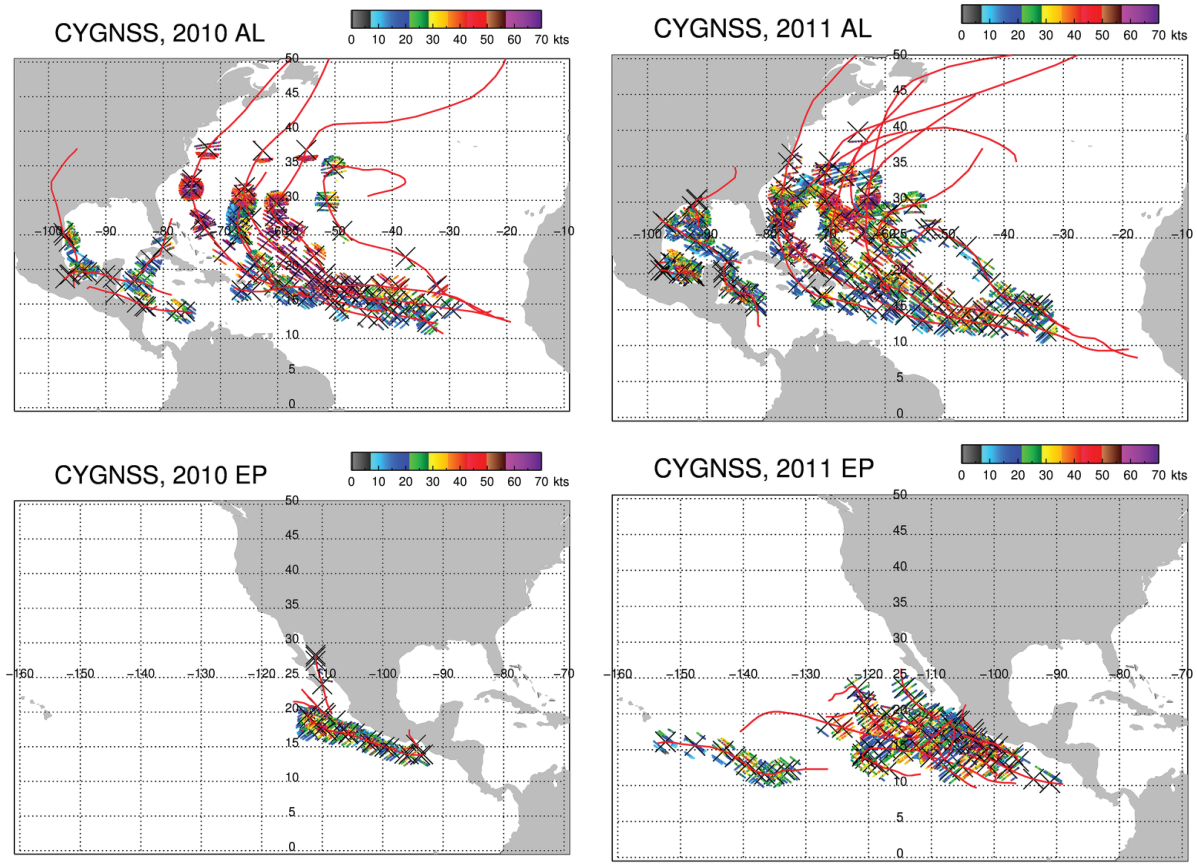

Figure 11.1. Storm tracks for the 43 tropical systems listed in Table 11.1 during 2010–2011 that were run through the E2ES. These tropical systems ranged in intensity from tropical depressions to category 4 strength hurricanes. *Top left panel reused from Said et al. (2016), © 2016 IEEE.*

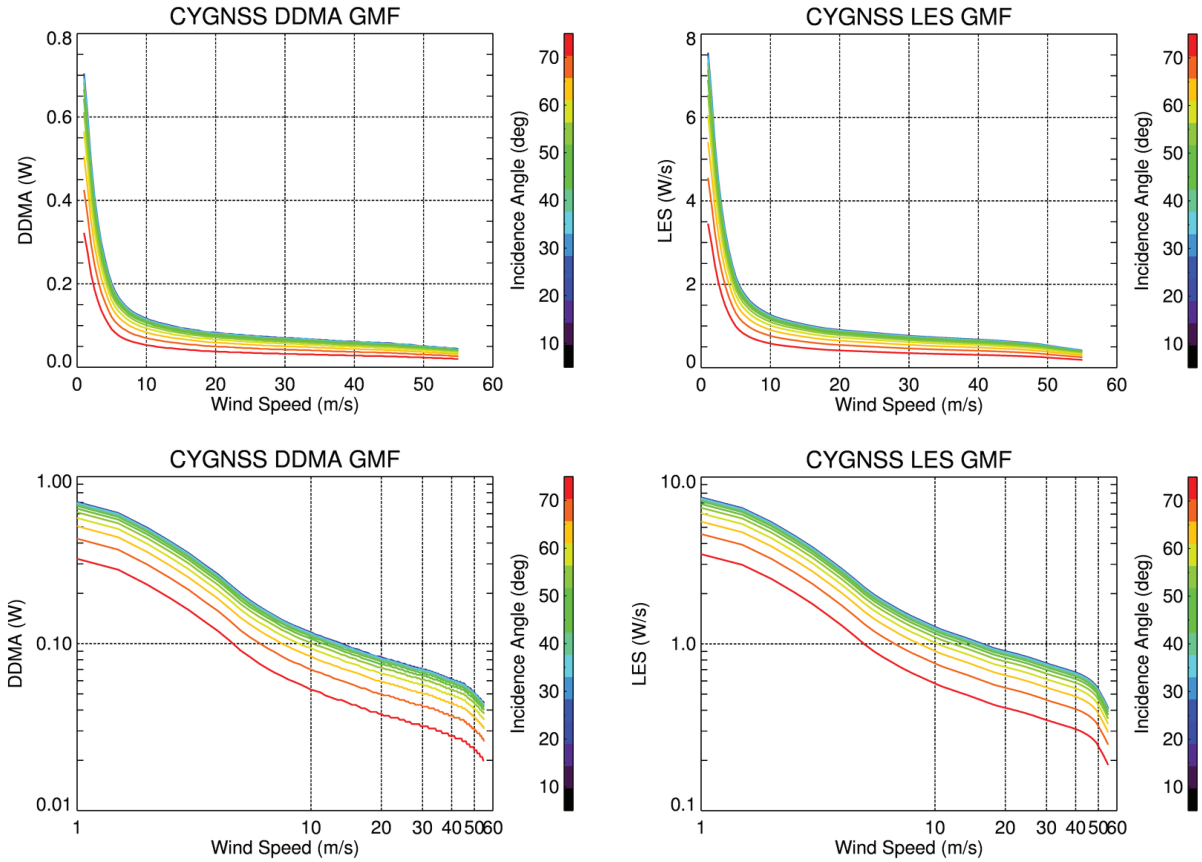

Figure 11.2. Prelaunch DDMA and LES GMFs. *Top two panels reused from Said et al. (2016), © 2016 IEEE.*

Validated wind speed data from other satellite sensors, such as scatterometers, can be compared more directly and provide some higher wind speed validation truth. Scatterometer wind retrievals have proven to be accurate in the hurricane intensities when the wind fields are broad in areal extent compared to the scatterometer footprint. This is typically seen in intense extratropical cyclones but is also encountered in some TCs. During the 2010–11 period of the simulated CYGNSS measurements, both the OSCAT and ASCAT scatterometers were available. A temporal and spatial matchup window criteria of 3 hours and 25 km will be utilized.

Validation at the highest wind speeds in hurricanes will require utilizing data that can accurately sample those winds at the spatial scales at which they occur. This will mean using wind speed data collected from aircraft based measurements such as GPS dropsondes or other remote sensing equipment that might be onboard, such as the Stepped Frequency Microwave Radiometer (SFMR) or the Imagining Wind and Rain Airborne Profiler (IWRAP).

F. Postlaunch Cal/Val Activities

After launch, when real CYGNSS measurements become available, many of the analyses that were done during this prelaunch effort will be repeated. Additional "truth" data will be collocated from available sources. There also exists the possibility of directing some under flights of CYGNSS in hurricanes with the NOAA P-3 aircraft for some additional direct comparison datasets at high wind speeds and in limiting environmental conditions. Being the first space-based GPS bistatic radar constellation system that will systematically provide wind speed retrievals over much of the world's oceans, CYGNSS will provide a unique opportunity to characterize and understand the performance of the GPS bistatic radar measurement technique for ocean surface wind speeds. Being the first also means there is no heritage or experience base that can be directly utilized, such as what exists with microwave imagers (SSM/I, AMSR-E, TMI, SSMIS, AMSR2, GMI, etc.) and microwave scatterometers (QuikSCAT, OSCAT, ASCAT, RapidScat,

etc.). Some of the CYGNSS specific challenges and opportunities include

- Are all of the CYGNSS receiver (and GPS transmitter) calibration characteristics consistent?
  - Evaluate and determine the performance of each receiver.
  - Determine overall system performance.
  - Data from individual CYGNSS receivers will be binned and analyzed to compare receiver characteristics and identify any anomalous behavior.
- What is the sensitivity to effects from other environmental parameters?
  - Sea state (confused seas versus fully developed; i.e., swell conditions)
  - Wind direction
  - Sea surface temperature
  - Rain impacts
  - Using a sufficiently large matchup database, the CYGNSS wind retrievals will be binned by the geophysical parameters of interest and analyzed for any dependencies.
- High wind speed validation
  - The high winds seen by CYGNSS will predominately be within TCs versus extratropical cyclones. Thus the "truth" data used for this validation will largely be a combination of specialized TC remote-sensing products and data collected from hurricane research/reconnaissance flights.
  - Opposite behavior from microwave scatterometers and radiometers: SNR decreases with increasing winds.
- How close to the coast are wind speed retrievals valid?
  - Wind retrievals in the coastal regions will be analyzed for any anomalous behavior as a function of distance to the coast.
  - The impacts of local bathymetry on wave behavior will need to be considered.
- Quality flagging—What quality flags do we need to implement for CYGNSS wind speed retrievals?
  - This will be determined via careful analysis of the collocation dataset.
- Tradeoff between spatial resolution and measurement uncertainty
  - Should we utilize different resolutions in the retrieval process?
- What is the impact of this and how would we automatically determine when to do this?
  - What is the proper balance for TCs given that SNR decreases for higher wind speeds? In essence, finer spatial resolution is required to resolve higher wind speeds in TCs, but this increases the measurement uncertainty.
- TCs present a very dynamic and challenging environment (sharp gradients in precipitation and wind speeds over relatively small spatial scales).
  - CYGNSS wind retrievals will need to be performed at several spatial resolutions. The retrievals will be collocated and binned with other data and analyzed statistically and in detail for individual cases to better quantify the spatial resolution and measurement uncertainty trade space.

Another facet of the validation effort will include engaging the operational forecasters at the NHC. After the hurricane season, the CYGNSS wind retrievals along with proper training will be provided to forecasters to utilize and evaluate during their postseason storm analysis. The objectives of this effort will be to evaluate the value of these data in the operational environment and to get validation feedback from forecasters. Experience has shown that viewing the data from a forecaster's perspective can reveal performance issues that can remain hidden in global statistics. Additionally, should CYGNSS data become available in near real time, an effort will be made to integrate these data into the NHC workstation environment so that it could be utilized and evaluated in near real time.

Reference

Said, F., Soisuvarn, S., Jelenak, Z., & Chang, P. (2016). Performance assessment of simulated CYGNSS winds in the tropical cyclone environment. *IEEE Journal of Selected Topics in Applied Earth Observations and Remote Sensing*. Manuscript in review.

12. NASA CYGNSS Applications Workshop Summary

Scientists from the federal government, research institutes, academia, and the private sector met at the NOAA Federal Complex in Silver Spring during May 27–29, 2015, for the first CYGNSS Applications Workshop. The overall focus of the workshop was to create an initial bridge between science and applications. The primary goal of the workshop was to foster community awareness and engagement with government, academia, and the private sector to identify CYGNSS applications and related science research needs to maximize impact and benefits of the mission. Key outcomes from the workshop are summarized here.

In addition to addressing the primary mission objectives, the workshop also explored applications of soil moisture, hydrology, coastal flooding, ocean wave modeling, and data assimilation. Combined, these accomplishments will allow NASA scientists and hurricane forecasters to provide improved advance warning of hurricane intensification, movement, and storm surge location and magnitude, thus aiding in the protection of human life and coastal community preparedness.

The outcomes of the workshop, which are detailed in the complete report on the NASA CYGNSS Mission Applications Workshop (Murray et al., 2015), comprise two primary elements:

- A report of workshop proceedings
- Detailed applications traceability matrices with requirements and operational considerations to serve broadly for development of value-added tools, applications, and products

In addition, the workshop successfully assembled a broad user team to ensure we are reaching a large applications community that will improve and use applications enabled by the participants of this workshop and establish a plan for a products working group.

In the areas of modeling, forecasting, and tropical convection applications, we recommend using CYGNSS to improve forecast model representation of the MJO. The ability to provide fast-repeat wind sampling unbiased by the presence of precipitation should enable improved observations of convectively induced phenomena such as westerly wind bursts and gust fronts. While lower data latency is always preferred, an MJO can last for several weeks, and CYGNSS data at standard latencies should still make a positive impact in longer term forecasts of MJO position and strength. For these same reasons, CYGNSS will be a valuable source of observations for the verification of other ocean surface wind measurements and numerical weather forecasts. There also are studies planned and applications that may be developed where the current data latency will not be a concern. Additionally, we noted that the CYGNSS fast-repeat wind sampling, especially in precipitating regions, will complement existing polar satellite ocean surface winds and should improve the prediction of atmospheric phenomena with connections to the tropics, such as monsoons, atmospheric rivers, and the extratropical transitions of TCs. For these forecasting applications, a lower data latency would be needed. We also noted that CYGNSS observations will provide a unique data source for coupled atmosphere/wave/ocean data assimilation and modeling—an active area of research that promises to extend numerical weather forecasting to the seasonal and subseasonal ranges.

For monitoring of TCs, we recommend the use of CYGNSS surface wind data to assess the intensity and intensity change rate that is critical for coastal preparations to protect life and property in landfalling storms. Of course, real-time monitoring applications will depend on rapid dissemination of data. TC applications that will also benefit from CYGNSS wind data are coupled atmosphere-ocean model numerical forecasts that can assimilate the unique inner-core observations. In addition, these data may lead to better understanding of the energy and momentum transfers in TCs, which are important for improved predictions.

In the area of coastal, terrestrial, and hydrological applications, we recommend pursuing soil moisture and wetlands extent mapping when CYGNSS samples the continental surfaces. These two applications are the most mature and aligned with the existing capabilities of the L-band sensor and mission design. The fast-repeat sampling characteristics of CYGNSS measurements of soil moisture would add value to existing sensors and possibly allow studies of subdiurnal soil moisture, crop evolution, and flood forecasting. The forward-scattering geometry also makes wetlands extent mapping a logical application and would be high impact since other sensors have difficulty in these conditions. To achieve these two application goals, we strongly recommend that a variable or shorter incoherent integration time be implemented for the land and inland water-surface-reflected signals (potentially using a land mask). A shorter integration time would allow better along-track spatial resolution and subsequent discrimination of changes in surface properties.

In the areas of physical oceanography and surface wave applications, we recommend performing the retrospective research required to improve stand-alone global predictions of the ocean and surface waves and also to improve coupled atmosphere-ocean-wave forecasts for both regional TC and global weather prediction applications. Optimal assimilation of CYGNSS wind measurements by atmospheric models now, and by all components of coupled prediction systems in the future, is the key step toward achieving forecast improvements. More accurate estimation of surface fluxes along with improved surface wind analysis products generated using CYGNSS observations will be highly valuable for evaluating and improving the performance of ocean and wave models within coupled systems. This retrospective work can be performed using the initial planned data latency while successful demonstration of improvements can provide justification for the reduced latency required to improve operational real-time forecasts. Another application achievable in a reasonable time frame is to use Level 3 CYGNSS products in conjunction with other atmosphere-ocean observations to study climate modes, such as the MJO and the ENSO cycle, which have signatures over the tropics and subtropics.

The CYGNSS mission was initially conceived to address the need to improve TC intensity forecasts. More broadly, in the areas of numerical weather forecasting and storm surge forecasting, the potential value of developing a fully coupled atmosphere and ocean model and data assimilation strategy stands out. This coupling of weather, air-sea interactions, and dynamical oceanography is something that the members of the CYGNSS science definition team have already started to address, and there is general agreement that the pay-off in developing applications based on this capability could be huge. For example, in the terrestrial hydrology area, there is an immediate need for a calibrated Level 1 science data product over land. The current Level 1 calibration is specific to the ocean and uses an Earth surface geoid model, rather than the digital elevation map (DEM) needed to work for land surfaces that are not close to sea level. After that, Level 2 algorithm development might be undertaken to produce science data products like soil moisture and related applications. These Level 2 products would then need to be calibrated and validated, and this effort could possibly leverage the instrumented watersheds that have already been developed by NASA for SMAP. Finally, there was a broad and general consensus in each of the workshop breakout sessions that lower data latency would be required to support the development of applications for a wide range of operational data users. This cuts across all the application areas to some degree, and for some of them, it is a critical enabler that must be considered.

Several months after the launch of the CYGNSS mission, currently scheduled for October 2016, the constellation of eight GPS bistatic radar equipped satellites that comprise the CYGNSS constellation is planned to have dispersed into formation to provide reflected GPS data over wide areas. Before then, however, the TechDemoSat-1 mission, a technology demonstration satellite that was launched in July 2014, has been taking data from a single receiver. These data were scheduled for released in the fall of 2015, and it is hoped that they will provide valuable insights for the planning of the next CYGNSS applications workshop, anticipated for soon after the CYGNSS mission is launched.

Building upon the first workshop, which is the subject of this report and entailed the identification of fundamental sciences questions and their potential applications, the focus of the second workshop will be on applications needs and opportunities for the entire panoply of CYGNSS applications to end

users. These users are expected to represent a very broad and diverse swath of the public and private sectors. This will better orient NASA to conduct the OSSEs, modeling and data assimilation, and the sector-specific research that will be needed to build viable applications for CYGNSS data. A concurrent effort for effective outreach and operational implementation through robust activities such as an Early Adopter Program will also be conducted.

While NASA is not an operational agency, it produces groundbreaking technologies, data, and information and accelerates its transition to operations. The NASA Applied Sciences Program's Disasters Area is taking the lead in the development and operational implementation of these applications, many of which are hoped to improve various aspects of national and international disaster planning, response, recovery, and mitigation. To accomplish this, NASA will continue to work closely with the science and applications communities, especially to identify and engage the many potential end users of CYGNSS data and products.

Reference

Murray, J. J., Ruf, C., Baker, N., Lang, T., Uhlhorn, E., Masters, D., Halliwell, G., Carey, K., Helms, D., Escobar, V., McCarty, W., Green D. S., Stough, T., & Molthan, A. (2015). *Report on the NASA CYGNSS mission applications workshop* (NASA-CP-2015-218993), published report, NASA. Retrieved from http://clasp-research.engin.umich.edu/missions/cygnss/reference/cygnss-mission/CYGNSS_Applications_Workshop_May2015.pdf

13. Project Publications

This section provides a table of CYGNSS-related publications and conference presentations at the time this handbook was originally compiled.

Table 13.1. CYGNSS publication list.

Author(s)	*Title*	*Conference/journal and year*	*Date*
Chen, D., Gleason, S., Ruf, C., Adjrad, M.	Spectral dependence of the response time of sea state to local wind forcing	IGARSS 2012	July 22–27
Ruf, C., Gleason, S., Jelenak, Z., Katzberg, S., Ridley, A., Rose, R., Scherrer, J., Zavorotny, V.	The NASA EV-2 Cyclone Global Navigation Satellite System (CYGNSS) mission	IEEE Aerospace Conference, 2013	March 2–9
Park, J., Johnson, J. T., Lowe, S. T.	Studies of GNSS-R ocean altimetry using full DDM-based retrieval	URSI National Radio Science Meeting, 2014	January 8–11
Ruf, C., Clarizia, M. P., O'Brien, A., Ridley, A., Johnson, J., Yi, Y.	The NASA Cyclone Global Navigation Satellite System (CYGNSS) mission	18th Conference on Integrated Observing and Assimilation Systems for Atmosphere, Oceans, and Land Surface, 2014 AMS Annual Conference	February 2–6
Voronovich, A., Zavorotny, V.	Full-polarization modeling of monostatic and bistatic radar scattering from a rough sea surface	IEEE Transactions on Antennas Propagation, 2014	March
Ruf, C., Clarizia, M. P., O'Brien, A., Johnson, J., Ridley, A., Yi, Y.	Enhanced spatial and temporal sampling of air/sea interaction in tropical cyclones by the NASA CYGNSS mission	31st Conference on Hurricanes and Tropical Meteorology, San Diego, CA, 2014	March 31–April 4
Park, J., Johnson, J. T., Lowe, S. T.	A study of the electromagnetic bias in GNSS-R altimetry	IGARSS 2014 / 35th CSRS (Quebec City, Canada)	July 13–18
Powell, S., Akos, D., Zavorotny, V.	GPS SBAS L1/L5 Bistatic Radar Altimeter	IGARSS 2014 / 35th CSRS (Quebec City, Canada)	July 13–18
Rose, R., Ruf, C., Wells, W., Rose, D., Nave, K., Pruitt, J., Dickinson, J.	The CYGNSS Microsatellite Constellation Earth Venture mission	IGARSS 2014 / 35th CSRS (Quebec City, Canada)	July 13–18
Ruf, C., Ridley, A., Clarizia, M. P., Gleason, S., Rose, R., Scherrer, J.	The NASA CYGNSS mission: Design and predicted performance	2014 International Geoscience and Remote Sensing Symposium	July 13–18
Zavorotny, V., Voronovich, A.	Recent progress on forward scattering modeling for GNSS reflectometry	IGARSS 2014 / 35th CSRS (Quebec City, Canada)	July 13–18
Rose, R., Ruf, R., Wells, W., Rose, D., Ridley, A., Nave, K.	Nanosat technology and managed risk: An update of the CYGNSS microsatellite constellation mission development	28th Annual AIAA/USU Conference on Small Satellites (SmallSat; Logan, UT, 2014)	August 5

(*continued*)

Table 13.1. CYGNSS publication list (continued).

Author(s)	*Title*	*Conference/journal and year*	*Date*
Rose, R., Gleason, S., Ruf, C.	The NASA CYGNSS mission: A pathfinder for GNSS scatterometry remote sensing applications	SPIE Remote Sensing Conference (Amsterdam), 2014	September 22–25
Clarizia, M. P., Ruf, C., Jales, P., Gommenginger, C.	Spaceborne GNSS-R minimum variance wind speed estimator	IEEE Transactions on Geoscience Remote Sensors, 2014	November
Ruf, C., Clarizia, M. P., Gleason, S., Rose, R., Ridley, A.	The NASA Cyclone Global Navigation Satellite System (CYGNSS) mission	Advanced RF Sensors and Remote Sensing Instruments 2014	November 4–7
Zavorotny, V., Gleason, S., Cardellach, E., Camps, A.	Tutorial on remote sensing using GNSS bistatic radar of opportunity	IEEE Geoscience and Remote Sensing Magazine, 2014	December
Fritz, M., Shoer, J., Singh, L., Henderson, T., McGee, J., Rose, R., Ruf, C.	Attitude determination and control system design for the CYGNSS microsatellite	IEEE Aerospace Conference, 2015	March 7–14
Rose, R., Ruf, C., Scherrer, J., Wells, J.	The CYGNSS flight segment; mainstream science on a micro-budget	IEEE Aerospace Conference, 2015	March 7–14
Shoer, J., Singh, L., Henderson, T.	Conical scanning approach for sun pointing on the CYGNSS microsatellite	IEEE Aerospace Conference, 2015	March 7–14
Wells, J., Scherrer, J., Van Noord, J., Law, R.	Early development of the first earth venture mission: How CYGNSS is using engineering models to validate the design	IEEE Aerospace Conference, 2015	March 7–14
Said, F., Soisuvarn, S., Katzberg, S., Jelenak, Z., Chang, P. S.	Estimation of maximum hurricane wind speed using simulated CYGNSS measurements	Geoscience and Remote Sensing Symposium (IGARSS), 2015	July 26–31
Buchanan, M., O'Brien, A., Block, B.	Design of a ground-based beacon signal for calibration of spaceborne GNSS remote sensing instruments	ION GNSS+ 2015	September 18
Rodriguez-Alvarez, N., Garrison, J. L.	Generalized linear observables for ocean wind retrieval from calibrated GNSS-R delay-Doppler maps	Geoscience and Remote Sensing, IEEE Transactions 2015	September 22
Ruf, C. S., Atlas, R., Chang, P. S., Clarizia, M. P., Garrison, J. L., Gleason, S., Katzberg, S. J., Jelenak, Z., Johnson, J. T., Majumdar, S. J., O'Brien, A., Posselt, D. J., Ridley, A. J., Rose, R. J., Zavorotny, V. U.	New ocean winds satellite mission to probe hurricanes and tropical convection	Bulletin of the American Meteorological Society, 2016	

14. Acronyms

ADCS	attitude determination and control system
AER	automated event recognition
AMSR	Advanced Microwave Scanning Radiometer
AMSR2	Advanced Microwave Scanning Radiometer 2
AMSR-E	Advanced Microwave Scanning Radiometer—Earth Observing System
ASCAT	Advanced Scatterometer
ATBD	algorithm theoretical basis document
BRCS	bistatic radar cross section
C/A	course acquisition
Cal/Val	calibration and validation
CCSDS	Consultative Committee for Space Data Systems
CDR	critical design review
CEOS	Committee on Earth Observation Satellites
CFDP	CCSDS File Delivery Protocol
CFSR	Climate Forecast System Reanalysis Dataset
COAMPS-TC	Coupled Ocean Atmosphere Mesoscale Prediction System Model
CU	University of Colorado
CYGNSS	Cyclone Global Navigation Satellite System
DAAC	(NASA) Distributed Active Archive Center
DD	delay Doppler
DDM	delay Doppler map
DDMA	delay Doppler map area
DDMI	delay Doppler mapping instrument
DEM	digital elevation map
DM	deployment module
DMR	delay mapping receiver
DOY	day of year
DWS	delay waveform slope (same as LES)
E2ES	end-to-end simulator
ECEF	Earth centered Earth fixed (coordinate system)
ECI	Earth centered inertial (coordinate system)
ECMWF	European Centre for Medium-Range Weather Forecasts
EFOV	effective field of view
EIRP	equivalent isotropically radiated power
EM	electromagnetic
EnKF	ensemble Kalman filter
ENSO	El Niño Southern Oscillation
ERS	European Remote Sensing Satellite
ESSP	Earth System Science Pathfinder Program
FPGA	field-programmable gate array
FWHM	full width half maximum
GFDL	Geophysical Fluid Dynamics Laboratory
GFS	Global Forecast System (from NOAA)
GMF	geophysical model function
GMI	GPM Microwave Imager
GNSS	global navigation satellite system
GNSS-R	global navigation satellite system reflectometry
GO	geometric optics
GOES	Geostationary Operational Environmental Satellites
GOTS	government off-the-shelf
GPM	Global Precipitation Measurement (satellite)
GPS	global positioning system
GPS-R	GPS-reflectometry
GSI	Gridpoint Statistical Interpolation
HWRF	Hurricane Weather Research and Forecasting Model
Hybrid	Hybrid GSI and EnKF Data Assimilation Scheme
IDW	integrated delay waveform
IFOV	instantaneous field of view
IGS	international GNSS service
IKE	integrated kinetic energy
IOC	initial operational capability
ITOS	Integrated Test and Operations System
ITU	International Telecommunication Union
IWRAP	Imagining Wind and Rain Airborne Profiler
KA	Kirchhoff approximation

LES	leading edge slope
LGEM	Logistic Growth Equation Model
LHCP	left hand circularly polarized
LNA	low noise amplifier
LUT	lookup table
MJO	Madden-Julian Oscillation
MOC	Mission Operations Center
MSS	mean square slope (appears as *mss* in equations)
MV	minimum variance
NASA	National Aeronautics and Space Administration
NAVGEM	Navy Global Environmental Model
NBRCS	normalized bistatic radar cross section
NCEP	National Centers for Environmental Prediction
NDBC	National Data Buoy Center
NESDIS	National Environmental Satellite, Data, and Information Service
NF	noise figure
NHC	National Hurricane Center
NMC	Network Management Center
NOAA	National Oceanic and Atmospheric Administration
NR	nature run
NSCAT	NASA Scatterometer
NWP	national weather prediction
OSCAT	Oceansat-2 Scatterometer
OSE	observing system experiment
OSSE	observing system simulation experiment
PDF	probability density function
PDR	preliminary design review
PI	principal investigator
PO.DAAC	(NASA) Physical Oceanography Data Active Archive Center
POES	Polar-Orbiting Environmental Satellites
PPT	peak power tracker
PRN	pseudorandom noise
QuikSCAT	NASA's Quik Scatterometer
RCG	range corrected gain
RFI	radio frequency interference
RHCP	right hand circularly polarized
RMS	root mean square
RSS	root sum square
RTM	radiative transfer model
Rx	receiving
SAR	synthetic aperture radar
SFMR	Stepped Frequency Microwave Radiometer
SHIPS	Statistical Hurricane Intensity Prediction Scheme Model
SIR	system integration review
SMMR	Scanning Multichannel Microwave Radiometer
SNC	Sierra Nevada Corporation
SNR	signal-to-noise ratio
SOC	Science Operations Center
SP	specular point
SRR	system requirements review
SSA	small slope approximation
SSA1	small slope approximation of the 1st order
SSA2	small slope approximation of the 2nd order
SSM/I	Special Sensor Microwave Imager
SSMIS	Special Sensor Microwave Imager/Sounder
SSS	sea surface salinity (sometimes *S* in equations)
SST	sea surface temperature (sometimes *T* in equations)
SWH	significant wave height
SwRI	Southwest Research Institute
TA	time averaging
TBD	to be determined
TC	tropical cyclone
TD	tropical depression
TMI	TRMM Microwave Imager
TRMM	Tropical Rainfall Measuring Mission (and satellite)
Tx	transmitting
UK	United Kingdom
UKMET	UK Meteorological Office
UM	University of Michigan
USN	Universal Space Network
UTC	Coordinated Universal Time
WAF	Woodward ambiguity function
WGCV	Working Group on Calibration and Validation
WRF	Weather Research and Forecasting Model

Appendix. Ocean Surface Bistatic Scattering Forward Model

I. Propagation

CYGNSS uses the GPS L1 frequency (1575 MHz), which suffers negligible rain attenuation, even under heavy precipitating conditions. For completeness, the expression for rain path attenuation, G_{rain}, is given by

$$G_{rain} = \exp(-\alpha h(\csc\theta_t + \csc\theta_r)) \quad \textbf{(A.1)}$$

where h is the freezing level in km, α is the specific attenuation (dB km^{-1}), and θ_t and θ_r are elevation angles to the transmitter and receiver, respectively. Note that each of these parameters will vary over the ocean surface, and this spatial variation is included in the complete forward model. For simplicity, the model assumes a constant rain rate from the surface up to the freezing level.

The specific attenuation α is obtained from the International Telecommunication Union (ITU) R838-3 model:

$$\alpha = aR^b \quad \textbf{(A.2)}$$

where R is the rain rate (mm hr^{-1}) and the coefficients a and b for circular polarization at the GPS L1 frequency are $a = 24.312 \times 10^{-5}$ and $b = 0.9567$. The values of the coefficients have been developed by curve-fitting to power-law coefficients derived from scattering calculations.

Figure A.1 shows a plot of rain attenuation versus rain rate for a freezing level of 6 km. In the figure, each curve corresponds to a different elevation angle. (The elevation angle to the receiver and transmitter are assumed equal, as would be the case at the SP.)

It should be noted that in simulated hurricane wind fields, extremely large rain rates have been observed; however, these convective cells are highly localized, move very rapidly, and evolve very quickly. While they can have a high rain rate, it typically last for only a few minutes. So the peak rain rates are very high but only occur for brief periods in fast-moving cells. Furthermore, the nature of the GPS ambiguity function causes the rain field to be effectively smoothed over approximately a 20 km area (in the same way as the wind fields are smoothed), so that the effects of small regions of high rain attenuation are effectively reduced.

II. Rough Surface Scattering

A. Introduction

In GPS bistatic radar, the complex amplitude of the received signal (the voltage) is cross correlated with

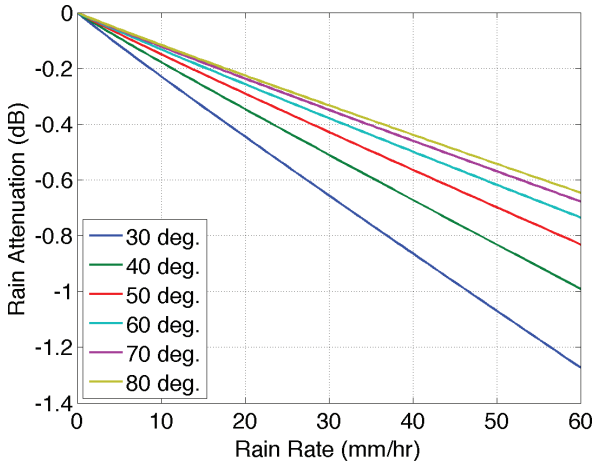

Figure A.1. Rain attenuation versus rain rate for various elevation angles.

a replica of the emitted signal over a coherent integration time, T_i. This procedure is often referred to as match-filter signal processing. The end result of this type of coherent signal processing is an ability to form a synthetic footprint that would ultimately determine the shape of the recorded 1D waveform (IDW), or 2D DDM, and the spatial resolution of the GPS bistatic radar. For every epoch, t_0, the code cross correlation relative to the received signal, u, taken at a variety of delays, τ, can be expressed as the integral (Parkinson et al., 1996; Zavorotny & Voronovich, 2000)

$$Y(t_0,\tau,f_c) = \int_0^{T_i} a(t_0+t')u(t_0+t'+\tau)\exp(2\pi i f_c t')dt' \quad \textbf{(A.3)}$$

Here Ti is the coherent integration time, and $a(t)$ is the replica of the PRN code sequence taking values of {−1,+1} over a time duration, τ_c. The coherent integration time Ti should be comparable to or smaller than the coherence time, τ_{cor}, of the scattered field at the receiver point in order to perform the convolution procedure (Equation A.3) with linear phase shift between replica $a(t)$ and signal $u(t)$. The oscillating factor containing f_c is meant to compensate for a possible Doppler shift of the signal $u(t)$ associated with this phenomenon. For signals received from spacecraft, the signal coherence time τ_{cor} has been observed to be on the order of 1 ms (Gleason et al., 2005; Gleason, 2006), while signals received from aircraft can remain coherent for considerably longer durations, on the order of 5–10 ms, depending on aircraft speed and altitude.

Only scattered waves with equal time delays and equal Doppler shifts could be successfully aligned with the code replica in order to produce a maximum correlation according to Equation A.3, and this always happens within the so-called glistening zone caused by a random distribution of the surface slopes. The size of the glistening zone is driven by the variance of surface slopes, where the larger the variance of surface slopes, the larger the glistening zone extends across the surface.

The scattering toward the receiver is produced mostly by specular reflections from a statistical ensemble of large scale (larger than several radio wavelengths) slopes of the surface. Therefore, the strongest scattered signal comes only from the center of the glistening zone near the nominal SP on the mean sea surface. Away from the glistening zone, the contribution from the quasi-specular reflections diminishes, eventually to be replaced with significantly weaker diffraction scattering from a small-scale surface component. Here we neglect this type of scattering, as it is too weak to make a significant contribution to the total received signal power. Using this understanding for the physical scattering mechanism, we can apply a Kirchhoff theoretical model to estimate the expected scattering behavior (Bass & Fuks, 1979). In essence, we are combining an ensemble of "smooth" reflection surfaces together to represent the signal scattering from a rough ocean surface, where every point on the surface is approximated by a local tangent plane.

The scattered GPS signal, $u(t)$, arriving at receiver position, $\vec{R}_r$, can then be modeled by the integral taken over the mean sea surface (Zavorotny & Voronovich, 2000):

$$u(\vec{R}_r,t) = \int D(\vec{\rho})a\left[t-(R_0(t)+R(t))/c\right]g(\vec{\rho},t)d^2\rho \quad \textbf{(A.4)}$$

where $D(\vec{\rho})$ is the amplitude footprint of the receiver antenna; $a(t)$ is the GPS signal PRN code; and $R0(t)$ and $R(t)$ are distances from the transmitter and the receiver, respectively, to some point $(\vec{\rho}, z=\zeta(\vec{\rho},t))$ on the "smoothed" rough sea surface with an elevation of $\zeta(\vec{\rho},t)$, fluctuating about the mean surface level. Over the individual local tangent planes, the Earth's curvature is neglected, $\vec{\rho}=(x,y)$, the transmitter and receiver positions are in the $x = 0$ plane, and z is a vertical axis or local surface normal.

The above analysis applies to the scattering of signals from surface components with spatial scales of at least several wavelengths greater than the incident carrier wavelength (i.e., the GPS L1 wavelength is ~19 cm). Alternatively, the contribution to scattering from surface components with spatial scales smaller than several radio wavelengths can be calculated separately using perturbation theory. Additionally, serious limitations occur for scattering at low grazing angles and from very rough surfaces. In this case, more sophisticated scattering models that take into account multiple scattering and diffraction effects due to sharp edges are required. On the other hand, when surfaces are very even and flat (such as with lakes and seas under low wind conditions or first-year, young

ice), the coherent component rises in the scattered GPS signal. Writing an expression for the received coherent component is a rather simple task.

In the KA, the function g describes the propagation and scattering processes:

$$g(\vec{\rho},t) = -\Re(\vec{\rho})q^2 \exp\left[ik\left(R_0(t)+R(t)\right)\right] / 4\pi i R_0 R q_z \quad \textbf{(A.5)}$$

where $\Re$ is the Fresnel reflection coefficient; $\vec{q} = k(\vec{n}-\vec{m})$ is the so-called scattering vector, where $k = 2\pi/\lambda$ is the wave number; $\vec{m}$ is the unit vector of the incident wave; and $\vec{n}$ is the unit vector of the scattered wave. Upon substituting Equation A.5 into A.4, and then into A.3, and assuming that integration over the accumulation time T_a is equivalent to averaging over a statistical ensemble of surface elevations via

$$\left\langle \left|Y(\tau,f)\right|^2 \right\rangle = \frac{1}{T_a}\int_0^{T_a} \left|Y(t_0,\tau,f)\right|^2 dt_0 \quad \textbf{(A.6)}$$

and after making some additional assumptions, we arrive at the bistatic radar equation for the DDM (Zavorotny & Voronovich, 2000):

$$\left\langle \left|Y_s(t_0,\tau,f)\right|^2 \right\rangle = T_i^2 \frac{P_T G_T \lambda^2 G_R}{(4\pi)^3} \iint F(\vec{\rho})\Lambda^2(\tau,\vec{\rho})\left|S(f,\vec{\rho})\right|^2 R_0^{-2}R^{-2}\sigma_0(\vec{\rho})d^2\rho \quad \textbf{(A.7)}$$

where P_T is the transmitter power; G_T is the transmit antenna gain; G_R is the receive antenna gain; $F(\vec{\rho})$ is the normalized directivity (beam) pattern for the receive antenna; $\Lambda^2(\tau,\vec{\rho})$ is the annulus function due to the cross correlation with the replica; $\left|S(f,\vec{\rho})\right|^2$ is the Doppler zone function due to the relative motions of both the transmitter and receiver with respect to the scattering surface; R_0 and R are distances from a point $\vec{\rho}$ on the surface to the transmitter and receiver, respectively; and $\sigma_0(\vec{\rho})$ is the NBRCS of the rough surface, which is generally a function of two angles, the incidence angle, and the scattering angle. Here, in Equation A.7, it is written as a function of surface coordinates. The scattered signal comes from the area formed by the intersection of the iso-range zones (from the annulus function, $\Lambda^2(\tau,\vec{\rho})$) and iso-Doppler zones (from the Doppler zone function, $\left|S(f,\vec{\rho})\right|^2$). The width of the iso-range zone depends on the code length (different for course acquisition [C/A] and P codes) and on all relevant geometric parameters of the problem. The width of the Doppler zone depends on the receiver velocity and is inversely proportional to the coherent integration time, as given by $f_{Dop} = 2/T_i$.

The product of the correlation function $\Lambda(\tau)$ and the Doppler zone function constitutes the WAF originally introduced in radar technique. The WAF that enters Equation A.7 is similar to the WAF used in the unfocused SAR technique (Elachi, 1988). For fixed positions of the transmitter and the receiver, both WAF and NBRCS are functions of the reference surface S coordinates. Looking at Equation A.7, it is straightforward to conclude that the DDM emerges as a convolution of the WAF with NBRCS function, σ_0. The WAF is close to unity within an area formed by the annulus zone and the Doppler zone and tends to zero outside of this area. The geometry of these zones for two different elevation angles for a typical spacecraft receiver is shown in Figures A.2a and A.2b.

B. Delay and Doppler Coordinate System

Consider the properties of the delay and Doppler zone in more detail. The scattered signal can be thought of as a superposition of components scattered from various points on the sea surface. Each component will have a shift in both the time at which the signal arrives at the receiver (delay shift) and the frequency of the signal (Doppler shift). The diversity in delay is due to different paths followed by each scattered signal, while different frequency shifts are caused by the relative motion between the transmitter, the scattering point on the surface, and the receiver. Each point in the glistening zone is therefore characterized by its own delay and Doppler shift.

The pair of delay-Doppler (DD) values to which each point in space can be associated represents a new domain in which the glistening zone can be mapped, and this is referred to as the delay-Doppler domain. Such a domain is fundamental for bistatic radar processing since it is the domain in which bistatic radar data are commonly presented and mapped, in the form of DDMs. However, different points on the sea surface will correspond to the same pair of delay-Doppler values. Lines corresponding to constant delays (iso-range) and constant Doppler shifts

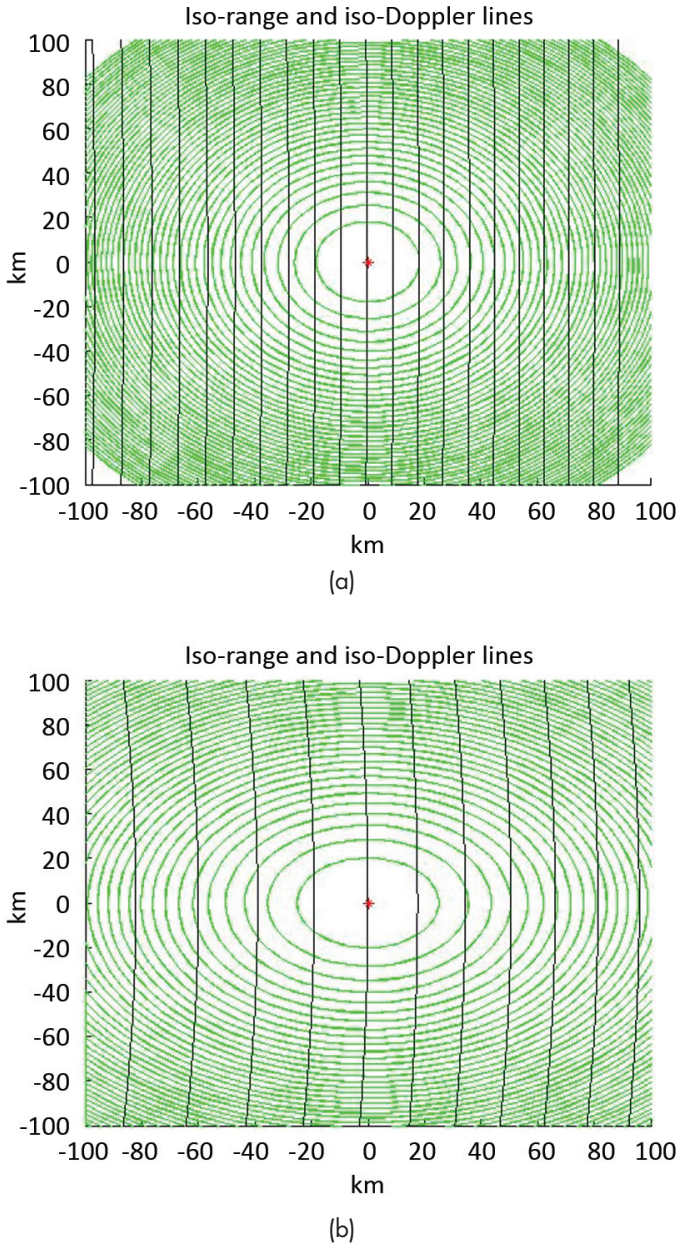

Figure A.2. Surface iso-range and iso-Doppler lines for cases of 10° (a) and 40° (b) incidence. *Figure taken from "GNSS Applications and Methods," Gleason & Gebre-Egziabher (© 2009), reused with authors' permission.*

(iso-Doppler) can be identified on the sea surface, and they have an elliptical and parabolic shape, respectively. Lines of constant delays, also called iso-range lines, are given by concentric ellipses around the SP, and they correspond to increasing delays for increasing distance from the SP, which is the point of minimum delay. Rigorously speaking, the iso-range lines are the intersections of spheroids (equi-range surfaces) having the receiver and transmitter as foci, with the sea surface, which causes the ellipses to be not exactly concentric as their centers move toward the transmitter (Zuffada et al., 2004). The iso-Doppler lines are parabolic shaped lines cutting through the glistening zone. They are also asymmetric and characterized by complicated equations, and lines of lower and higher Doppler frequency shifts cannot be predicted, since they strictly depend on the relative velocities among the transmitter, the scattering point

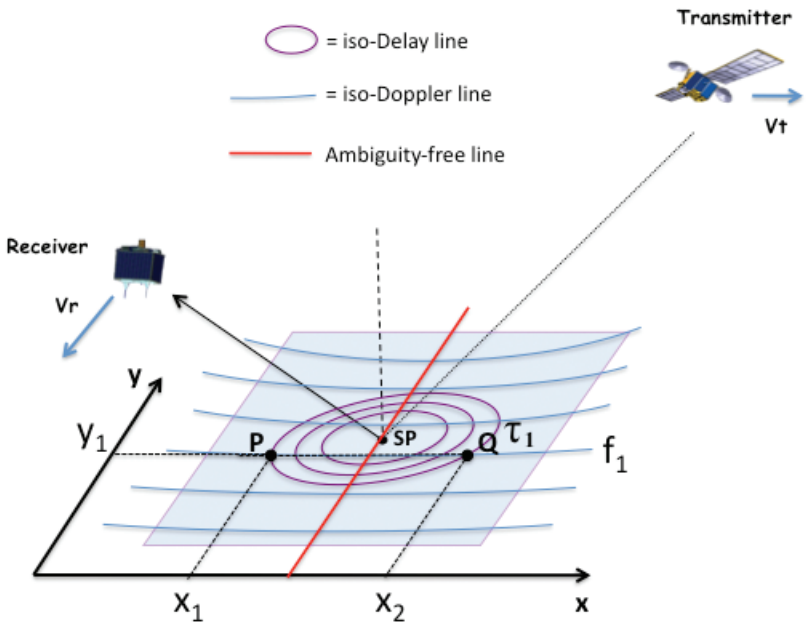

Figure A.3. DD coordinates in bistatic radar and their relation to the space coordinate system. *Reused from Clarizia & Ruf (2016), © 2016 IEEE.*

and the receiver. From Figure A.3, we note that a generic point, *P*, on the glistening zone can be described by a delay and Doppler coordinate. Such a correspondence is, however, not unique, as there is an ambiguity since the intersection between an iso-range and iso-Doppler line consists of two points in space, which will have the same delay and Doppler frequency, such as the points *P* and *Q* in Figure A.3. Despite that, it is interesting to note that there exists a line free of ambiguity, which can be thought of as the transverse axis of the hyperbolic iso-Doppler lines, shown in red in Figure A.3.

The space-to-DD transformation of coordinates is also what gives the DDM a characteristic horseshoe shape. Such transformation operates on the spatial domain by "folding" the glistening zone along the free ambiguity line and by "bending" it at the SP, or at the peak power point in the DDM. The scattered power at the SP corresponds, therefore, to the central point of the horseshoe shape, and the horseshoe branches correspond to the scattered power from the glistening zone, with areas farther from the SP spanning larger delays and Doppler shifts.

One other important aspect of the DD coordinate system is its dependence on the geometry, and in particular on the incidence angle, which strongly influences the configuration of the iso-delay and iso-Doppler lines. Figure A.4 shows the change in the iso-delay contours over a footprint of 100 × 100 km^2, for different incidence angles, where the incidence angle is the angle between the transmitter or receiver range and the normal to the surface. The iso-delay ellipses tend to stretch out and become wider for higher incidence angles. Here the transmitter and receiver altitudes have been assumed to be ~20,200 km and 475 km, respectively.

Figure A.5 shows the range of maximum delays (a) and maximum Doppler frequencies (b) within a 50 × 50 km footprint, as a function of incidence angle. In Figure A.5b, a specific velocity vector has been assumed for the GPS and the receiver satellite. In principle, once the geometry is known (i.e., transmitter and receiver altitudes, incidence angles and velocity vectors), the range of delays and Doppler frequencies spanned by a footprint of given size can be calculated numerically.

C. The Bistatic Radar Cross Section: Geometric Optics (GO) Approximation

The effect of surface roughness is described by σ_0, the NBRCS of the rough surface. In the geometric-optics limit of the Kirchhoff approximation, this term is represented by the following expression (Barrick, 1968; Bass & Fuks, 1979):

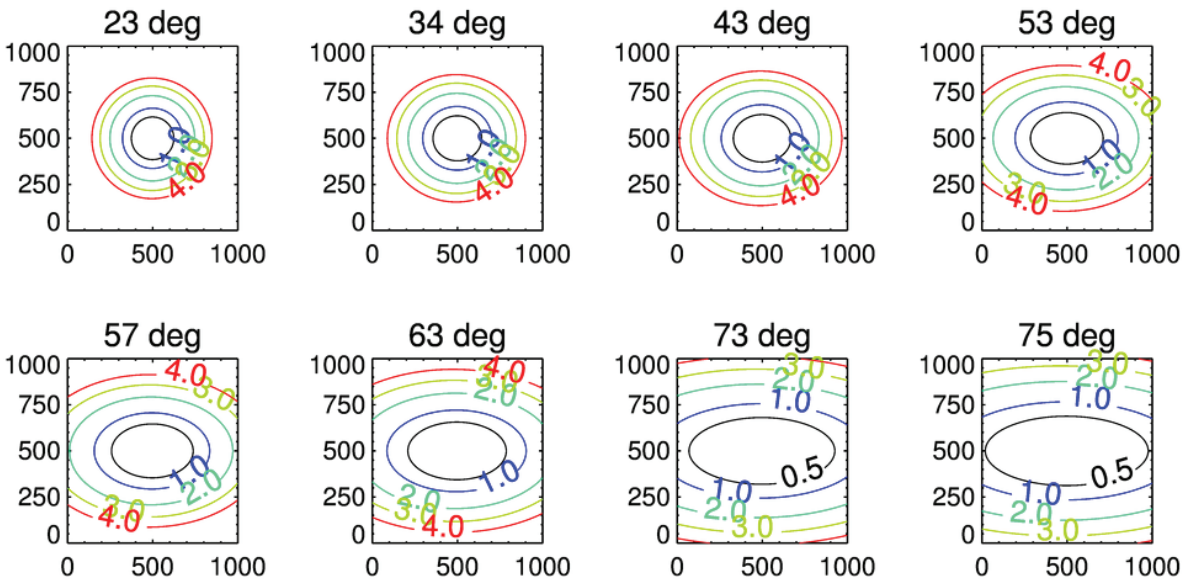

Figure A.4. Iso-delay contours over a footprint of 100 × 100 km, for the following incidence angles (top, left to right): 23°, 34°, 43°, 53°; (bottom, left to right): 57°, 63°, 73°, 75°.

$$\sigma_0 = \pi \left|\Re\right|^2 \left(q / q_z\right)^4 P\left(-q_\perp / q_z\right) \qquad \textbf{(A.8)}$$

Although this value is a function of the scattering vector, $\vec{q}$, for fixed positions of the transmitter and the receiver above a surface, this vector can be regarded as a function of the coordinate $\vec{\rho}$ in the mean surface plane. The value of σ_0 depends on the complex Fresnel coefficient $\Re$, which in turn depends on a signal polarization state; the complex dielectric constant of the reflecting medium, ε; and the local incidence angle. In the case of GPS, the polarization state of the reflected signal is LHCP. In this case, the Fresnel reflection coefficient $\Re$ for seawater is

$$\Re = \frac{1}{2}\left[\frac{\varepsilon\cos\theta - \sqrt{\varepsilon - \sin^2\theta}}{\varepsilon\cos\theta + \sqrt{\varepsilon - \sin^2\theta}} - \frac{\cos\theta - \sqrt{\varepsilon - \sin^2\theta}}{\cos\theta + \sqrt{\varepsilon - \sin^2\theta}}\right] \qquad \textbf{(A.9)}$$

where ε is the complex dielectric permittivity of seawater and θ is the local incidence angle (Zavorotny & Voronovich, 2000).

According to the Klein-Swift model (Klein & Swift, 1977), at S = 35 ppt and T = 10°C, ε = 74.62+i51.92 for L1 = 1.57542 GHz and ε = 75.02+i62.39 for L2 = 1.22760 GHz. At S = 30 ppt T = 10°C ε = 76.16+i55.30 for L1; ε = 75.02+i62.39: for L2.

Factor $P(\vec{s})$ in Equation A.8 is the PDF of large scale "smoothed" surface slopes, $\vec{s} = \nabla_\perp \zeta(\vec{\rho})$. Usually the most probable orientation of surface slopes is parallel to the mean plane, $z = 0$. Then the PDF has a maximum at $s = 0$, and the bistatic cross section σ_0 has a maximum at $\vec{q}_\perp = 0$ (i.e., in the nominal specular direction with respect to the mean surface). Note that the width of σ_0 in terms of ρ describes a glistening zone produced by quasi-specular points on the surface.

Some GPS reflection receivers have the capability to sample the waveform only with respect to time delay, τ, while the frequency offset f is fixed and intended to compensate the Doppler shift associated with the nominal SP on the Earth's surface. In this case, we deal with 1D delay waveforms, as shown in Figure A.6. The leading edge of such waveforms up to the peak value is produced by the central elliptic annulus zone (filtered by the S function) when it expands from zero to its maximal value. The 1D waveform forms a decreasing trailing edge after the peak because of the WAF's behavior as a function of time lag and/or because of the BRCS recession in radial directions according to the distribution of surface slopes. As a result of the latter reason, the specific shape of the leading edge and the exact position of the correlation power peak are functions of surface roughness. For rougher surfaces, the leading edge is more stretched, and the peak is more shifted toward later time lags.

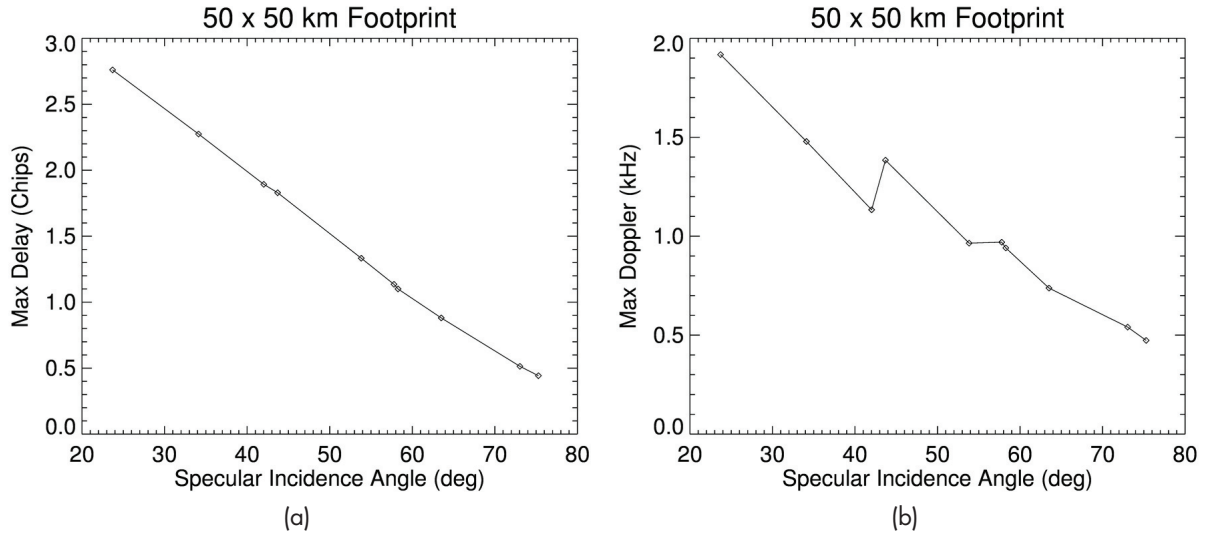

Figure A.5. (a) Maximum delay as a function of incidence angle, within a 50 × 50 km^2 footprint; (b) maximum Doppler frequency as a function of incidence angle, within the same footprint.

Equation A.7 deals with values obtained by averaging over a limited number of independent samples. Such values themselves contain residual noise, which might affect our ability to accurately measure the average waveform. (The issue of noise in waveforms and their impact on the accuracy of remote sensing of ocean wind is addressed in Part III, "Statistics of the GPS Reflected Signal," of this Appendix.) Equation A.7 relies on the condition that $T_i < \tau_{cor}$. The coherence time can be estimated as $\tau_{cor} = \rho_{coh} / v_r$, where ρ_{coh} is the coherence length of the scattered field at the reception point and v_r is the velocity of the receiver. According to Van-Cittert-Zernike theorem, ρ_{coh} in the far zone increases linearly with the distance from the instantaneous footprint patch on a scattering surface. The size of the footprint patch, or in our case, an annulus zone, depends on the current time delay between the replica and the reflected signal. Therefore a computation of the coherence time becomes a nontrivial problem that was addressed in Zuffada and Zavorotny (2001), You et al. (2004), and You et al. (2006).

The strength of the bistatically scattered signal from the ocean surface is mostly affected by the surface roughness, since variations in salinity of the ocean are rather small. It is believed that for linear surface gravity waves, the slope PDF $P(\vec{s})$ can be approximated by the anisotropic bivariate Gaussian distribution (Zavorotny & Voronovich, 2000; Soulat, 2004; Elfouhaily et al., 2002):

$$P(\vec{s}) = \frac{1}{2\pi\sqrt{\det(M)}} \exp\left[-\frac{1}{2}\begin{pmatrix} s_x \\ s_y \end{pmatrix}^{\dagger} M^{-1} \begin{pmatrix} s_x \\ s_y \end{pmatrix}\right] \qquad \textbf{(A.10)}$$

where matrix M is

$$M = \begin{pmatrix} \cos\varphi_0 & -\sin\varphi_0 \\ \sin\varphi_0 & \cos\varphi_0 \end{pmatrix} \cdot \begin{pmatrix} \sigma_u^2 & 0 \\ 0 & \sigma_c^2 \end{pmatrix} \cdot \begin{pmatrix} \cos\varphi_0 & \sin\varphi_0 \\ -\sin\varphi_0 & \cos\varphi_0 \end{pmatrix} \qquad \textbf{(A.11)}$$

where φ_0 is the angle between the up-down wind direction and *x*-axis, which is chosen here to lie within the incidence plane; σ_u^2 is an upwind MSS; and σ_c^2 is a crosswind MSS. $\sigma_{u,c}^2$ are wind dependent and can be derived from a surface elevation spectrum $\Psi(\vec{\kappa})$ by integration over wave numbers κ smaller than a scale-dividing wave number κ_*. Sometimes it is convenient to characterize the statistics of slopes by a single parameter, called a total MSS. There are two definitions of the total MSS. One is the arithmetic

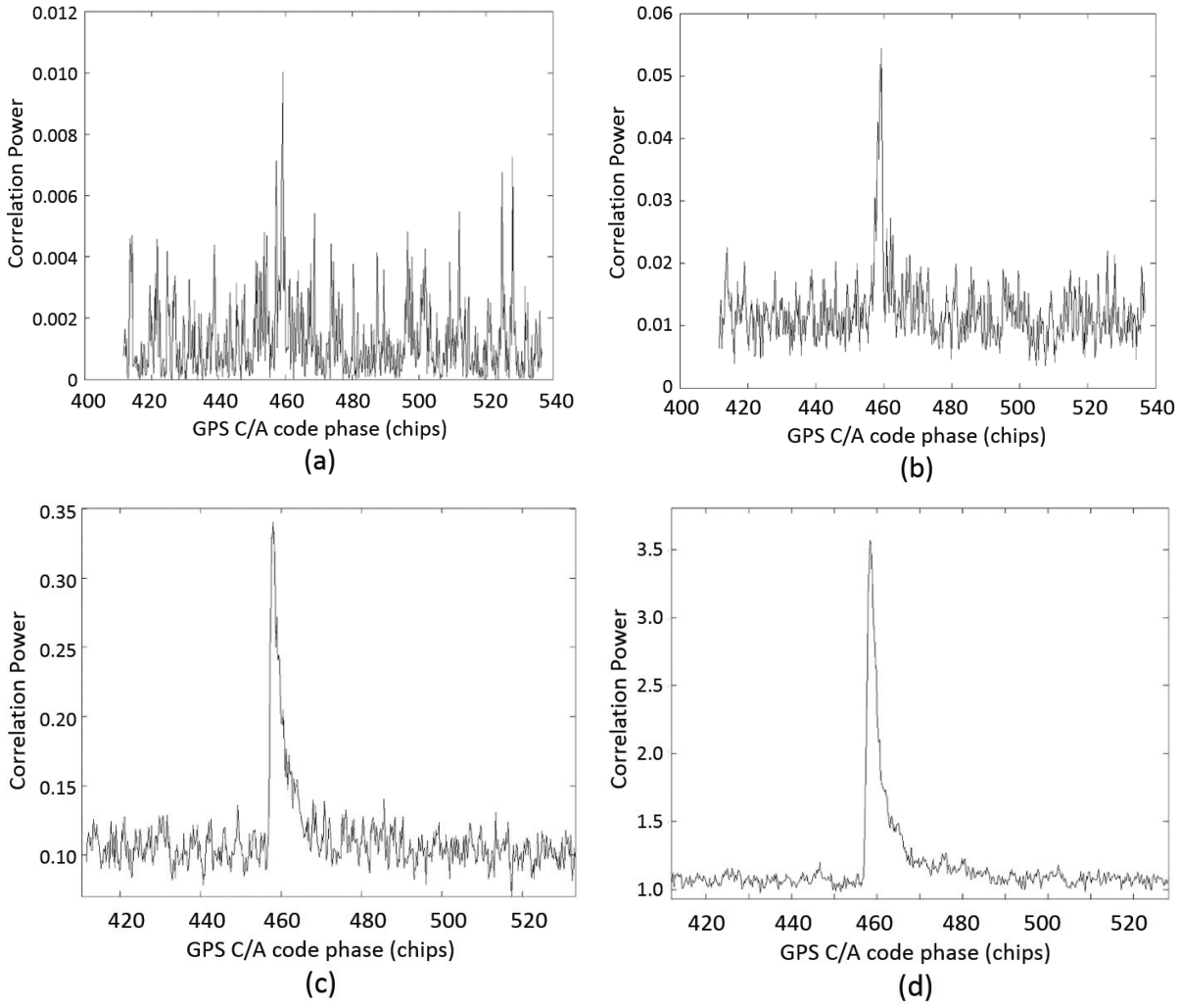

Figure A.6. Examples of GNSS reflected waveforms observed in the UK-DMC satellite experiment on March 23, 2004, for GPS satellite PRN28, using incoherent integration times of (a) 1 ms, (b) 10 ms, (c) 100 ms, and (d) 1 s. *Figure taken from "GNSS Applications and Methods," Gleason & Gebre-Egziabher (© 2009), reused with authors' permission.*

mean of the two orthogonal components (Elfouhaily et al., 1997):

$$\sigma_{tot,1}^2 = \sigma_u^2 + \sigma_c^2 \tag{A.12}$$

Another definition of the total MSS is the geometric mean of the two orthogonal components (Soulat, 2004):

$$\sigma_{tot,2}^2 = 2\sigma_u\sigma_c \tag{A.13}$$

The definition in Equation A.12 is used more frequently in the literature.

Regardless of the wind direction, Equation A.10 can be rewritten in general Cartesian terms as

$$P(\vec{s}) = \frac{1}{2\pi\sigma_x\sigma_y\sqrt{(1-b_{x,y}^2)}} \exp\left[-\frac{1}{2(1-b_{x,y}^2)}\left(\frac{s_x^2}{\sigma_x^2} - 2b_{x,y}\frac{s_x s_y}{\sigma_x\sigma_y} + \frac{s_y^2}{\sigma_y^2}\right)\right] \tag{A.14}$$

where σ_x^2 and σ_y^2 are MSSs of the sea surface for two orthogonal components and $b_{x,y}$ is the correlation coefficient between two slope components:

$$\sigma_{x,y}^2 = \left\langle s_{x,y}^2 \right\rangle = \iint_{\kappa<\kappa_*} \kappa_{x,y}^2 \Psi(\vec{\kappa}) d^2\kappa \tag{A.15}$$

$$b_{x,y} = \left\langle s_x s_y \right\rangle / \sigma_x\sigma_y \tag{A.16}$$

$$\left\langle s_x s_y \right\rangle = \iint\limits_{\kappa<\kappa_*} \kappa_x \kappa_y \Psi(\vec{\kappa}) d^2\kappa \qquad \textbf{(A.17)}$$

The PDF of slopes can be also expressed in terms of the up/down wind and across the wind direction components, $\sigma^2_{u,c}$, and angle φ_0 introduced above in Equation A.11. Generally, regardless of the origin of the surface roughness, φ_0 is the angle between the *x*-axis and the slope distribution principle axis. In the case of locally generated wind waves, angle φ_0 is a wind direction angle. For this representation, it is more convenient to use a polar representation for slopes: $s_x = s\cos\psi, s_y = s\sin\psi$. Then Equation A.14 takes this shape:

$$P_s(s,\psi) = \frac{1}{2\pi\sigma_u\sigma_c} \exp\left(-\frac{s^2}{2\sigma_c^2\sigma_u^2}\left[\sigma_u^2+\sigma_c^2-2\left(\sigma_u^2-\sigma_c^2\right)\cos\varphi_0\sin\varphi_0\cos\psi\sin\psi\right]\right) \qquad \textbf{(A.18)}$$

One advantage of a Gaussian distribution is that the variance of slope components in Equations A.14 and A.18 can be derived solely from a wave spectrum, $\Psi(\vec{\kappa})$, of full surface elevations by integrating it over wave numbers, κ, which are smaller than a dividing parameter, κ_*.

There are some indications that the actual PDF of slopes does not exactly follow a Gaussian shape at its tails (Cardellach & Ruis, 2008). In terms of the glistening zone, it implies that this departure affects a periphery of the zone. This would translate into some discrepancy for the value of the waveform, at relatively large time delays, τ, and large frequency offsets, *f*. An ability to discern the difference caused by the departure from the Gaussian PDF of slopes depends on the residual noise in the measurements for the peripheral area of the DDM.

One of the most popular models for the spectrum $\Psi(\vec{\kappa})$ is the model proposed by Elfouhaily et al. (1997). The integrand in Equation A.15 is called a slope spectral density. An example of the Elfouhaily et al. (1997) slope spectrum taken along the wind direction is shown in Figure A.7.

This model describes wind-driven waves in deep water under diverse wave age (often called "fetch") conditions and agrees with the in situ observations of the first sun-glint-derived wave slope measurements of Cox and Munk (1954), performed several decades ago. According to the Elfouhaily et al. (1997) model, an elevation spectrum of a well-developed, wind-driven sea surface can be represented as a product of the radial, or omnidirectional, part of the spectrum and the azimuthal part of the spectrum. The azimuthal part of the spectrum reproduces two main features of the directional spectrum: its anisotropy, or directionality, and the wave number dependence of the angular spectral width. The azimuthal part of the spectrum is a two-sided function; it does not distinguish between up- and down-wind directions. There are other situations when wind direction does not coincide with the maximum of the spectrum (e.g., when gravity waves undergo refraction on currents or on bathymetry, or waves generated by a local wind are superimposed with a swell, or waves generated under hurricane conditions). Such complicated scenarios are not described by the Elfouhaily et al. (1997) spectrum.

As was pointed out above, the MSSs that determine the BRCS through the PDF of slopes are not full wave slopes, even though the sea surface contains wave harmonic components both larger and shorter than the L-band EM waves. The short waves can be disregarded in a process of forward quasi-specular reflection under the GO approximation adopted in Equation A.7. Therefore, the full surface spectrum should be cut off at the high end of wave numbers. There are various choices of cutoff wave numbers, κ_*. For example, there exists a "three-lambda" heuristic criterion for κ_* proposed by G. Brown (1978) based on fitting modeled curves for microwave back scattering cross sections, with cross sections obtained in experiments with satellite radar altimeters. The same criterion was initially applied for use of the Kirchhoff approximation for the two-scale calculations of the bistatic cross sections (Zavorotny & Voronovich, 2000). Later on, a reasonable $\kappa_* = \kappa\cos\theta/3$ on the incidence angle θ was assumed in (Garrison et al., 2002). In the paper (Thompson et al., 2005), an expression for κ_* is obtained that also contains a dependence on wind speed, $\kappa_* = k\cos\theta\left(1+U_{10}/20\right)/7.5$. It was obtained by fitting modeled curves for GPS BRCSs with cross sections obtained in that particular aircraft experiment.

An alternative approach is to obtain an empirical model for the MSS $\left(\sigma^2_{u,c}\right)$ of slopes versus wind speed by performing multiple measurements of GPS waveforms under controlled wind conditions. The best fit between measured waveforms and modeled ones using Equation A.7 for various MSS values

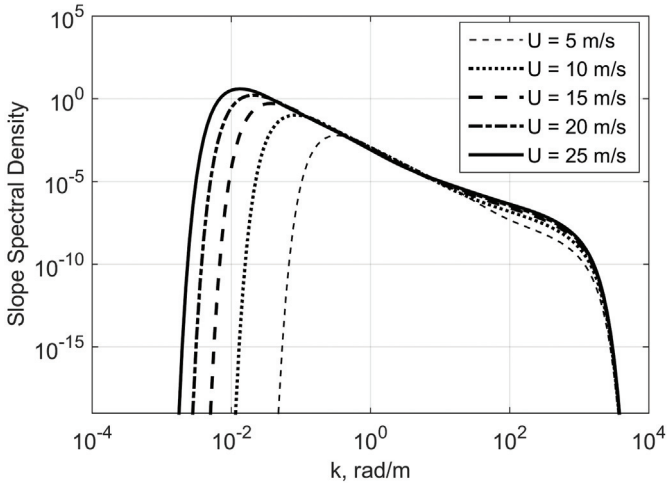

Figure A.7. An example of the Elfouhaily et al. (1997) slope spectrum taken along the wind direction for various wind speed values.

will give the sought dependence MSS versus wind speed. This approach was adopted in Katzberg et al. (2006). The empirical model from Katzberg et al. (2006) gives the following expression:

$$\begin{aligned} mss_{\parallel} &\equiv \sigma_u^2 = 0.45 \cdot (0.00 + 0.00316 f(U)) \\ mss_{\perp} &\equiv \sigma_c^2 = 0.45 \cdot (0.03 + 0.00192 f(U)) \end{aligned} \quad \textbf{(A.19)}$$

where

$$f(U) = \begin{cases} U & 0.00 < U < 3.49 \\ 6 \cdot \ln(U) - 4.0 & 3.49 < U < 46 \\ 0.411 \cdot U & 46.0 > U \end{cases} \quad \textbf{(A.20)}$$

Wind speed U here is m s^{-1} and measured at 10 m height. The extension of $f(U)$ beyond $U = 46$ m s^{-1} proposed in Katzberg et al. (2006) was rather arbitrary because GPS reflection data were not available for such high winds.

Below in Figure A.8, we present comparisons between MSS calculated using all three approaches: two based on the Elfouhaily et al. (1997) spectrum with two different cutoff numbers κ_* from Garrison et al. (2002) and Thompson et al. (2005), and the empirical one from Katzberg et al. (2006). Normal incidence is assumed here.

Figure A.8 demonstrates a comparison between three GO models for MSS in the up/down wind direction (solid curves) and in the crosswind direction (dashed curves) for the range of winds between 0 and 25 m s^{-1}. Some disagreement between them is seen, but overall it is not significant. Figure A.9 shows a comparison between three modeled MSS and MSS retrieved from DDM measurements during aircraft experiments (Rodriguez-Alvarez et al., 2013; Valencia et al., 2014).

In order to make a choice between these three models, we performed calculations of σ_0 using a more accurate (than the GO) approximation (i.e. the SSA, which does not require use of spectral dividing parameter, κ_*). This material is presented below.

D. Integrated Scattering Model: The Bistatic Radar Cross Section in SSA

The SSA was developed earlier (Voronovich, 1994; Voronovich, 1999) and was used successfully for solving various scattering and radiometric problems (see, e.g., Voronovich & Zavorotny, 2001; Elfouhaily & Guérin, 2004; Bourlier et al., 2005; Johnson, 2005; Arnold-Bos et al., 2007a; Arnold-Bos et al., 2007b; Johnson & Elfouhaily, 2007; Soriano & Guérin, 2008; Guérin et al., 2010; Johnson & Ouellette, 2014; Voronovich & Zavorotny, 2014). The geometry of the scattering problem is shown in Figure A.10. Three typical scenarios are depicted, although the model considered below allows any possible combination of incident, scattering, and azimuthal angles and arbitrary polarization states. There are two known approximations of the SSA—the SSA of the 1st order and the SSA of the 2nd order. The latter is more accurate than the former and is required for solving backscattering

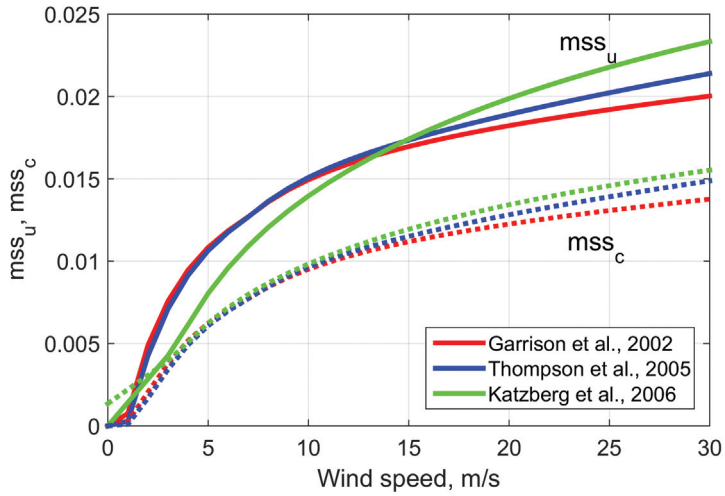

Figure A.8. Comparisons between MSS calculated using three different approaches.

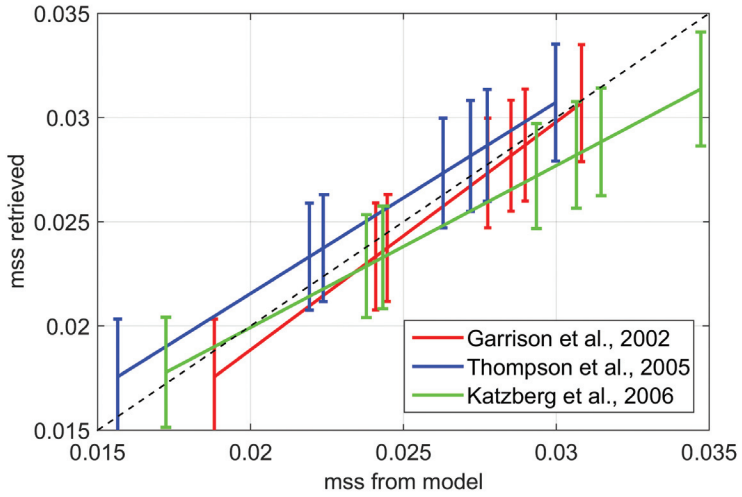

Figure A.9. Comparison between modeled and experimentally measured MSS.

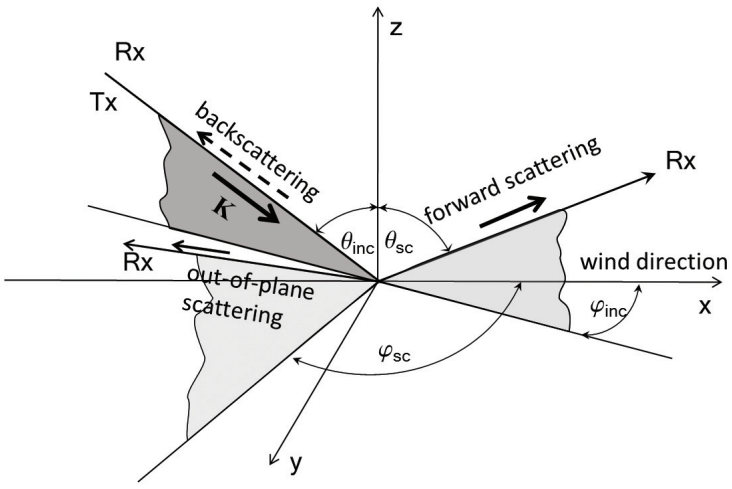

Figure A.10. Bistatic scattering geometry. *Reused from Voronovich & Zavorotny (2014).*

problems with shorter EM wavelengths such as the X- and K-band. Practice shows that for the L-band and for the forward scattering regime, it is sufficient to use the SSA of the 1st order, or SSA1.

Note that the expression for the scattering amplitude in SSA1 coincides with the expression for scattering amplitude in the KA to the accuracy of the preintegral factor. The major difference, however, is that KA gives a correct answer only for the roughness $h(\vec{r})$, which is smooth on the wavelength scale; in this case, the corresponding integral can be evaluated by the stationary phase method, thus leading to the GO approximation. The difference between the GO and KA approximations most likely exceeds the accuracy of the KA itself. In contrast to the KA, SSA1 allows $h(\vec{r})$ to contain a component with a horizontal scale comparable (or even less) than the wavelength, provided that the slope remains small. In this case, the corresponding integral also describes the Bragg scattering process and cannot be calculated by the stationary phase method.

For the case of a large Rayleigh parameter, when the contribution from the average-field-related terms can be neglected, the SSA1 gives the following expression for the BRCS (Johnson, 2005):

$$\sigma_{\alpha\beta,\alpha'\beta'}\left(\vec{k},\vec{k}_0\right) = \frac{4q_k^2 q_0^2}{\pi\left(q_k+q_0\right)^2} B_{\alpha\beta}\left(\vec{k},\vec{k}_0\right)\overline{B}^{*}_{\alpha'\beta'}\left(\vec{k},\vec{k}_0\right) \int_{r<r_{\max}} \exp\left[-i\left(\vec{k}-\vec{k}_0\right)\vec{r}-\left(q_k+q_0\right)^2\left(C(0)-C(\vec{r})\right)\right]d\vec{r} \quad \textbf{(A.21)}$$

where r_{max} determines the area significant for integration. $\alpha,\beta,=1,2$ and $\alpha',\beta'=1,2$ are linear polarization indices for incident and scattering waves, respectively. Function $B_{\alpha,\beta}\left(\vec{k},\vec{k}_0\right)$ in Equation A.21 is a 2 × 2 matrix representing polarizations (1 stands for vertical and 2 stands for horizontal linear polarization), respectively; they depend on the scattering geometry and dielectric constant of the medium. Expressions for them can be found in Voronovich and Zavorotny (2001). Expressions for the LHCP BRCS can be expressed through corresponding cross sections for linear polarization as follows (Zuffada et al., 2004):

$$\sigma_{RL} = \frac{1}{4}\{\sigma_{11,11}+\sigma_{22,22}+\sigma_{12,12}+\sigma_{21,21}+ 2\left[-\mathrm{Re}\,\sigma_{11,22}+\mathrm{Re}\,\sigma_{12,21}-\mathrm{Im}\left(\sigma_{11,12}+\sigma_{11,21}+\sigma_{12,22}+\sigma_{21,22}\right)\right]\} \quad \textbf{(A.22)}$$

We performed calculations of BRCS using Equations A.21 and A.22 and compared them with corresponding BRCS based on the above described GO models for a typical CYGNSS setting and for a range of incidence angles and winds. These results are discussed below.

E. BRCS as a Function of the Incidence Angle and Wind Speed: Comparisons between Three Models

Here we present comparisons between the SSA results and results obtained with the GO model, one using an MSS based on the Elfouhaily et al. (1997) spectrum and the cutoff frequency from (Garrison et al., 2002), and another one using the empirical MSS model from Katzberg et al. (2006). We will call these two GO models the "VZ model" and the "SK model," respectively. First, we present plots showing the corresponding LHCP NBRCS σ_0 in a forward, specular direction as a function of the zenith scattering angle (which in this case equals the incidence angle) for a range of wind speeds from 4 to 30 m s^{-1}. The results for the VZ, KS, and SSA models are shown in Figures A.11a, A.11b, and A.12, respectively. Each plot has 12 curves. The top curve on each plot corresponds to wind speed U = 4 m s^{-1}. The rest of the curves correspond to 5, 6, 7, 8, 9, 10, 12, 15, 20, 25, 30 m s^{-1}, consecutively.

This dependence on wind speed reflects the fact that increased wind produces a stronger surface roughness that, in turn, decreases scattering in the specular direction. One can see that σ_0 behaves differently for each of these models at scattering angles larger than 60°–70°. Remember that none of those models are valid at large scattering angles, so we can disregard this discrepancy. For the case of a CYGNSS antenna pointing angle of about 30°, this discrepancy is not relevant. Note that the SK model from Katzberg et al. (2006) was built on GPS reflection data obtained for low incidence/scattering angles, <45°; therefore, it might not reflect the actual behavior of the scattering at larger angles. At the same time, all three models demonstrate a quite similar behavior over wind speeds for angles below 45°.

To investigate this behavior in more detail, we plot the wind dependence of σ_0 for a set of small scattering angles and for a fixed moderate incidence angle below 45°. Of interest is how predictions for σ_0 from all three models correspond to each other

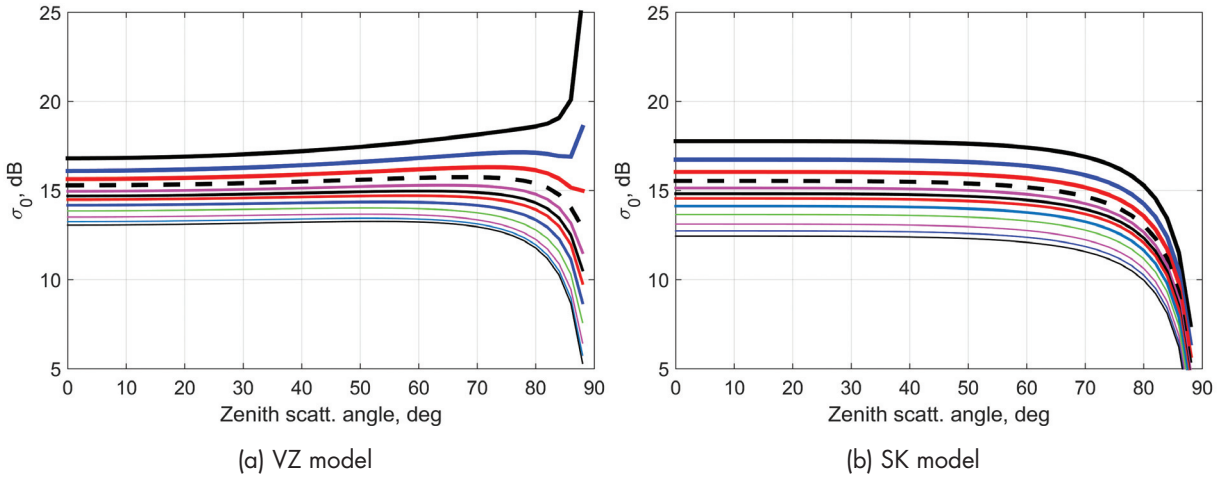

Figure A.11. The LHCP NBRCS σ_0 in a forward, specular direction as a function of the zenith scattering angle for VZ (a) and SK (b) models, respectively. *Reused from Zavorotny & Voronovich (2014).*

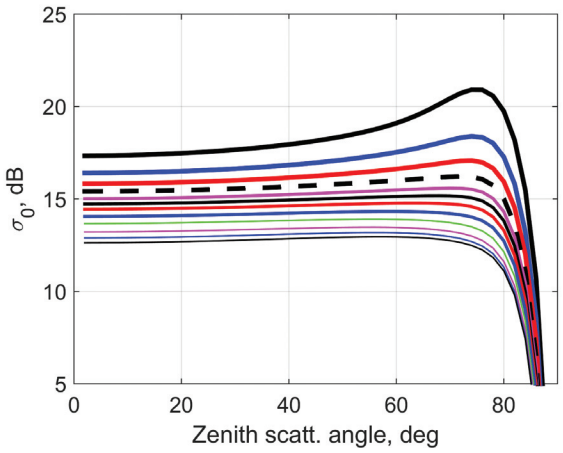

Figure A.12. The LHCP BRCS σ_0 in a forward, specular direction as a function of the zenith scattering angle for the SSA model. *Reused from Zavorotny & Voronovich (2014).*

for scattering originated from various points on the surface area, limited to some number of delay zones that contribute to the DDM. The corresponding scattering geometry is shown in Figure A.13.

Notation in Figure A.13 is as follows: a_n and b_n are major semiaxes of the elliptic delay zones, where index n corresponds to a. They can be expressed through the chip length l, receiver altitude H, and incidence angle θ_{in}:

$$a_n = b_n / \cos\theta_{in}, \quad b_n = \left(2nlH / \cos\theta_{in}\right)^{1/2}. \qquad \textbf{(A.23)}$$

Figure A.14 shows how angles $\theta_{sc,\min}$, $\theta_{sc,\max}$, and ϕ_{sc} from Figure A.13 can be related to the corresponding points on the delay-zone ellipse for a range of delay-zone indices (from 0 to 10). The curves are plotted for θ_{in} = 30°, H = 600 km, and l = 300 m (or C/A code). The data in this figure shows that for the first delay zone, the maximum azimuth scattering angle is equal to 2.56°.

In Figure A.15, we present plots of σ_0 obtained with the three models for θ_{in} = 30°, H = 600 km, and for four directions of the scattering vector described by the following combinations of zenith and azimuth scattering angles: (a) θ_{sc} = 30°, ϕ_{sc} = 0°; (b) θ_{sc} = 30°, ϕ_{sc} = 2.56°; (c) θ_{sc} = 28°, ϕ_{sc} = 0°; and (d) θ_{sc} = 32°, ϕ_{sc} = 0°. This set of angles gives an angular extent for the first delay zone (n = 1). Case (a) describes a nominal specular direction originating

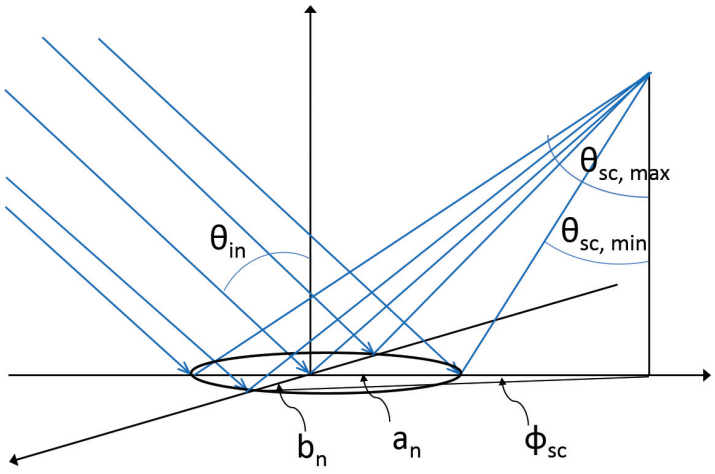

Figure A.13. Scattering geometry, where a_n and b_n are major semiaxes of the elliptic delay zones, where index n corresponds to a.

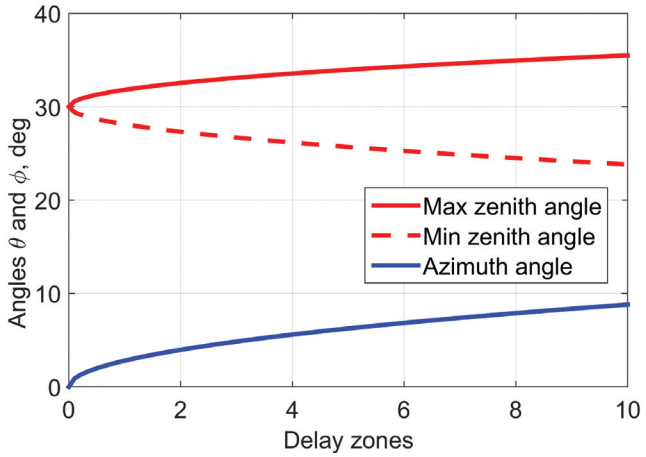

Figure A.14. Relationship between values of scattering and zenith angles and the corresponding points on the delay-zone ellipse for a range of delay-zone indices (from 0 to 10).

from the center of the delay zone. Case (b) describes a scattering direction originating from both the left and right most distant (in a cross direction) points of the first delay-zone ellipse. This is an example of out-of-plane scattering. Here, by "plane" we mean a specular plane that, by definition, passes through the SP on the surface and both transmitter and the receiver points. Case (c) describes a scattering direction originating from the closest point on the first delay-zone ellipse. Correspondingly, case (d) is for the farthest point on the first delay-zone ellipse.

One can see that the curves in Figure A.15 practically repeat themselves at each panel. This means that while LHCP BRCS σ_0 is changing with the wind speed, it does not appreciably change over the angles within the first delay zone. The discrepancy between curves for all three models are within 0.5 dB for wind speed below 15–17 m s^{-1}, which is rather negligible, given such adverse factors as speckle noise and natural wind speed variability that accompany real measurements. The discrepancy between the SSA curve and the SK curve (which we use in the E2ES) is less than 0.5 dB for the entire range of wind speeds used for this simulation (i.e., below 30 m s^{-1}). More important is that the steepness of these two curves are close to each other, which would result in a similar accuracy of the wind retrievals from the real bistatic radar data.

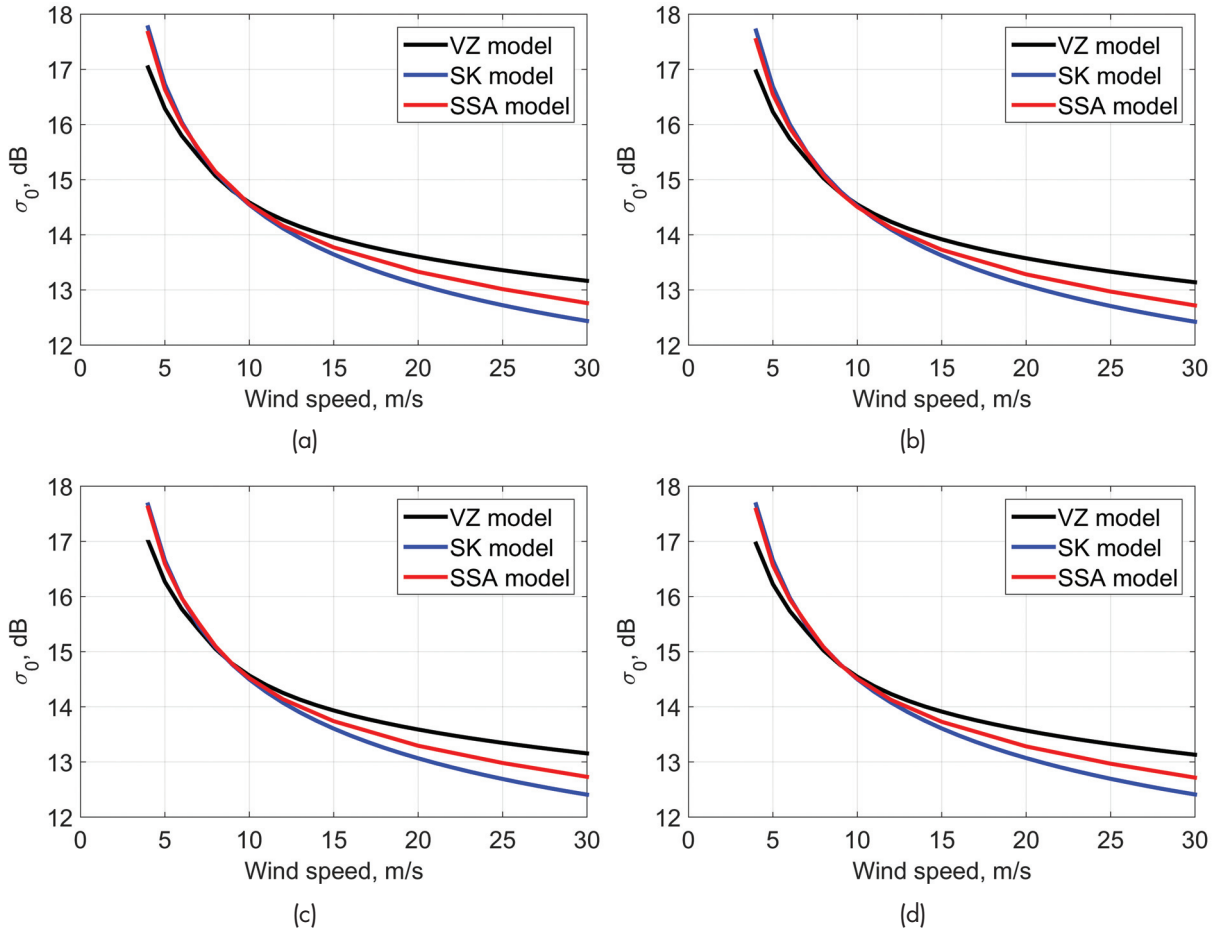

Figure A.15. The LHCP BRCS σ_0 as a function of wind speed for three models for (a) a nominal specular direction originated from the center of the delay zone, (b) a scattering direction originating from both the left and right most distant (in a cross direction) points of the first delay-zone ellipse, (c) a scattering direction originated from the closest point on the first delay-zone ellipse, and (d) for the farthest point on the first delay-zone ellipse.

In Figures A.16, we present similar plots of σ_0 obtained with the three models for the same basic geometry with an angular extent for the tenth delay zone (n = 10). The tenth delay zone covers the surface area, which contributes to the DDM that will be routinely used during the CYGNSS mission. Here, therefore, (a) $\theta_{sc} = 30°, \phi_{sc} = 0°$ (this plot repeats plot [a] from the previous figure; it is given for comparison purposes); (b) $\theta_{sc} = 30°, \phi_{sc} = 8°$; (c) $\theta_{sc} = 25°, \phi_{sc} = 0°$; and (d) $\theta_{sc} = 35°, \phi_{sc} = 0°$.

As one can see, there is no significant difference between this set of plots and the one from the previous figure. Therefore, the same statement about σ_0 behavior can be made here for the case of the tenth delay zone.

F. Section Summary

In this section, we described how the NBRCS σ_0 of the ocean, wind-driven rough surface emerges within the framework of the bistatic radar equation, which governs the average bistatic radar signal in the delay-Doppler domain. We presented two alternative approaches to simulate σ_0. One of them is based on the GO limit of the KA (Barrick, 1968; Bass & Fuks, 1979), and another one is the Voronovich SSA1 (Voronovich, 1994; Voronovich, 1999; Voronovich & Zavorotny, 2014). The latter approach is superior to the former one because it combines two scattering mechanisms: quasi-specular reflections at steep incidence and the Bragg resonant scattering at the shallower incidence, whereas the GO approximation re-

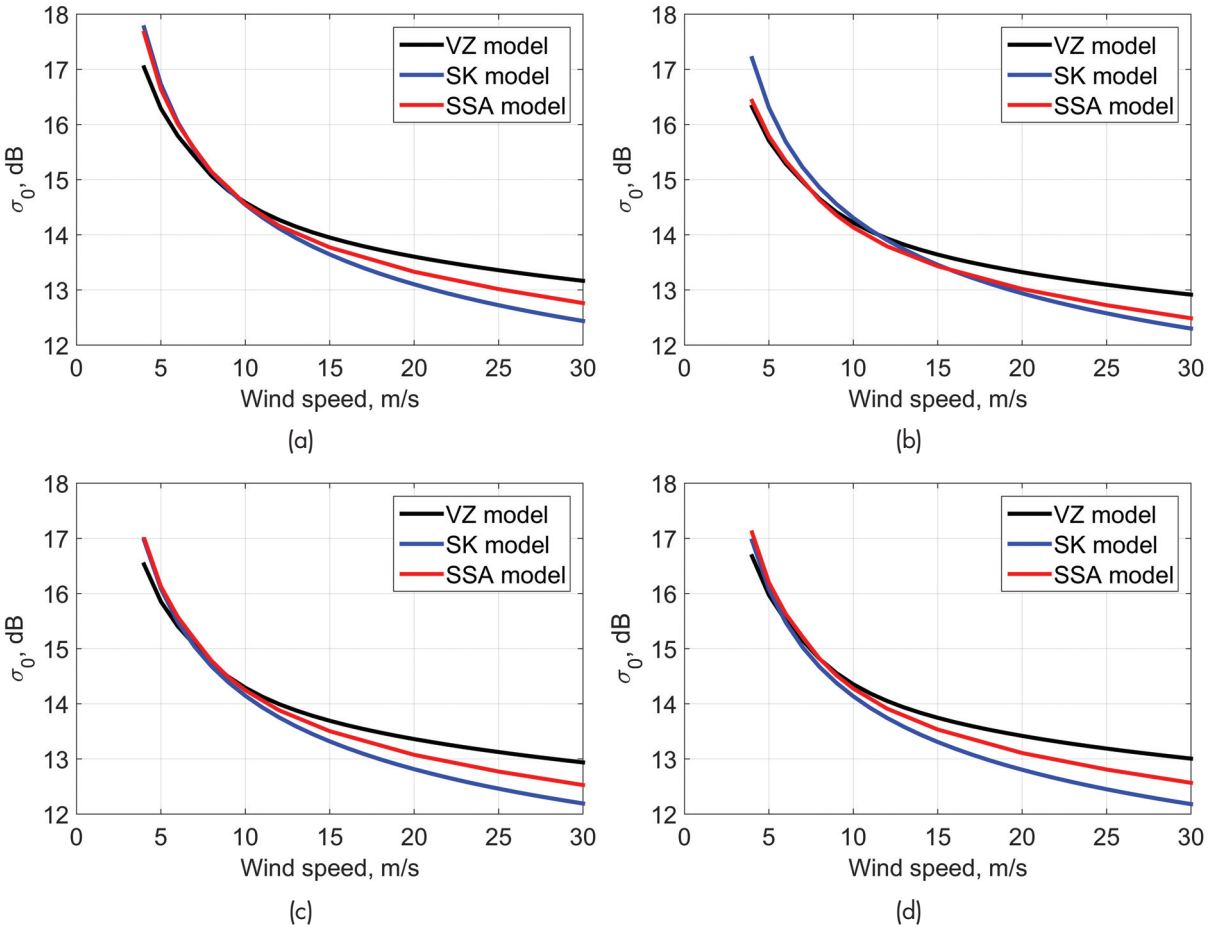

Figure A.16. Same as in Figure A.15 but for an angular extent that corresponds to the tenth delay zone (n = 10).

lies only on the first mechanism for the whole range of incidence angles. Both of these approaches require knowledge of the ocean wave spectrum or, as in the case of the GO approach, the model of the MSS will suffice. To this end, the theoretical model based on Elfouhaily's ocean wave spectrum (Elfouhaily et al., 1997) with two different frequency cutoffs was tested, as well as the Katzberg empirical MSS model (Katzberg et al., 2006). All these models demonstrate good agreement for weak and intermediate winds. They depart from each other only for strong winds, and this departure is rather tolerable given such adverse factors as speckle noise and natural wind speed variability that accompany real measurements.

Originally, the Katzberg empirical MSS model has been used in the E2ES for simulating DDMs. This choice was made because this model is based on a collection of aircraft GPS reflection measurements obtained for a large variety of wind speeds, including for hurricane conditions. Comparisons between σ_0 modeled with both the GO and the SSA approaches show that for the geometry of CYGNSS orbital observatories and for the range of winds up to 30 m s^{-1}, the GO approximation with Katzberg's empirical MSS model works very well. The advantage of the GO approximation is its simplicity and high speed of calculations, whereas the SSA approximation is more time consuming. All this makes our choice for the σ_0 computational algorithm even more substantiated.

Previously, some concerns have been expressed (see, e.g., Thompson et al., 2000) that the GO approximation might not work well for the GNSS reflectometry because it cannot properly account for out-of-plane scattering. Generally, the GO approximation has its own limitations, especially for calculations of the RHCP σ_0, and particularly for the out-plane

configuration. However, as it was demonstrated here, for small deviations from the specular plane, the LHCP σ_0 is quite close to that one predicted by the more accurate SSA approximation.

The more fundamental limitation of all above models lies in the fact that they either have been proven only for global winds below 25–30 m s^{-1} (such as for those based on the Elfouhaily et al. [1997] spectrum), or their accuracy is not high for strong hurricane winds (such as in the case of Katzberg's MSS model). For hurricane conditions, a feasible wave-spectral model should include, apart from a local wind speed, several other parameters such as a distance from the hurricane center, azimuthal angle (a quadrant), the hurricane velocity, and other hurricane parameters.

Plans are to use an existing WAVEWATCH III wave model (Tolman, 1997) developed at the NOAA NCEP, which is now widely used for hurricane long-wave predictions (e.g., Fan et al., 2009). As a first step, it is expected that this model will be able to provide us with the long-wave portion of the sea state spectrum (so called "fresh swell") in the hurricane eye specifically and everywhere in general. More challenging would be to extend this model toward much shorter waves up to the cutoff frequency introduced above. Also, plans are to verify the DDM output of such a model with already available radiometric, scatterometric, and bistatic radar data obtained in hurricanes. For this, archives of past aircraft bistatic radar overpasses of hurricane eyes can be used in order to assemble time series records of the MSS and to infer surface wind speed in the eye. Other surface wind estimates (e.g., from flight level winds or SFMR) are also available. Raw DDM-grade bistatic radar data from Hurricanes Ike (2008), Rafael (2012), and Sandy (2012) obtained with the University of Colorado (CU) bistatic GPS radar can also be used for validation purposes. The processing of these data for CYGNSS purposes is currently being performed.

III. Statistics of the GPS Reflected Signal

A. Mean Power and Signal-to-Noise Ratio

Let us represent the instantaneous complex signal (the voltage) u, which is acquired directly by the receiver from the antenna output or as a result of some coherent processing, in the form

$$u(t) = s(t) + n(t) \tag{A.24}$$

where $s(t)$ is the complex amplitude of the scattered signal and $n(t)$ is the complex amplitude of the additive noise. We assume that $s(t)$ and $n(t)$ are two uncorrelated, stationary random processes; both obey circular Gaussian statistics and have different time scales, and different variances $\sigma_1^2 \equiv \sigma_{Res}^2 \equiv \sigma_{Ims}^2$ and $\sigma_2^2 \equiv \sigma_{Ren}^2 \equiv \sigma_{Imn}^2$, both with zero means. The Gaussian statistics for $s(t)$ can be justified if the signal at the antenna is formed by contributions from a large number of independent surface scatterers. Here we exclude from a consideration fluctuations of the signal caused by propagation through ionospheric and tropospheric irregularities. Fluctuations of $s(t)$ generate multiplicative, self-noise (also called interference noise, Rayleigh fading, and speckle noise), which is proportional to the signal, whereas fluctuations of $n(t)$ produce additive, background noise (i.e., thermal noise or shot noise). In a more complex situation, the additive noise could include extraneous emitted signals. So, in what follows, we limit that background noise to thermal noise.

A coherent processing of the scattered GPS signal by the correlator channel of the CYGNSS receiver consists of the convolution (correlation) of voltage $u(t)$ with the replica a of the GPS broadcast signal over a relatively short (milliseconds) coherent integration time T_i:

$$Y(t_0, \tau) = \int_0^{T_i} a(t_0 + t')u(t_0 + t' + \tau)\,dt' \tag{A.25}$$

Taking into account (A.24), we obtain from (A.25) that

$$Y(t_0, \tau) = Y_s(t_0, \tau) + Y_n(t_0, \tau) \tag{A.26}$$

where

$$Y_s(t_0, \tau) = \int_0^{T_i} a(t_0 + t')s(t_0 + t' + \tau)\,dt' \tag{A.27}$$

$$Y_n(t_0, \tau) = \int_0^{T_i} a(t_0 + t')n(t_0 + t' + \tau)\,dt' \tag{A.28}$$

Therefore, the quantities in Equations A.27 and A.28 are short-integrated (practically, instantaneous) correlation voltages, respectively, for the signal and noise. The next step of the signal processing is

obtaining the mean power of the correlator output. It is obtained by an additional averaging of $\left|Y(t_0,\tau)\right|^2$ over a long enough observation time, so both thermal and surface-induced fluctuations are substantially averaged out. The result is

$$\left\langle \left|Y(t_0,\tau)\right|^2 \right\rangle = \left\langle \left|Y_s(t_0,\tau)\right|^2 \right\rangle + \left\langle \left|Y_n(t_0,\tau)\right|^2 \right\rangle \quad \textbf{(A.29)}$$

The first term in Equation A.29 is an average signal introduced above in Equation A.7. The second term in Equation A.29 is the background noise term. It can be written as a double integral over the coherent integration time:

$$\left\langle \left|Y_n(t_0,\tau,f)\right|^2 \right\rangle = \int_0^{T_i} dt' \int_0^{T_i} dt'' a(t_0+t',f) a(t_0+t'',f) \times \left\langle n(t_0+\tau+t') n^*(t_0+\tau+t'') \right\rangle \quad \textbf{(A.30)}$$

Assume that the thermal noise is the "white" (delta-correlated) noise—in other words,

$$\left\langle n(t') n^*(t'') \right\rangle = kT^\circ B_n b_n(t'-t'') \quad \textbf{(A.31)}$$

where k is Boltzmann constant, T° is the receiver noise equivalent temperature in Kelvin, $B_n = 1/T_{cor}$ is the receiver-front-end bandwidth, and T_{cor} is a temporal correlation scale of the noise filtered by the front end:

$$b_n(t) = \int W_n(f) \exp(2i\pi f t) df \qquad \int_0^{T_i} b_n(t)\, dt = T_{cor} \quad \textbf{(A.32)}$$

Here $W_n(f)$ is the normalized temporal spectrum of the noise. Usually background noise has a much smaller temporal correlation scale, T_{cor}, than the C/A chip-length, $\tau_{chip} = 1\,\mu$s. In other words, the noise bandwidth is much greater than the bandwidth of the C/A pseudorandom phase modulation of the GPS signals. Thus we can regard function $b_n(t'-t'')$ as a delta function, so two integrations over time can be performed trivially. The result is

$$\left\langle \left|Y_n(t_0,\tau,f)\right|^2 \right\rangle = T_i^2 kT^\circ B_D \quad \textbf{(A.33)}$$

where $B_D = 1/T_i$ is the Doppler bandwidth of the signal.

The thermal noise is correlated between delay-Doppler bins. The cross-correlation function between the noise in different bins is given by

$$\left\langle Y_n(t_0,\tau,f) Y^*{}_n(t_0,\tau',f') \right\rangle = \int_0^{T_i} dt' \int_0^{T_i} dt'' a(t_0+t',f) a^*(t_0+t'',f') \times \left\langle n(t_0+\tau+t') n^*(t_0+\tau'+t'') \right\rangle \quad \textbf{(A.34)}$$

Since the noise is uncorrelated with the reference signal, the reference signal acts as a filter for the noise, causing it to be correlated with respect to delay and Doppler according to the GPS C/A code ambiguity function. Equation A.34 can be reduced to

$$\left\langle Y_n(t_0,\tau,f) Y^*{}_n(t_0,\tau',f') \right\rangle = T_i^2 kT^\circ B_D \Lambda^2(d\tau) \left|S(df)\right|^2 \quad \textbf{(A.35)}$$

In the forward model, zero mean white Gaussian noise is generated with respect to delay and Doppler using the power level in Equation A.7 and then convolved with the ambiguity function to produce the correct bin-to-bin correlations.

Now we can construct the SNR. There are various definitions of SNR. We use here the simplest one, which shows how much the mean power of the signal exceeds the mean noise level:

$$SNR = \left\langle \left|Y_s(t_0,\tau)\right|^2 \right\rangle \Big/ \left\langle \left|Y_n(t_0,\tau)\right|^2 \right\rangle \quad \textbf{(A.36)}$$

Recall that the SNR is the function of parameters τ and f_{dop} (i.e., the SNR is different for different portions of waveforms taken at different time delays and Doppler frequency offsets).

B. Statistics of the Partially Averaged GPS Reflected Signal Affected by Both Thermal and Speckle Noise

Previously, we considered the effect of additive thermal noise on the average SNR. It exists due to the physical temperature of both the receiver and the scene even in the absence of the GPS reflected signal. Another type of noise, the multiplicative one, is a result of distractive and constructive interference of coherent signals arriving at the antenna upon scattering from a rough ocean surface. It is called Rayleigh fading, or speckle noise, and it is proportional to the signal itself. Below we consider statistics of the partially averaged signal affected by both thermal and speckle noise.

In a real situation, we deal with values averaged over a finite time interval. It happens for at least two reasons. First, any measuring device has a finite time response. Second, signals often need to be accumulated over some time in order to improve the SNR.

Since the integration or averaging time is finite, the procedure does not lead to constant time-independent values. These partially averaged values are still random quantities and need to be described in statistical terms. Note that an instantaneous power U of the signal + noise is not only comprised of the sum of the instantaneous powers S and N for the signal and the noise, respectively. It contains also cross terms of s and n. Indeed, according to Equation A.24,

$$U(t) \equiv |u(t)|^2 = \left[s(t)+n(t)\right]\left[s^*(t)+n^*(t)\right] = S(t)+N(t)+C(t)+C^*(t) \quad \textbf{(A.37)}$$

where

$$C(t) = s(t)n^*(t) \quad \textbf{(A.38)}$$

During the measurement we obtain an estimate of the signal + noise from the power of the received signal + noise averaged over an arbitrary time interval T (a bar above refers to that type of averaging):

$$\bar{U}(t) \equiv \bar{S}(t)+\bar{N}(t)+\bar{C}(t)+\bar{C}^*(t) = \frac{1}{T}\int_{-T/2}^{T/2}\left[S(t+t')+N(t+t')+C(t+t')+C^*(t+t')\right]dt' \quad \textbf{(A.39)}$$

An estimate of the signal can be done by obtaining an estimate of the signal + noise, then obtaining an estimate of noise from an independent measurement, and then subtracting one from another:

$$\tilde{S}(t) = \bar{U}(t) - \bar{N}(t_0) \quad \textbf{(A.40)}$$

Since these estimates are obtained from an averaging over the finite period of time, the estimate of the signal, $\tilde{S}(t)$, is a fluctuating quantity. The accuracy of the estimate is governed by the variance of estimate $\tilde{S}(t)$. Since $\bar{U}(t)$ and $\bar{N}(t_0)$ are statistically independent, the following equality holds:

$$\sigma_{\tilde{S}}^2 = \sigma_{\bar{U}}^2 + \sigma_{\bar{N}}^2 \quad \textbf{(A.41)}$$

Observe that the mean value of the estimated power of the signal + noise is simply

$$\left\langle \bar{U} \right\rangle = \left\langle S \right\rangle + \left\langle N \right\rangle \quad \textbf{(A.42)}$$

The variance of the total power of signal + noise is

$$\sigma_{\bar{U}}^2 = \frac{1}{T^2}\left\langle \left| \int_{-T/2}^{T/2}\left[S(t')+N(t')+C(t')+C^*(t')\right]dt' \right|^2 \right\rangle - \left\langle \bar{U} \right\rangle^2 \quad \textbf{(A.43)}$$

The variance of the noise power is

$$\sigma_{\bar{N}}^2 = \frac{1}{T^2}\left\langle \left| \int_{-T/2}^{T/2} N(t')\,dt' \right|^2 \right\rangle - \left\langle N \right\rangle^2 \quad \textbf{(A.44)}$$

Assuming statistical stationarity of both the signal and the noise and making several additional simplifying assumptions, without loss of generality, the standard deviation of the estimated signal power can be obtained in the following form:

$$\frac{\sigma_{\hat{S}}}{\left\langle S \right\rangle} = \left[\left(1+2\left\langle S \right\rangle + 2T_{\text{int}} / \tau_{cor}\left\langle S \right\rangle^2\right)/N\right]^{1/2} \quad \textbf{(A.45)}$$

For $T >> \tau_{cor}$, the parameter $N = T / \tau_{cor}$ is the number of correlation intervals contained within the measurement time, T. Or it could be interpreted as a number N of independent samples.

In order to proceed further, we need to choose the value of the correlation time of the signal, τ_{cor}. The approach for calculation of the correlation time based on the power spectrum of the scattered signal or, equivalently, through the coherence function of the signal that was developed in Zuffada and Zavorotny (2001), You et al. (2004), and You et al. (2006).

Actually, the time correlation can be estimated using the Van Cittert-Zernike theorem. From this theorem, the size of the field correlation zone at a wavelength λ is

$$r_{cor} = \lambda R / D \quad \textbf{(A.46)}$$

where R is a distance from the surface to the receiver and D is a size of the illuminated area. At the peak correlation power, the illuminated area is the first annulus zone modified by the smaller Doppler zone. The smallest size matters because it created the biggest r_{cor}, which translates into the largest correlation time $\tau_{cor} = r_{cor} / v_{sat}$ (see, e.g., Figure 1 in Zuffada & Zavorotny, 2001). The size of the Doppler zone is dictated by the coherent integration time. The analysis shows that $\tau_{cor} \approx 2T_i$; therefore, if T_i is 1 ms, $\tau_{cor} = 2$ ms. Taking this into account, Equation A.45 simplifies:

$$\frac{\sigma_{\hat{S}}}{\langle S\rangle} = \left(1 + 2\langle S\rangle^{-1} + 2T_{\text{int}}\tau_{cor}^{-1}\langle S\rangle^{-2}\right)^{1/2} N^{-1/2} \approx \frac{1+1/\langle S\rangle}{\sqrt{N}} \quad \textbf{(A.47)}$$

From here we can produce an expression for the standard deviation of S (the SNR) after incoherent averaging over N statistically independent samples:

$$\sigma_{SNR} = = \frac{\langle S\rangle + 1}{\sqrt{N}} \quad \textbf{(A.48)}$$

Therefore, in this case, the standard deviation of partially averaged SNR is proportional to the average SNR plus one and can be reduced by $\sqrt{N}$. In a general case of arbitrary τ_{cor} and T_i,

$$\sigma_{SNR} = \frac{\sqrt{\langle S\rangle^2 + 2\langle S\rangle + 2T_{\text{int}}\tau_{cor}^{-1}}}{\sqrt{N}} \quad \textbf{(A.49)}$$

IV. Simulation of Speckle Noise

The reflected signal received by each CYGNSS observatory is formed by contributions from a large number of independent surface scatterers. This random scattering generates multiplicative self-noise (i.e., Rayleigh fading or speckle noise), which is proportional to the signal. This is in contrast to thermal noise, which is additive. This section describes how this speckle noise is accounted for in the forward model.

Recall the bistatic radar equation from Part II A. The expected value of the power of the reflected signal versus delay and Doppler can be rewritten as

$$\left\langle \left|Y_s(t_0,\tau,f)\right|^2 \right\rangle = \iint H(\vec{\rho})\Lambda^2(\tau,\vec{\rho})\left|S(f,\vec{\rho})\right|^2 d^2\rho \quad \textbf{(A.50)}$$

where

$$H(\vec{\rho}) = T_i^2 \frac{P_T G_T \lambda^2 G_R}{(4\pi)^3} R_0^{-2} R^{-2} \sigma_0(\vec{\rho}) \quad \textbf{(A.51)}$$

represents the contribution of each location on the surface to the total expected power of the reflected signal at a particular delay and Doppler.

In the forward model, DDMs are formed from integrations performed over finite time intervals rather than expected values (such as in Equation A.50). We must model the effect of speckle noise, but for the surface areas involved in spaceborne GPS reflectometry, it would be unrealistic to instantiate the actual random rough surface and use a computational electromagnetics approach. Rather we have chosen a suitable method to accurately capture the effects of speckle noise.

First, we take the square root of the power contribution in Equation A.51 and include a time varying phase term $\phi(t,\rho)$ to make the contribution complex,

$$h(t,\rho) = \sqrt{H(\rho)}e^{i\phi(t,\rho)} \quad \textbf{(A.52)}$$

This is an approximate representation of the contribution of each location on the surface to the voltage DDM and can be thought of as the transfer function over the surface. The approximate voltage DDM is given by

$$Y_s(t,\tau,f) = \iint h(t,\vec{\rho})\Lambda(\tau,\vec{\rho})S(f,\vec{\rho})d^2\rho \quad \textbf{(A.53)}$$

If the DDM is formed by integrating for 1 second, t will be between t_0 and (t_0+1), where t_0 is the start of the integration. This produces

$$\left|Y_s(t_0,\tau,f)\right|^2 = \int_{t_0}^{t_0+T} Y_s(t,\tau,f)Y^*{}_s(t,\tau,f)dt, \quad \textbf{(A.54)}$$

where T =1. The phase term $\phi(t,\rho)$ must be chosen such that the expectation of Equation A.54 is equal to one from Equation A.50. Also, it must result in the temporal correlation of speckle noise.

First, a random phase, $\phi_0(\rho)$, is associated with each location on the surface. This random phase is assumed uniformly distributed between 0 and 2π and represents the phase shift caused by the random rough surface at that location. This phase will evolve in time according to the changing geometry of the satellites. Thus the total phase associated with the reflection of a particular point on the surface is a combination of the random phase and phase associated the total path length,

$$\phi(\rho) = \phi_0(\rho) + \frac{2\pi}{\lambda}R(t,\rho) \quad \textbf{(A.55)}$$

where λ is the wavelength at the GPS L1 center frequency and $R(t,\rho)$ is the total path length from the transmitter to the surface location at ρ and up to the receiver at time t. Since it is such a short duration, the time variation in the path length can be accurately approximated using the Doppler at the start of the integration $f_D(t_0,\rho)$,

$$R(t,\rho) = R(t_0,\rho) - (t-t_0)\lambda f_D(t_0,\rho) \quad \textbf{(A.56)}$$

Each point on the surface will exhibit a different time varying phase, depending on the relative motion of the satellites. Over short time delays (e.g., less than one millisecond), the change in geometry will be small and the speckle noise will remain correlated in time. For longer delays, the speckle noise will be completely decorrelated, as is expected from reflections from a real ocean surface.

References

Arnold-Bos, A., Khenchaf, A., & Martin, A. (2007a). Bistatic radar imaging of the marine environment—Part I: Theoretical background. *Geoscience and Remote Sensing, IEEE Transactions On*, *45*(11), 3372–3383. doi: 10.1109/TGRS.2007.897436

Arnold-Bos, A., Khenchaf, A., & Martin, A. (2007b). Bistatic radar imaging of the marine environment—Part II: Simulation and results analysis. *Geoscience and Remote Sensing, IEEE Transactions On*, *45*(11), 3384–3396. doi: 10.1109/TGRS.2007.899812

Barrick, D. E. (1968). Relationship between slope probability density function and the physical optics integral in rough surface scattering. *Proceedings of the IEEE*, *56*(10), 1728–1729. doi: 10.1109/PROC.1968.6718

Bass, F. G., & Fuks, I. M. (1979). *Wave scattering from statistically rough surfaces* (Vol. 93). Elmsford, NY: Pergamon.

Bourlier, C., Déchamps, N., & Berginc, G. (2005). Comparison of asymptotic backscattering models (SSA, WCA, and LCA) from one-dimensional Gaussian ocean-like surfaces. *Antennas and Propagation, IEEE Transactions On*, *53*(5), 1640–1652. doi: 10.1109/TAP.2005.846800

Brown, G. S. (1978). Backscattering from a Gaussian-distributed perfectly conducting rough surface. *Antennas and Propagation, IEEE Transactions On*, *26*(3), 472–482. doi: 10.1109/TAP.1978.1141854

Cardellach, E., & Rius, A. (2008). A new technique to sense non-Gaussian features of the sea surface from L-band bi-static GNSS reflections. *Remote Sensing of Environment*, *112*(6), 2927–2937. doi: 10.1016/j.rse.2008.02.003

Clarizia, M. P., & Ruf, C. (2016). Wind speed retrieval algorithm for the Cyclone Global Navigation Satellite System (CYGNSS) mission. *IEEE Transactions on Geoscience and Remote Sensing*. Manuscript in review.

Cox, C., & Munk, W. (1954). Measurement of the roughness of the sea surface from photographs of the sun's glitter. *Journal of the Optical Society of America*, *44*(11), 838–850. doi: 10.1364/JOSA.44.000838

Elachi, C. (1988). *Spaceborne radar remote sensing: Applications and techniques*. New York, NY: IEEE Press.

Elfouhaily, T., Chapron, B., Katsaros, K., & Vandemark, D. (1997). A unified directional spectrum for long and short wind-driven waves. *Journal of Geophysical Research-Oceans*, *102*(C7), 15781–15796. doi: 10.1029/97JC00467

Elfouhaily, T. M., & Guérin, C. A. (2004). A critical survey of approximate scattering wave theories from random rough surfaces. *Waves in Random Media*, *14*(4), R1–R40. doi: 10.1088/0959-7174/14/4/R01

Elfouhaily, T., Thompson, D. R., & Linstrom, L. (2002). Delay-Doppler analysis of bistatically reflected signals from the ocean surface: Theory and application. *Geoscience and Remote Sensing, IEEE Transactions On*, *40*(3), 560–573. doi: 10.1109/TGRS.2002.1000316

Fan, Y., Ginis, I., Hara, T., Wright, C. W., & Walsh, E. J. (2009). Numerical simulations and observations of surface wave fields under an extreme tropical cyclone. *Journal of Physical Oceanography*, *39*(9), 2097–2116. doi: http://dx.doi.org/10.1175/2009JPO4224.1

Garrison, J. L., Komjathy, A., Zavorotny, V. U., & Katzberg, S. J. (2002). Wind speed measurement using forward scattered GPS signals. *Geoscience and Remote Sensing, IEEE Transactions On*, *40*(1), 50–65. doi: 10.1109/36.981349

Gleason, S. (2006). *Remote sensing of ocean, ice and land surfaces using bistatically scattered GNSS signals from low earth orbit* (Doctoral dissertation, University of Surrey).

Gleason, S., & Gebre-Egziabher, D. (Eds.). (2009), *GNSS applications and methods*. Norwood, MA: Artech House.

Gleason, S., Hodgart, S., Sun, Y., Gommenginger, C., Mackin, S., Adjrad, M., & Unwin, M. (2005). Detection and processing of bistatically reflected GPS signals from low Earth orbit for the purpose of ocean remote sensing. *Geoscience and Remote Sensing, IEEE Transactions On*, *43*(6), 1229–1241. doi: 10.1109/TGRS.2005.845643

Guérin, C. A., Soriano, G., & Chapron, B. (2010). The weighted curvature approximation in scattering from sea surfaces. *Waves in Random and Complex Media*, *20*(3), 364–384. doi: http://dx.doi.org/10.1080/17455030903563824

Johnson, J. T. (2005). A study of ocean-like surface thermal emission and reflection using Voronovich's small slope approximation. *Geoscience and Remote Sensing, IEEE Transactions On*, *43*(2), 306–314. doi: 10.1109/TGRS.2004.841480

Johnson, J. T., & Elfouhaily, T. M. (2007). Computation of oceanlike surface thermal emission and bistatic scattering with the reduced local curvature approximation. *Geoscience and Remote Sensing, IEEE Transactions On*, *45*(7), 2108–2115. doi: 10.1109/TGRS.2006.890420

Johnson, J. T., & Ouellette, J. D. (2014). Polarization features in bistatic scattering from rough surfaces. *Geoscience and Remote Sensing, IEEE Transactions On*, *52*(3), 1616–1626. doi: 10.1109/TGRS.2013.2252909

Katzberg, S. J., Torres, O., & Ganoe, G. (2006). Calibration of reflected GPS for tropical storm wind speed retrievals. *Geophysical Research Letters*, *33*(18). doi: 10.1029/2006GL026825

Klein, L., & Swift, C. T. (1977). An improved model for the dielectric constant of sea water at microwave frequencies. *Antennas and Propagation, IEEE Transactions On*, *25*(1), 104–111. doi: 10.1109/TAP.1977.1141539

Parkinson B. W., Spilker, J. J., Axelrad, P., & Enge, P. (Eds.). (1996). *Global positioning system: Theory and applications* (Vol. 2). Washington, DC: AIAA.

Rodriguez-Alvarez, N., Akos, D. M., Zavorotny, V. U., Smith, J., Camps, A., & Fairall, C. W. (2013). Airborne GNSS-R wind retrievals using delay-Doppler maps. *Geoscience and Remote Sensing, IEEE Transactions On*, *51*(1), 626–641. doi: 10.1109/TGRS.2012.2196437

Soriano, G., & Guérin, C. A. (2008). A cutoff invariant two-scale model in electromagnetic scattering from sea surfaces. *Geoscience and Remote Sensing Letters, IEEE*, *5*(2), 199–203. doi: 10.1109/LGRS.2008.915746

Soulat, F. (2004). *Sea surface remote sensing with GNSS and sunlight reflections*. (Doctoral dissertation, Universitat Politecnica de Catalunya).

Thompson, D. R., Elfouhaily, T. M., & Garrison, J. L. (2005). An improved geometrical optics model for bistatic GPS scattering from the ocean surface. *Geoscience and Remote Sensing, IEEE Transactions On*, *43*(12), 2810–2821. doi: 10.1109/TGRS.2005.857895

Thompson, D. R., Elfouhaily, T. M., & Gasparovic, R. F. (2000). Polarization dependence of GPS signals reflected from the ocean. In *Geoscience and Remote Sensing Symposium, 2000. Proceedings. IGARSS 2000. IEEE 2000 International* (Vol. 7, pp. 3099–3101). Honolulu, HI. doi: 10.1109/IGARSS.2000.860349

Tolman, H. L. (1997). A new global wave forecast system at NCEP. *Ocean Wave Measurements and Analysis*, *2*, 777–786.

Valencia, E., Zavorotny, V. U., Akos, D. M., & Camps, A. (2014). Using DDM asymmetry metrics for wind direction retrieval from GPS ocean-scattered signals in airborne experiments. *Geoscience and Remote Sensing, IEEE Transactions On*, *52*(7), 3924–3936. doi: 10.1109/TGRS.2013.2278151

Voronovich, A. (1994). Small-slope approximation for electromagnetic wave scattering at a rough interface of two dielectric half-spaces. *Waves in Random Media*, *4*(3), 337–368. doi: 10.1088/0959-7174/4/3/008

Voronovich, A. G. (1999). *Wave scattering from rough surfaces* (2nd ed.). Berlin: Springer.

Voronovich, A. G., & Zavorotny, V. U. (2014). Full-polarization modeling of monostatic and bistatic radar scattering from a rough sea surface. *Antennas and Propagation, IEEE Transactions On*, *62*(3), 1362–1371. doi: 10.1109/TAP.2013.2295235

Voronovich, A. G., & Zavorotny, V. U. (2001). Theoretical model for scattering of radar signals in k_u-and c-bands from a rough sea surface with breaking waves. *Waves in Random Media*, *11*(3), 247–269. doi: 10.1080/13616670109409784

You, H., Garrison, J. L., Heckler, G., & Smajlovic, D. (2006). The autocorrelation of waveforms generated from ocean-scattered GPS signals. *Geoscience and Remote Sensing Letters, IEEE*, *3*(1), 78–82. doi: 10.1109/LGRS.2005.856704

You, H., Garrison, J. L., Heckler, G., & Zavorotny, V. U. (2004). Stochastic voltage model and experimental measurement of ocean-scattered GPS signal statistics. *Geoscience and Remote Sensing, IEEE Transactions On*, *42*(10), 2160–2169. doi: 10.1109/TGRS.2004.834628

Zavorotny, V. U., & Voronovich, A. G. (2000). Scattering of GPS signals from the ocean with wind remote sensing application. *Geoscience and Remote Sensing, IEEE Transactions On*, *38*(2), 951–964. doi: 10.1109/36.841977

Zavorotny, V. U., & Voronovich, A. G. (2014, July). Recent progress on forward scattering modeling for GNSS reflectometry. In *Geoscience and Remote Sensing Symposium (IGARSS), 2014 IEEE International* (pp. 3814–3817). Quebec, Canada. doi: 10.1109/IGARSS.2014.6947315

Zuffada, C., Fung, A., Parker, J., Okolicanyi, M., & Huang, E. (2004). Polarization properties of the GPS signal scattered off a wind-driven ocean. *Antennas and Propagation, IEEE Transactions On, 52*(1), 172–188. doi: 10.1109/TAP.2003.822438

Zuffada, C., & Zavorotny, V. (2001). Coherence time and statistical properties of the GPS signal scattered off the ocean surface and their impact on the accuracy of remote sensing of sea surface topography and winds. In *Geoscience and Remote Sensing Symposium, 2001. IGARSS'01. IEEE 2001 International* (Vol. *7*, pp. 3332–3334). Sydney. doi: 10.1109/IGARSS.2001.978344